Aeolus Data Innovation Science Cluster
DISC

Verification report for phase 1 of the fourth reprocessing campaign for the FM-B laser from June 2019 till October 2022

DISC-Ref.: AEDF-TN-ECMWF-GEN-007

Issue: V 1.05

Date: 09/08/2024

ECMWF

Document Title

Verification report for phase 1 of the fourth reprocessing campaign for the FM-B laser from June 2019 till October 2022

aeolus DISC

Document Change Log

Issue	Date	New pages	Modified pages (after introducing new pages)	Observations	Name
V 1.0	15 May 2024	-	-	Initial version for 4th reprocessing starting from 3rd reprocessing doc and including L2B verification.	Michael Rennie
V 1.01	24 June 2024			Include results from IFS-COMPO O-B departures for L2A backscatter. Include L2A attenuated backscatter monitoring.	Michael Rennie, Will McLean, Mark Fielding
V 1.02	5 July 2024			Include monitoring of SCA from TROPOS and IRCs from DLR	Dimitri Trapon, Uwe Marksteiner
V 1.03	23 July 2024			Include KNMI results on L2A AEL-FM/AEL-PRO	Ping Wang
V1.04	6 August 2024			Include a summary of AUX_PAR_2B changes and AUX_ZWC and L1B results from DLR	Jos de Kloe, Uwe Marksteiner and Vittoria Filomarino
V1.05	9 August 2024			Include review changes from DLR	Stefanie Knobloch and Oliver Reitebuch

ECMWF

Document Title

Verification report for phase 1 of the fourth reprocessing campaign for the FM-B laser from June 2019 till October 2022

aeolus DISC

Table of Contents

1 Introduction

1.1 Compliance Statement

The Verification report for phase 1 of the fourth reprocessing campaign for the FM-B laser from June 2019 till October 2022 is fully compliant with the management requirements of the Aeolus DISC Phase F1 ESA Contract No. 4000144330/24/I-AG.

1.2 Applicable Documents

[AD-1] DLR (2020): DISC Project Management Plan. AEDF-MP-DLR-GEN-001, V 1.01, 12/07/2024.

1.3 Reference Documents

[RD-1] Abdalla, S., de Kloe, J., Flament, T., Krisch, I., Marksteiner, U., Reitebuch, O., Rennie, M., Weiler, F., Witschas, B. (2020), Verification report of first Reprocessing campaign for FM-B covering the time period 2019-06 to 2019-12, Aeolus DISC Technical Note, AED-TN-ECMWF-GEN-040, v1.

[RD-2] Abdalla, S., Flament, T., Krisch, I., Marksteiner, U., Reitebuch, O., Rennie, M., Trapon, D., Weiler, F. (2021), Verification report of the second reprocessing campaign for FM-B from 24 June 2019 till 9 October 2020, Aeolus DISC Technical Note, AED-TN-ECMWF-GEN-060, v1.1.

[RD-3] Masoumzadeh, N. et al. (2022), Third Reprocessing campaign for FM-A covering the time period 2018-08 to 2019-06, Aeolus DISC Technical Note, AED-TN-DLR-GEN-061, v2.

[RD-4] Aeolus DISC (2021), The dark side of Aeolus during the IOCV phase. Aeolus DISC Technical Note, AE-TN-DLR-7300-2, issue 1.1, also available as a handover report file AE-TN-ESA-SY-094_Dark_Signal_Analysis_V1_1.pdf. Available from the internal DISC web site: https://csde.esa.int/confluence/display/AEOLUSDISC/dL1B_037?preview=%2F143105764%2F143105785%2FAE-TN-ESA-SY-094_Dark_Signal_Analysis_V1_1.pdf

[RD-5] Weiler, F., Kanitz, T., Wernham, D., Rennie, M., Huber, D., Schillinger, M., Saint-Pe, O., Bell, R., Parrinello, T., and Reitebuch, O. (2021), "Characterization of dark current signal measurements of the ACCDs used on board the Aeolus satellite", Atmos. Meas. Tech., 14, 5153–5177, https://doi.org/10.5194/amt-14-5153-2021.

[RD-6] Weiler, F. (2020), "Detecting hot pixel induced steps in the Aeolus atmospheric signals", Master thesis, Department of Mathematics, University of Innsbruck, 85pp.

[RD-7] Weiler, F. (2021), "Detecting hot pixel induced steps in Aeolus atmospheric signals", Aeolus DISC Technical Note, AED-TN-L1B-GEN-064, v 1.0.

[RD-8] Weiler, F. (2022), "Reprocessing – Hot Pixel Correction", Presentation during WM 177 on 12 Jan. 2022, PowerPoint presentation file: E2_WM177_FW_Reprocessing_hot_pixel_correction.pptx

[RD-9] Weiler, F. (2022), "Aeolus 3rd reprocessing FM-A period - DCMZ generation and validation", Aeolus DISC analysis report in a form of PowerPoint presentation file: FM_A_reprocessing_AUX_DCMZ_validation_FW_25_01_2022.pptx.

[RD-10] Marseille, G.-J., de Kloe, J., Marksteiner, U., Reitebuch, O., Rennie, M. & de Haan, S. (2022), NWP calibration applied to Aeolus Mie channel winds. Quarterly Journal of the Royal Meteorological Society, 148(743), 1020–1034. Available from: https://doi.org/10.1002/qj.4244

[RD-11] Abdalla, S., Flament, T., Krisch, I., Marksteiner, U., Masoumzadeh, N., Reitebuch, O., Rennie, M., Trapon, D., Weiler, F. (2023), Verification report of the third reprocessing campaign for first FM-A period from September 2018 till June 2019, Aeolus DISC Technical Note, AED-TN-ECMWF-GEN-080, v1.01 (06/06/2023)

[RD-12] Masoumzadeh, N. et al. (2023), Fourth Reprocessing campaign for the full mission time period from August 2018 to end of mission, Aeolus DISC Technical Note, AED-TN-DLR-GEN-081, v1.0 (01/03/2023).

[RD-13] Rennie, M., and Isaksen, L. (2024), The NWP Impact of Aeolus Level-2B Winds at ECMWF, ESA Contract Report, doi:10.21957/d4ea1c09d4

[RD-14] Aeolus DISC consortium (2024), Aeolus DISC Phase E2 final report, AED-PR-DLR-GEN-013, v2.0 (14/06/2024)

[RD-15] Baron, A., Chazette, P., Khaykin, S., Payen, G., Marquestaut, N., Bègue, N., & Duflot, V. (2023). Early evolution of the stratospheric aerosol plume following the 2022 Hunga Tonga-Hunga Ha'apai eruption: Lidar observations from Reunion (21°S, 55°E). Geophysical Research Letters, 50, e2022GL101751. https://doi.org/10.1029/2022GL101751

1.4 Acronyms & Abbreviations

An up-to-date list of abbreviations used within DISC and in this document can be found in the Aeolus DISC Wiki: https://csde.esa.int/confluence/display/AEOLUSDISC/Aeolus+DISC+Acronym+List.

2 Background

The first, second and third Aeolus reprocessing campaigns (see Figure 1) have been successfully performed covering:

1. **First reprocessing (B10):** Flight Model B (FM-B) laser from 24 June 2019 to 31 December 2019 ([RD-1]).
2. **Second reprocessing (B11):** FM-B laser from 24 June 2019 to 9 October 2020 ([RD-2]).
3. **Third reprocessing (B14):** FM-A laser from 31 August 2018 to 16 June 2019 ([RD-11]).

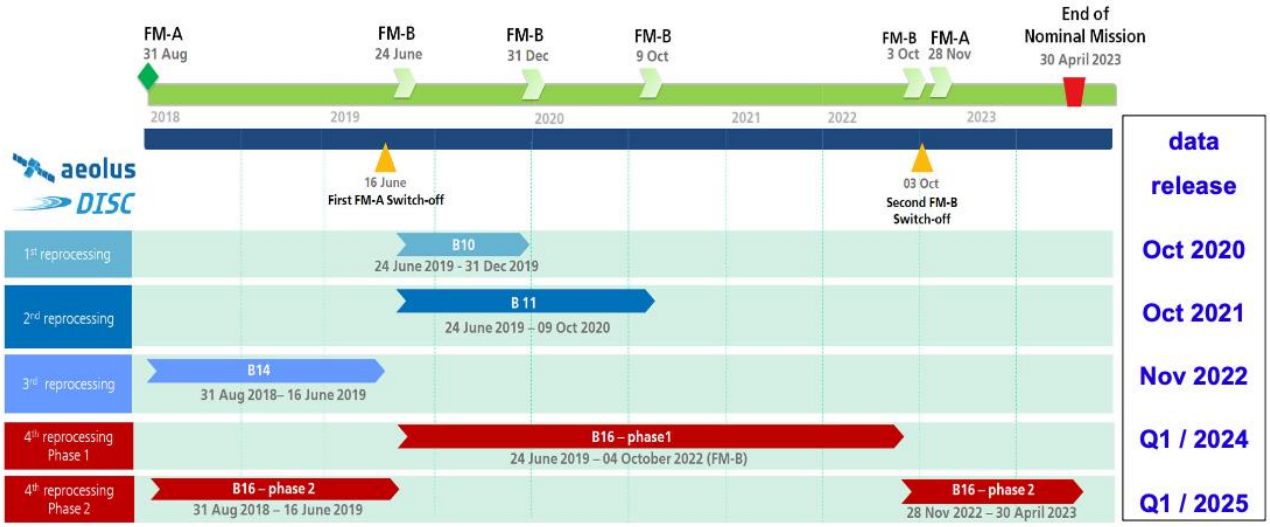

Figure 1: Timeline of reprocessing campaigns and product baselines for Aeolus data products.

This document focusses on the verification on **phase 1** of the **fourth reprocessing** campaign covering the period using the **FM-B laser** from **24 June 2019 to 4 October 2022**. This is the longest consistently reprocessed data period for the mission so far. The reprocessing covers L1A, L1B, L2A and L2B data products as well as the respective auxiliary files. The data was made available to the public on 22 May 2024[1].

It was performed using the processor versions deployed by the PDGS in near-real time (NRT) generation from 18 April 2023 using baseline 16 (B16) (processor versions: L1bP 7.14.3, L2aP 3.16.4, L2bP 3.90). However, the auxiliary files have been adjusted to suit the FM-B laser data of the reprocessing period. The FM-B data quality has improved a lot due to the many processing algorithm improvements developed since the second reprocessing which used a baseline (B11) which was first deployed by PDGS for NRT data on 8 October 2020.

[1] It can be found on ESA's website (https://aeolus-ds.eo.esa.int/oads/access/collection). See the "Aeolus B16 Reprocessing Campaign" section.

This baseline also includes new L2A aerosol products down to ~3 km horizontal resolution: Aeolus Feature Mask (AEL-FM), Aeolus Profile (AEL-PRO) and Maximum Likelihood Estimation (MLEsub). The finer resolution already helped capturing aerosol layers and this may facilitate cross analysis with ground-based measurement. The first usable L2A and L2B products are available from 28 June 2019 onwards after the instrument settled following the finalisation of the instrument settings (for that initial period).

A separate TN will report on the verification of phase 2 of the fourth reprocessing which will cover the remaining data of the mission for the FM-A laser in 2018/2019 (31 August 2018 to 16 June 2019 and in 2022/2023 (28 November 2022 to 30 April 2023, not including the End-of-Life testing period). Further information on the fourth reprocessing campaign can be found in [RD-12].

The various auxiliary and Level-2 products are verified in this Technical Note. The sections of this report are as follows. The reprocessed auxiliary data were validated by comparison against their original counterparts. Section 3 presents the validation of AUX_ZWC data while Section 4 shows the validation of files resulting from the Instrument Response Calibration procedure: AUX_MRC and AUX_RRC data. Section 5 focuses on the verification of L1B products. Verification of L2A optical properties and L2B wind products are presented in Sections 6 and 7. The conclusions are provided in Section 8.

3 AUX_ZWC

The verification of the AUX_ZWC (Zero Wind Correction) files was carried out *only for the first verification round*, that is comparing the Near-Real-Time data from the 2nd reprocessing (Baseline 11, where available) against Sandbox products from the 4th reprocessing. The verification was performed with the DLR harmonic-bias estimator (HBE) tool, which uses the AUX_ZWC files as input. Improvements are considered as such, if there are more ground returns than in the data from the last reprocessing, if the ground velocities have a median closer to zero and a smaller mean absolute deviation (MAD).

Table 1 provides the following parameters:

- Number of valid ground correction velocities after additional QC by the HBE tool
- Additional QC by the HBE-tool for NRT / RPRO4:
    - Minimum Useful Signal (for both Rayleigh and Mie): 10.000 LSB
    - Minimum SNR: 1
    - Minimum no. of valid meas. per observation: 1
- Median Absolute Deviation (MAD) of the residual in m/s after subtraction of the HBE fit

In general, the reprocessing of the AUX_ZWC files yields variable results regarding the number of ground returns as well as for the MAD of the residual for Mie and Rayleigh. Depending on the case (whole test week) the number of ground returns can increase or decrease for the RPRO4 data set compared to RPRO2 or NRT. The same holds for the MAD.

Document Title

Verification report for phase 1 of the fourth reprocessing campaign for the FM-B laser from June 2019 till October 2022

Table 1: Summary table for the verification of the AUX_ZWC files produced by Sandbox versus the NRT and the second reprocessing (RPRO2) or Baseline 11.

Test week		Num. of files			Total points			Mie points			Ray Points			Mie MAD m/s			Ray MAD m/s		
		NRT	RPRO2	RPRO4	NRT	RPRO2	RPRO4	NRT	RPRO2	RPRO4	NRT	RPRO2	RPRO4	NRT	RPRO2	RPRO4	NRT	RPRO2	RPRO4
1. 2019 July		104	104	104	9076	9285	9269	4618	4867	4811	4458	4418	4458	0.3	0.2	0.3	1.1	1.2	1.1
2. 2019 Sept.		104	104	103	8182	9503	9369	4441	5069	4890	3741	4434	4479	0.1	0.2	0.2	0.8	0.9	0.9
3. 2020 June.		103	103	103	8027	11051	10897	3938	5290	5190	4089	5761	5707	0.2	0.2	0.4	1.1	1.3	1.3
4. 2020 Aug.		106	104	104	8161	8155	8076	3883	3880	3844	4278	4275	2432	0.2	0.2	0.2	1.1	1.1	1.1
5. 2021 Sept.		104	-	104	6736	-	7274	3016	-	3587	3720	-	3677	0.2	-	0.2	1	-	1.1
6. 2022 Jan.		104	-	104	12295	-	14492	4751	-	6912	7544	-	7580	0.1	-	0.2	1	-	1
7. 2022 June		103	-	103	8312	-	9557	3368	-	4604	4944	-	4953	0.1	-	0.2	1	-	1
8. 2022 Sept.		119	-	119	10524	-	8950	358	-	4235	4686	-	4715	0.2	-	0.2	1	-	1

4 AUX_MRC and AUX_RRC

To verify the Instrument Response Calibration (IRC) files i.e. AUX_MRC (Mie Response Calibration) and AUX_RRC (Rayleigh Response Calibration) files provided by the PDGS from the 4th reprocessing campaign (RPRO4), we look at the plausibility of their content, specifically at the values obtained for slope (sensitivity), intercept (zero frequency) and offset frequency. Comparisons are performed between the PDGS dataset (Baseline 16) and a mixed set of original near-real-time IRCs (Baseline 12 – 15) and two manually reprocessed IRCs (Baseline 12), as listed in Table 2.

Table 2: Details on the set of IRCs used for comparison against the PDGS dataset from the 4th reprocessing.

Mode	Number	Date	Laser	Baseline	Comment
IRC	062 – 063	2021-05-06 - 2021-05-13	FM-B	12	reprocessed manually with L1B v.7.10
IRC	064 – 081	2021-06-03 - 2021-11-15	FM-B	12	near real-time versions L1B v.7.10
IRC	081 – 096	2021-12-06 - 2022-03-28	FM-B	13	near real-time versions L1B v.7.11
IRC	097 – 119	2022-04-04 - 2022-09-12	FM-B	14	near real-time versions L1B v.7.12
IRC	120 – 121	2022-09-19 - 2022-09-26	FM-B	15	near real-time versions L1B v.7.13

For the comparisons, only the period from the resumption of the IRCs (#062 on 2021-05-06) after the almost 1.5 years of suspension until the switch back to FM-A (IRC #2021 on 2022-09-26) is considered. The comparison dataset with the older IRC versions comprises 60 IRCs in total, 20 of which processed with L1B v.7.10 (Baseline 12), 15 with L1B v.7.11 (Baseline 13), 23 with L1B v.7.12 (Baseline 14) and 2 with L1B v.7.13 (Baseline 15). However, the dataset of the 4th reprocessing provides only 59 IRCs for the selected period because IRC #088 from 2022-01-24 is missing in the respective "Jan2022-aux-tar" package. The data from the 4th reprocessing was taken from the ftp server: aeolus-ops-repo.eo.esa.int (131.176.221.243).

Per default the Sandbox does not provide output for calibration modes, however, during preparation activities for the 4th reprocessing campaign, all IRCs from the FM-B period were made available as Baseline 16 version (L1B v.7.14) by Jos de Kloe (KNMI) on request after additional Sandbox runs. These IRCs were successfully checked for plausibility of their content but no detailed checks or comparisons against previous baselines were performed.

The L1B processor v.7.14 (Baseline 16) included several improvements, amongst others an update of the Rayleigh SNR calculation, a new DCO correction method (mode mean), a new QC for the DCMZ mode, the introduction of the EMSR (estimated Mie signal response) and corrected calculation of the Rayleigh_Average_Ground_Wind_Bin_Thickness.

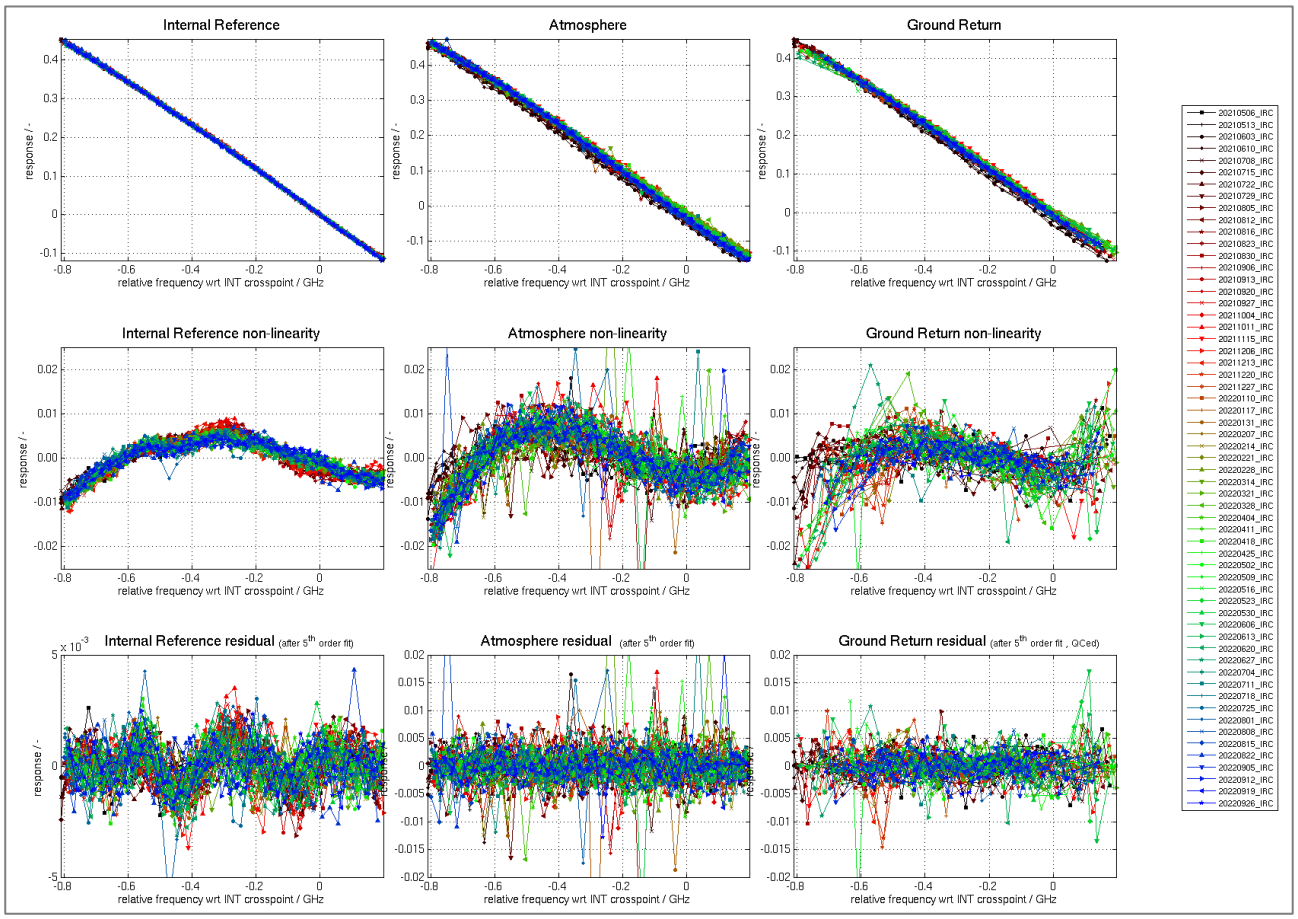

Figure 2: Rayleigh response curves (top), non-linearities (middle) and residuals (bottom) for the internal reference (left), atmosphere (centre) and ground return (right) of the selected 59 RRCs from the PDGS reprocessed dataset.

Figure 2 and Figure 3 show the Rayleigh response curves, their non-linearities and the residuals after having subtracted a 5th order polynomial fit for the PDGS dataset from the 4th reprocessing and the comparison dataset, respectively. Improvement, i.e. better performance of the RPRO4 dataset, becomes visible in single points, for example:

- on the atmospheric path residual for the 2021-08-16 around [-0.75 GHz / 0.015]
- on the atmospheric path residual for the 2021-08-30 around [-0.6 GHz / 0.016]
- for the ground return residual for the 2021-08-30 around [-0.8 GHz / 0.011]

- for the ground return residual for the 2022-01-17 around [0.0 GHz / -0.017]

We attribute these improvements to the new features of the L1B v.7.14. (Baseline 16) as mentioned above.

The overall shape and distribution of the residuals of the atmospheric path and the ground returns give the strong impression of a reduced/improved random error of the responses of the RPRO4 data set.

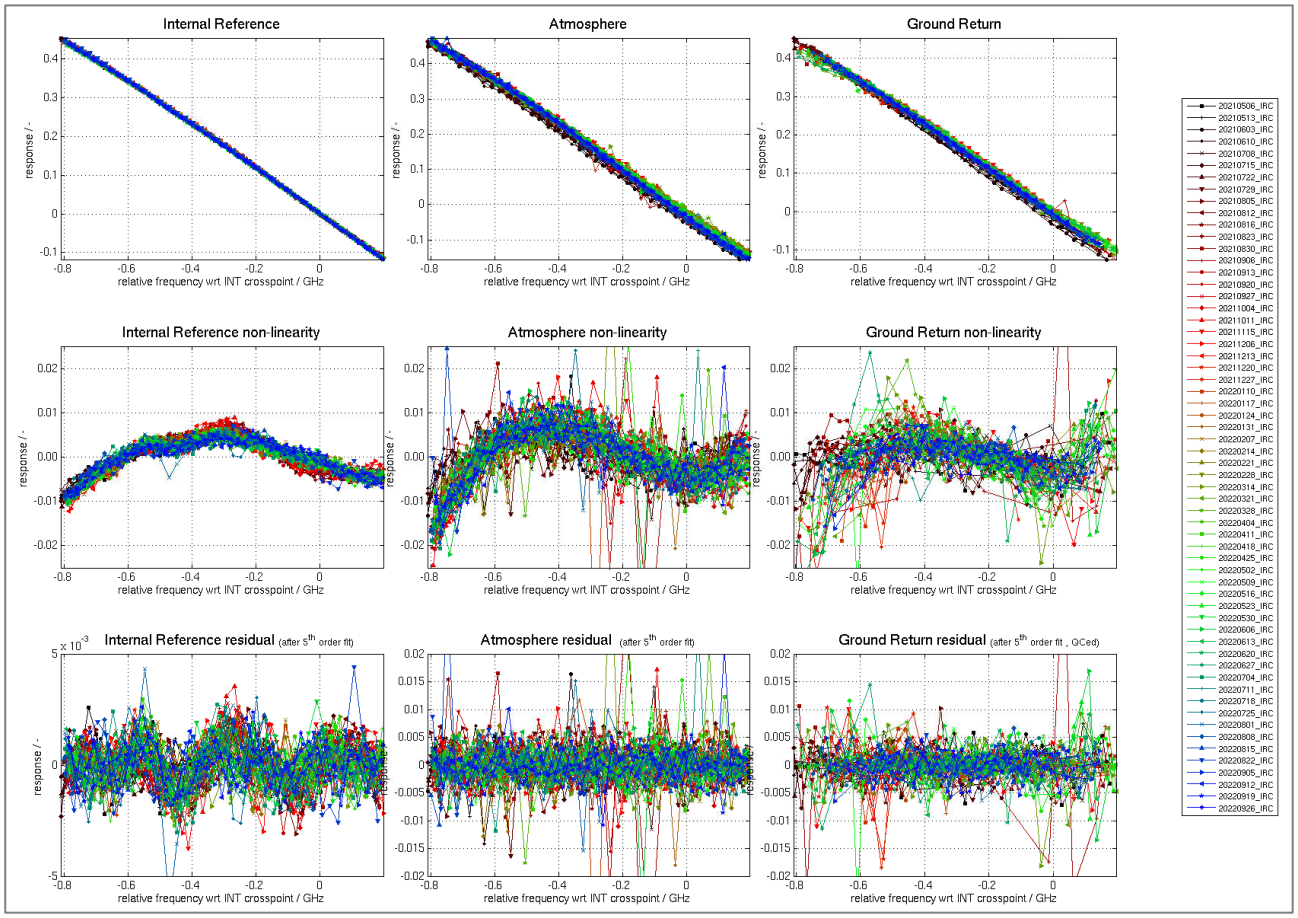

Figure 3: Rayleigh response curves (top), non-linearities (middle) and residuals (bottom) for the internal reference (left), atmosphere (centre) and ground return (right) of the selected 60 RRCs from the comparison dataset.

Continuous timelines of the slope, intercept (intersection with y-axis) and offset frequency (intersection with x-axis) are presented in Figure 4, Figure 5 and Figure 6 for the RPRO4 dataset. The continuity itself and the fact that there are no obvious outliers show that the content of the AUX_RRC files is valid and reasonable.

Document Title

Verification report for phase 1 of the fourth reprocessing campaign for the FM-B laser from June 2019 till October 2022

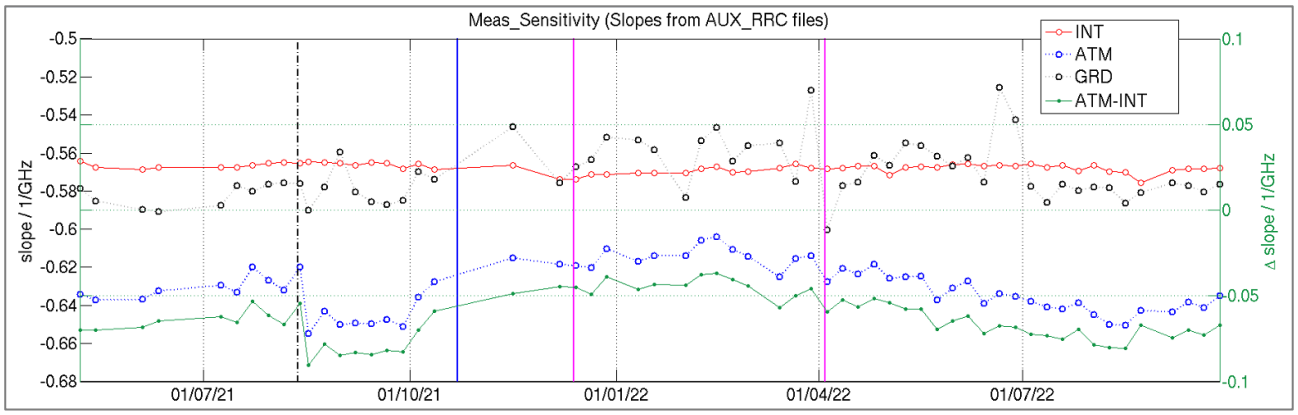

Figure 4: Slope (Mean_Sensitivity) for the internal reference (INT), atmosphere (ATM) and ground return (GRD) of the selected 59 RRCs from the PDGS reprocessed dataset. The difference between ATM and INT is given in green on a second y-axis.

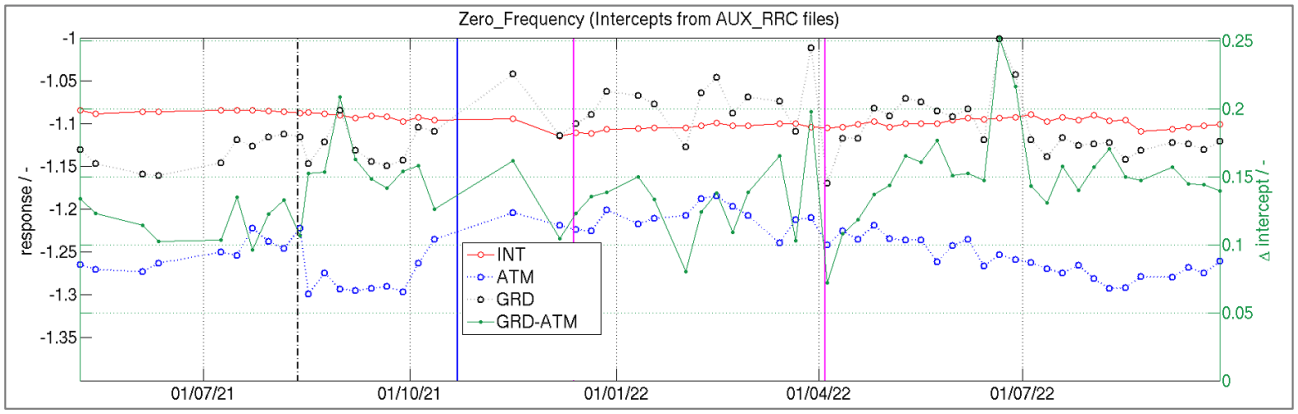

Figure 5: Intercept (Zero_Frequency) for the internal reference (INT), atmosphere (ATM) and ground return (GRD) of the selected 59 RRCs from the PDGS reprocessed dataset. The difference between ATM and INT is given in green on a second y-axis.

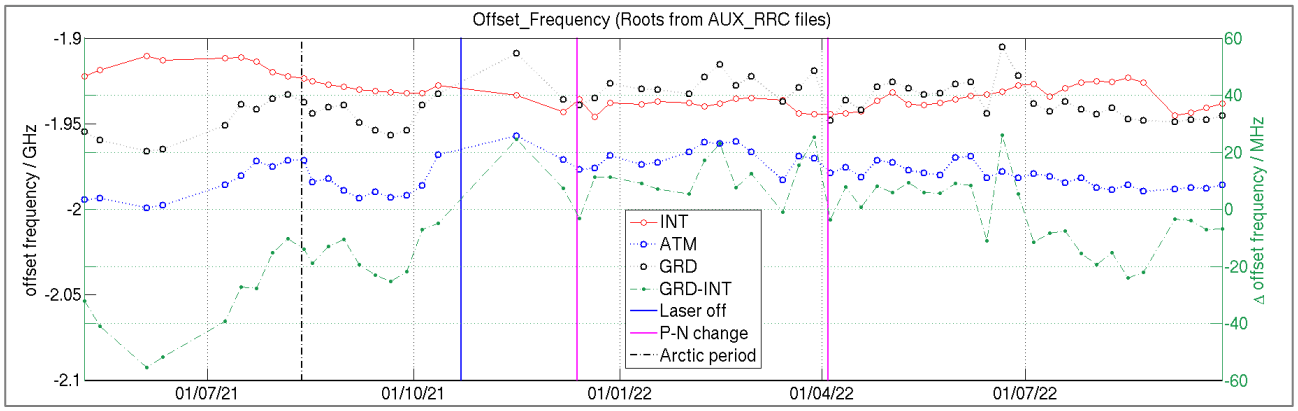

Figure 6: The x-axis intersection (Offset_Frequency) for the internal reference (INT), atmosphere (ATM) and ground return (GRD) of the selected 59 RRCs from the PDGS reprocessed dataset. The difference between ATM and INT is given in green on a second y-axis.

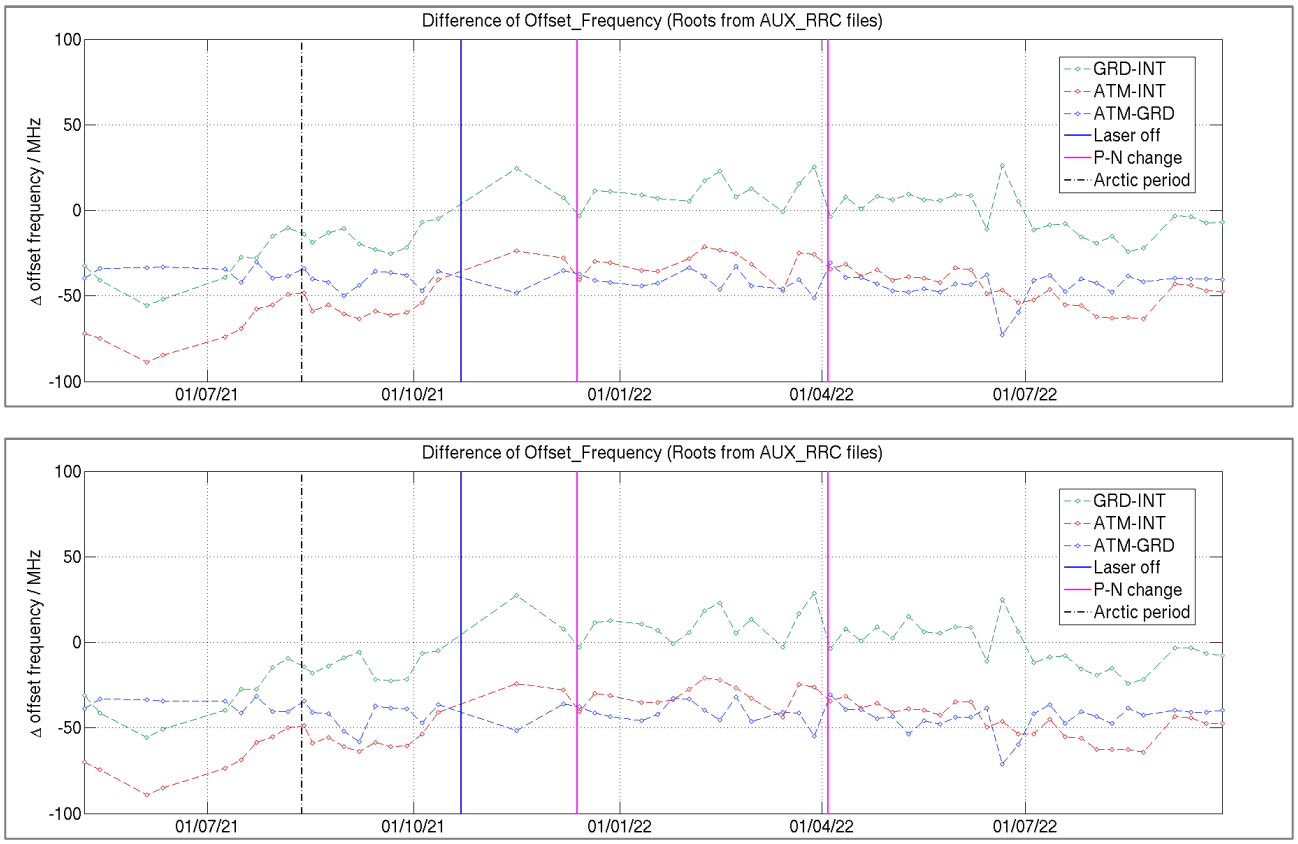

Figure 7: The mutual differences in the x-axis intersection (Offset_Frequency) between the internal reference (INT), atmosphere (ATM) and ground return (GRD) for the RPRO4 dataset (top) and the comparison dataset (bottom).

Continuous timelines of the differences in the x-axis intersection (Offset_Frequency) between internal reference path, atmospheric path and ground return are presented in Figure 7. A detailed comparison shows that the RPRO4 dataset produces smoother curves for GRD-INT and ATM-GRD, most obvious in the period around May 2022. Consequently, this improvement seems to be based on processor improvements affecting the ground return.

Continuous timelines of the standard deviation of the residuals of the Rayleigh response curves for the internal reference path, the atmospheric path and the ground return are presented in Figure 8. A detailed comparison shows that the RPRO4 dataset provides smoother curves for the atmospheric path and the ground return, most obvious in September 2021 and March 2022. Consequently, this improvement is attributed to respective improvements in the L1B processor to Baseline 16.

An improvement on the internal reference path is hardly recognizable. This is expected since the internal reference signal is recorded under favourable conditions in terms of SNR.

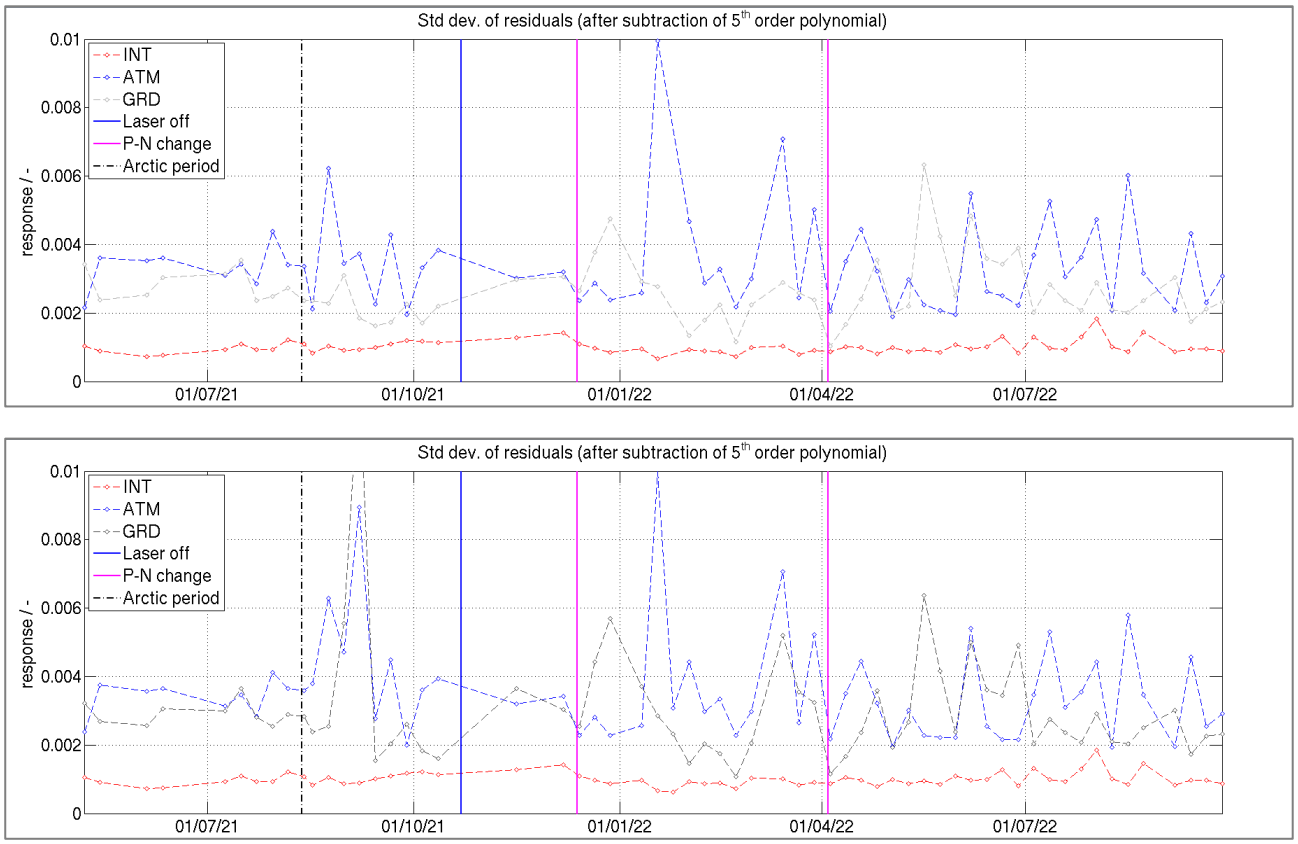

Figure 8: The standard deviation of the residuals of the Rayleigh response curves for the internal reference (INT), atmosphere (ATM) and ground return (GRD) for the RPRO4 dataset (top) and the comparison dataset (bottom).

Figure 9 and Figure 10 show the Mie response curves, their non-linearities and the residuals after having subtracted a 5th order polynomial fit for the PDGS dataset from the 4th reprocessing and the comparison dataset, respectively. An improvement, i.e. better performance of the RPRO4 dataset, on the example of selected single frequency steps (as done for the RRCs) is not easily recognizable due to the dominating effect of the overall change of the non-linearity shape. This change of the non-linearity shape is attributed to the application of the EMSR correction during the 4th reprocessing with L1B v.7.14. (Baseline 16).

The overall shape and distribution of the residuals of the ground return shows a more regular pixel-related modulation in terms amplitude for the RPRO4 dataset.

Continuous timelines of the intercept, slope and offset frequency (intersection with x-axis) are presented in Figure 11, Figure 12 and Figure 13 for the RPRO4 dataset and the comparison dataset. The continuity itself and the fact that there are no obvious outliers show that the content of the AUX_MRC files is valid and reasonable.

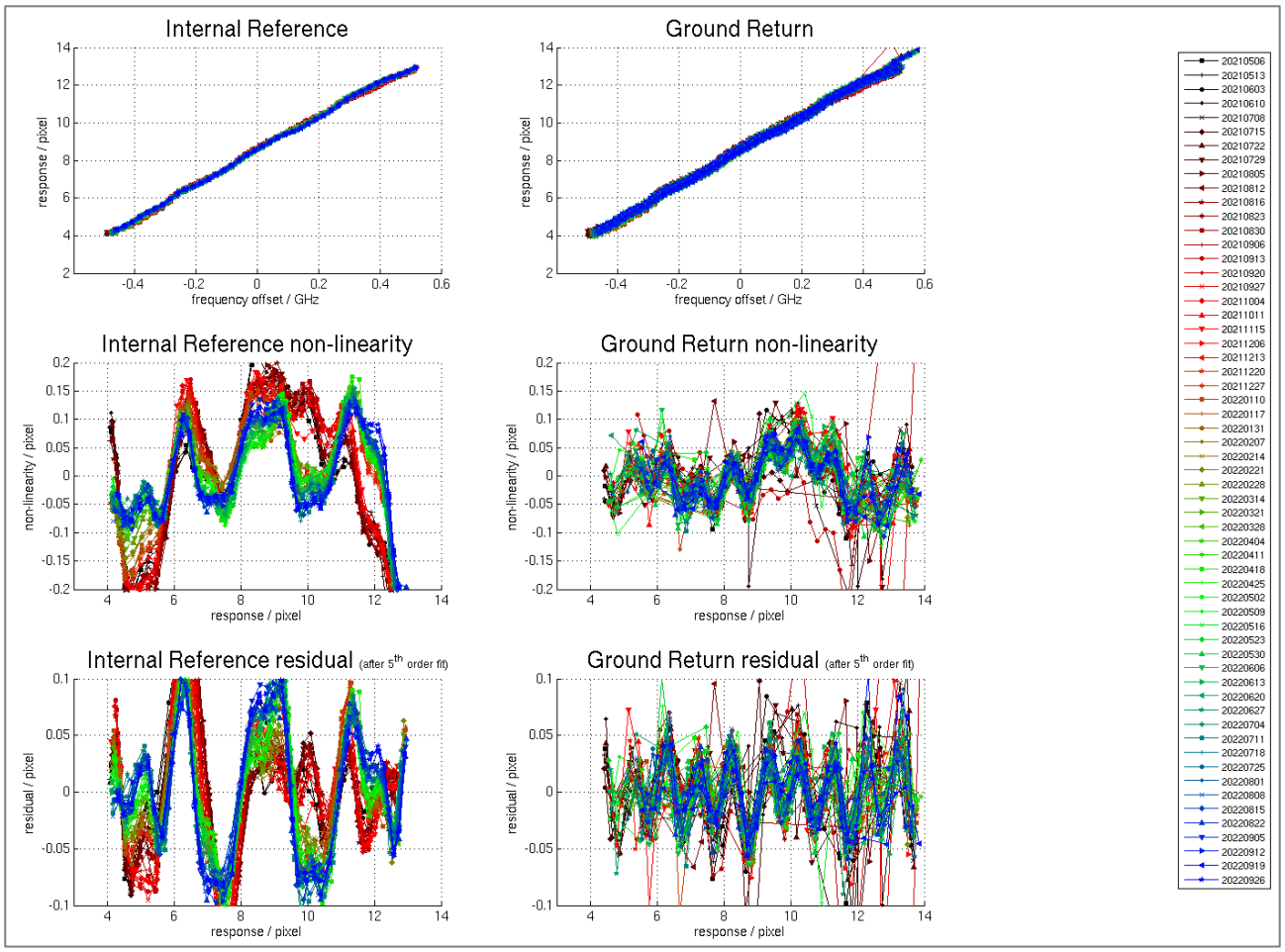

Figure 9: Mie response curves (top), non-linearities (middle) and residuals (bottom) for the internal reference (left) and the ground return (right) of the selected 59 MRCs from the PDGS reprocessed dataset.

A detailed comparison of the intercepts shows that the RPRO4 dataset produces more constant intercept values for the ground return (referring to an almost general increase for the period between May 2021 and January 2022) and a generally smoother curve, most obvious in the period between May 2022 and July 2022. Consequently, this improvement seems to be based on processor improvements affecting the ground return, notably the application of the EMSR for the atmospheric path. No changes are visible for the internal reference.

A detailed comparison of the slopes shows that the RPRO4 dataset produces a smoother timeline, most obvious between May 2022 and July 2022. Consequently, this improvement seems to be based on processor improvements affecting the ground return. No changes are visible for the internal reference.

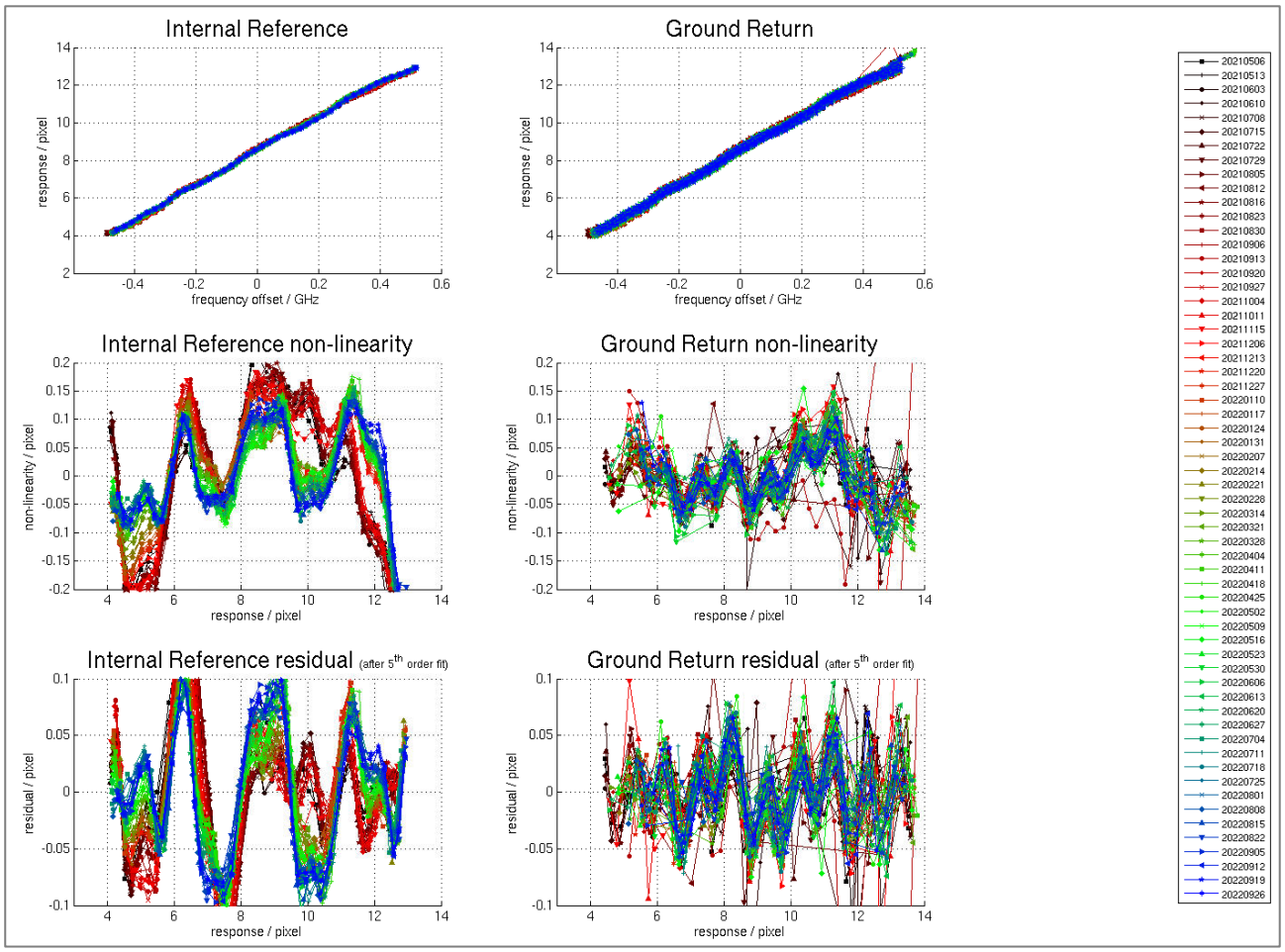

Figure 10: Mie response curves (top), non-linearities (middle) and residuals (bottom) for the internal reference (left) and the ground return (right) of the selected 60 RRCs from the comparison dataset.

A detailed comparison of the offset frequencies shows that the RPRO4 dataset produces a timeline with a mostly lower offset frequency (towards more negative values), starting most obviously from around September 2021 until the end of FM-B. Consequently, this improvement seems to be based on processor improvements affecting the ground return, i.e. the atmospheric path, for example the use of the EMSR.

Document Title

Verification report for phase 1 of the fourth reprocessing campaign for the FM-B laser from June 2019 till October 2022

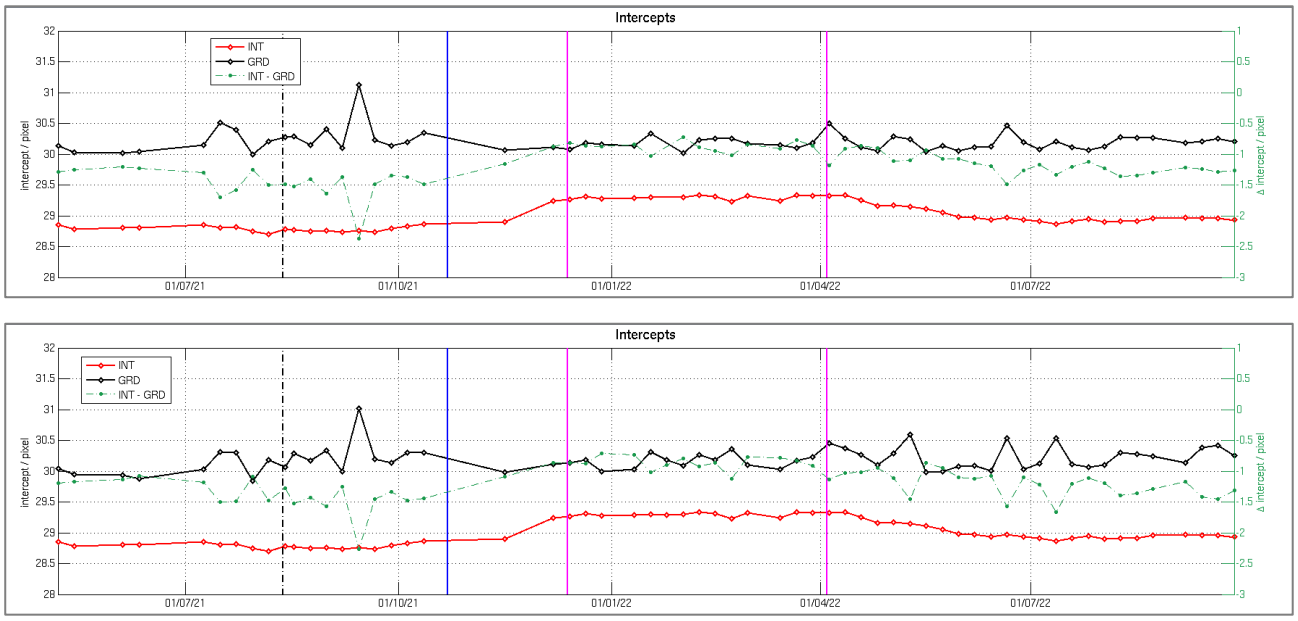

Figure 11: The intercept (Zero_Frequency) for the internal reference (INT) and the ground return (GRD) for the RPRO4 dataset (top) and the comparison dataset (bottom).

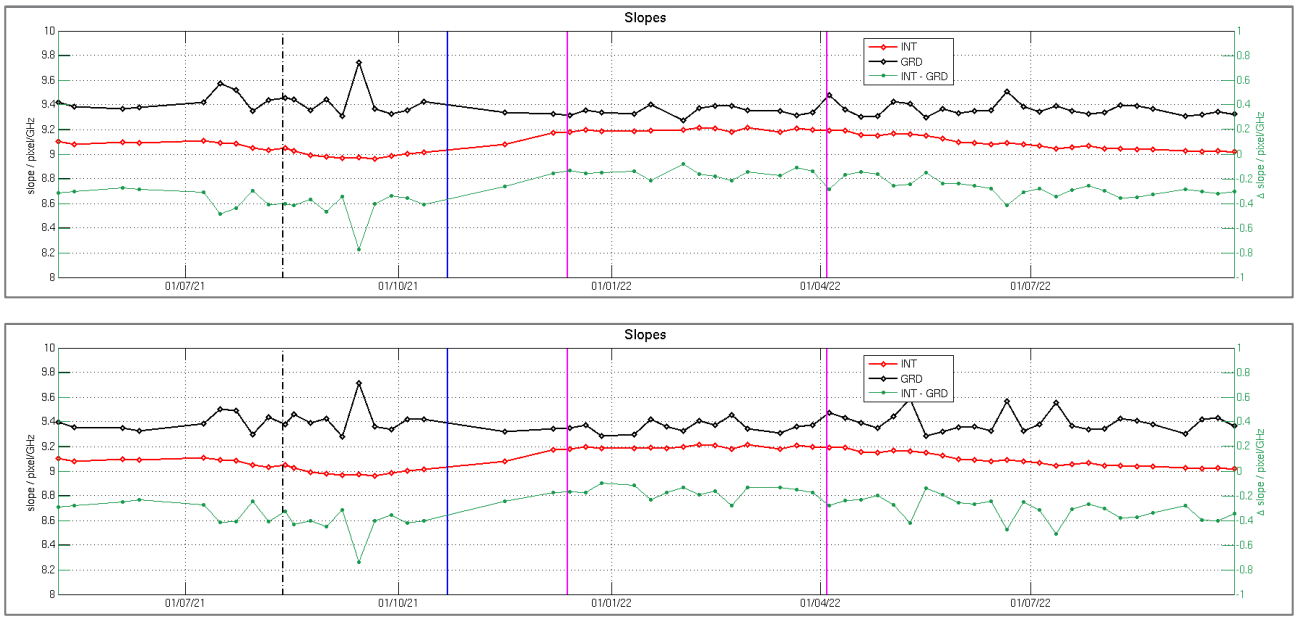

Figure 12: The slope (Mean_Sensitivity) for the internal reference (INT) and the ground return (GRD) for the RPRO4 dataset (top) and the comparison dataset (bottom).

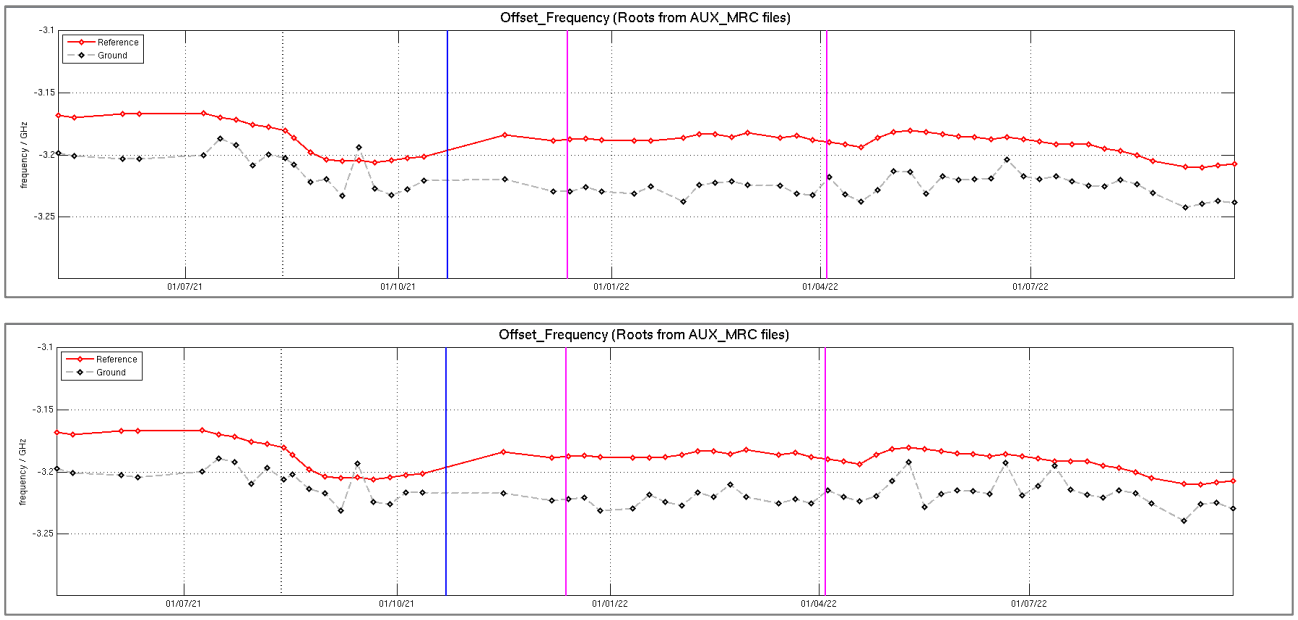

Figure 13: The x-axis intersection (Offset_Frequency) for the internal reference (INT) and the ground return (GRD) for the RPRO4 dataset (top) and the comparison dataset (bottom).

The AUX_MRC and AUX_RRC dataset was analysed by the means of the DLR Matlab Plot Tool. The following findings can be noted down:

- The overall assessment is based on plausibility checks, the detailed visual inspection of randomly selected single files and comparison of response curves and timelines against a dataset comprised of IRCs from previous baselines.
- The AUX_MRC and AUX_RRC files show the expected content and structure. Differences in specific values are explainable for example using improved corrections with Baseline 16 and the use of the new EMSR correction.
- Effects of improved quality control are visible for the Rayleigh atmosphere and ground return response curves, namely an improved random error of the residuals of the Rayleigh atmosphere and ground return response curves.
- The correct usage of the provided AUX_PAR_1B files during the reprocessing of the IRCs can be confirmed (checks performed but not shown here).
- IRC #088 from 2022-01-24 is missing in the dataset ("Jan2022-aux-tar") provided by PDGS.

The overall quality of the reprocessed dataset is within the expectations and shows improvements with respect to previous baselines. Despite the missing IRC #088, the IRC dataset from the 4th reprocessing by PDGS is accepted.

5 Verification of L1B products

The first step of the verification of the 4th reprocessed L1B dataset consisted of the comparison of the Baseline 16 DISC-internal Sandbox reprocessed dataset (from KNMI) to the operational Near-Real-Time data with different baselines (provided by ESA Payload Data Ground Segment PDGS). This first step considered 8 test weeks in the period from 27 June 2019 to 4 October 2022, where specific instrument and measurement settings were used, onsets of new hot pixels occurred, or under-flights of airborne campaigns were performed (see Table 3).

Table 3. 8 weeks selected for testing the FM-B dataset obtained from the Sandbox and from PDGS during the 4th reprocessing campaign. Background information about the specific reason that led to the selection is given in the rightmost column.

Week #	Start	Stop	Background
1	2019-07-18	2019-07-24	LFA on 2019-07-21 → different altitude-dependent L2B Rayleigh wind biases before/after this event
2	2019-09-11	2019-09-17	5 Aeolus underflights during AVATAR-I
3	2020-06-22	2020-06-28	Problems with DCMZ correction for 2nd campaign (wiki REPRO 004): check again
4	2020-08-17	2020-08-23	2 new HPs + end of eclipse phase
5	2021-09-08	2021-09-14	4 Aeolus underflights during JATAC/AVATAR-T campaign
6	2022-01-20	2022-01-26	1 test week with N=15/P=38
7	2022-06-22	2022-06-28	2 new HP with large bias for Rayleigh
8	2022-09-09	2022-09-17	JATAC/ASKOS campaign for L2A retrieval

Table 4. L1B products analysed per test week.

Week #	L1B product
1	AE_OPER_ALD_U_N_1B_**20190719T20**4623022_005423998_005248_0002.DBL
2	AE_OPER_ALD_U_N_1B_**20190914T09**3559030_005399992_006145_0001.DBL
3	AE_OPER_ALD_U_N_1B_**20200622T19**5423034_005423999_010623_0002.DBL
4	AE_OPER_ALD_U_N_1B_**20200822T21**0423037_005087997_011591_0001.DBL
5	AE_OPER_ALD_U_N_1B_**20210910T13**4632029_005435996_017676_0001.DBL
6	AE_OPER_ALD_U_N_1B_**20220125T13**0705039_005411988_019848_0001.DBL

7	AE_OPER_ALD_U_N_1B_**20220623T150**105034_005471995_022212_0001.DBL
8	AE_OPER_ALD_U_N_1B_**20220916T044**305034_005435995_023553_0001.DBL

Table 4 lists L1B products analysed per test week. For test week #1, #4 and #7 the selected products each contain the onset of a hot pixel.

The following L1B parameters were compared visually, to evaluate the effect of the transition from the baselines used during NRT processing to the new baseline 16 onto the most vital product variables, such as winds, scattering ratio and signal to noise ratio. Listed below is the entire set of analysed variables.

- Mie/Rayleigh Useful signal (LSB) **at observation level.**
- Mie/Rayleigh HLOS Wind (m/s) **at observation level**
- Mie_refined_scattering_ratio **at both measurement and observation level**
- Mie_refined_signal_to_noise_ratio **at both measurement and observation level**
- Mie core residual error **at observation level**
- Mie/Rayleigh Mean emitted frequency and Standard deviation of mean emitted frequency **at observation level**
- Mie/Rayleigh Ground parameters: ground correction velocity and ground useful signal **at observation level**

This first verification step (Sandbox vs. NRT data) led to the following conclusions:

- All Mie refined SNR values for the analysed orbits are shifted to lower values (Figure 14); this behaviour is not observed in other variables. One clearly visible effect can be seen in test week #2, where the PSC features have a more detailed and pronounced structure in the Sandbox reprocessed dataset compared to the NRT data (Figure 15).
- Hot pixel Mie [4,11] ([bin, pixel index] counting from 1), which appeared on 19 July 2019, is corrected.
- Hot pixel Rayleigh [3,13], which appeared on 22 August 2020, is corrected.
- Consideration of a hot pixel on the Mie channel, as spotted in the L2A product and also visible in the L1B Mie refined scattering ratio.
- Hot pixel Mie [14,14], which appeared on 23 June 2022 (orbit 22212) was not corrected.

- In the next orbit (22213) a hot pixel-like signature in the Mie range-bin #7 is removed, while the structure remains visible for Mie range-bin #15. The hot pixel Mie [14,14] remains uncorrected also in this orbit.

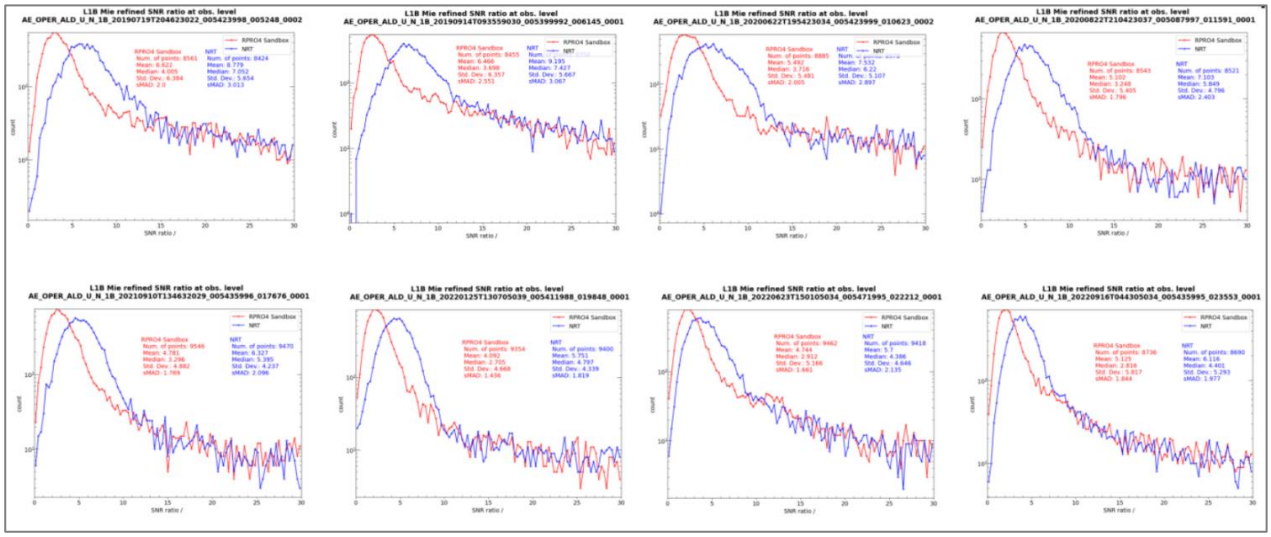

Figure 14: Mie refined SNR distribution for the Sandbox (red) and NRT (blue), one L1B product per test period.

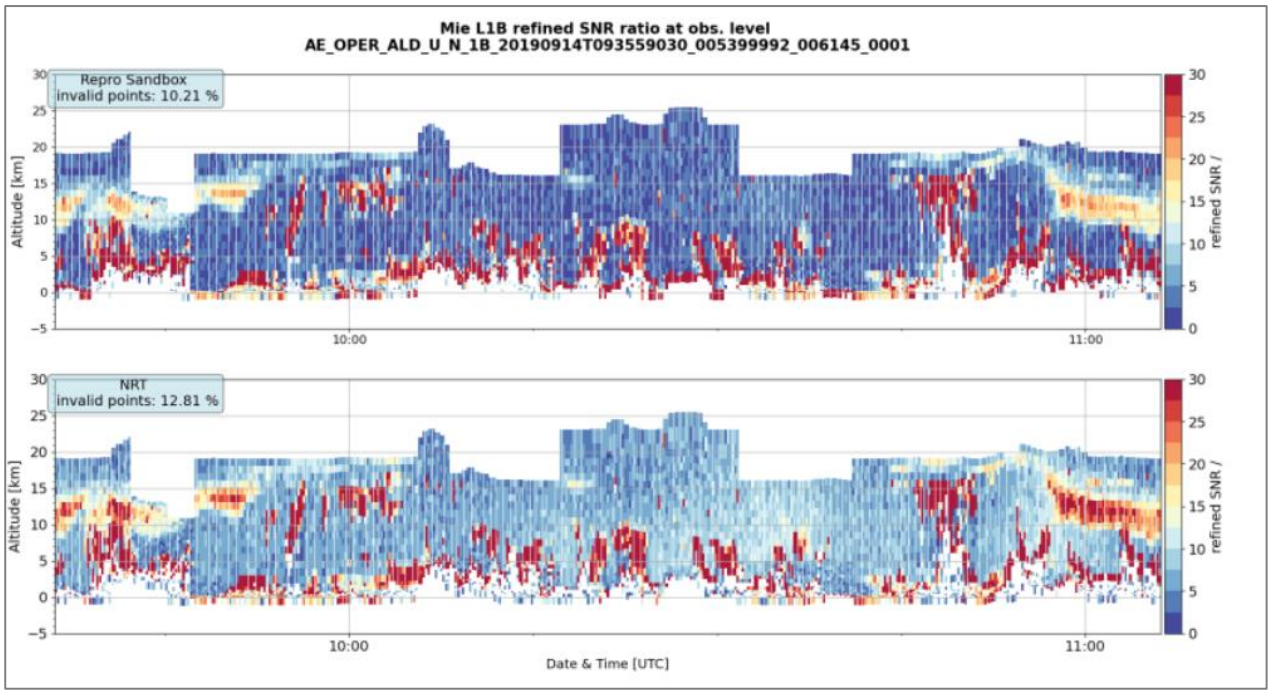

Figure 15: L1B Mie refined SNR ratio for the Sandbox Baseline 16 reprocessed dataset (top) and the corresponding Near-Real-Time orbit file (bottom) for test week #2.

The second step of the verification of the 4th reprocessing campaign covering FM-B consisted in a 'delta verification' approach. This was performed via a visual inspection of the same L1B parameters listed above, but this time for DISC internal Sandbox B16 L1B products compared to ESA´s PDGS reprocessed B16 L1B products. All L1B variables for all the selected orbits were found to be identical for the two product sources, see Figure 16. The only difference was found in the ground detection parameters of the L1B product. The PDGS reprocessed dataset appears to have systematically more valid ground returns. For each analysed product 3 to 17 additional ground returns were detected. It was verified that the AUX_PAR_1B input files used in the two processes were the same.

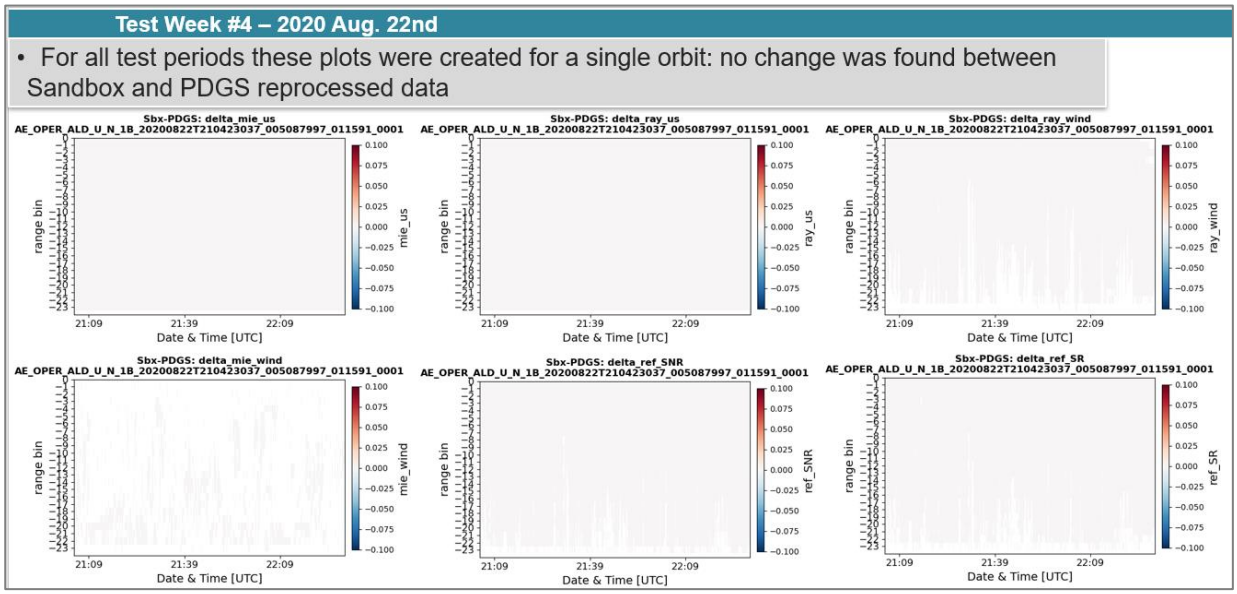

Figure 16: Example for test week #4 for the delta verification. Each plot is related to a specific L1B variable such as Mie useful signal or wind and shows the difference for Sandbox minus PDGS (both Baseline 16 reprocessing).

An investigation on these extra ground returns was carried out with the aim of assessing whether extra ground bins found in the PDGS dataset are due to computational rounding errors or if they represent some sort of correlation or show systematic behaviour.

For a total of 3574 observations (8 orbits), PDGS data products showed 87 more valid ground returns than the Sandbox products.

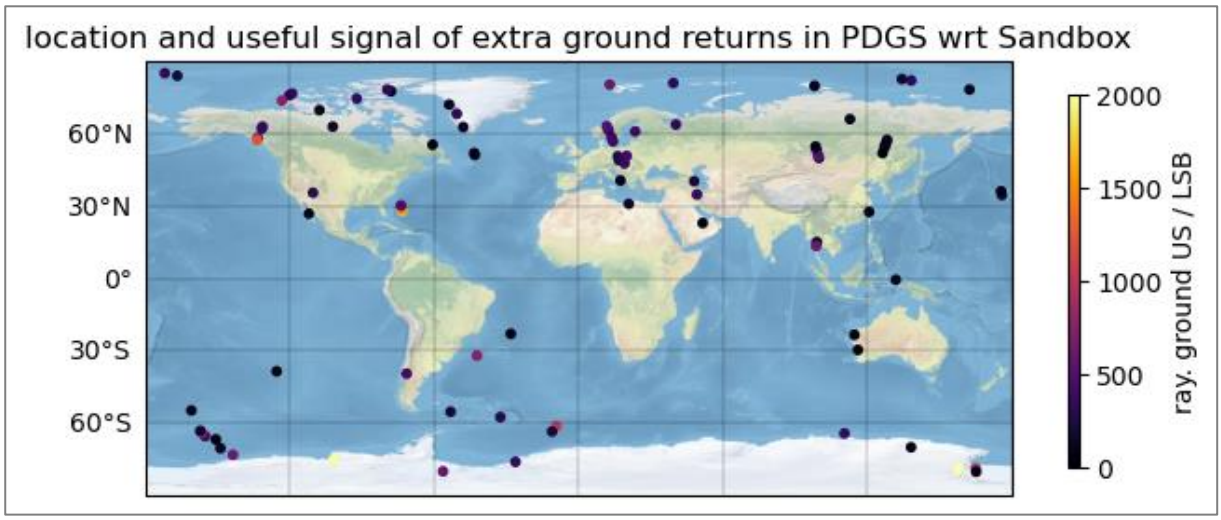

Figure 17: Geographical distribution of the extra ground returns with a heatmap showing their respective useful signal.

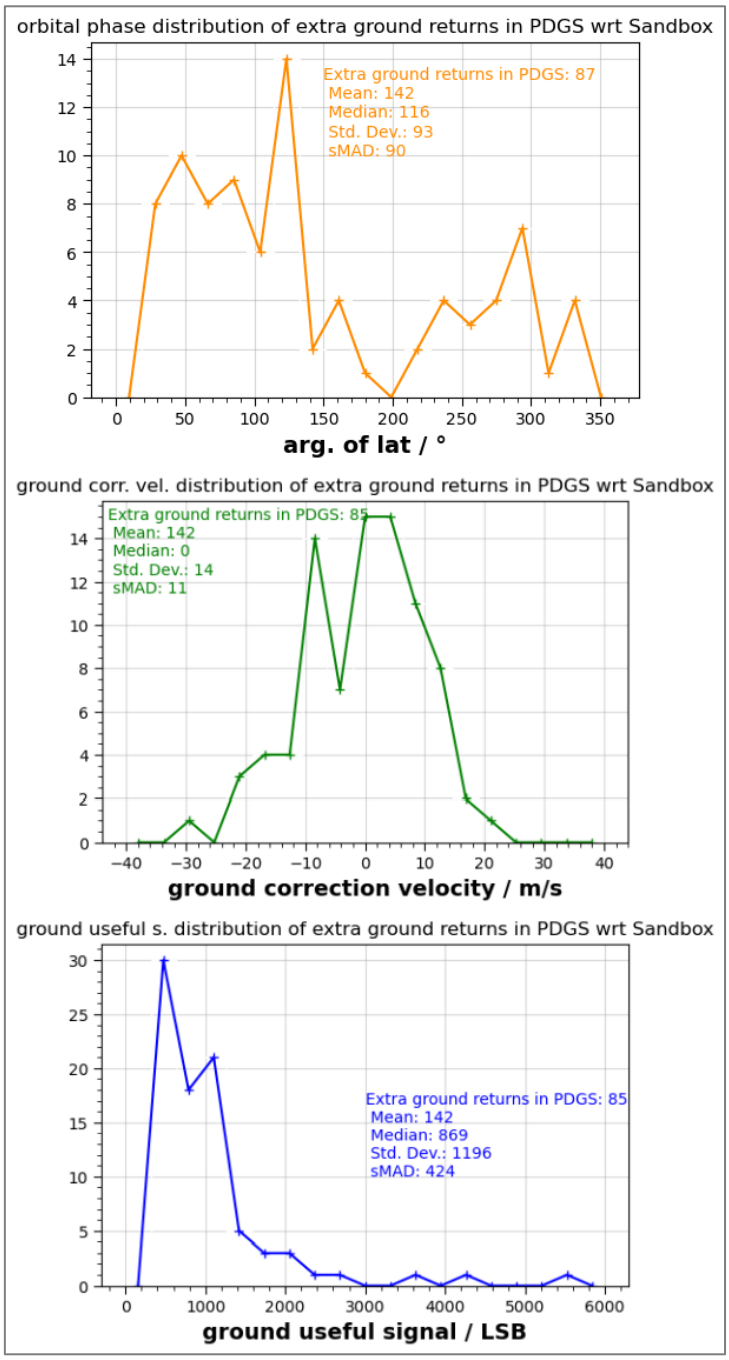

Figure 18: The three histograms show the distribution of the extra ground return depending on their corresponding argument of latitude (orbital position), ground correction velocity and useful signal.

The conclusion is that there is no correlation between the PDGS extra ground returns and geographical position, wind speed in the ground bin or useful signal in the ground bin. It can be noted that most of these extra ground returns have low useful signals with the implication that they would be ignored when an accordingly strict useful signal quality control is applied.

6 Verification of L2A products

6.1 De-noising of SCA backscatter and extinction coefficients: The SCAmid and MLE algorithms concept

Because of the Standard Correct Algorithm (SCA) principle (i.e. direct inversion of the lidar equation assuming particles free condition in top range bin), the aerosol retrievals are highly affected by signal noise. The particle extinction and backscatter coefficients are indeed retrieved independently, and the extinction is normalized using the signals in the first range bin. This bin has a low SNR and the noise in this first computed bin is propagating downwards through the whole extinction profile. Averaging the signal over consecutive vertical bins helps decreasing the noise contamination and correspond to the SCAmid algorithm. Nevertheless, this does not allow to remove all the contamination, and it increases the negative bias of the backscatter.

A physical regularization scheme has then been implemented within L2A processor to reduce the noise contamination of SCA optical product. It is called Maximum Likelihood Estimation (MLE). It can mainly be seen as an alternative to the SCA processing of crosstalk corrected signals. This algorithm consists in finding the profiles of the optical parameters (i.e. backscatter coefficient for particles and lidar ratio) that achieve the best agreement with real signals assuming vertical collocation between extinction and backscatter. Pre-defined physical bounds are applied, i.e. positive local optical depth and lidar ratio bounded between 2 and 200 sr.

6.2 Information at sub-BRC level with higher horizontal resolution: The MLEsub algorithm

The MLE improved stability to the noise was used to refine the horizontal resolution and the aerosol retrievals were implemented at sub BRC (Basic Repeat Cycle i.e. 12 seconds) scale, i.e. accumulated measurements per sub profile depending on settings for the number of accumulated laser pulses P per measurement and number of measurement N per observation. This MLEsub addition hence provides profiles with resolution of ~17.4 km for FM-B 4th reprocessed dataset covering June 2019 to October 2022.

Figure 19 illustrates the improvement of the extinction coefficient for particles retrieved by the MLE and MLEsub compared to SCA and SCAmid algorithms using the 4th reprocessed dataset labelled baseline 16 for June 2020. The extinction coefficient in the top range bins appears noisy for the SCA but not for the MLE. The MLE then provides de-noised extinction for particles with better horizontal homogeneity. Nevertheless, a known positive bias can be seen in lowermost bins close to the ground. Note that these differences are less pronounced with backscatter retrievals. The MLEsub helps to capture the extent of a Saharan Air Layer (i.e. light-yellow feature at ~3 km altitudes 08:11 UTC) increasing the horizontal resolution by a factor 5.

Document Title

Verification report for phase 1 of the fourth reprocessing campaign for the FM-B laser from June 2019 till October 2022

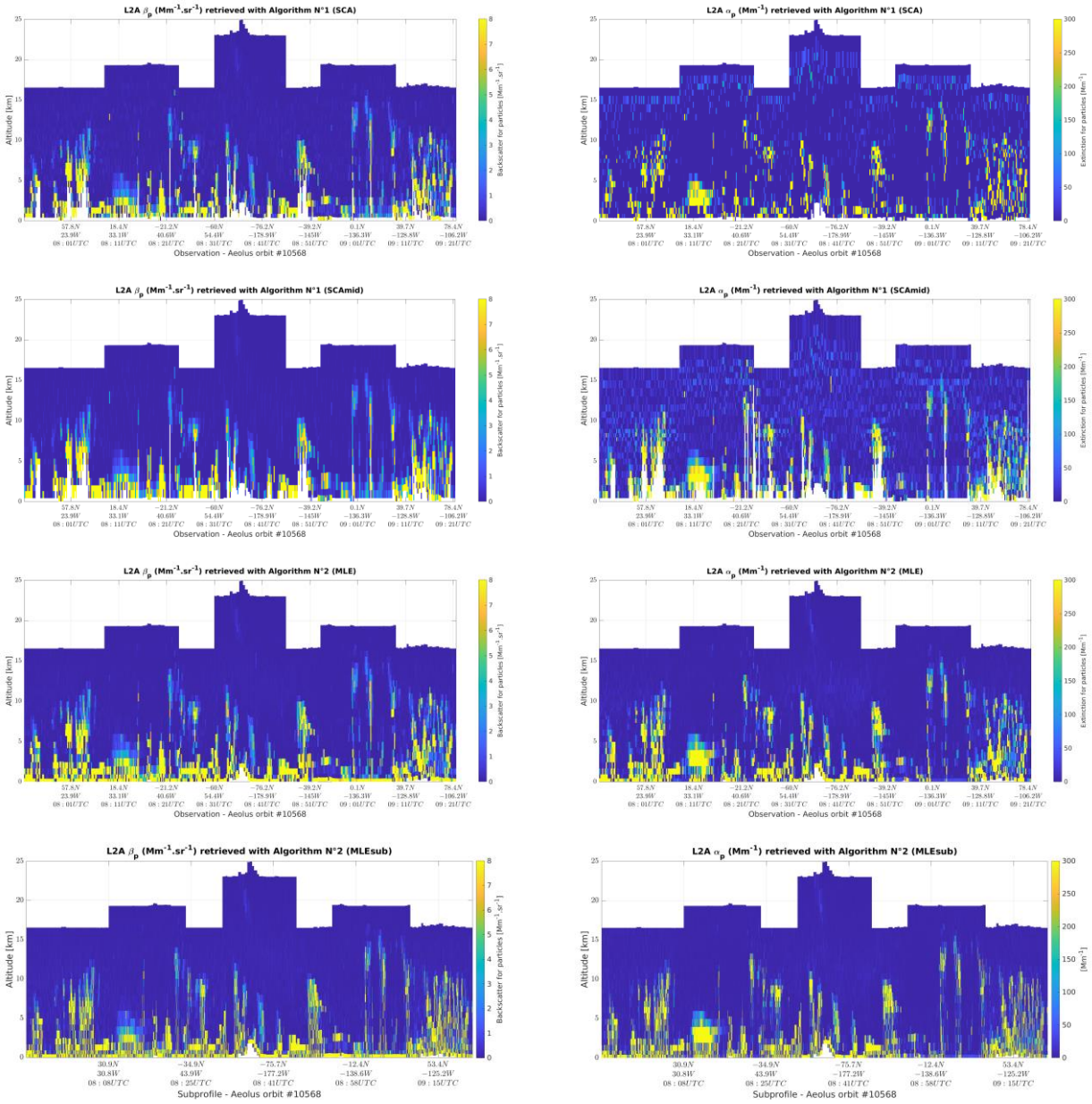

Figure 19. SCA (top row), SCAmid (second row), MLE (third row) and MLEsub (bottom row) backscatter (left column) and extinction coefficients (right column) for particles for a whole orbit in June 2020.

6.3 Overview of impacts on L2A products: Improvements and limitations

The FM-B dataset is homogeneously processed with L2A processor v3.16.4 which means:

- Final implementation of the Maximum Likelihood Estimation (MLE) at sub-BRC level (i.e. accumulation of measurements for 5 sub profiles per Basic Repeat cycle).
- Fine-tuning of the MLE number of iterations and Quality Check (QC) flags for both BRC level and sub-BRC.
- The calibration coefficients characterizing the radiometric efficiency of the receivers, i.e. K_{ray} and K_{mie}, are estimated from signal prediction in particle-free regions of the atmosphere (i.e. scattering ratio below 1.124) for mid-altitudes 6 to 16 km. They are calculated per observation using a multiple linear regression based on telescope temperatures oscillations.

Limitations:

- The L2A SCA and MLE algorithms show limitations for truncated orbits and specific conditions due to special operations, e.g. topmost range bin set below 16 km leading to non-optimized radiometric correction performs in aerosol-free atmosphere between 6 km and 16 km.

6.4 Quick analysis of reprocessed dataset

6.4.1 Calibration coefficients K_{ray} and K_{mie}: key proxies for radiometric efficiency

The K_{ray} and K_{mie} coefficients given per observation have been checked over the whole 4th reprocessing FM-B laser period, i.e. from June 2019 to October 2022. Figure 15 below shows the timeline for both coefficients with continuous decrease average of 1% per week due to signal loss despite the N/P settings adjustment performed on December 13, 2021, and April 04, 2022. The overall loss is ~80% for K_{ray} and ~75% for K_{mie}. The deviations per orbit appear to decrease despite some peaks observed for localized periods, e.g. 28 October to 11 November 2019 due to AMV range-bin settings, 6 to 9 July 2020 because of M1 mirror control temperatures test, 22 March to 13 April 2021 because of ALADIN switch-off, 4 to 11 April 2022 due to wrong solar background integration time. Isolated values with truncated profiles due to special operations (e.g. DUDE measurement, Orbit Correction Manoeuvre, temperatures sensitivity test) exceed the valid range of AUX_PAR_QC leading to degraded orbit.

2019 (Jun. to Dec)

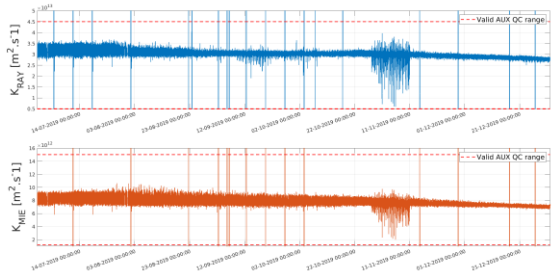

2020 (Jan. to May)

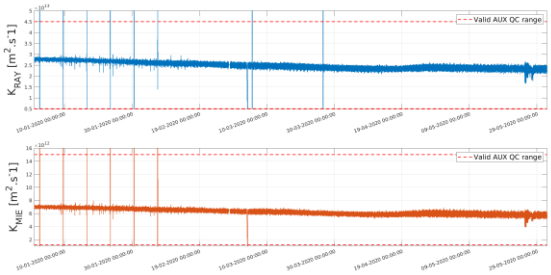

2020 (Jun. to Dec.)

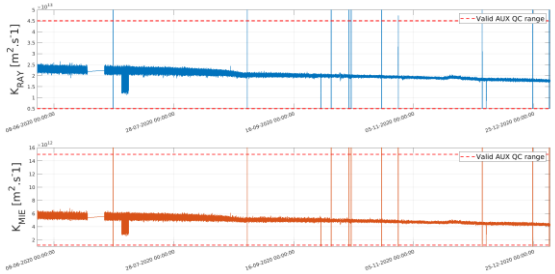

2021 (Jan. to May)

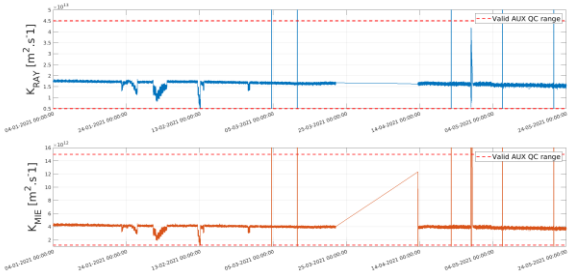

2021 (Jun. to Dec.)

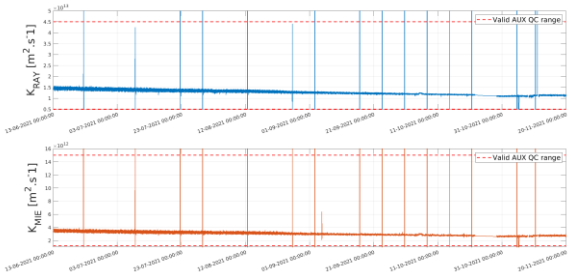

2022 (Jan. to Oct.)

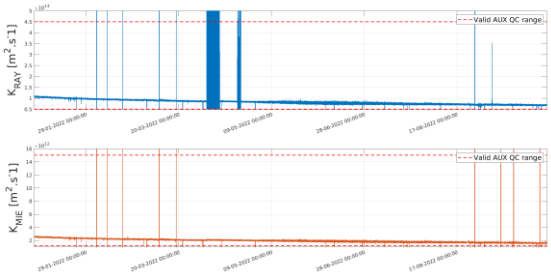

Figure 20. K_{ray} (blue) and K_{mie} (orange) timeline given per observation from M1 temperatures regression for FM-B laser period and processed by L2Ap v3.16.4.

6.4.2 Outliers in SCA and SCAmid backscatter and extinction for L2Ap V3.16.4

The extinction and backscatter values are sorted into four categories to easily characterize the occurrence of anomalous values:

1) values larger than 200 Mm^{-1} for extinction and 200 $Mm^{-1}sr^{-1}$ for backscatter,

2) values <0,

3) not computed and set to -1,

4) bin flagged by Quality Check (QC) flags.

Figure 21 below shows the timeline for SCA backscatter coefficients. The scores look similar to the previous reprocessed dataset verification with big outliers less than 1%, negative values of ~30% and non-computed of ~15%. The QC flagged bins increase from 10% in 2019 to 60% for ending 2022 due to signal loss and restrictive thresholds (remaining identical for the whole dataset and mainly based on SNR). Localized degraded scores match the periods with lower radiometric efficiency, e.g. November 2019 (AMV range-bin settings) and April 2022. As regards the extinction coefficients, the number of negative values is close to 0% but the QC flagged bin reached higher values up to 60% for 2022. The SCAmid scores are close to SCA except higher QC flagged bin.

2019 (Jun. to Dec)

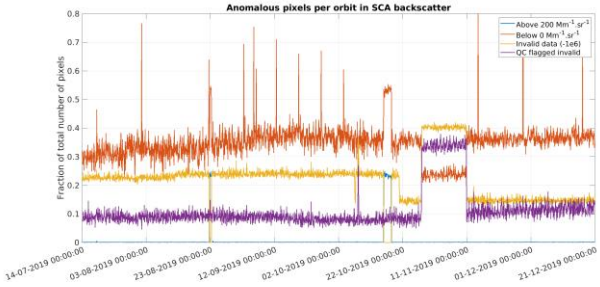

2020 (Jan. to May)

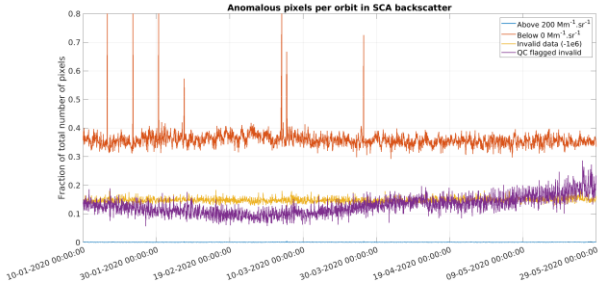

2020 (Jun. to Dec.)

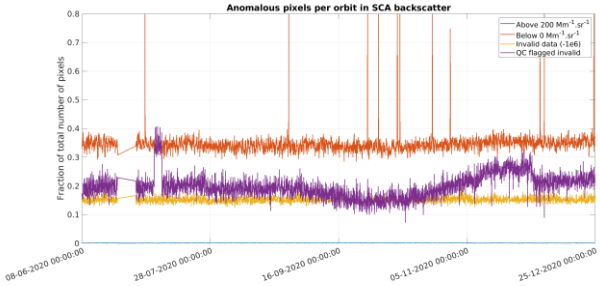

2021 (Jan. to May)

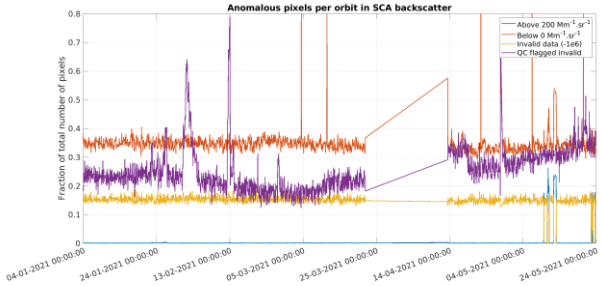

2021 (Jun. to Dec.)

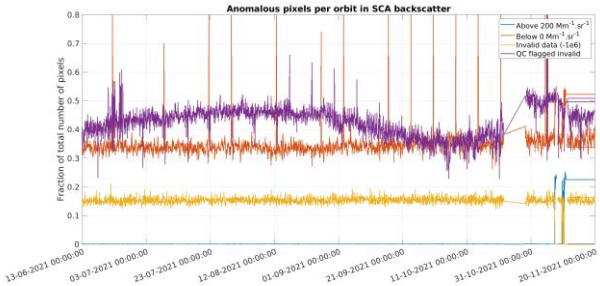

2022 (Jan. to Oct.)

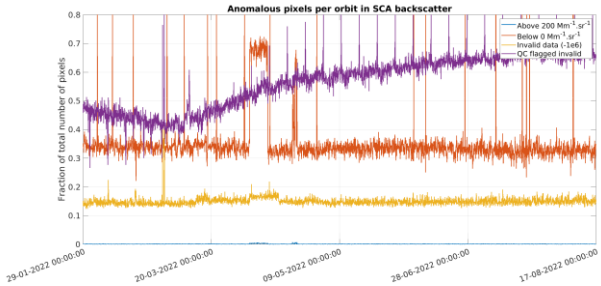

Figure 21. Fraction of SCA anomalous values in extinction: outliers with high values (blue), with values <0 (orange), not computed and set to -1 (yellow) and flagged by QC (violet).

6.4.3 Outliers in MLE and MLEsub backscatter and extinction for L2Ap V3.16.4

The extinction and backscatter values are sorted into four categories to easily characterize the occurrence of anomalous values:

1) values larger than 200 Mm^{-1} for extinction and 200 $Mm^{-1}sr^{-1}$ for backscatter,

2) values <0,

3) not computed and set to -1,

4) bin flagged by Quality Check (QC) flags.

Due to the pre-defined physical bounds included in MLE algorithm no negative extinction or backscatter are given in output contrary to SCA. Focusing on the MLE extinction both values non-computed and larger than 200 Mm^{-1} are lower than 15%. An increasing amount of QC flagged bin can also be seen similarly to the SCA and SCAmid by 2020. Investigation revealed that these QC flagged bins mainly occur in low altitudes with low SNR. The statistics being computed per orbit the MLEsub (not shown) look very similar to the MLE.

2019 (Jun. to Dec)

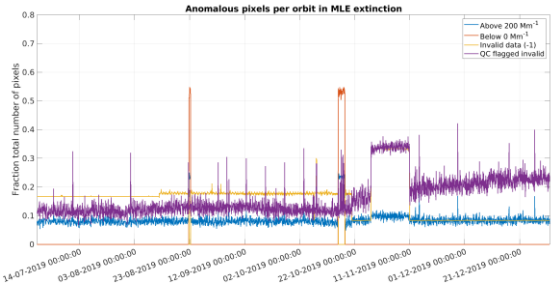

2020 (Jan. to May)

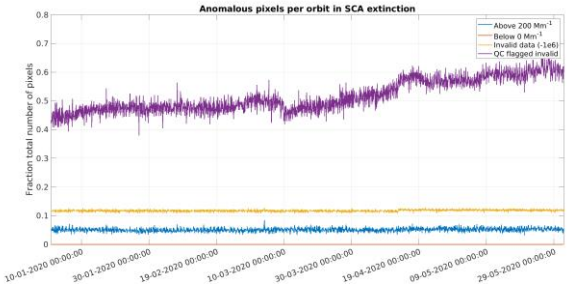

2020 (Jun. to Dec.)

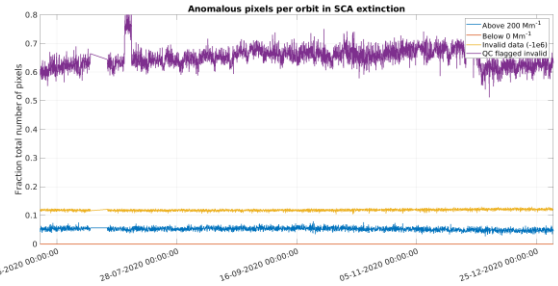

2021 (Jan. to May)

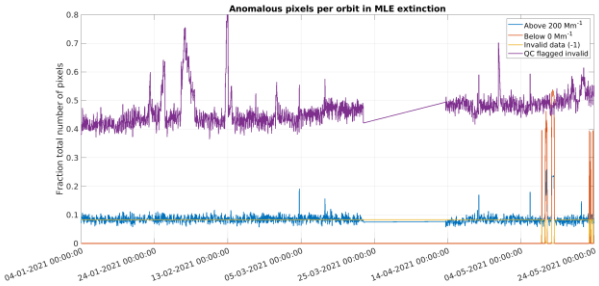

2021 (Jun. to Dec.)

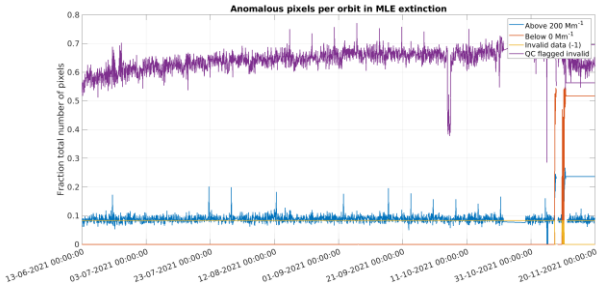

2022 (Jan. to Oct.)

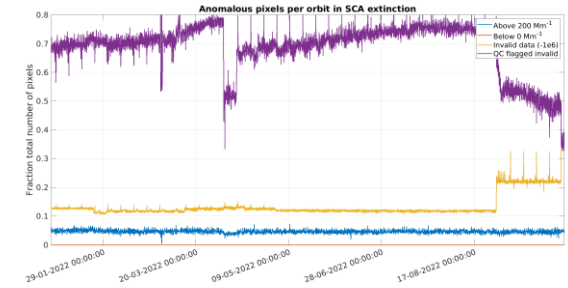

Figure 22. Fraction of MLE anomalous values in extinction: outliers with high values (blue), with values <0 (orange), not computed and set to -1 (yellow) and flagged by QC (violet).

6.4.4 Outliers in SCA attenuated backscatters for L2Ap V3.16.4

The SCA attenuated molecular and particulate backscatters values are sorted into two categories to easily characterize the occurrence of anomalous values:

1) values =0,

2) values <0.

The SCA crosstalk is known to be imperfect hence negative values observed in particulate attenuated backscatters (of ~40% for all years), the molecular attenuated backscatter being less affected (~10% negative). The fraction of values equal to zero appears constant and close to 0% by 2020.

2019 (Jun. to Dec)

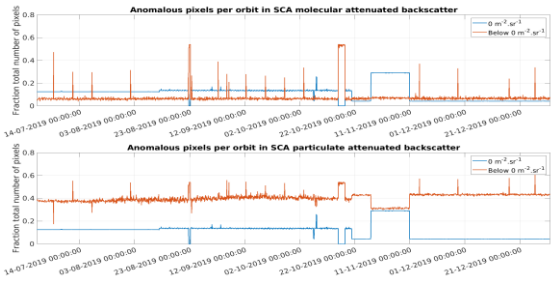

2020 (Jan. to May)

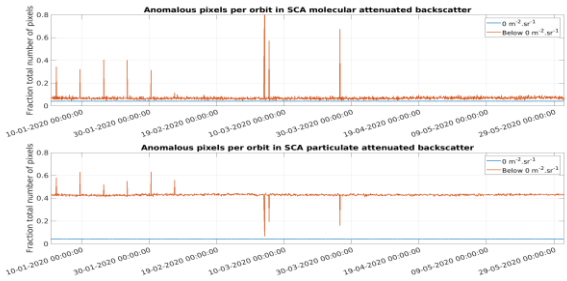

Figure 23. Fraction of anomalous values in SCA attenuated backscatter (molecular is top row, particulate is bottom row), until May 2020: outliers with values of zero (blue) and values less than zero (orange).

6.5 Visual inspection of a few orbits: Orbits with peaks in anomalous pixel fraction

The Level-2A product shows limitations for certain periods with specific conditions. It includes truncated orbits due to special operations and localized ones with topmost bin set to relatively low altitude. Examples of cases are illustrated below. For example: Figure 24 shows a degraded orbit #7043 (November 10, 2019) due to AMV range-bin settings; Figure 25 shows orbit #2109 (April 10, 2022) with an imperfect solar background range-bin integration time setting (too short, causing saturation, following a change to N/P settings) and Figure 26 showing degraded aerosol and wind product, truncated orbit #1078 (this may have been an orbit manoeuvre). In each case the K_{ray} and K_{mie} provided per observation exceed the valid range because of non-optimized radiometric correction. Non-physical backscatter can then be observed.

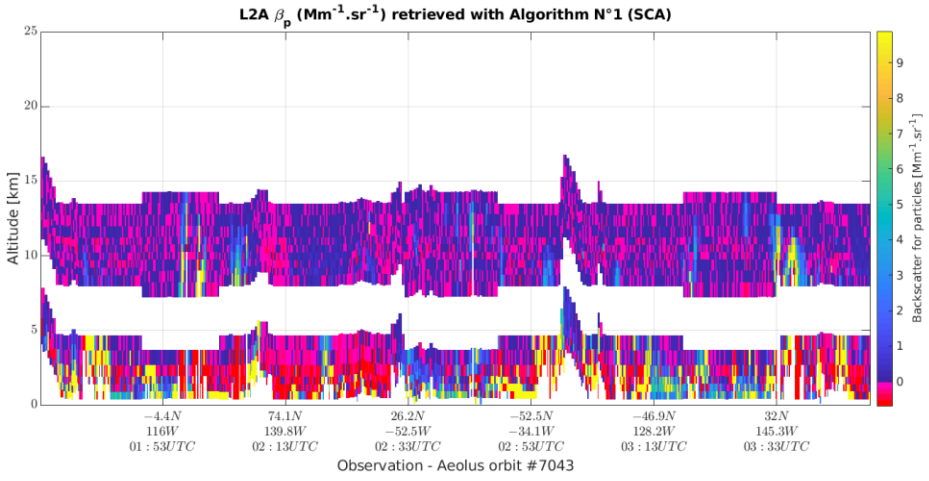

Figure 24. SCA backscatter coefficient for orbit #7043 on 10th November 2019 with top-most bin at low altitude and invalid profiles in mid-altitudes due to the period of AMV range-bin settings (higher vertical resolution with Mie and Rayleigh bins not overlapping well).

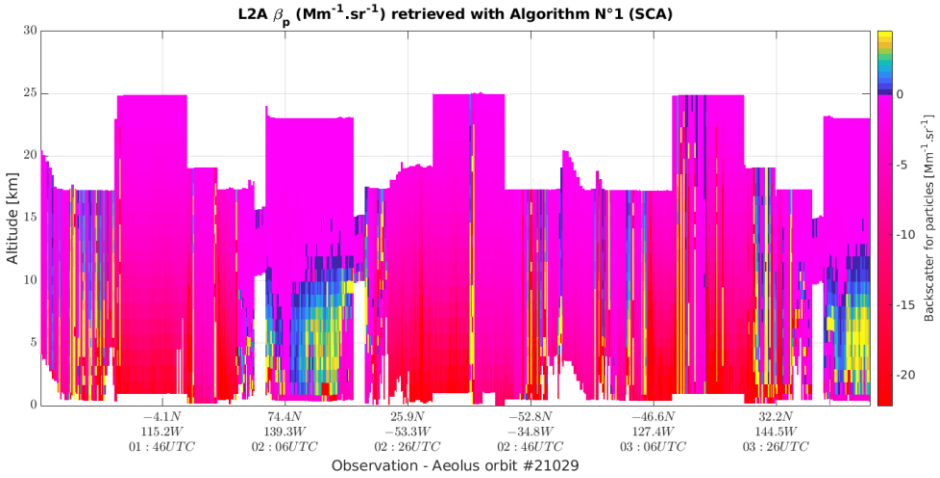

Figure 25. SCA backscatter coefficient for orbit #2109 on 10 April 2022. Due to an issue with imperfect settings for the solar background range-bin (25) integration time.

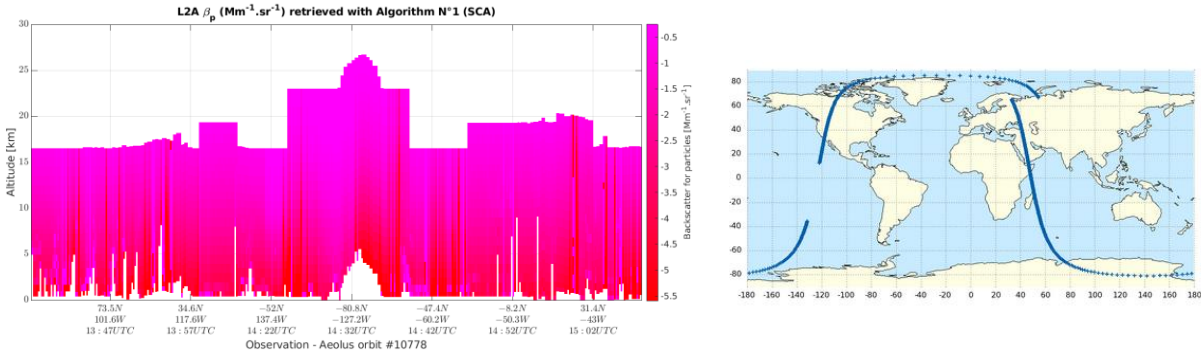

Figure 26. SCA backscatter coefficient (left) for truncated orbit #1078 on 2 July 2020.

6.6 Verification and validation of L2A AEL-FM/AEL-PRO products

This Section evaluates the fourth reprocessing of AEL-FM/AEL-PRO for the FM-B laser period. The data used here is taken from the PDGS processed datasets. The sandbox test dataset is the same as the PDGS dataset, so we did not rerun our analysis. The AEL-PRO product is for the first time included in the reprocessing v4.

6.6.1 EMSR

The Effective Mie Spectrometer Response (EMSR) is an array with 16 values corresponding to 16 ACCD pixels excluding 2 pixels from each side of the 20 ACCD pixels. The EMSR is calculated per orbit and used to derive the Mie and Rayleigh attenuated backscatters (ATBs) using only the Mie spectrometer data.

We checked the EMSR for one orbit per month from 201907 to 202210 (with some extra days) using sandbox test dataset. Figure 27 shows the EMSR time series. Figure 28 shows the mean EMSR per year. There is some degree of evolution and variation. The EMSR is a normalized quantity, so it is unaffected by changes in the absolute optical efficiency of the instrument (e.g. changes in laser energy). The odd EMSR values close to orbit #15576 are on 2021-02-01. On this day, data in all orbits look noisy in the sandbox data and also in the PDGS reprocessed data B16. This odd feature is not caused by hot-pixels. In the mean EMSR, the odd features were filtered.

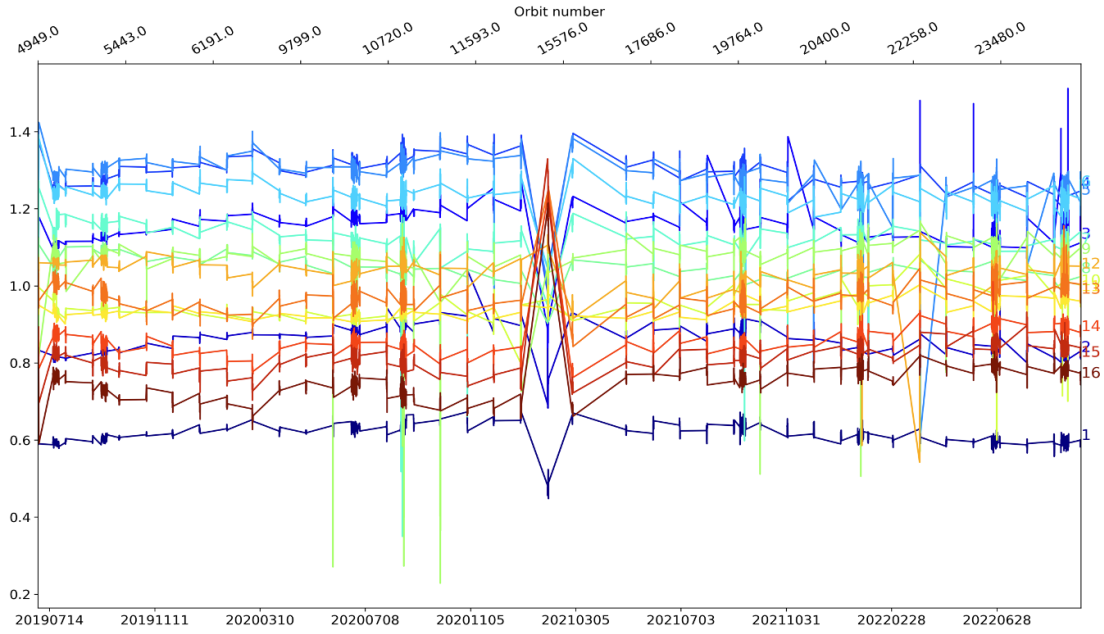

Figure 27. EMSR time series from 201907 to 202210 one day per orbit with some extra days.

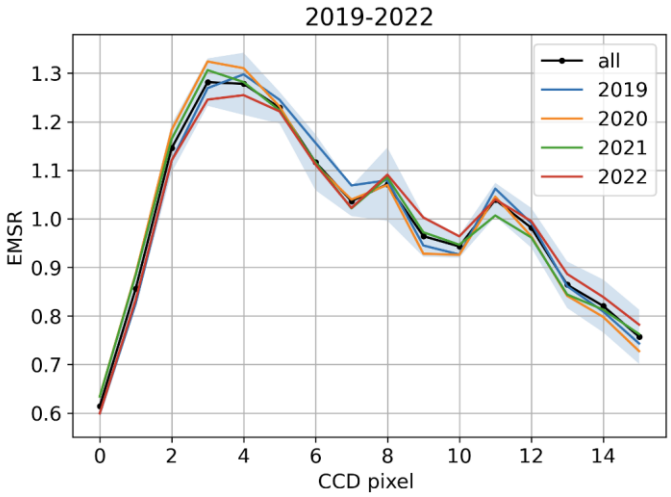

Figure 28. Mean EMSR per year, using the same data as in Figure 27.

6.6.2 Validation of AEL-FM feature mask

We have verified the AEL-FM feature mask in the reprocessing v4 using the prototype codes and found almost identical results. Here we show the feature mask comparison with CALIPSO feature on 2020-06-19 and 2020-06-24. Figure 29 illustrates the CALIPSO and Aeolus orbit on 2020-06-19 and the dust plume over ocean.

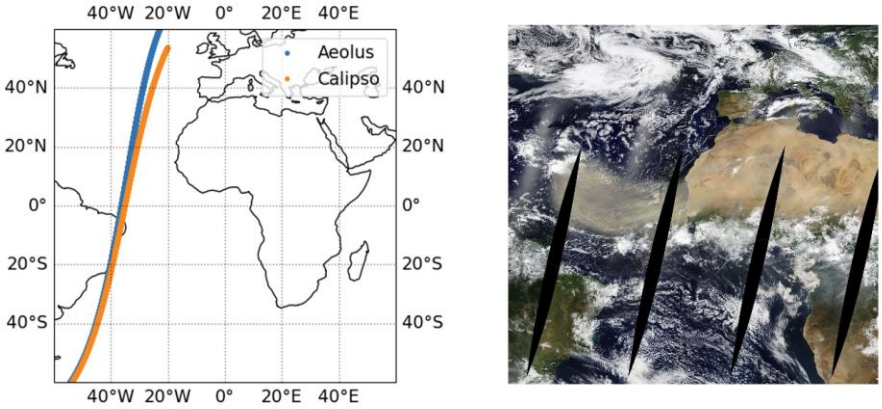

Figure 29. (left) Aeolus and CALIPSO obits on 2020-06-19. (right) Dust plume on MODIS true colour image on 2020-06-19.

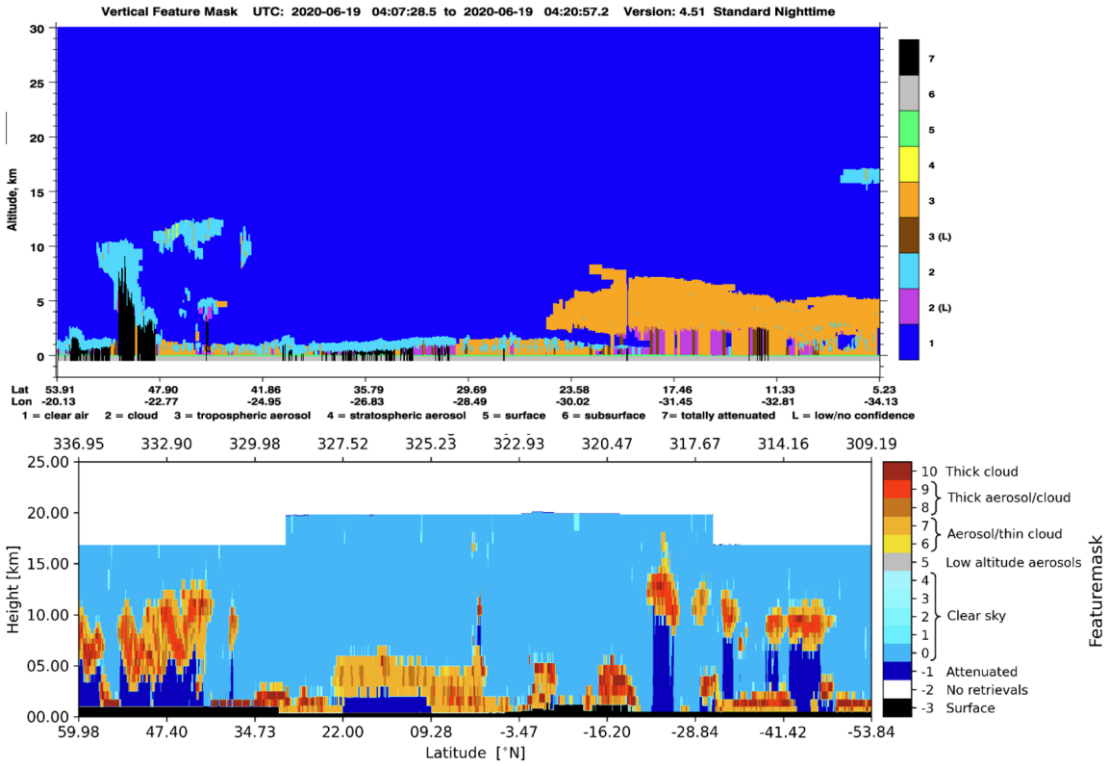

Figure 30. Aeolus orbit 10568 and CALIPSO feature mask on 2020-06-19. (top) CALIPSO feature mask, (bottom) Aeolus AEL-FM feature mask.

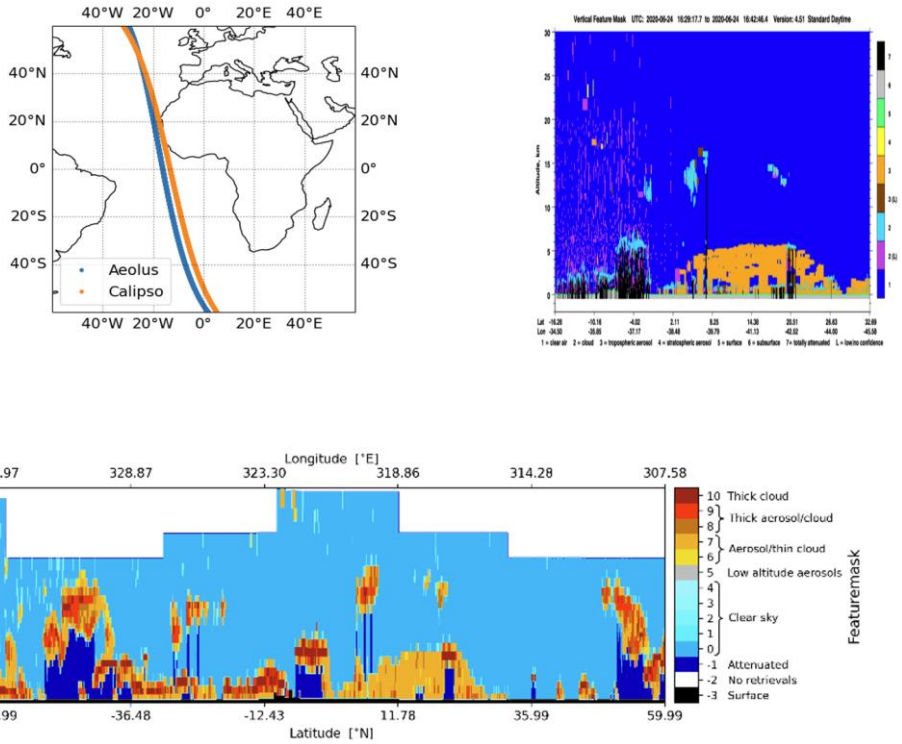

Figure 31. Aeolus orbit 10655 and CALIPSO feature mask on 2020-06-24. (top-left) Aeolus and CALIPSO orbits, (top-right) CALIPSO vertical feature mask, (bottom) Aeolus AEL-FM feature mask.

The dust plume patterns measured by Aeolus are similar to those measured by CALIPSO. We checked two dust cases and one day of stratospheric aerosol cases with collocated CALIPSO orbits. Figure 30 shows the AEL-FM and CALIPSO feature mask on 19 June 2020. Figure 31 shows the AEL-FM and CALIPSO feature mask on 24 June 2020. Note that the Aeolus feature mask is plotted for a larger latitude range to be consistent with the extinction profile images. On 19 June, the aerosols were thick, the Aeolus signals were almost fully attenuated close to the surface between the latitude range of 9 and 22 degree north. In the similar region, the CALIPSO feature mask identified the attenuated signals as clouds but with low confidence. On the 24 June the dust layer is found for both CALIPSO and Aeolus with a liquid cloud detected at the top of the layer in both cases. Cirrus clouds are detected between 10 and 15 km above the dust layer.

6.6.3 Validation of AEL-PRO extinction coefficients

6.6.3.1 Dust aerosols

AEL-PRO extinction coefficient and lidar ratio profile images are shown for the two dust cases and compared with CALIPSO extinction coefficient (see Figure 32 to Figure 35). The AEL-PRO extinction coefficients are plotted for all data and tropospheric aerosols (classification =103). The AEL-PRO aerosol extinction coefficient images are comparable to the CALIPSO extinction images. However, the Aeolus

extinction images have more low extinction values below the tropopause compared to CALIPSO. Clouds were removed successfully in the AEL-PRO aerosol extinction images but at the top of the dust plumes, a few altitude bins with aerosols were removed as clouds, for example in Figure 32 between distance 4000-6000 km on 2020-06-19, Figure 34 between distance 8000-9000 km. The mean extinction coefficient profiles and AOTs (Aerosol Optical Thicknesses) are also very similar between Aeolus and CALIPSO. We can see clearly the higher spatial and horizontal resolution of CALIPSO data (5 km horizontal, 60 m vertical). The agreement between Aeolus and CALIPSO AOT is better on 24 June than 19 June 2020. The CALIPSO AOT was taken from the CALIPSO L2 5 km aerosol profile product v4.51. The Aeolus AOT was calculated using aerosol extinction profiles directly. There were some very large AOT values (>10?), which were filtered out in the mean AOT. An Angström coefficient of 0.55 is used to convert the CALIPSO AOT at 532 nm to 355 nm.

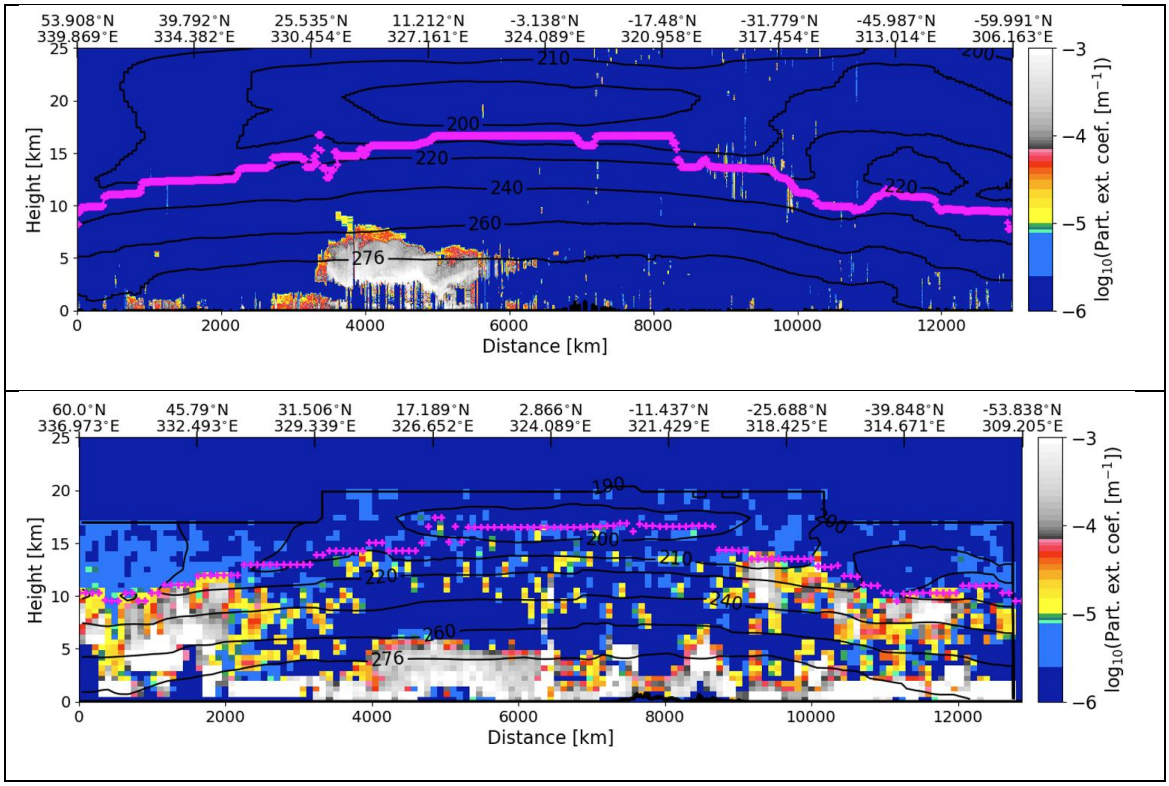

Document Title

Verification report for phase 1 of the fourth reprocessing campaign for the FM-B laser from June 2019 till October 2022

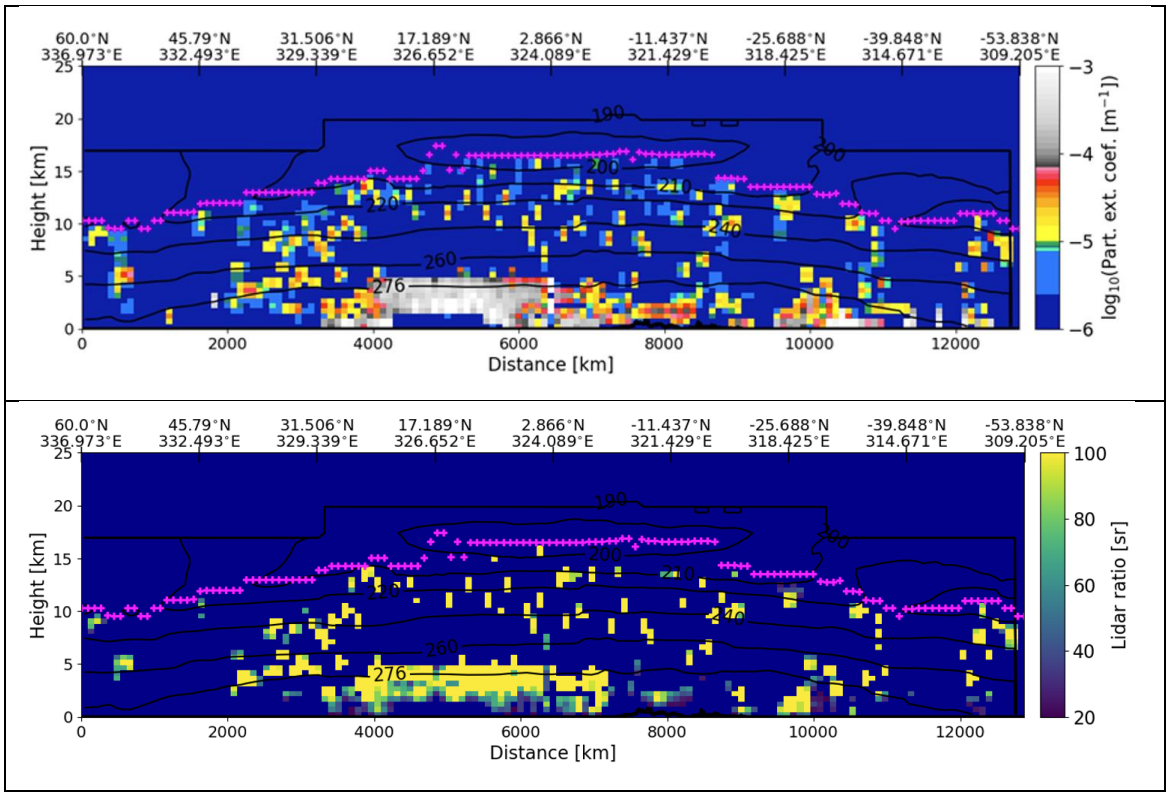

Figure 32. Panels from top to bottom are: CALIPSO aerosol tropospheric aerosol extinction coefficient image on 2020-06-19, Aeolus AEL-PRO extinction coefficient image, Aeolus AEL-PRO aerosol extinction coefficient (classification =103), AEL-PRO aerosol lidar ratio (classification =103, extinction coefficient > 1.e-5 m^{-1}). The magenta symbols indicate the tropopause height. The thin black contours indicate the atmospheric temperature.

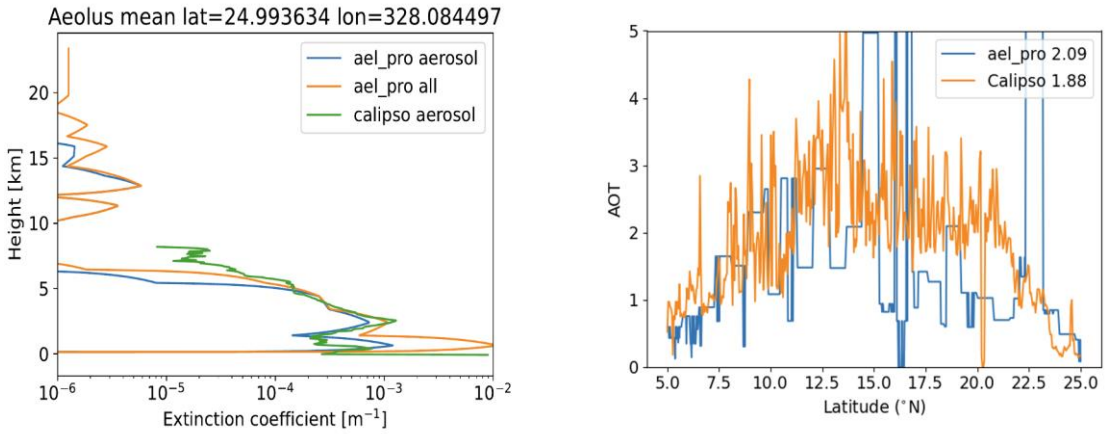

Figure 33. Left: Aeolus and CALIPSO mean extinction profile along orbit from 5 to 25 degrees latitude. Right: Aeolus and CALIPSO AOT (Aerosol Optical Thickness) from 5 to 25 degrees latitude. Same data as in Figure 32.

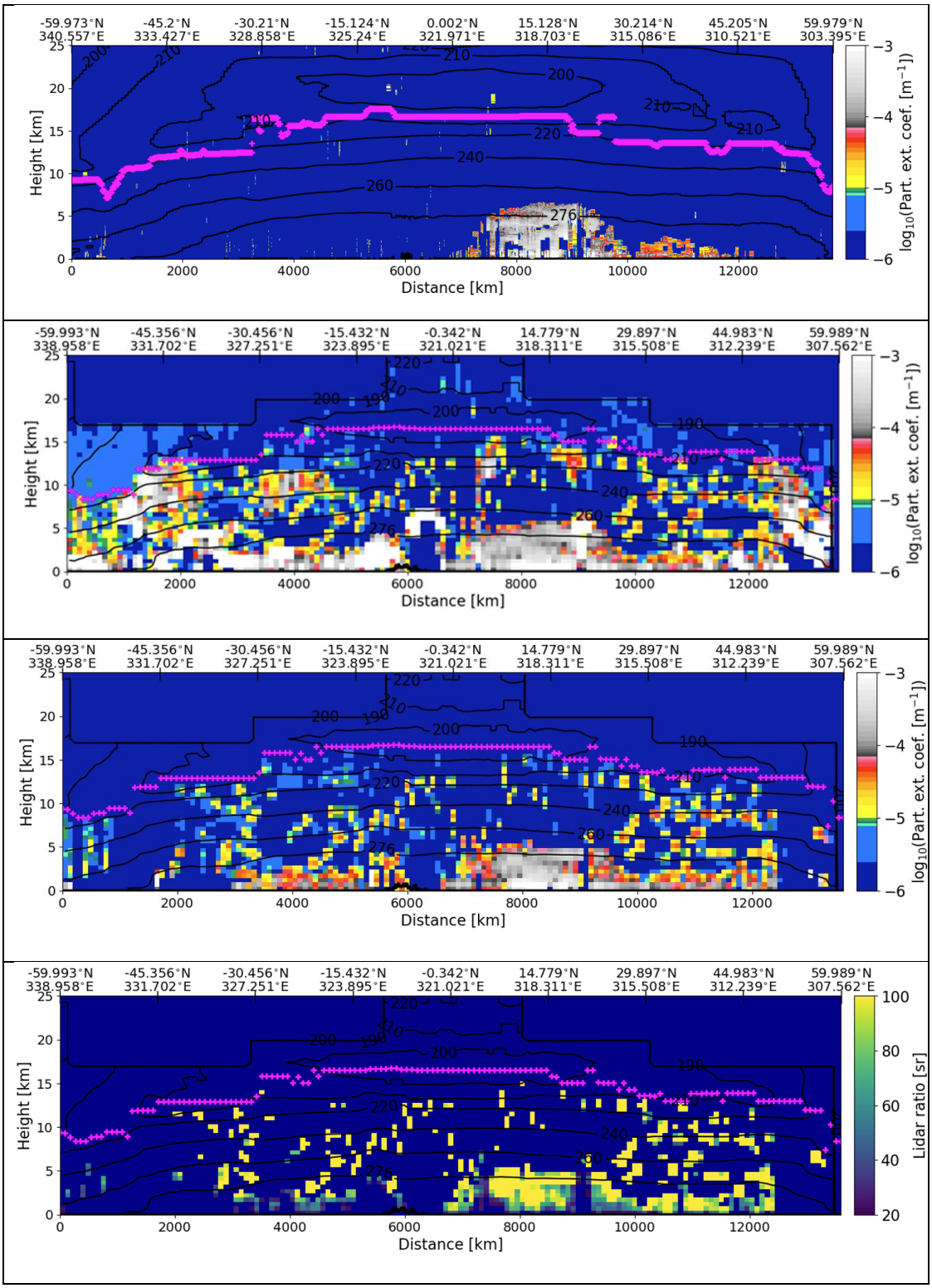

Figure 34. Panels from top to bottom are: CALIPSO aerosol tropospheric aerosol extinction coefficient image on 2020-06-24, Aeolus AEL-PRO extinction coefficient image, Aeolus AEL-PRO aerosol extinction coefficient (classification =103), AEL-PRO aerosol lidar ratio (classification =103, extinction coefficient > 1.e-5 m^{-1}). The magenta symbols indicate the tropopause height. The thin black contours indicate the atmospheric temperature.

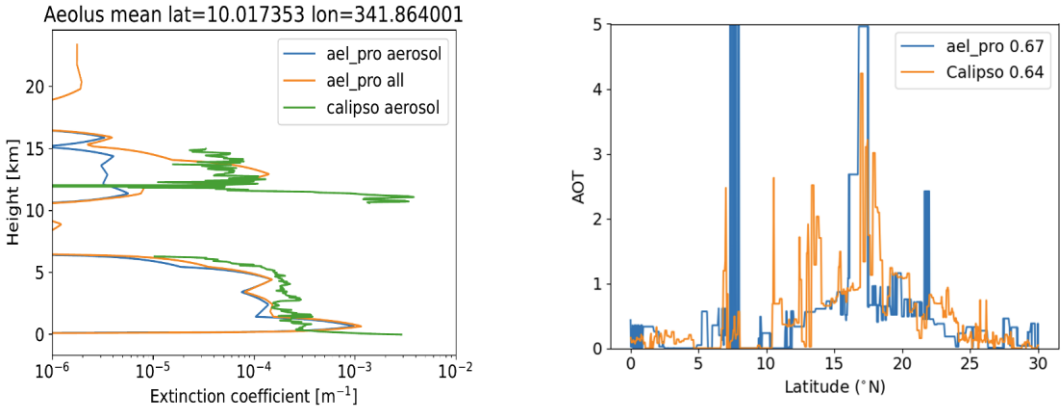

Figure 35. Left: Aeolus and CALIPSO mean extinction profile along orbit from 10 to 25 degrees latitude. Right: Aeolus and CALIPSO AOT (Aerosol Optical Thickness) from 0 to 30 degrees latitude on 2020-06-24. Same data as in Figure 34.

6.6.3.2 Stratospheric aerosols

We checked the stratospheric aerosols in February 2022 after the eruption of the Hunga Tonga–Hunga Ha'apai volcano. Here we show two collocated orbits as examples on 2 February 2022. The stratospheric aerosols were at southern hemisphere at about 25 km with a thickness of 2-3 km, see Figure 36 and Figure 37. AEL-PRO has classification for stratospheric aerosols, but for simplicity, we plotted all the data. We can see that the Aeolus and CALIPSO measured the same aerosol plumes from the shape, altitude, location. However, Aeolus aerosol extinction coefficients are systematically lower than the CALIPSO extinction coefficients. The Angström coefficient for stratospheric aerosol has a large variation, which can be negative or a small positive value. We still need to find out the proper Angström coefficient for the validation. [RD-15] reported negative Angström exponents for the Tonga-Hunga volcanic aerosols with the maximum value of -0.8 ±0.8, which is consistent with our findings.

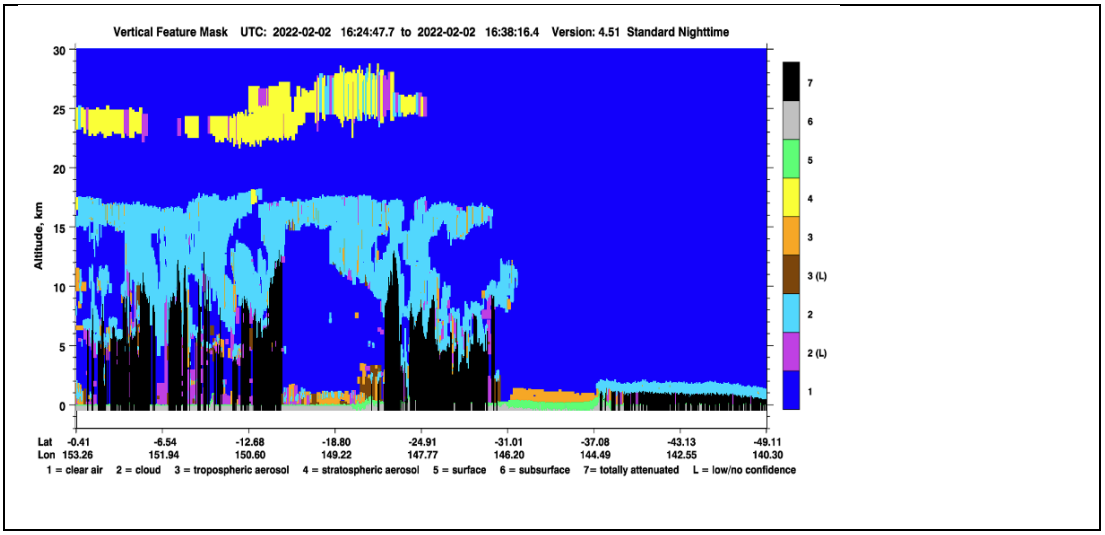

Document Title

Verification report for phase 1 of the fourth reprocessing campaign for the FM-B laser from June 2019 till October 2022

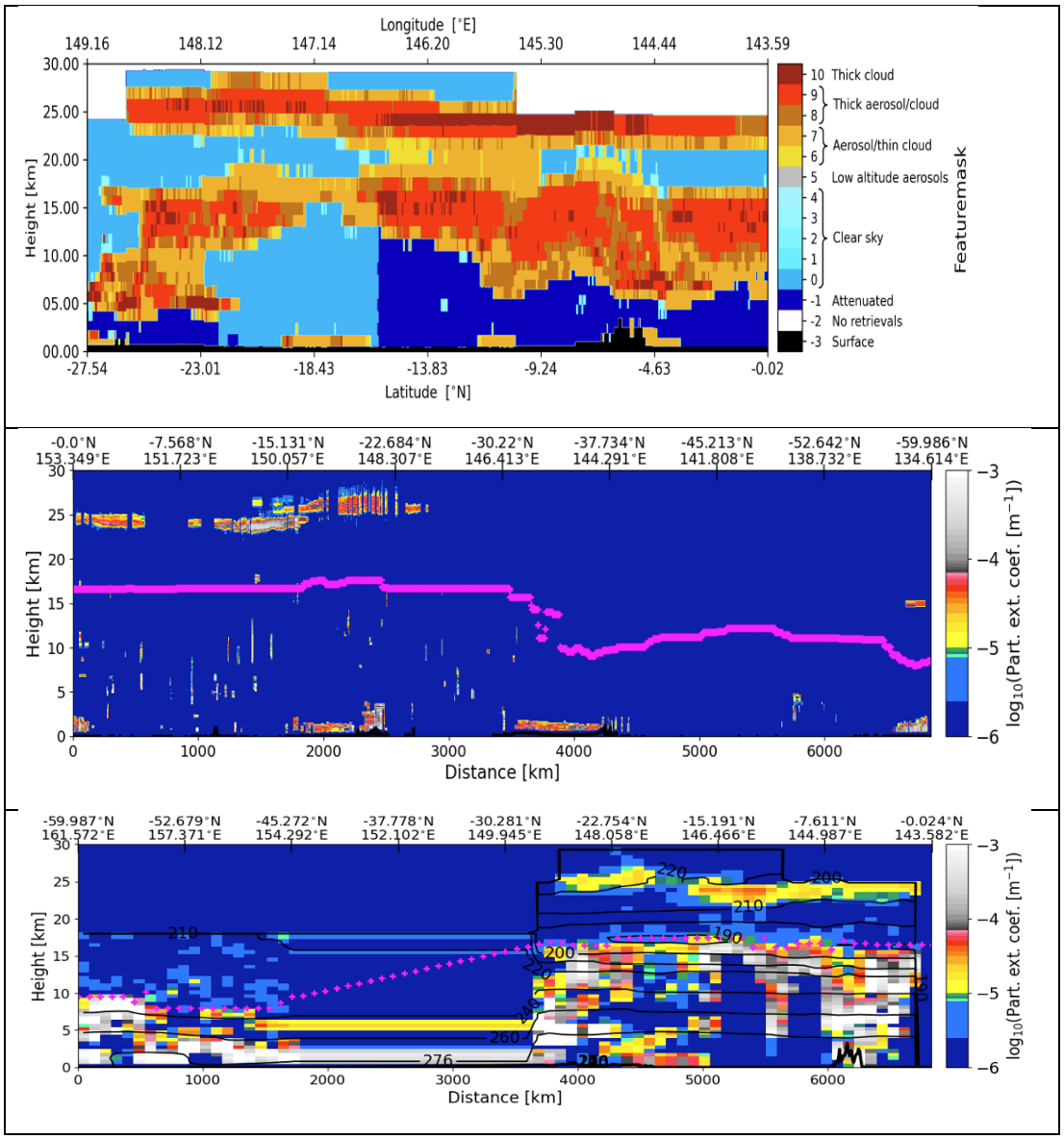

Figure 36. Panels from top to bottom are: CALIPSO and AEL-FM feature masks, CALIPSO aerosol extinction coefficient image on 2022-02-02, Aeolus AEL-PRO extinction coefficient image for orbit #19971. The magenta symbols indicate the tropopause height. The thin black contours indicate atmospheric temperature.

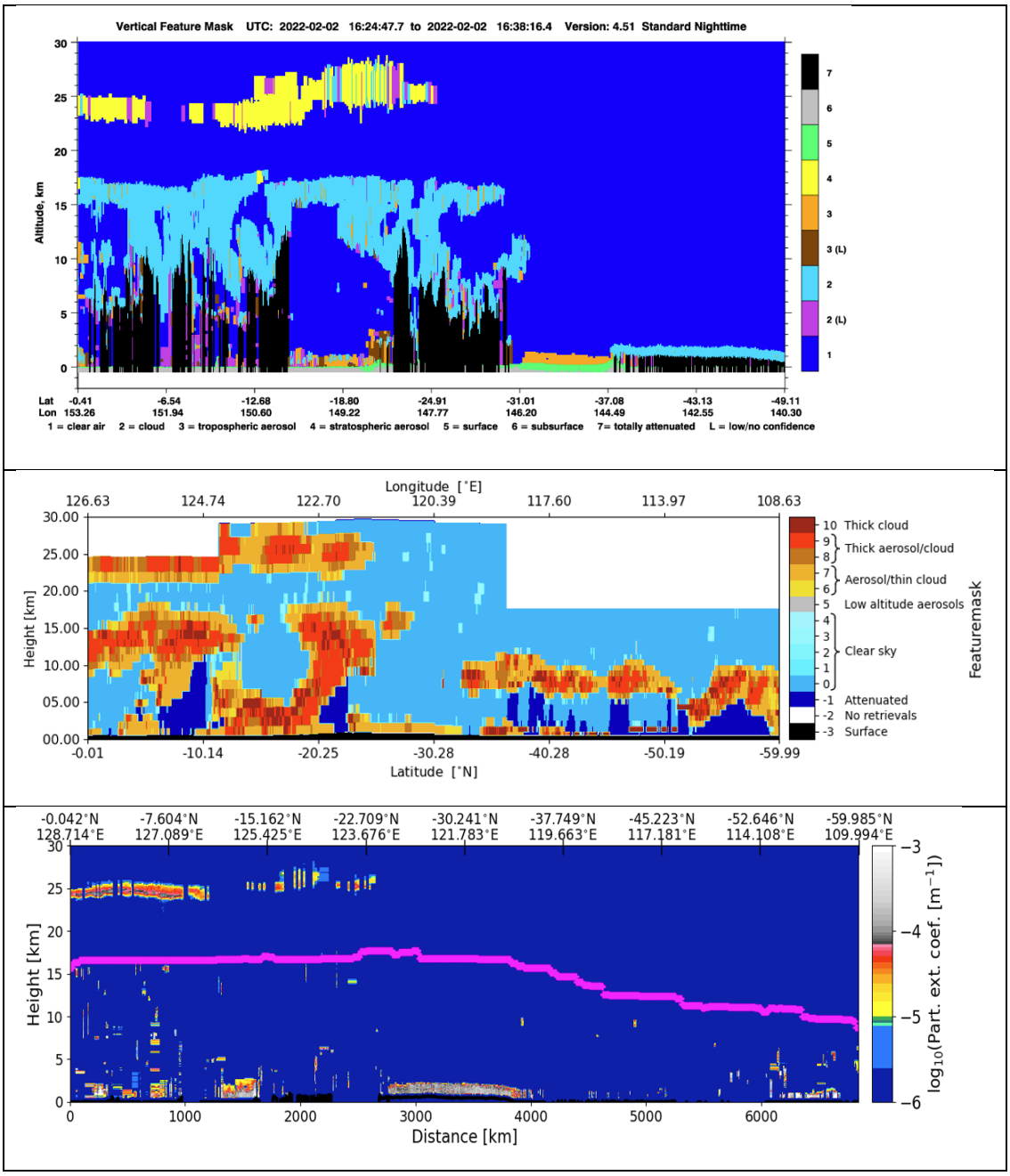
Vertical Feature Mask UTC: 2022-02-02 16:24:47.7 to 2022-02-02 16:38:16.4 Version: 4.51 Standard Nighttime
Altitude, km
Lat -0.41 -6.54 -12.68 -18.80 -24.91 -31.01 -37.08 -43.13 -49.11
Lon 153.26 151.94 150.60 149.22 147.77 146.20 144.49 142.55 140.30
1 = clear air 2 = cloud 3 = tropospheric aerosol 4 = stratospheric aerosol 5 = surface 6 = subsurface 7= totally attenuated L = low/no confidence
Longitude [°E]
126.63 124.74 122.70 120.39 117.60 113.97 108.63
Height [km]
Latitude [°N]
-0.01 -10.14 -20.25 -30.28 -40.28 -50.19 -59.99
Thick cloud
Thick aerosol/cloud
Aerosol/thin cloud
Low altitude aerosols
Clear sky
Attenuated
No retrievals
Surface
Featuremask
-0.042°N 128.714°E
-7.604°N 127.089°E
-15.162°N 125.425°E
-22.709°N 123.676°E
-30.241°N 121.783°E
-37.749°N 119.663°E
-45.223°N 117.181°E
-52.646°N 114.108°E
-59.985°N 109.994°E
Height [km]
Distance [km]
log10(Part. ext. coef. [m-1])

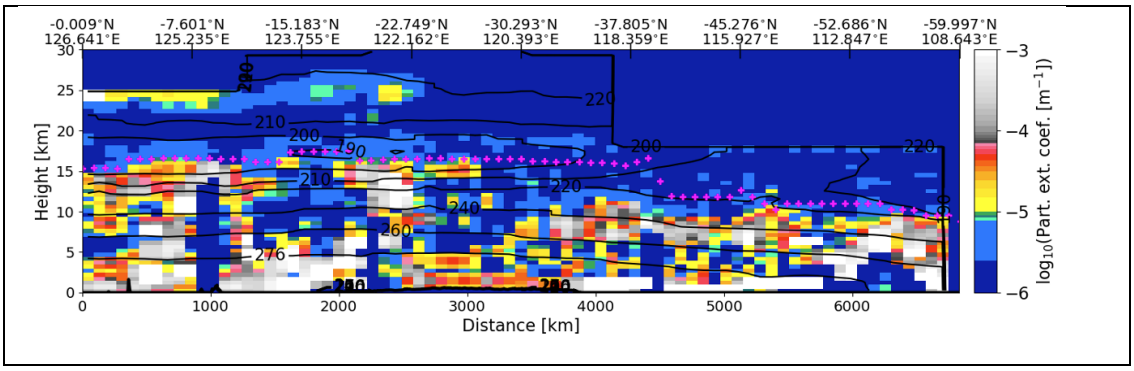

Figure 37. Panels from top to bottom are: CALIPSO and AEL-FM feature masks, CALIPSO aerosol extinction coefficient image on 2022-02-02, Aeolus AEL-PRO extinction coefficient image for orbit #19979. The magenta symbols indicate the tropopause height. The thin black contours indicate atmospheric temperature

6.6.4 Summary of L2A AEL-FM/AEL-PRO products

We think AEL-FM, AEL-PRO products in fourth reprocessing using Baseline 16 are in good shape. The data is good for analysing dust aerosols, stratospheric aerosols, and monthly mean climatology extinction and lidar ratio profiles. However, more validation using ground-based measurements is needed. The AEL-FM and AEL-PRO products must be used carefully e.g. some extreme values need to be filtered and the estimate errors need to be considered when using the data.

The AEL-FM feature mask and AEL-PRO extinction coefficient, lidar ratio profiles are available in the 4th reprocessing. All products are provided at Mie measurement-scale altitude grid and geolocation (mie_geolocation_heigh_bin), although they are averaged along track in case of aerosols and thin clouds.

The AEL-FM and AEL-PRO products are consistent with the prototype products. The feature mask shows clear features of aerosols and clouds. The AEL-PRO extinction coefficients are comparable to the CALIPSO extinction coefficients. This is checked with collocated orbits for some desert dust aerosol.

We suggest using the lidar ratio when extinction coefficients are greater than 1.e-5 m^{-1}. As a standard all retrieved extinction coefficients and lidar ratios are provided by AEL-PRO. In general, the associated error estimates provide a good way for cleaning the data. The most reliable extinction coefficients are between 1.e-6 and 1.e-3 or 1.e-2 m^{-1}. The lidar ratio is usually between 20 and 200. The extinction coefficients in the order of <1e-10 or > 1e3 m^{-1} should not be used.

The separation (using classification field) between aerosols and clouds is not always reliable, especially in the areas when clouds are on top of aerosols directly.

The particle effective area radius can be used for ice clouds, but not for aerosols. This is not a main product. It must be used carefully.

The known limitations of the data products are as follows:

- No cut-off in extinction coefficients for extreme large and small values. This shall be improved in Baseline 17.
- Some hot-pixels still exist in the reprocessed data. They show up as high values in attenuated_mie_backscatter_msp close to surrounding values and low values in attenuated_rayleigh_backscatter_msp.
- The retrieved_lidar_calibration_constant is set to 0, the retrieved values will be added in next version (Baseline 17).
- There is no general quality index available at this point for AEL-PRO product, this will be added in Baseline 17.

6.7 L2A aerosol backscatter O-B departure statistics from the ECMWF IFS-COMPO system

This section aims to assess the quality of L2A aerosol backscatter observations using observation minus background departure statistics (O-B) for the L2A backscatter data ingested into the ECMWF IFS-COMPO system. However, note that the realism of the aerosol backscatter in the IFS-COMPO model is relatively poor compared to, for example, well established meteorological fields, such as winds in the nominal IFS for Numerical Weather Prediction (well established in the L2B assessment). This makes it more difficult to disentangle the random and systematic errors of the observations versus the background from the departure statistics. The IFS-COMPO background aerosol backscatter is predominantly constrained by the assimilation of passive remote sensing aerosol optical depth observations, meaning the vertical distribution of aerosol is not very well constrained.

The forward modelled lidar backscatter from the IFS-COMPO system (CY48R1) is the 355 nm aerosol-only backscatter (i.e. it does not include cloud ice/water backscatter). The experiments which provided the departures for monitoring had an outer loop has a resolution of TL511 (~40 km grid spacing). As it is currently implemented, the IFS-COMPO forward model provides the full aerosol backscatter i.e. it does not simulate the circularly polarised co-polar backscatter that ALADIN is limited to, since information on particulate shape and hence polarisation is not available in the model. Therefore, the Aeolus backscatter values are expected to be negatively biased compared to the background in depolarising scenes, such as mineral dust, typically seen in and around the Sahara Desert and Arabian Peninsula.

Aeolus struggles to distinguish between cloud and aerosol backscatter due to the lack of depolarisation channel, hence the L2A products do not have accurate methods to flag the backscatter as coming from aerosol or ice/water clouds. Therefore, the presence of backscatter from clouds in the observation tends to generate positive bias in the mean(O-B) statistic when the forward model only considers aerosol. However, the AEL-PRO retrieval does have some classification information, but this is not expected to be perfect. To mitigate the cloud-contamination issue, the IFS-COMPO L2A assimilation code employs its own check using the background forecast clouds to try to screen-out cloud affected

backscatter, but this method is also imperfect, since the model does not represent clouds perfectly and the background forecast often misplaces them (particularly convective clouds).

We have assessed two month-long periods of 4th reprocessing B16 L2A data: July 2019 and June 2020. July 2019 had unusually large amounts of wildfire smoke over high northern latitudes and the Raikoke volcanic eruption plume and the instrument SNR was at its peak. June 2020 was chosen due to the "Godzilla" dust event (19-23 June 2020), where larger quantities of dust were advected from the Saharan desert westward across the Atlantic Ocean (the largest event in 50 years).

6.7.1 SCA mid-bin backscatter departure statistics

Firstly, we show the zonal average O-B departure statistics using the L2A SCA mid-bin backscatter for July 2019 in Figure 38 and June 2020 in Figure 39. There is no aerosol-cloud classification information available for this retrieval type, hence the background forecast cloud QC check is the only way to try to avoid the cloud backscatter influencing the statistics.

Both months have similar patterns for the O-B departures with large positive biases towards the poles and around the ITCZ (~10 degrees latitude) associated with cloud backscatter contamination. There is a patch of negative bias (~-0.5 $Mm^{-1}sr^{-1}$) at ~700 hPa for 10-30 degrees latitude associated with depolarising mineral dust. Comparing the mean observed and background values individually highlights the cloud contamination, since the background has small aerosol backscatter above 600 hPa, whereas the observation does not. Given that the mean observation and model values of backscatter reach ~3 $Mm^{-1}sr^{-1}$, the peak standard deviation of O-B (random differences) near the surface of ~3-4 $Mm^{-1}sr^{-1}$, is relatively very large. There is a patch of larger stdev(O-B) between 50-70 degrees in July 2019, which is thought to be associated with wildfire smoke (possibly the background is more in error here). The positive biases are also relatively large compared to the mean observed or modelled values, with biases reaching > 1.5 $Mm^{-1}sr^{-1}$ near the surface.

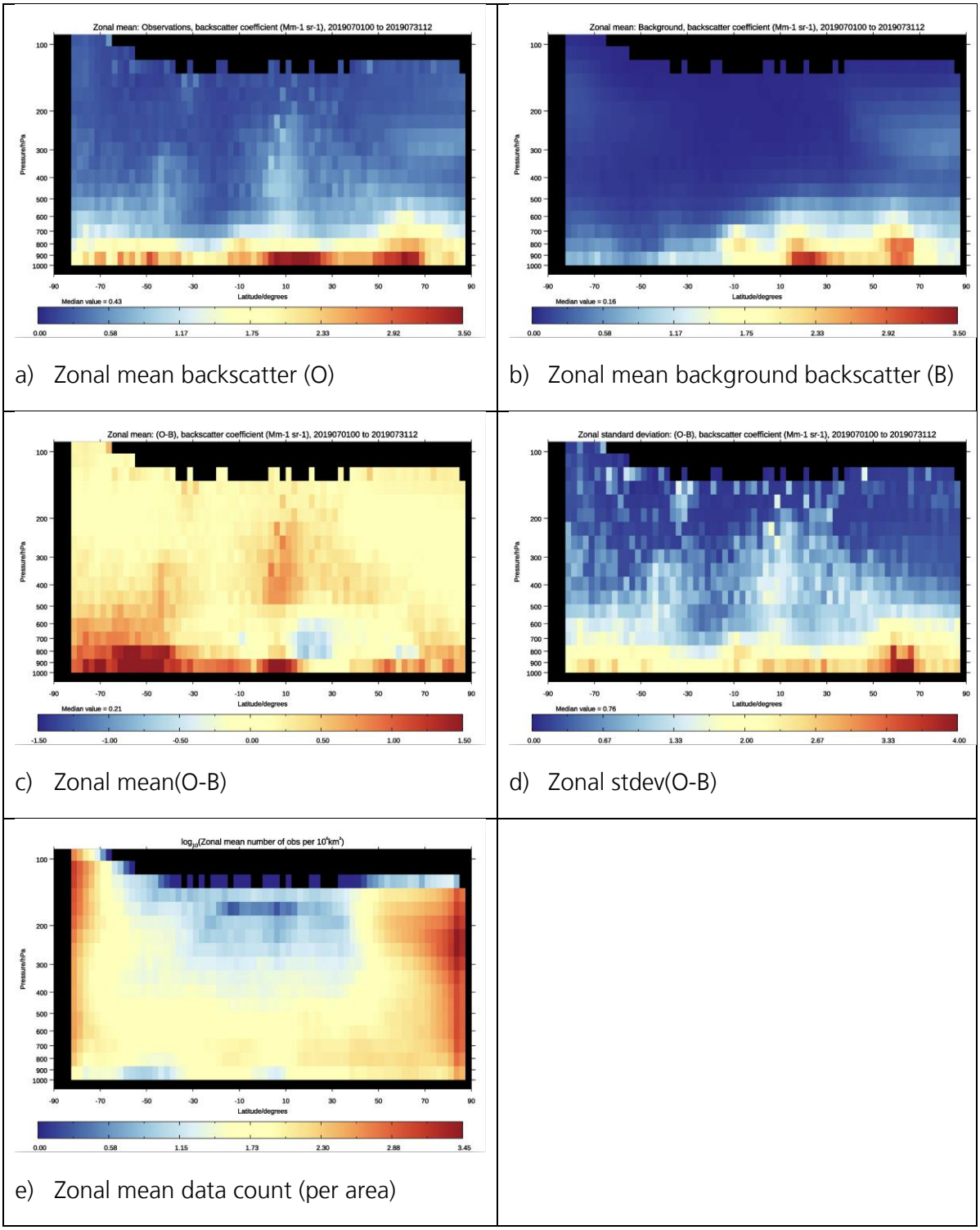

a) Zonal mean backscatter (O)

b) Zonal mean background backscatter (B)

c) Zonal mean(O-B)

d) Zonal stdev(O-B)

e) Zonal mean data count (per area)

Figure 38. Zonal average departure statistics for L2A SCA mid-bin backscatter data, for 1-31 July 2019 (expid=i9qw). Units: $Mm^{-1}sr^{-1}$.

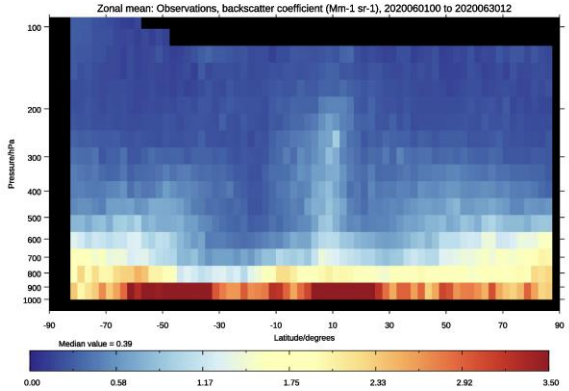

a) Zonal mean backscatter (O)

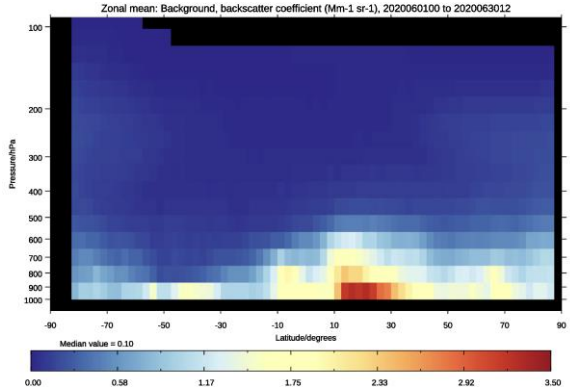

b) Zonal mean background backscatter (B)

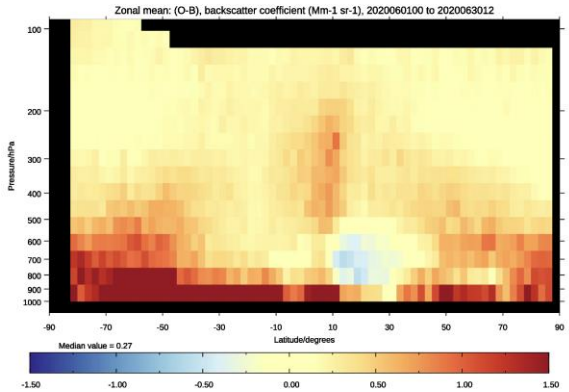

c) Zonal mean(O-B)

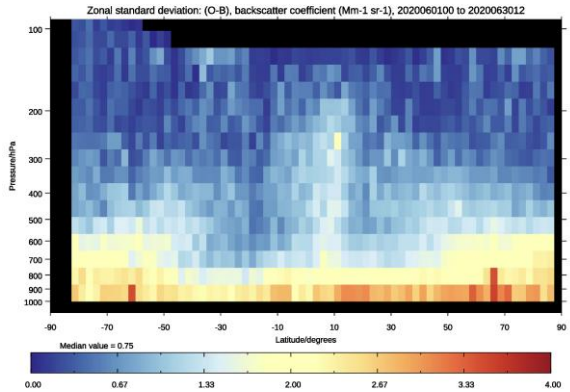

d) Zonal stdev(O-B)

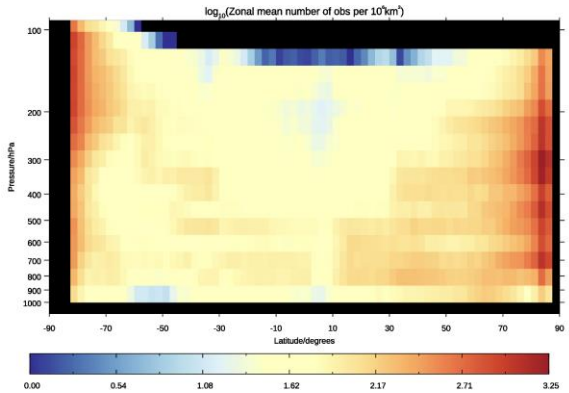

e) Zonal mean data count (per area)

Figure 39. Zonal average departure statistics for L2A SCA mid-bin backscatter data, for 1-30 June 2020 (expid=i9s8). Units: $Mm^{-1}sr^{-1}$.

6.7.2 AEL-PRO (without classification) backscatter departure statistics

The zonal average statistics using the L2A AEL-PRO backscatter (firstly ignoring the classification flag, so all data) are shown for July 2019 in Figure 40 and June 2020 in Figure 41. Therefore, the check on background forecast cloud is the only way to try to avoid the cloud backscatter in this case.

This is somewhat similar to the SCA mid-bin result; however, the cloud contamination seems stronger in the Tropics between -10 to +30 degrees latitude and near the surface at -50 degrees latitude. The negative bias associated with desert dust is stronger for AEL-PRO (in July 2019 less than -1.50 $Mm^{-1}sr^{-1}$) compared to the SCA mid-bin. The data counts are larger with AEL-PRO versus the SCA mid-bin: perhaps being a variational retrieval method there is less noise and so more coverage. The patch of larger stdev(O-B) between ~60-70 degrees in July 2019 is more obvious in the AEL-PRO than the SCA mid-bin.

6.7.3 AEL-PRO (with classification as aerosol) backscatter departure statistics

The zonal average statistics using the L2A AEL-PRO backscatter using the *aerosol classification flag* are shown for July 2019 in Figure 42 and June 2020 in Figure 43. In addition, the check on background forecast cloud is used to try to avoid the cloud backscatter.

The AEL-PRO dataset with classification=aerosol dataset removes much of the positive mean(O-B) due to cloud contamination in the troposphere particularly above 900 hPa in the SH extratropics. It also reduces the cloud contamination significantly in the worst cloud contamination area: the tropical upper troposphere, however, there is a still too much bias present in July 2019 (but data counts are quite low in that area). The tropical cloud contamination bias is smaller in June 2020 versus July 2019; the reason is unknown. A strong positive bias remains near the surface in the SH extratropics, which according to the map in Figure 44 g), occurs mostly over the oceans. This may be due to low level cloud that is incorrectly flagged as aerosol e.g. low-level cloud is prevalent in the Indian Ocean in both periods according to Nasa Worldview (https://worldview.earthdata.nasa.gov). Alternatively, Aeolus could be detecting more sea salt aerosol backscatter than is present in the background.

In Figure 42 for July 2019, the mean observed values do not clearly show the enhanced backscatter associated with mineral dust when compared the mean background values. The strong negative mean(O-B) peaking at ~700-800 hPa at 20 degrees latitude in the zonal average is mostly associated with Saharan and Arabian desert dust. The bias is stronger in July 2019 compared to June 2020 for reasons not yet understood, but it may be an SNR issue related to range-bin setting changes[2].

[2] Since the AEL-PRO retrieval uses the Mie channel only (novel method to distinguish Mie peak from Rayleigh background across the ACCD), perhaps the thicker Mie range-bin settings near the surface in June 2020 versus July 2019 helped the SNR.

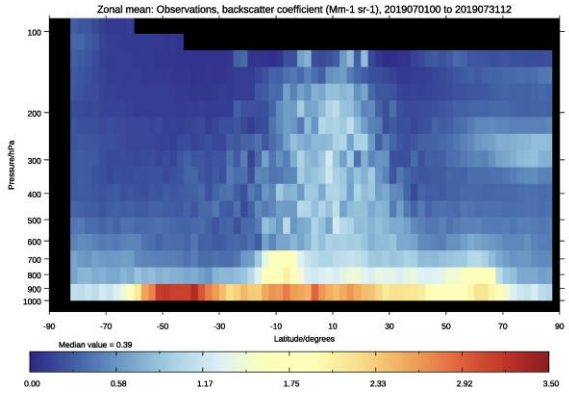

a) Zonal mean backscatter (O)

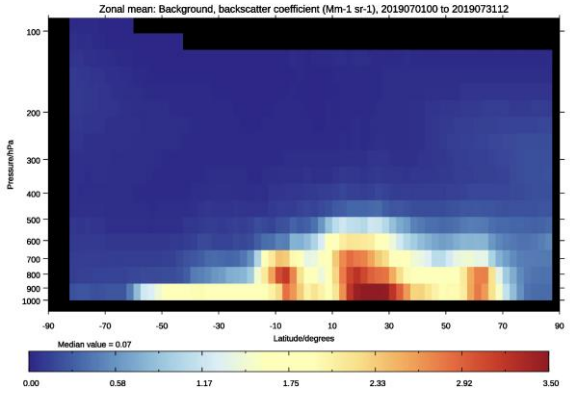

b) Zonal mean background backscatter (B)

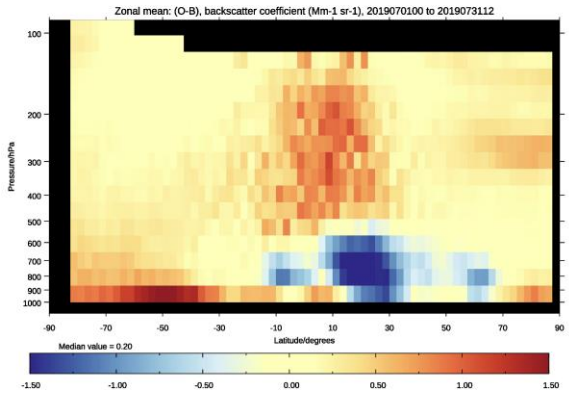

c) Zonal mean(O-B)

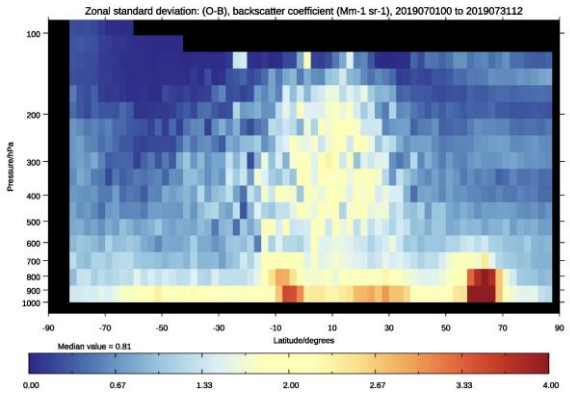

d) Zonal stdev(O-B)

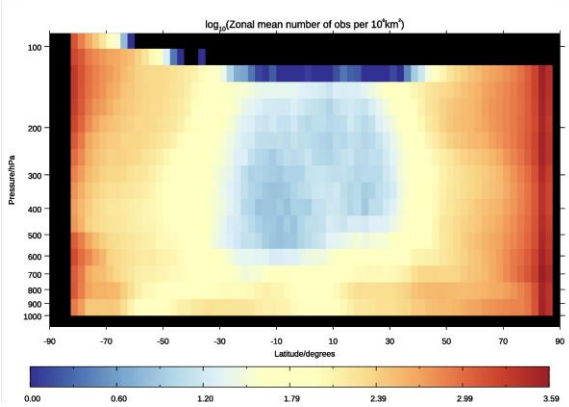

e) Zonal mean data count (per area)

Figure 40. Zonal average departure statistics for L2A AEL-PRO backscatter data, classification=all types, for 1-31 July 2019 (experiment-id=idax). Units: $Mm^{-1}sr^{-1}$.

Document Title

Verification report for phase 1 of the fourth reprocessing campaign for the FM-B laser from June 2019 till October 2022

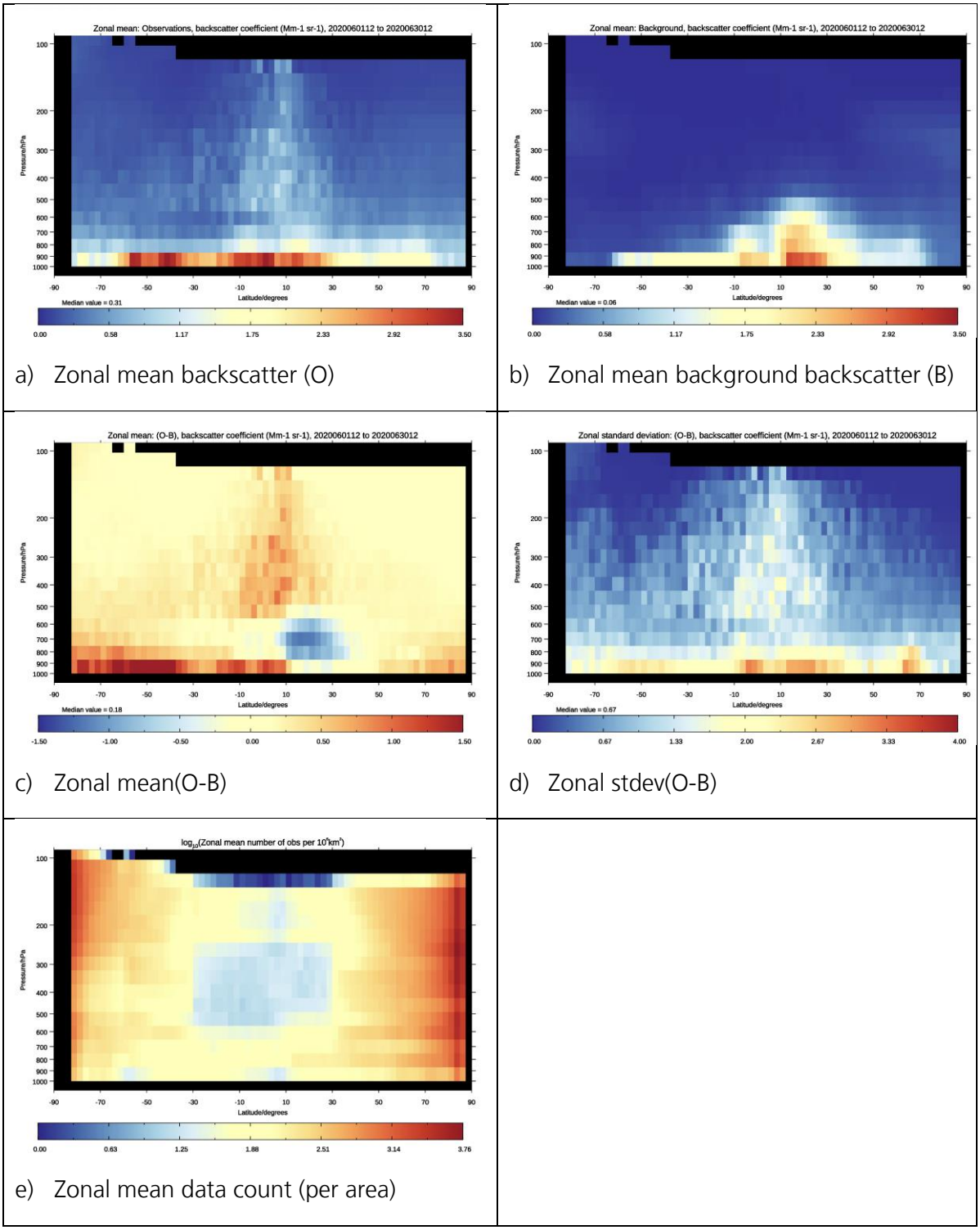

a) Zonal mean backscatter (O)

b) Zonal mean background backscatter (B)

c) Zonal mean(O-B)

d) Zonal stdev(O-B)

e) Zonal mean data count (per area)

Figure 41. Zonal average departure statistics for L2A AEL-PRO backscatter data, classification=all types, for 1-30 June 2020 (expid=icqq). Units: $Mm^{-1}sr^{-1}$.

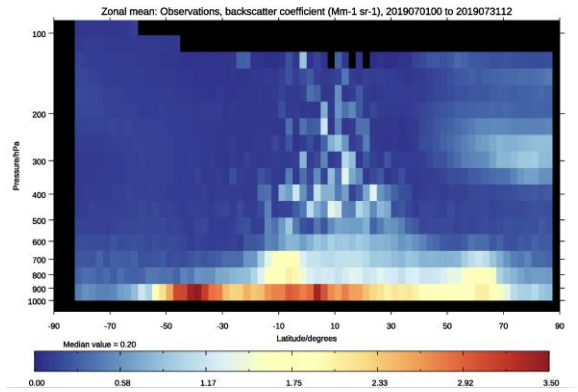

a) Zonal mean backscatter (O)

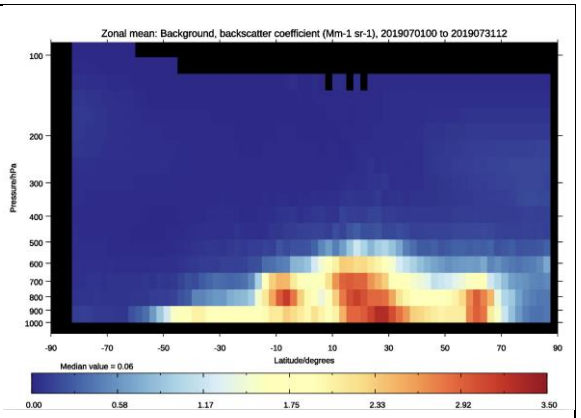

b) Zonal mean background backscatter (B)

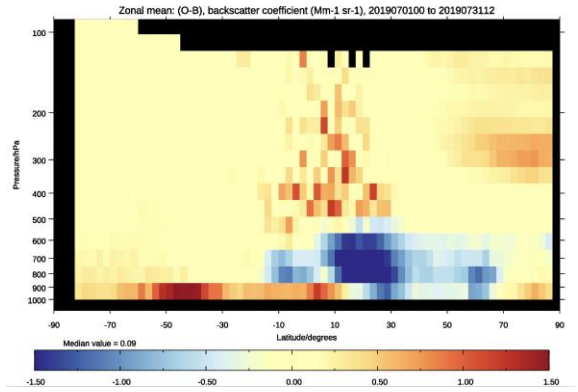

c) Zonal mean(O-B)

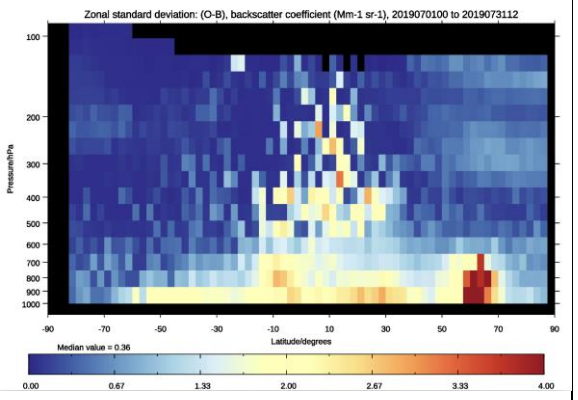

d) Zonal stdev(O-B)

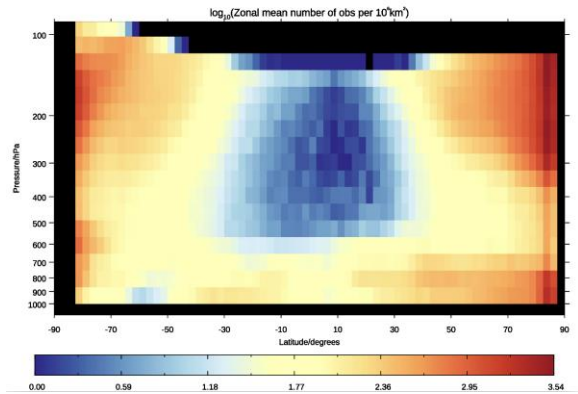

e) Zonal mean data count (per area)

Figure 42. Zonal average departure statistics for L2A AEL-PRO backscatter data, classification=aerosol-only, for 1-31 July 2019 (expid=ie4m). Units: $Mm^{-1}sr^{-1}$.

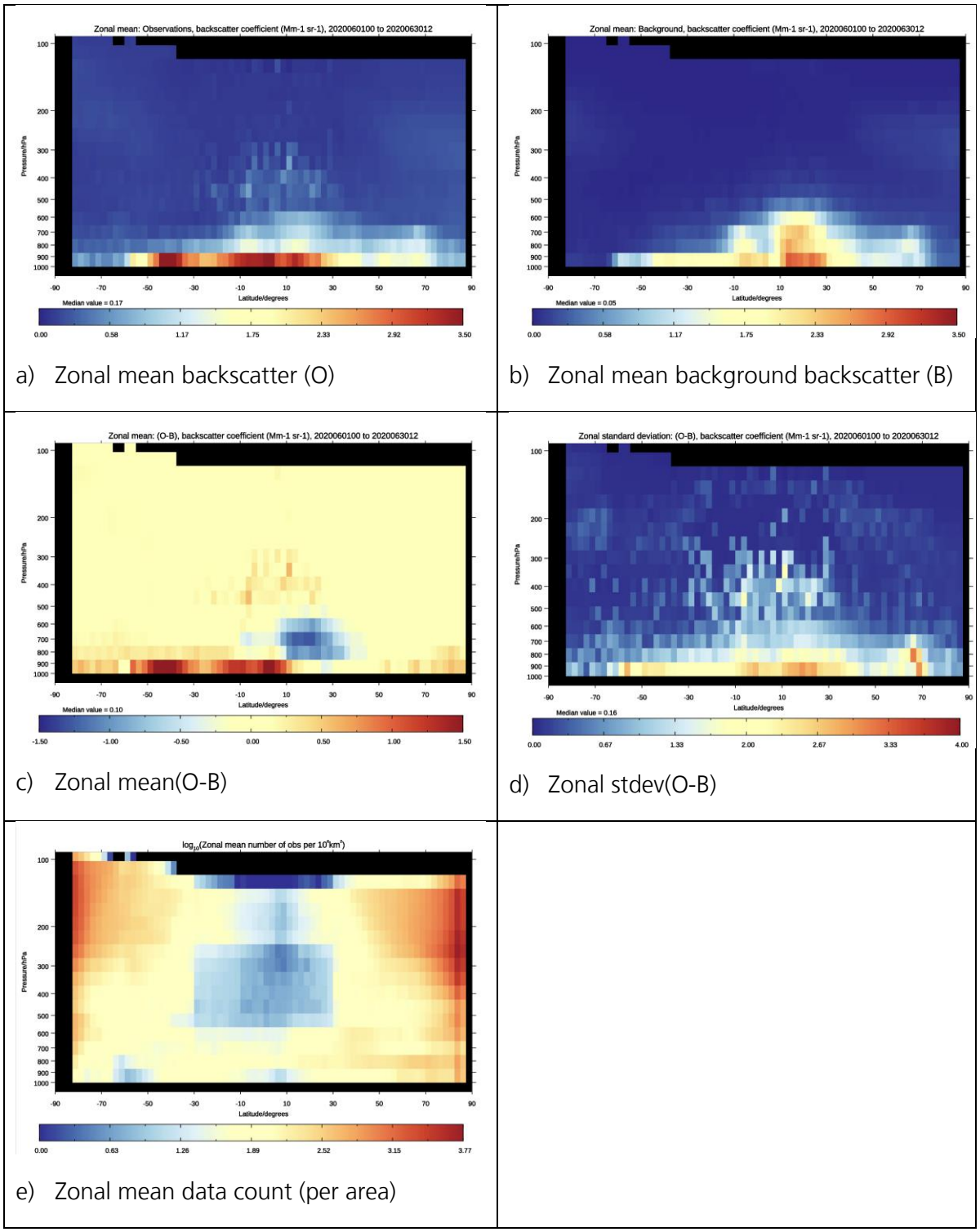

a) Zonal mean backscatter (O)

b) Zonal mean background backscatter (B)

c) Zonal mean(O-B)

d) Zonal stdev(O-B)

e) Zonal mean data count (per area)

Figure 43. Zonal average departure statistics for L2A AEL-PRO backscatter data, classification=aerosol-only, for 1-30 June 2020 (expid=icub). Units: $Mm^{-1}sr^{-1}$.

In July 2019 the geographical pattern of negative bias is evident in the maps of Figure 44 h) and i) – covering most of North Africa, mid-Atlantic, Arabian Peninsula. There are also patches of negative

mean(O-B) towards the poles in North America and Asia and central Africa, which are probably associated with wildfire smoke. Wildfire smoke is only weakly depolarising, so a negative bias suggests the background forecast smoke backscatter is too strong or perhaps there. Are other sources of negative bias issues in AEL-PRO backscatter. There are associated patches of larger stdev(O-B) in Alaska, Siberia and central Africa from the surface to ~700 hPa associated with wildfire smoke – suggesting the background random errors may be larger in such areas (perhaps issues in the geolocation of the smoke plumes in the vertical).

Figure 45 shows maps for June 2020. The mineral dust backscatter stands out more clearly (from the noise) than in July 2019, due to the Godzilla event. The higher dust aerosol loads are evident from the mean background backscatter over the Sahara and Atlantic Ocean in 2020. The negative bias is less strong in June 2020 vs July 2019 for dust areas, which also suggests perhaps there is a combination of negative bias due to depolarisation but also perhaps due to low SNR and ALADIN not being sensitive enough to detect the smaller dust backscatter values in July 2019.

The AEL-PRO with aerosol-only classification highlights the aerosol backscatter present at > 50 degrees north, peaking at ~300 hPa – causing a positive bias in mean(O-B) in Figure 42. These aerosols have been previously confirmed (via L2B Mie-cloudy wind investigations, see [RD-13]) to be associated with wildfire smoke which is trapped around the tropopause with a peak aerosol-load in July 2019. Interestingly the IFS-COMPO background has a faint hint of such aerosol, however it is negligible compared to the monthly average ~1 $Mm^{-1}sr^{-1}$ of the AEL-PRO data; see Figure 46. It should be checked if the IFS-COMPO is expected to represent such aerosols correctly.

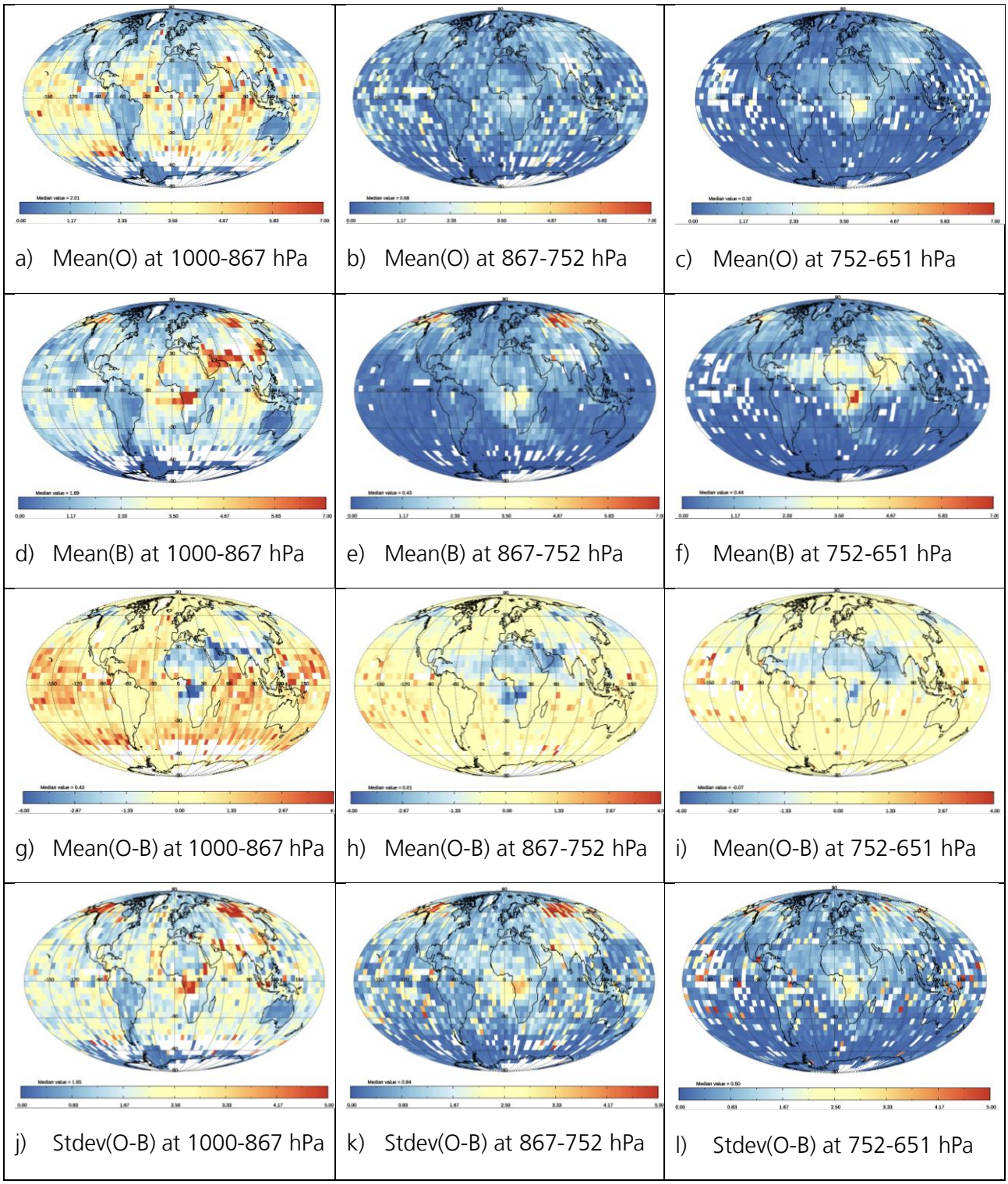

a) Mean(O) at 1000-867 hPa | b) Mean(O) at 867-752 hPa | c) Mean(O) at 752-651 hPa

d) Mean(B) at 1000-867 hPa | e) Mean(B) at 867-752 hPa | f) Mean(B) at 752-651 hPa

g) Mean(O-B) at 1000-867 hPa | h) Mean(O-B) at 867-752 hPa | i) Mean(O-B) at 752-651 hPa

j) Stdev(O-B) at 1000-867 hPa | k) Stdev(O-B) at 867-752 hPa | l) Stdev(O-B) at 752-651 hPa

Figure 44. Mapped departure statistics for L2A AEL-PRO data, classification=aerosol, for 1-31 July 2019 (expid=ie4m). Units: $Mm^{-1}sr^{-1}$.

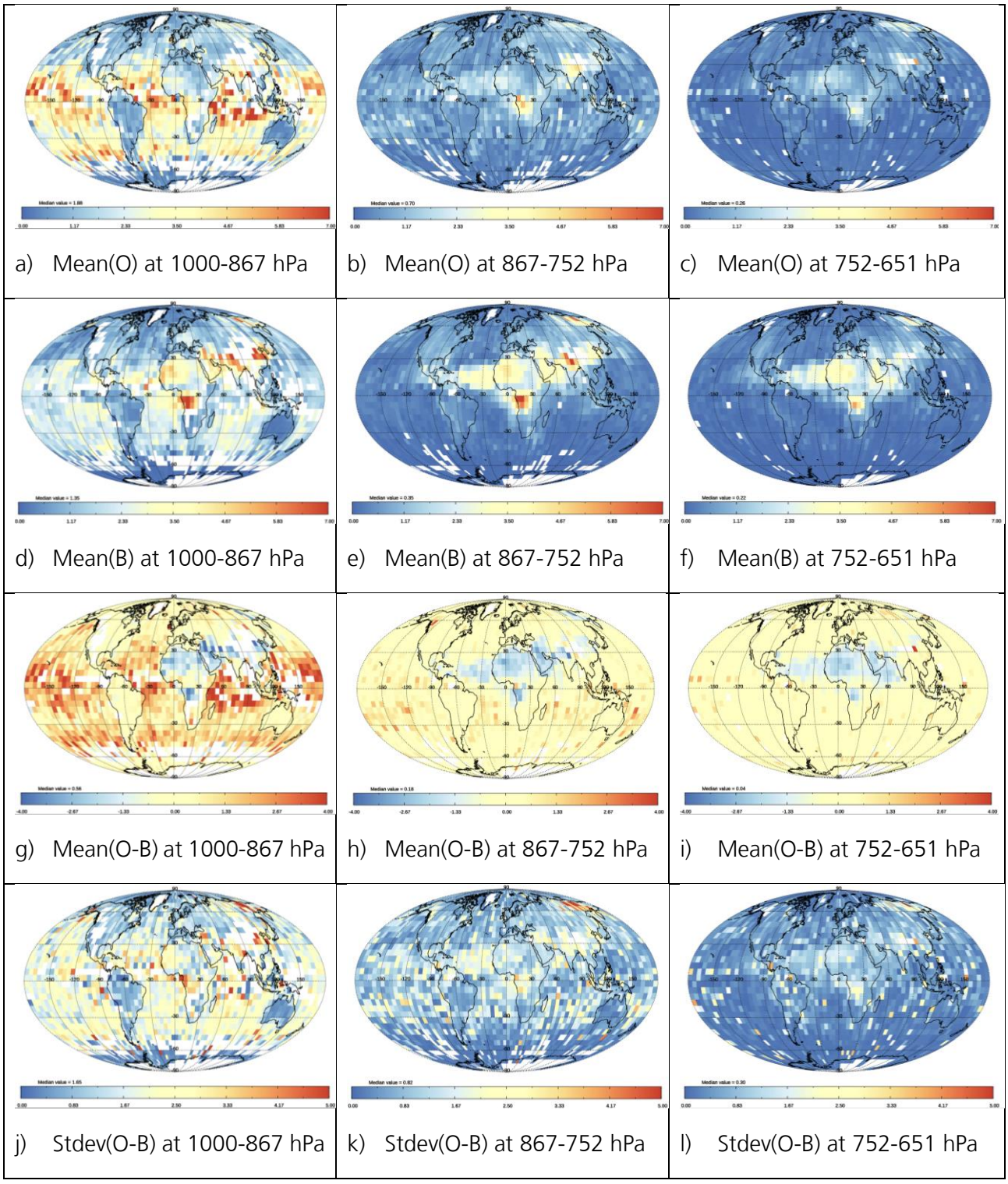

a) Mean(O) at 1000-867 hPa | b) Mean(O) at 867-752 hPa | c) Mean(O) at 752-651 hPa

d) Mean(B) at 1000-867 hPa | e) Mean(B) at 867-752 hPa | f) Mean(B) at 752-651 hPa

g) Mean(O-B) at 1000-867 hPa | h) Mean(O-B) at 867-752 hPa | i) Mean(O-B) at 752-651 hPa

j) Stdev(O-B) at 1000-867 hPa | k) Stdev(O-B) at 867-752 hPa | l) Stdev(O-B) at 752-651 hPa

Figure 45. Mapped departure statistics for L2A AEL-PRO data, classification=aerosol, for 1-30 June 2020 (expid=icub. Units: $Mm^{-1}sr^{-1}$.

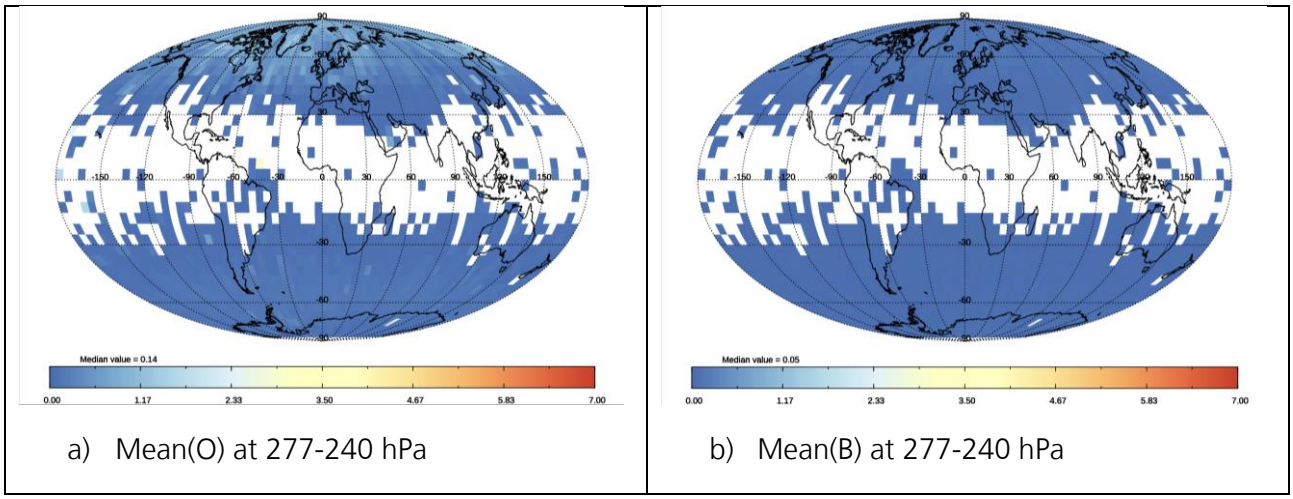

a) Mean(O) at 277-240 hPa

b) Mean(B) at 277-240 hPa

Figure 46. Mapped statistics for L2A AEL-PRO backscatter, classification=aerosol, for 1-31 July 2019 (expid=ie4m) focussing on 277-240 hPa (~10 km) to highlight wildfire smoke aerosol present in the observations. Units: $Mm^{-1}sr^{-1}$.

6.7.4 Time-series of backscatter departure statistics

Figure 47, Figure 48 and Figure 49 show time series of globally-averaged mean background and analysis backscatter departures below 700 hPa (where most aerosol occurs) for July 2019 and June 2020, along with the corresponding standard deviation of each, for COMPO-IFS experiments assimilating the SCA mid-bin, AEL-PRO all types, and AEL-PRO with aerosol classification, respectively. As is the case for the zonally averaged plots and maps of the previous section, the SCA mid-bin departures are positively biased, because of the remaining cloud contamination following the IFS based cloud screening. These positive biases are reduced in AEL-PRO all types (particularly in 2019, not so much in 2020), with even further reduction for the AEL-PRO meeting the aerosol classification criteria. This leads to a mostly negative bias in 2019 (but close to zero in 2020), which is to be expected, as Aeolus does not measure the full backscatter, yielding a negative bias for particles with relatively lower sphericity, such as mineral dust. The standard deviation (noise) is improved with AEL-PRO results vs SCA mid-bin, particularly in 2020, and particularly using the aerosol classification. The statistics look reasonably stable with time, indicating that the L2A products do not show anomalous time periods in these months. There are some spikes in the standard deviation of O-B in 22-25 June 2020, which could possibly be associated with the Godzilla dust event.

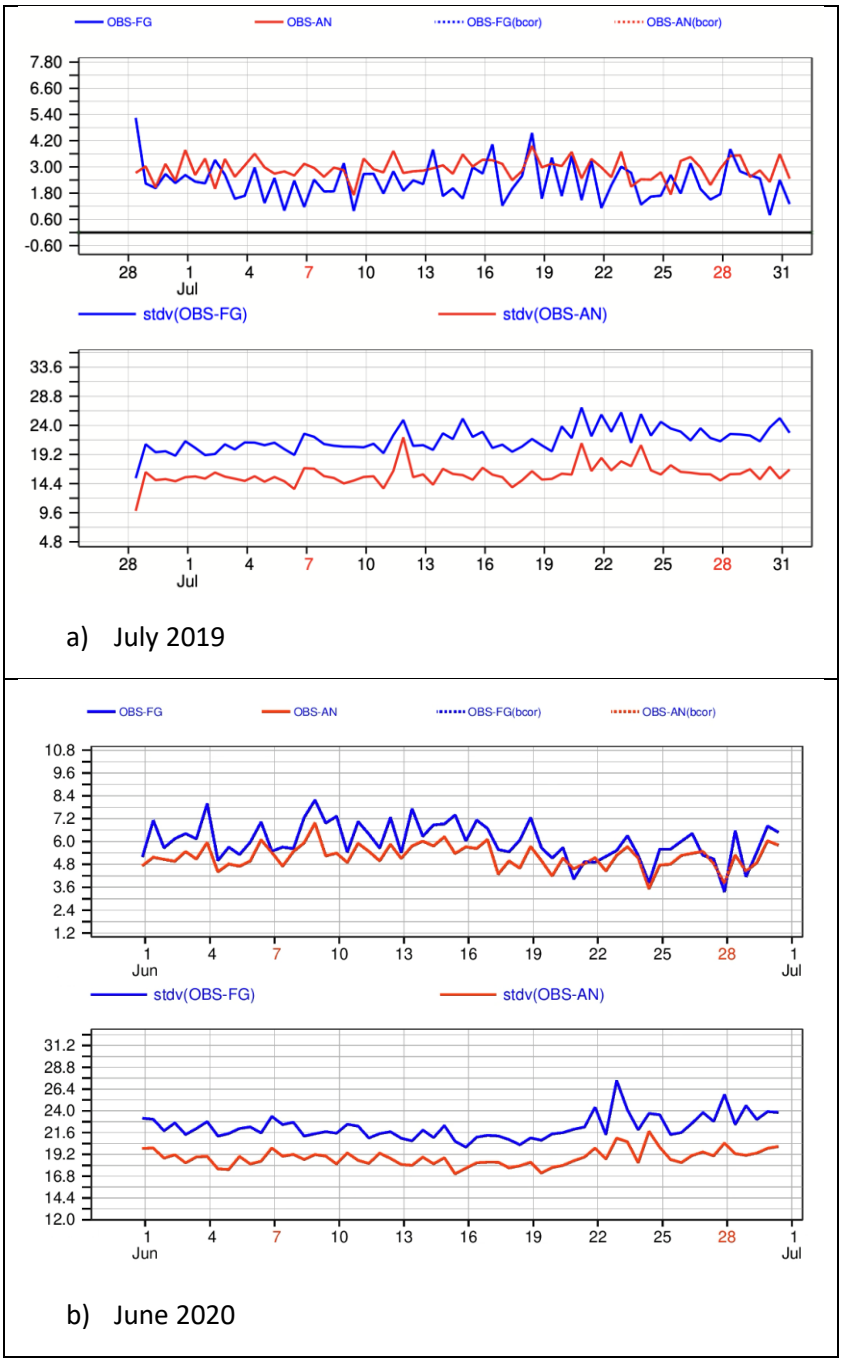

Figure 31. Time series of background departures (blue) and analysis departures (red) from L2A SCA mid-bin backscatter for a) July 2019 (expid=i9qw) and b) June 2020 (expid=i9s8). Top plots show the mean and bottom plots show the standard deviation. Values are global averages over the pressure range 700-1013.25 hPa. Units: $Mm^{-1}sr^{-1}$.

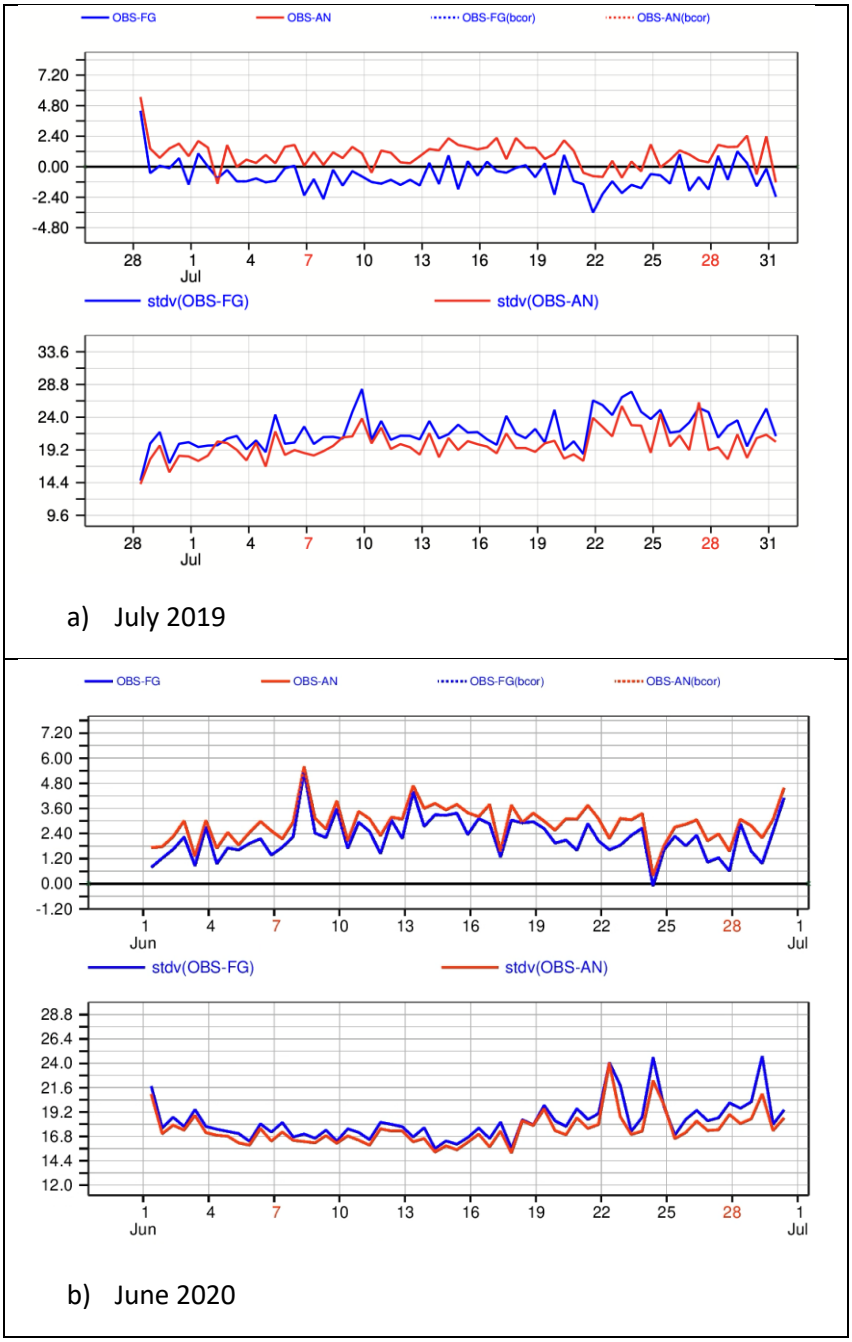

Figure 32. Time series of background departures (blue) and analysis departures (red) from L2A AEL-PRO (all types) backscatter for a) July 2019 (expid=idax) and b) June 2020 (expid=icqq). Top plots show the mean and bottom plots show the standard deviation. Values are global averages over the pressure range 700-1013.25 hPa. Units: $Mm^{-1}sr^{-1}$.

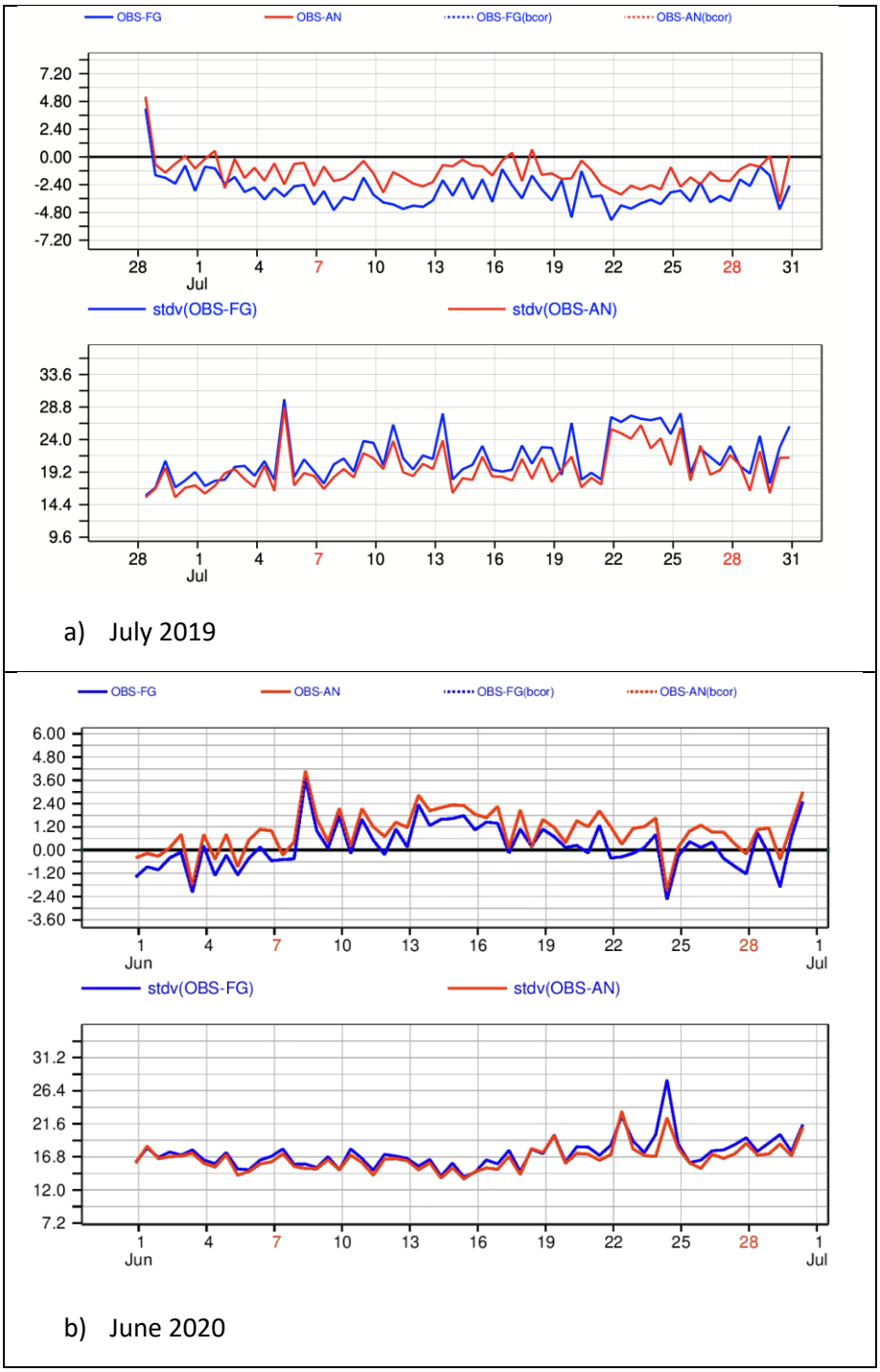

Figure 33. Time series of background departures (blue) and analysis departures (red) from L2A AEL-PRO (aerosol classification applied) backscatter for a) July 2019 (expid=ie4m) and b) June 2020 (expid=icub). Top plots show the mean and bottom plots show the standard deviation. Values are global averages over the pressure range 700-1013.25 hPa. Units: $Mm^{-1}sr^{-1}$.

6.7.5 Conclusions on B16 L2A aerosol backscatter verification with O-B departures

- Cloud contamination is a major issue (even after the background forecast cloud QC check) for assessing SCA mid-bin backscatter products in aerosol-only conditions. Cloud (even after background cloud QC check) causes positive biases of ~1.5 $Mm^{-1}sr^{-1}$, which is a large fraction of maximum aerosol loads ~3.5 $Mm^{-1}sr^{-1}$.
- AEL-PRO's aerosol classification significantly helps in reducing the cloud contamination for aerosol backscatter. The classification flag performed better in June 2020 compared to July 2019 in reducing cloud contamination, with only large positive biases remaining near the surface (>900 hPa) presumably due to cloud. In July 2019 the median of the zonal averaged stdev(O-B) greatly reduced from 0.81 to 0.36 $Mm^{-1}sr^{-1}$ from "all data" to aerosol-only" classification, and for June 2020 from 0.67 to 0.16 $Mm^{-1}sr^{-1}$.
- Further details from the AEL-PRO backscatter "aerosol-only" dataset investigations:
    - Negative biases for dust and smoke aerosol backscatter are perhaps exacerbated by the ability of AEL-PRO to detect smaller aerosol backscatter in low SNR conditions, and not simply due to underestimated backscatter due to depolarisation issues. However, this proposition is uncertain due since a significant part of the negative bias may be explained by the IFS-COMPO 355 nm aerosol backscatter being too large[3].
    - The negative backscatter biases for Aeolus compared to the background in dust areas in June 2020 are typically -1 to -2 $Mm^{-1}sr^{-1}$, for areas with background forecast backscatter of ~3.5 $Mm^{-1}sr^{-1}$, so relative errors of ~50%. This agrees reasonably well with the expectation of underestimation of backscatter due to ALADIN measuring circularly polarised copolar backscatter only[4].
    - Aeolus measures significant aerosol backscatter at ~300 hPa (~10 km) at > 50 degrees latitude in July 2019. This is missing from the IFS-COMPO background forecast.
    - Larger random departures in wildfire smoke areas suggests information in the observations that could benefit the IFS-COMPO e.g. positioning of smoke plumes not quite right in background.

[3] Comparisons of the IFS-COMPO Aerosol Optical Depth (500 nm) to Aeronet ground stations observations do show a 10-20% overestimations in the global average by IFS-COMPO.

[4] The reduction factor accounting for ALADIN measuring circularly polarised copular backscatter is: $\frac{1-\delta_{lin,355}^{part}}{1+\delta_{lin,355}^{part}}$ which for typical mineral dust linear depolarisation ratio ($\delta_{lin,355}^{part}$) of 0.3, gives a factor ~0.54. For wildfire smoke the factor is ~0.9.

6.8 L2A cloud attenuated backscatter departure statistics from the ECMWF IFS system

As part of preparatory studies for the EarthCARE ATLID 355 nm lidar via the ESA-funded PEARL project, Mark Fielding (ECMWF) has been investigating the assimilation of Aeolus L2A attenuated backscatter products, which are provided at the measurement-scale under the SCA optical properties, for the cloud information. The molecular and particulate attenuated backscatter products have been assessed using the IFS model as a reference.

The IFS forward modelling of the attenuated backscatter (complicated compared to e.g. HLOS wind) has been adapted from that developed for ATLID to account for the different off-nadir pointing angle and copolar-only backscatter measurements for ALADIN. The forward model accounts for attenuation from atmospheric cloud and gases; it does not consider aerosol, since that is only available to include in the forward model via the IFS-COMPO configuration. The main information content of such measurements is expected to come from cloud information i.e. the enhanced particulate backscatter for clouds and the enhanced attenuation from clouds in the molecular backscatter.

The measurement-scale (e.g. 3 km horizontally in 2020) data are regridded to 70 km horizontally and 1 km vertically to better match the model effective resolution. A comparison of the O-B departure statistics for molecular and particulate attenuated backscatter in B11 and B16 was made for the whole of 2020. Note that the attenuated backscatter observations are converted to a decibel value: $dB\beta_{att} = 10\log_{10}\beta_{att}$ to make the error distribution more Gaussian for data assimilation purposes.

Daily, whole profile O-B departure statistics are shown for molecular attenuated backscatter in Figure 47 and for particulate attenuated backscatter in Figure 48. The data at B16 is improved compared to B11 for the stdev(O-B), i.e. the noise, and the data counts were increased (apart from a period in end of May, reason unknown). B16 rectified a negative bias problem for the NRT B11 observations in October-November 2020. For the particulate attenuated backscatter, the negative bias and noise are improved with B16 compared to B11. It was noticed that short periods of strongly negatively biased observations were found in both B11 and B16 in the hour following orbit manoeuvres. B17 should aim to flag this data invalid in the L2A product using the L1B AOCS attitude-on-target flag, as is done in e.g. L2B data.

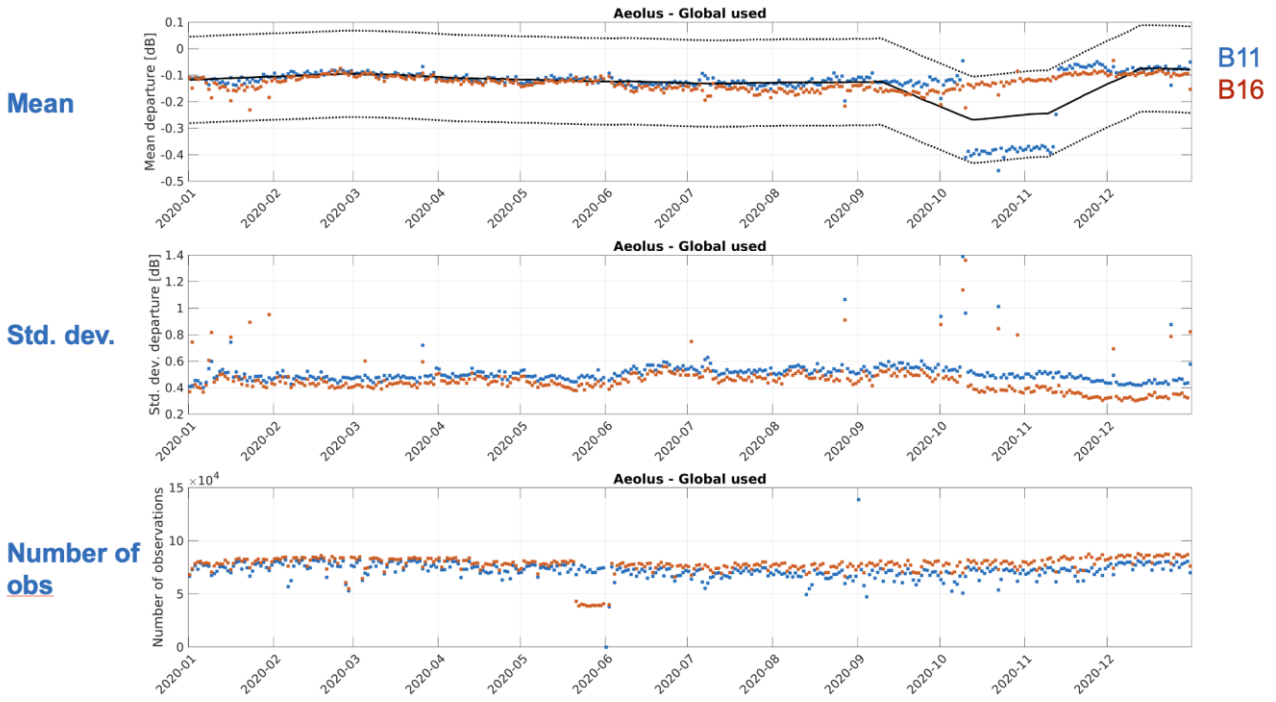

Figure 47. Daily, whole profile O-B departure statistics for L2A molecular attenuated backscatter. Top is the mean(O-B), middle is the stdev(O-B) and bottom the daily observation count. Baseline 16 data (B16) is in orange and baseline 11 (B11) in blue.

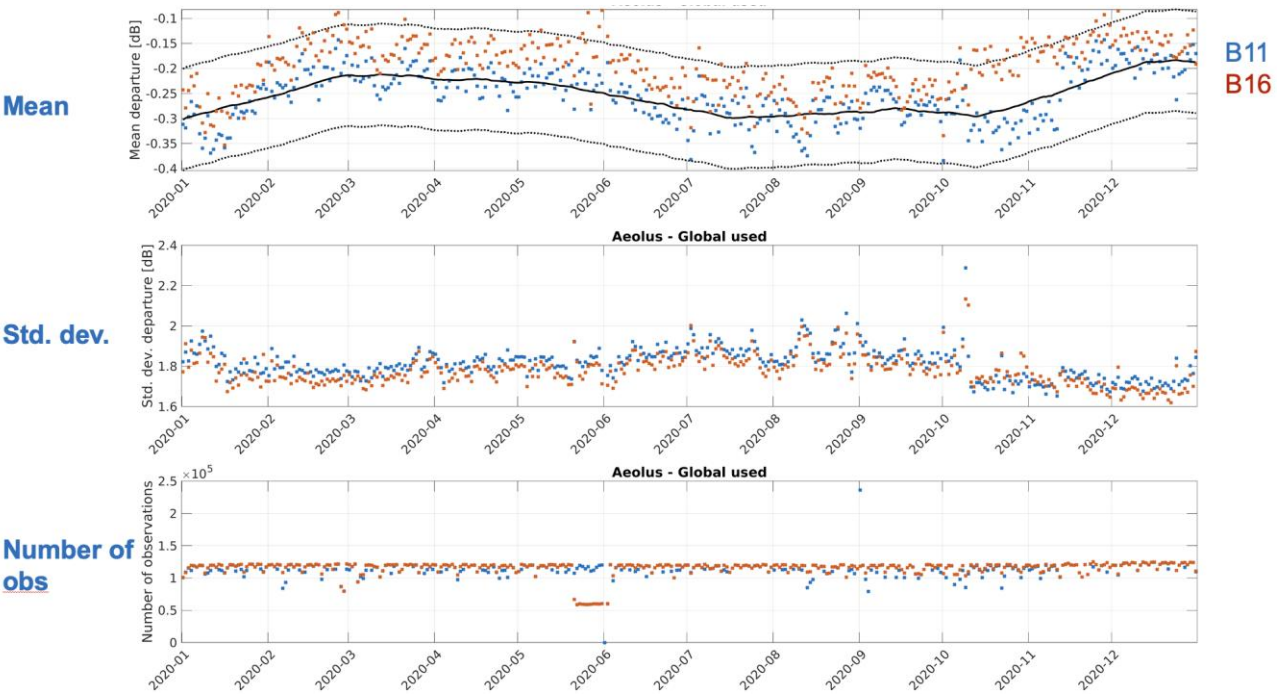

Figure 48. Daily, whole profile average O-B departure statistics for L2A particulate attenuated backscatter. Top is the mean(O-B), middle is the stdev(O-B) and bottom the daily observation count. Baseline 16 data (B16) is in orange and baseline 11 (B11) in blue.

7 Verification of L2B products

7.1 General notes

Some general notes are given here about the data files containing the Aeolus L2B horizontal line of sight (HLOS) wind speed observations that were provided to the DISC by the PDGS (via the FTP server) for phase 1 (FM-B laser only) for the fourth reprocessing:

- L2B Earth Explorer format Data block (.DBL) and the corresponding header (.HDR) files were provided. Also, the L2B .BUFR files were provided (for ingestion into NWP systems).
- The total number of DBL (and HDR) files is 17449 pairs of files.
- The L2B files had different version numbers, distributed as in Table 5. Duplicates were avoided by only retaining the largest file versions from the duplicates found[5].

Table 5: Number of pairs of files for each file version.

Version number	0001	0002	0003	Total
Number of files	16483	965	1	17449

- Overall sensing period (UTC) covers: 2019-06-28T13:54:23 to 2022-10-04T14:34:04.
- There were two long periods without L2B data due to the instrument not measuring winds:
  - From 2021-03-22T02:56:59 until 2021-04-01T15:09:32, due to the FM-B laser switching off automatically (Survival Mode).
  - From 2021-10-22T13:46:32 until 2021-10-29T07:56:41, due to the FM-B laser switching off automatically (Survival Mode).
- Twelve (shorter) periods occurred where the L2B winds were deliberately flagged invalid (via the L2B settings file; AUX_PAR_2B) due to poor data quality (following pre-assessment by DISC of

[5] ESA (PDGS) shall resolve issues with duplicates (mostly due to early processing of test periods) when the data is made available via public release. The issues regarding duplicates only affected the data provided from PDGS to DISC via the FTP server.

O-B statistics). These periods were related to instrumental tests/problems or adjustments, see Table 6 below.

Table 6. Periods flagged invalid for L2B winds.

Reason	Start (UTC)	Stop (UTC)
Instrument Telescope Refocusing and TxA sensitivity test	2019-07-01T18:17:00	2019-07-02T03:00:01
Laser Frequency Adjustment and Rayleigh cover temperature change	2019-07-22T00:00:00	2019-07-22T04:00:00
Reconfiguration from star-tracker A to B caused wind bias	2019-09-03T07:50:00	2019-09-03T14:40:00
Instrument Telescope Refocusing	2020-05-25T07:54:00	2020-05-28T00:00:00.
Start of M1 telescope thermal control test	2020-07-06T00:00:00	2020-07-06T06:00:01
End of M1 telescope thermal control test	2020-07-09T00:00:00	2020-07-09T06:00:01
M1 optimisation tests	2021-01-23T00:00:00	2021-01-27T00:00:00
Further M1 optimisation tests	2021-01-31T00:00:00	2021-02-04T00:00:00
Further M1 optimisation tests	2021-02-12T00:00:00	2021-02-15T00:00:00
Data after laser switch had poor quality	2021-04-01T00:00:00	2021-04-13T12:00:00
Laser Frequency Adjustment	2021-04-28T00:00:00	2021-04-28T09:00:01
Reconfiguration from star-tracker A to B caused wind bias	2021-04-29T00:00:00	2021-05-01T00:00:00

- In the end five AUX_PAR_2B files were applied:
    - AE_OPER_AUX_PAR_2B_20190624T000000_20190722T000100_0001.EEF

- AE_OPER_AUX_PAR_2B_20210322T020000_20211022T140000_0001.EEF
- AE_OPER_AUX_PAR_2B_20190722T000100_20210322T020000_0001.EEF
- AE_OPER_AUX_PAR_2B_20211022T140000_20211213T000000_0001.EEF
- AE_OPER_AUX_PAR_2B_20211213T000000_20221005T235959_0001.EEF

- A summary of changes made to the AUX_PAR_2B optimised for the reprocessing period:
  - Blacklisting was tuned (5 iterations)
  - AMD_Matchup_Params->Max_Allowed_Time_Diff was tuned
  - The RR_Ref_Method was changed from RR_Ref_Fixed_Method to RR_Ref_from_MieEmitFreq_Method and the MieRespFreq_to_RR_slope was tuned. Because of this several different AUX_PAR_2B files were needed with different MieRespFreq_to_RR_offset values as the instrument settings changed with time.
  - Max_Horizontal_Accumulation_Length was tuned for the Mie channel to 12 km to accommodate changes in the N/P settings during the period
  - L1B_Geolocation_Screening_Params->Altitude_Check->Lower_Threshold was tuned
  - Mie-non-linearity correction tables for 2 periods were tuned (4 iterations)
  - Rayleigh-cloudy parameters for 3 different periods were tuned (2 iterations)
  - Rayleigh_Response_Check was tuned for 2 different periods

Verification of the Aeolus L2B HLOS wind speed product has been performed with respect to its equivalent computed from the atmospheric fields of the ECMWF Integrated Forecast System (IFS) Numerical Weather Prediction (NWP) model. For Aeolus L2B purposes the NWP information can be obtained from two sources. Firstly, NWP information is available as part of the L2B product, via the NRT-produced AUX_MET files (profiles of the operational ECMWF IFS TcO1279 L137 background forecast along Aeolus predicted ground-tracks). The nearest AUX_MET wind data in time to the L2B HLOS wind result is selected in the L2B processing. This method has been checked to have similar results to the other method of providing the O-B statistics i.e. ingesting the L2B BUFR data into the IFS data assimilation system (analysis experiments) to calculate the O-B departure statistics there. The departures are archived in ODB files containing the observation and background forecast (and analysis) from which departure statistics can be calculated.

The Aeolus L2B observations are classified into Mie-cloudy, Mie-clear, Rayleigh-clear and Rayleigh-cloudy. If the L2B processing settings are well-tuned, then there should be zero Mie-clear wind results. The data counts for "valid" Mie-clear in this reprocessing campaign are negligible and hence they are not considered any further.

The L2B observations are subject to quality control (QC) with the aim of removing a small fraction of gross errors which exist, which can spoil non-robust statistics such as mean and standard deviation. The QC always uses the L2B overall validity flag (based on several criteria in the L2B processing). For some of the verification methods we additionally use a threshold on the L2B processor produced HLOS wind error estimate (standard error) provided with each wind result (derived predominantly from signal levels and counting noise assumptions). When using departures from IFS analysis experiments, we avoided the L2B processor HLOS wind error estimates as a threshold for QC, due to estimates changing from one processing baseline to the next and average values changing a lot with signal levels and instrument settings. Instead, QC based on the absolute size the O-B departure is used, which is more comparable for different reprocessing campaigns due to the stability of the NWP model (not changing too much from one IFS cycle to the next). The QC applied for each verification method used will be described as appropriate in the following Sections.

7.2 Processing chain improvements for the 4th reprocessing (B16) compared to the 2nd reprocessing campaign for early FM-B (B11) and NRT datasets

The following lists changes in the ground processing software algorithms which have influenced the L2B product quality for the 4th reprocessing of FM-B, relative to the 2nd reprocessing of FM-B.

- B16 (used for NRT data production from 18 April 2023):
    - L2Bp:
        - A "residual error" threshold option was included in QC for the Mie Core algorithm output. This helps discard gross errors from the low signal Mie winds (e.g. in aerosols), which are otherwise hard to detect as gross errors (unless using O-B departures from the NWP model).
        - A new Rayleigh channel wind bias correction based on the Mie channel estimated emitted frequency was added. This reduces wind biases in the Rayleigh channel caused by oscillations in the pressure inside the laser housing, which impact the laser frequency. The bias caused by this pressure oscillation had a magnitude of roughly ±0.6 ms^{-1} with a period of 4.3 h at the end of 2022 (for the FM-A laser, thought to be less important in other periods).
        - A correction was applied for start/stop latitude/longitude values. The new calculation adds half a measurement length to the reported accumulation to give a better estimate of the accumulated region. This also solves the problem of having identical start/stop locations in case a wind is derived from a single measurement, which became more common when using the N=5, P=114 setting (N: number of measurements per observation, P: number of pulses per measurement) after 4 April 2022.

- L1Bp:
  - L1B Rayleigh signal-to-noise-ratio (SNR) calculation was updated to be more realistic: The detection chain offset and read-out noise are included in the L1B Rayleigh SNR calculation. As a result, the median of the L2B HLOS wind estimated error for Rayleigh-clear winds increased by ~60% in June 2020 (and relatively even more as the useful signal decreased in 2021).
  - New detection chain offset (DCO) correction in L1B using orbital means: This improved the random errors of the L2B wind products by ~1-2%.

- B15 (used for NRT data production from 13 September 2022):
  - L2Bp:
    - A new threshold check was added to catch gross errors on measurement level Rayleigh response, i.e. if one of the channels A or B has an abnormally high signal and the other does not (likely due to cosmic ray affecting the ACCD), then we consider this an artefact that is not related to wind and flag the resulting measurement invalid so it is not used in the wind retrieval. This improves the standard deviation of L2B Rayleigh-clear O-B significantly by reducing gross errors.
    - A climatological sanity check was added on the L2B wind results, to ensure unrealistic large absolute HLOS wind results are flagged invalid (after some outliers with very large wind speeds were noticed).

- B14 (used for NRT data production from 29 March 2022):
  - L2Bp:
    - A switch was added so that moon-blinding does not lead to L1B measurements being flagged as invalid and therefore can be used for the L2B wind retrieval, but in case the moon-blinding has occurred, the resulting L2B wind result can be flagged invalid. This means the wind results during moon-blinding are still available for use if one ignores the validity flag.
    - The AUX_TEL_generator was modified to also allow the correction of harmonic (sinusoidal) biases with argument of latitude (orbit phase). The L2BP was adapted to allow using these harmonic factors for wind bias correction. This corrects for opposing biases (< 0.5 ms^{-1} magnitude) in ascending and descending orbits that was evident in October and March in previous reprocessing campaigns (possibly related to the angle of the sun on the satellite).
  - L1Bp:
    - Bug-fixes to remove a longitudinal offset (0.075° ~8 km at the equator) in the geolocation of all Aeolus products.

- B13 (used for NRT data production from 6 December 2021):
  - L2Bp:
    - A new parameterization to correct the Rayleigh Response as a function of (collocated) L1B (Mie channel) scattering ratio was added. The parameters are derived via NWP-based calibration. This improves the O-B statistics of the Rayleigh cloudy winds.
    - Ground detection algorithms were extended for detection if the surface is near (but not intersecting with) the bottom of the range bin. This can be used to account for DEM inaccuracies and for the range bin signal overlap (crosstalk between bins) which may result in wrong winds close to the surface. In addition, a new check was added based on the digital elevation model (DEM) value provided via the AUX_MET_12 file.
- B12 (used for NRT data production from 26 May 2021):
  - L2Bp:
    - Step changes in L2B Rayleigh wind bias were detected and found to be associated with noise/jumps in the Rayleigh channel internal reference signal in December 2020. To avoid this the internal Rayleigh response can be not used via a switch to apply a fixed internal reference value. Switches were added for both Rayleigh and Mie channels.
    - The new moon-blinding flag from the L1B measurements can be used to avoid moon-blinding affected measurements from being used in the L2B wind retrieval. This avoids biases occurring for parts of the orbit of up to 4 ms^{-1}, due to moon-blinding affecting the satellite pointing due to its effect on the star-trackers.
    - An array of Mie non-linear response corrections can be provided via the AUX_PAR_2B for use in correcting the issue of "wiggling" biases with wind speed due to uncertainty in the Mie calibration non-linearity. NWP-based calibration to derive the Mie-nonlinearity array can be done.
  - L1Bp:
    - Several additional Attitude and Orbit Control System (AOCS) flags (e.g. moon blinding status, eclipse status, star tracker status) were added to the L1B product for better quality control.
    - Negative signal counts in Mie spectral data were no longer set to zero.

7.3 L2B monitoring via the .HDR file O-B statistics

A limited set of O-B statistics are calculated as part of the L2B processing and stored in the XML format .HDR (header) files. These provide a useful verification source which can be quickly processed and plotted. The B in the O-B statistics is calculated from the AUX_MET data wind components (and the L1B azimuth angle) and therefore is based on NRT operational ECMWF short-range forecasts that were used to generate AUX_MET. The AUX_MET data used in the various reprocessing campaigns has not been reprocessed; it is still the NRT-produced AUX_MET from ECMWF's operations[6]. The QC applied when producing the statistics is based on the L2B wind overall validity flag being true and the L2B processor estimated HLOS wind error being smaller than 12 ms^{-1} for the Rayleigh and 5 ms^{-1} for the Mie winds (parameters that are defined in the AUX_PAR_2B).

The global average (data over all available geolocations per L2B file) statistics for the various L2B wind types are shown in Figure 49 for the whole time-period of the reprocessing. The gradual increase in noise (via stdev(O-B)) for the Rayleigh-clear and the more general decreasing valid data counts (those passing the QC) is evident. This occurs due to decreasing atmospheric path signal due to losses on the emission path when using the FM-B laser (see Figure 12 of [RD-14]). The Rayleigh-clear stdev(O-B) started at ~4.8 ms^{-1} in July 2019 and increased to 7-8 ms^{-1} by September 2022. The Mie-cloudy random errors (via stdev(O-B)) remain steady (~4.5 ms^{-1}) for a long period until some reductions occurred associated with changes in the laser on-board accumulation settings from N=30 (measurements per BRC) to N=15 on 13 December 2021 (reduced to ~4 ms^{-1}) and then to N=5 on 4 April 2022 (reduced to ~3.5 ms^{-1}). These changes in N were also accompanied with a slight dip in the Mie-cloudy data counts, due to increases in the L2B processor estimated error for the Mie-cloudy winds associated with the change in N (which is unexplained), interacting with the estimated error QC threshold of 5 ms^{-1}. The Rayleigh-cloudy random errors (via stdev(O-B)) gradually increased with time from ~6.3 ms^{-1} to 7-8 ms^{-1}.

The L2B file average wind bias (mean(O-B)) is well constrained (close to 0 ms^{-1}, mostly < 1 ms^{-1}) for the Rayleigh-clear and Mie-cloudy winds, but it is positively biased (up to 1.5 ms^{-1}) for the Rayleigh-cloudy winds and varying quite a lot with time.

[6] There is not thought to be a great benefit (but not yet tested) from reprocessing it e.g. due to IFS model improvements in recent cycles, or perhaps improved L1B geolocations compared to predicted orbit NRT GRND_TRACK files.

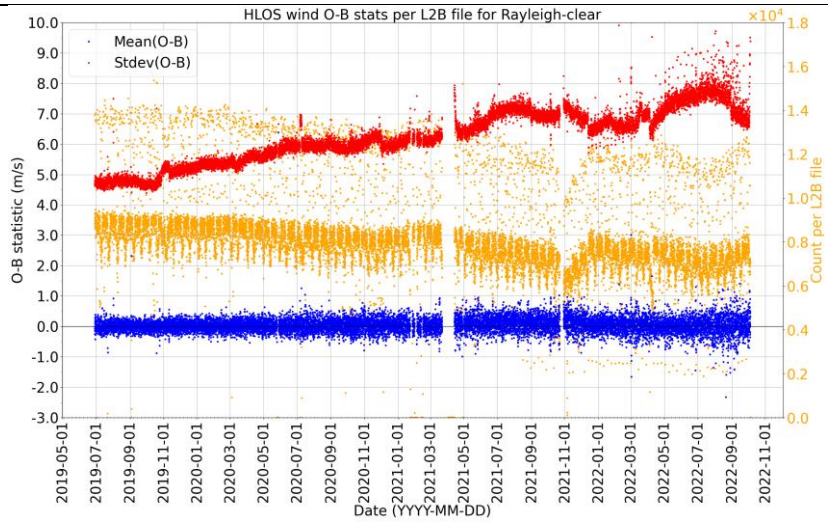

a) Rayleigh-clear

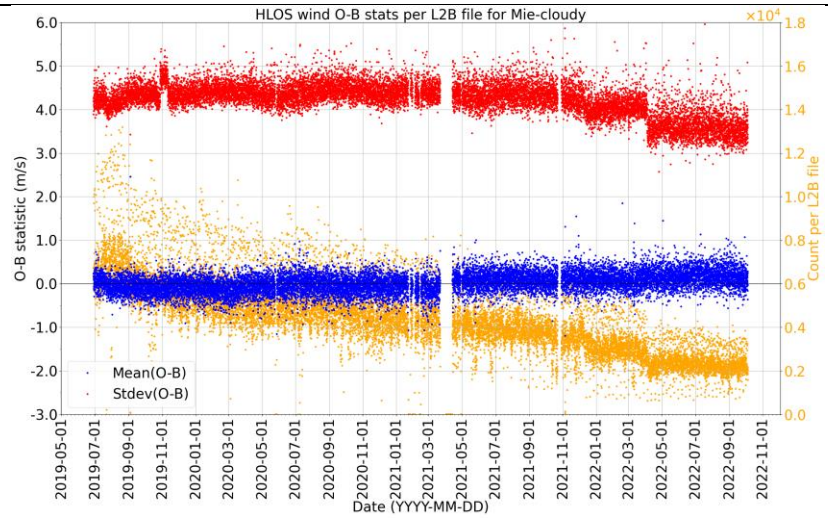

b) Mie-cloudy

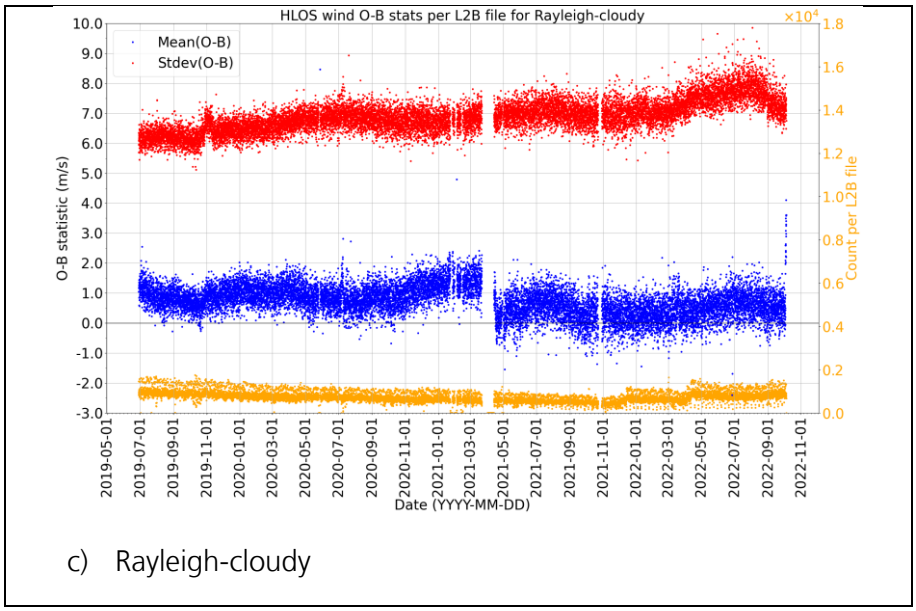

c) Rayleigh-cloudy

Figure 49. Profile average time-series from the L2B .HDR file O-B statistics for: a) Rayleigh-clear, b) Mie-cloudy (note different scale for y-axis) and c) Rayleigh-cloudy from the PDGS 4th reprocessing for FM-B. One value per L2B file. Standard deviation of (O-B) is in red, mean of (O-B) is in blue, with left-hand axis, and orange is data counts with the right-hand axis.

The wind bias on specific range-bins is also available in the .HDR files; see mean(O-B) per range-bin as a function of time in Figure 50. This is useful for assessing hot-pixel related wind biases (affecting specific range-bins) and for assessing the bias variation in the vertical dimension (although with significantly varying range-bin settings (RBS) during the mission, the altitudes for a given range-bin index varied a lot).

There is a tendency with the Rayleigh-clear winds to have a negative bias at lower altitudes (higher range-bin IDs) and positive bias at higher altitudes (lower range-bin IDs) from July 2019 until March 2021. From April 2021 the bias tends to lose this variation with altitude, due to a change in the applied AUX_RBC_L2 (Rayleigh-Brillouin look-up table for calibration) file after the FM-B laser switched off (went into survival mode on 22 March 2021) and was then switched on again on 1 April 2021. This issue of altitude-varying bias is a long-standing issue that also affected the 2nd reprocessing. It is thought to be related to a temperature-dependence of the Rayleigh-bias due to errors in the Rayleigh response versus frequency calibration curves, which vary with temperature and pressure (as provided via the AUX_RBC_L2). The improvement in bias from April 2021 was noticed too late to consider possible application of the second AUX_RBC_L2 in the earlier period to mitigate the bias (DISC testing showed that it does mitigate the bias in 2019).

There is a tendency for negative bias on the lowest altitude Mie range-bins, with more positive above; the source of this is not yet known. However, note that the scale of the bias plot is only half of the Rayleigh-clear plot, so not too concerning.

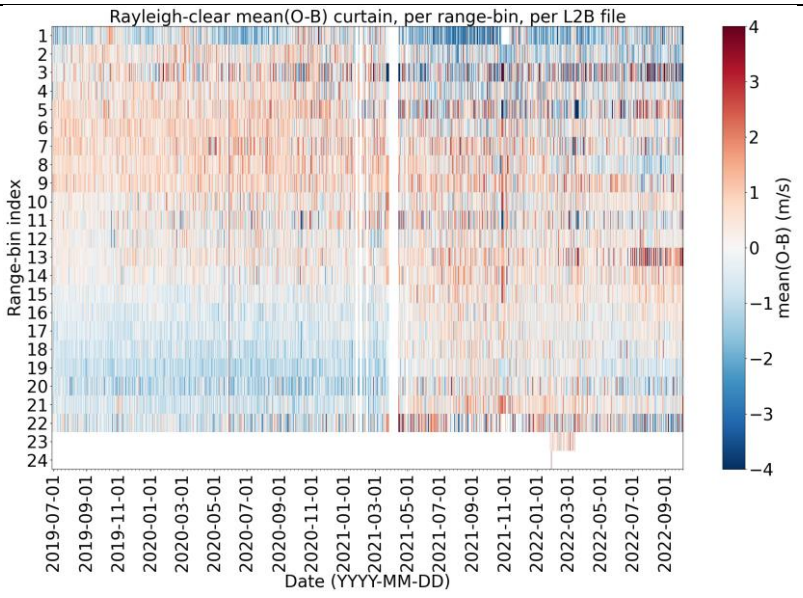

a) Rayleigh-clear

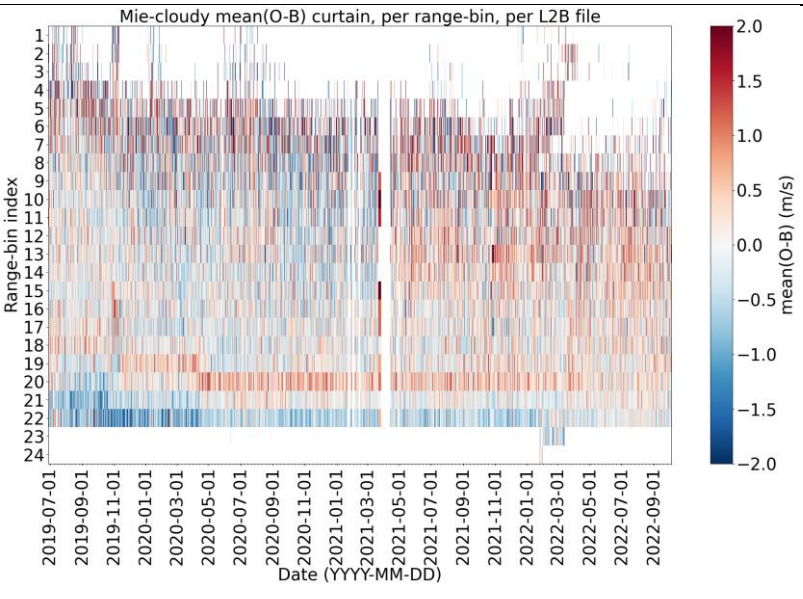

b) Mie-cloudy

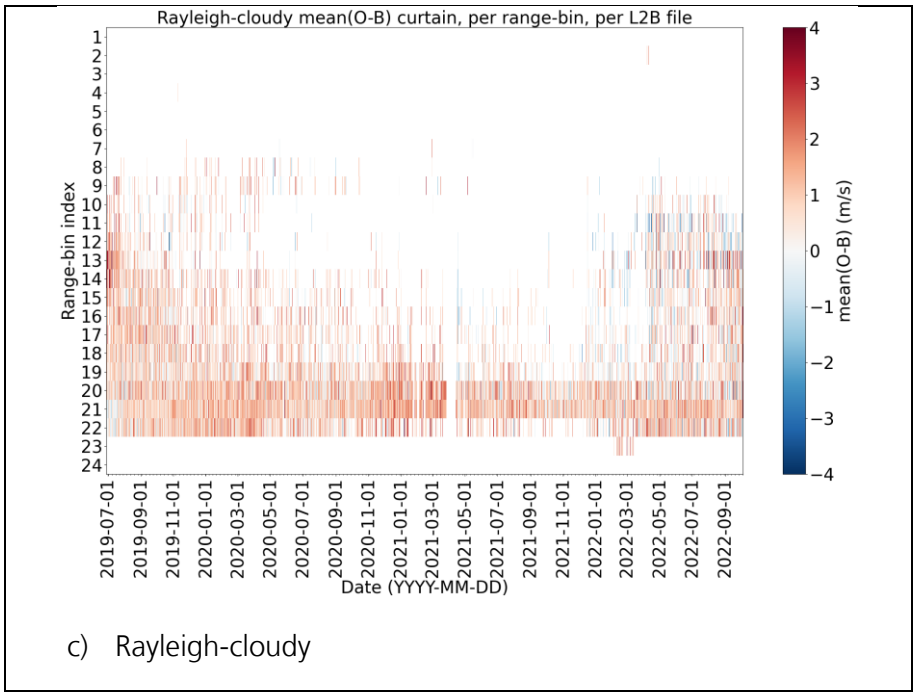

Figure 50. Time-series from the L2B .HDR file O-B statistics of mean(O-B) per range-bin, per L2B file for: a) Rayleigh-clear, b) Mie-cloudy (note different bias colour scale) and c) Rayleigh-cloudy.

In terms of hot-pixel related biases, the situation worsened with time, particularly for the Rayleigh-clear winds in the upper range-bins (lower useful signals at higher altitudes leads to greater sensitivity to dark current corrections). The hot-pixel related wind bias fluctuations became particularly large in 2021 and 2022 for the Rayleigh-clear. Covariance matrices for Rayleigh-clear mean(O-B) per range-bin for the 4th reprocessing and for comparison the NRT-produced data for 2022 is shown in Figure 51. The DISC reprocessing of L1B DCMZ (Dark Current in Memory Zone) files, aimed at detecting jumps in hot-pixel levels between DUDEs, has improved the biases for range-bins 5, 9, 22 and 24 compared to NRT data. However, range-bins 3, 5, 11, 13 and 22 remain problematic and may not be able to be corrected further without using O-B statistics.

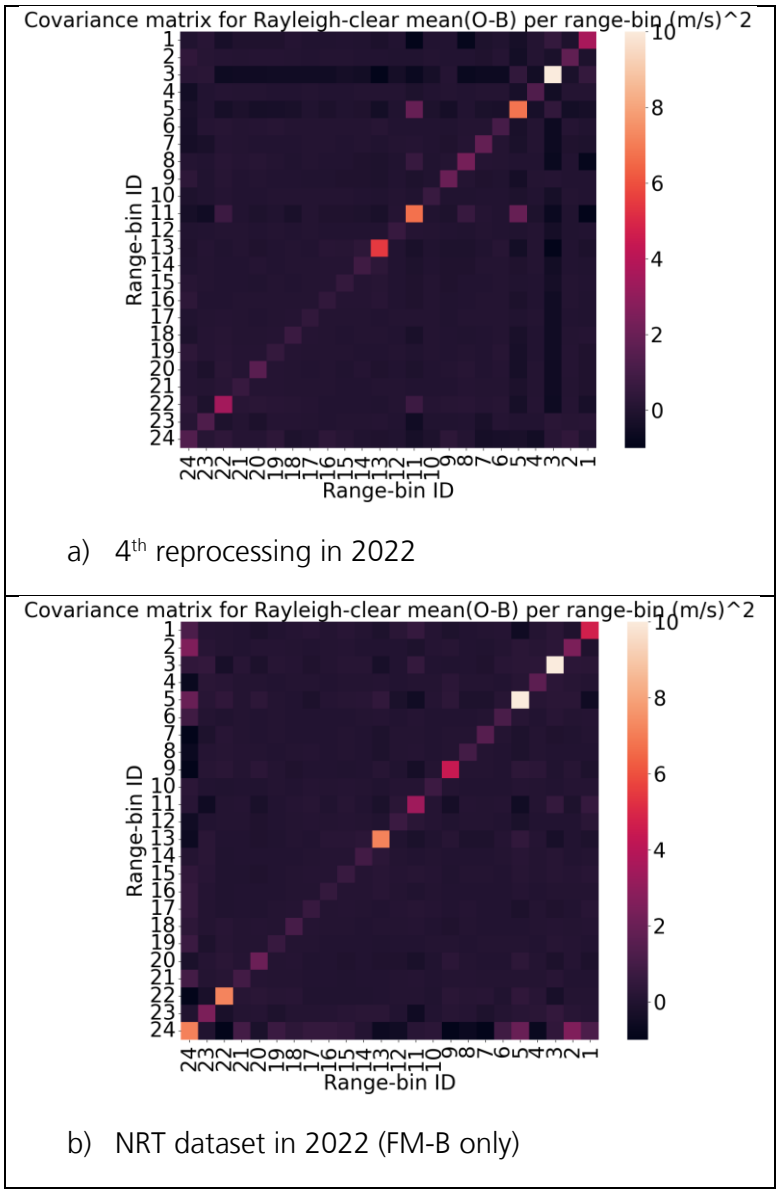

Figure 51. Covariance of the mean(O-B) per range-bin for the L2B Rayleigh-clear winds for a) 4th reprocessing in 2022 and b) NRT data in 2022 for the FM-B laser only.

The standard deviation of O-B per range-bin as a function of time is shown in Figure 52. The increasing noise with time for the Rayleigh-clear was particularly marked for the upper altitude range-bins, as expected due to lower atmospheric path signals with altitude. An increase in noise from 28 October to 10 November 2019 occurred due to special "AMV" range-bin settings, which generally reduced the range-bin thickness to focus on lower altitude winds for improved collocations with geo-stationary satellite feature-tracked winds.

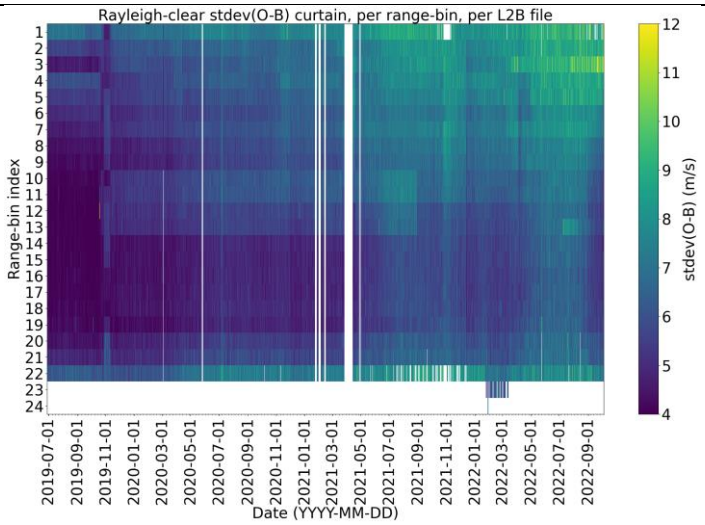

a) Rayleigh-clear

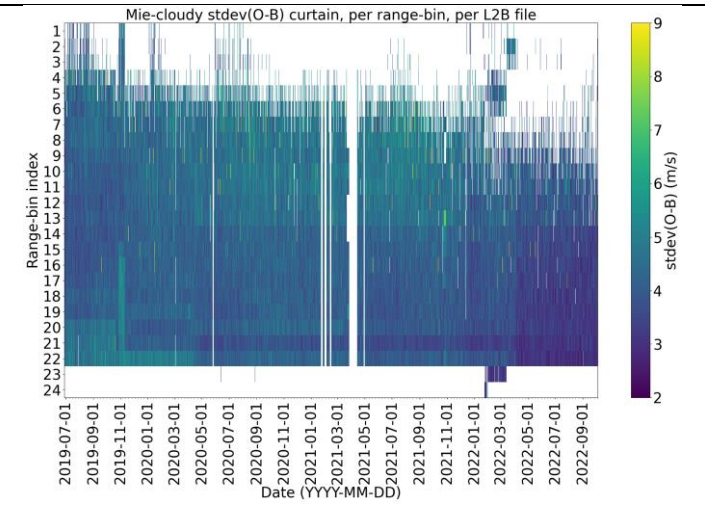

b) Mie-cloudy

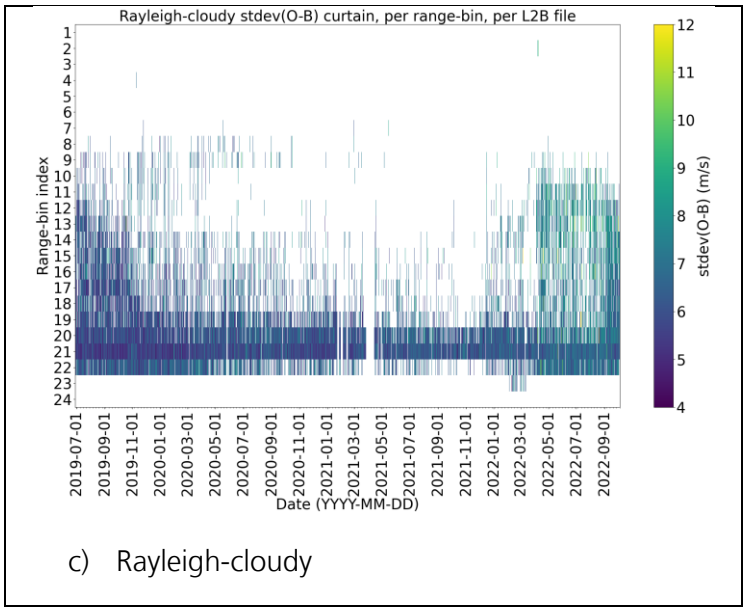

Figure 52. Time-series from the L2B .HDR file O-B statistics of standard deviation(O-B) per range-bin, per L2B file for: a) Rayleigh-clear, b) Mie-cloudy (note different colour scale) and c) Rayleigh-cloudy.

A comparison of the O-B statistics per L2B file from the 4th reprocessing versus the 2nd reprocessing (B11) (therefore limited to the period of the 2nd reprocessing: 28 June 2019 to 9 October 2020), is shown in Figure 53.

A significant improvement in the Rayleigh-clear O-B standard deviation and bias is evident: the standard deviation of O-B for the 4th reprocessing is improved by ~15% in July 2019 and ~25% in October 2020 compared to the 2nd reprocessing. There is an influence from the L2Bp estimated error for the Rayleigh being larger in B16 compared to B11, due to the inclusion of more realistic treatment of noise terms in the L1B Rayleigh SNR calculation (readout and DCO correction). Figure 54 compares the L2B estimated error distributions for B11 and B16 and compares them to the noise estimated from O-B departures. The median value of L2B estimated error increased from 4.2 ms^{-1} for B11 to 6.6 ms^{-1} for B16, so ~60% larger on this example day in June 2020. The figure shows that for B16 the L2B estimated error better matches the stdev(O-B)[7] for the bulk of the distribution (lies closer to the diagonal) and so is more realistic. B11 L2B estimated error was underestimated (for L2B estimated error range 2.5-15 ms^{-1}), however B16 is roughly correct in the 4-10 ms^{-1} estimated error range, but overestimated for values larger than 10 ms^{-1}. With a fixed 12 ms^{-1} QC threshold for the .HDR statistics the QC is stricter for B16, however the data counts are reasonably similar, so it is believed that the noise reduction in Figure 53 comes from the many improvements listed earlier.

[7] Note that the stdev(O-B) is dominated by the observation random errors when ~4 ms^{-1}, due to the background random errors (1-σ) being ~2 ms^{-1}, therefore the mean L2B estimated error should match stdev(O-B) for typical Rayleigh-clear statistics.

Document Title

Verification report for phase 1 of the fourth reprocessing campaign for the FM-B laser from June 2019 till October 2022

	2nd reprocessing	4th reprocessing
Rayleigh-clear	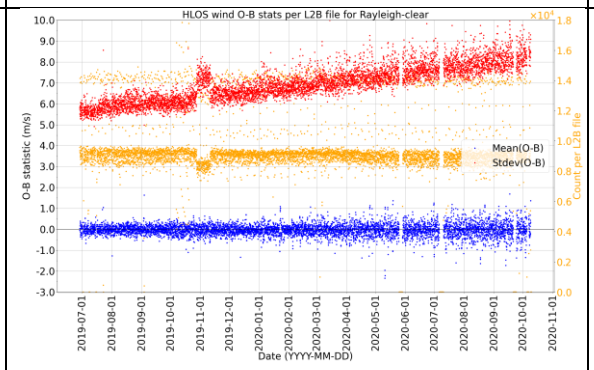	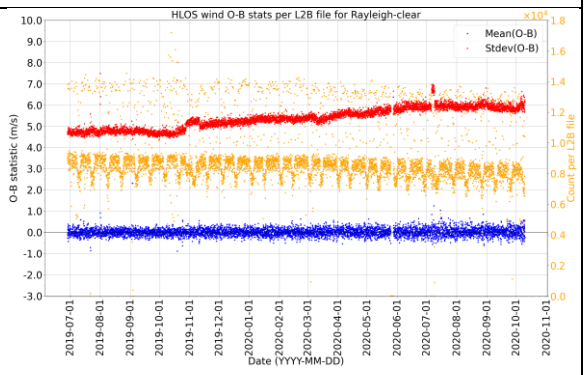
Mie-cloudy	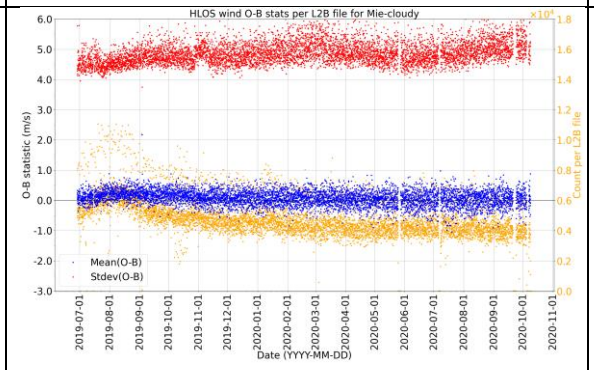	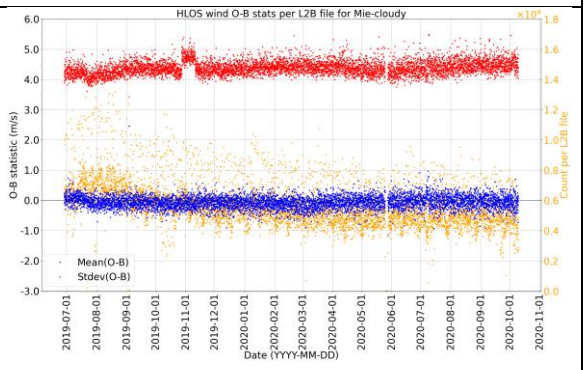
Rayleigh-cloudy	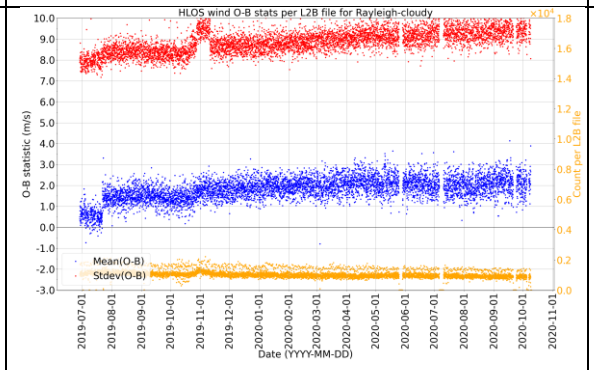	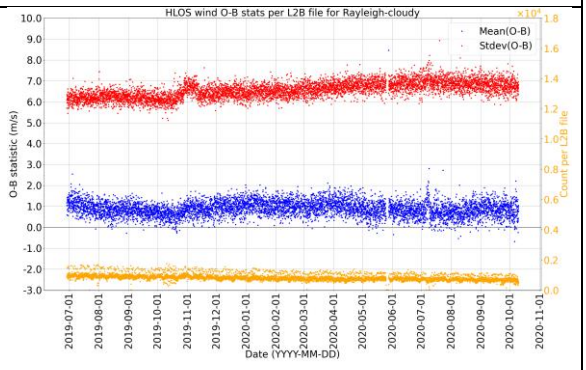

Figure 53. Profile average time-series from the L2B .HDR file O-B statistics. Comparison between 2nd and 4th reprocessing for the various L2B wind types, for the common period of 28 June 2019 to 9 October 2020. One value per L2B file. Red is stdev(O-B), blue is mean(O-B) with left-hand axis and orange is data counts with the right-hand axis.

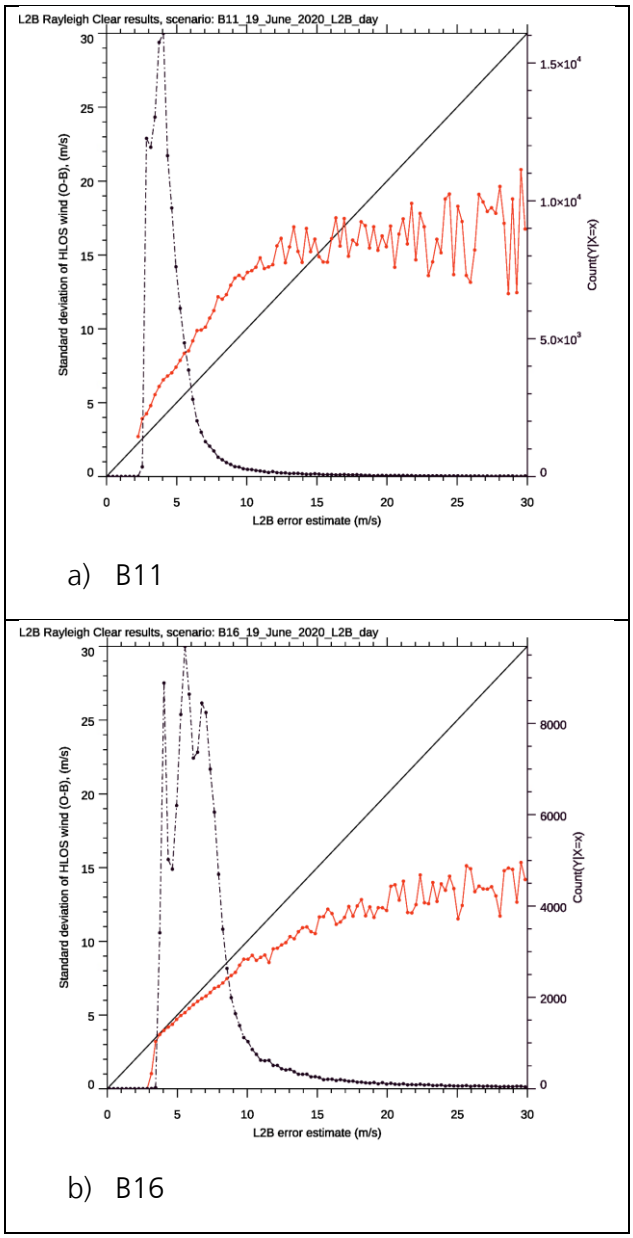

Figure 54. L2B Rayleigh-clear standard deviation of O-B departure (red line) binned as a function of L2B estimated error for data on 19 June 2020 (as an example) for a) B11 and b) B16.

There are reductions in the data counts every two weeks seen in Figure 53 for the 4th reprocessing (particularly evident in the Rayleigh-clear plot). This is due to the application of the moon-blinding L2B QC which was not available for the 2nd reprocessing, this particularly reduces the data counts in the tropics, where moon-blinding events mostly occur.

The Mie-cloudy noise is also improved with the 4th reprocessing compared to the 2nd reprocessing by ~9%, whilst the data count increased, so it is certainly an improved quality dataset. The Rayleigh-cloudy winds also show a large improvement (~25%) in noise due to the B11 to B16 changes, and improved bias due to the new parameterised correction based on scattering ratio.

For the year 2022, the 4th reprocessing improves upon the NRT-produced data (B13 to B15) as is shown in Figure 55. This improvement is seen for wind bias and noise for all L2B wind types, adding confidence to the assertion that the L2B data quality has improved with reprocessing. Some of the improvement is thought to be due to using the L2B O-B statistics of the day in the AUX_TEL_12 generation in reprocessing, compared to the previous day which was applied for the NRT processing.

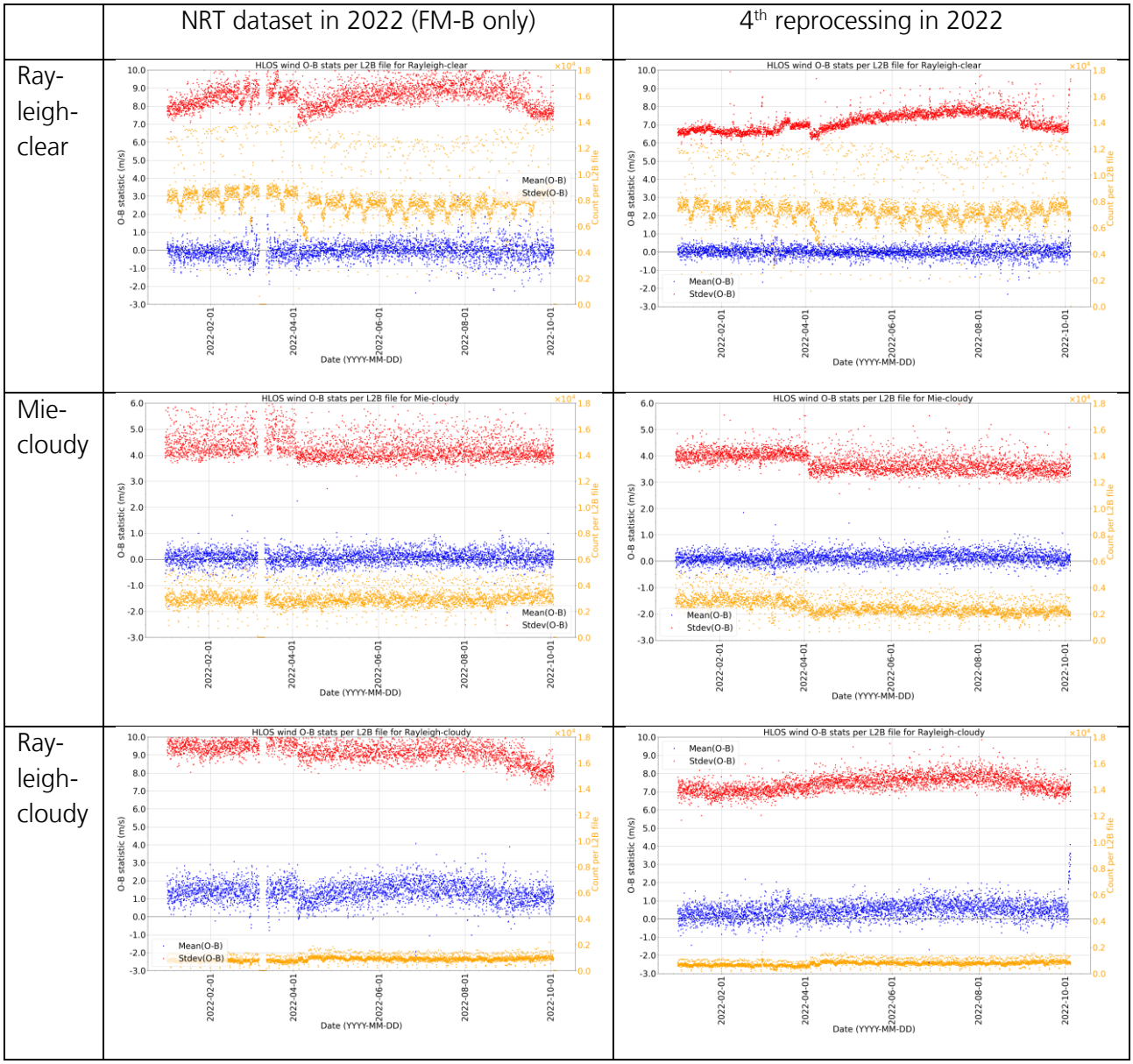

Figure 55. Profile average time-series from the L2B .HDR file O-B statistics. Comparison NRT data and the 4th reprocessing for the common period of 1 January 2022 to 4 October 2022. One value per L2B file. Red is stdev(O-B), blue is mean(O-B) with left-hand axis and orange is data counts with the right-hand axis.

In summary, the. HDR based O-B statistics have shown that the 4th reprocessing is a significant improvement in data quality compared to the 2nd reprocessing and with respect to the NRT data quality.

7.4 L2B Mie-cloudy winds, detailed verification

More in-depth verification statistics are derived from the "control" of Observing System Experiments (OSEs) in which Aeolus was not assimilated (passively available for monitoring) and so the NWP model was not influenced by Aeolus winds. These experiments ingest the 4th reprocessing L2B BUFR data into the ECMWF IFS[8]. The QC applied for the verification of the Mie-cloudy is to reject winds with abs(O-B)> 10 m/s or if the L2B validity flag is false. The reliance on O-B departure size for QC is so to avoid using the L2Bp estimated error which can vary significantly during the reprocessed period due to changes in instrument quality and settings e.g. N/P settings. The threshold of 10 m/s was a compromise between data count and the influence of gross errors for the Mie-cloudy winds; it is roughly 3σ for most Mie-cloudy (cloud backscatter, rather than aerosol) winds. The verification plots in this section (and equivalent sections for Rayleigh-clear and Rayleigh-cloudy) are based on the OSE-derived statistics.

Since geometric heights are converted to pressure as the vertical co-ordinate for L2B winds in the IFS, Figure 56 is provided to aid in the conversion of pressures (seen in the following plots) to heights.

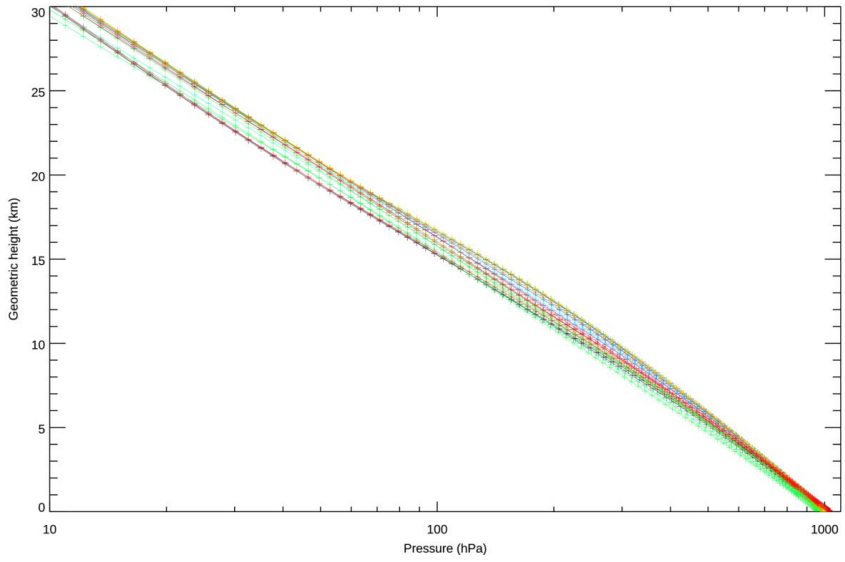

Figure 56. The variation of geometric height (altitude) with pressure from ECMWF's IFS global model (which has 137 vertical levels) for a sample of meteorological conditions across the globe, along a simulated Aeolus orbit (different coloured lines). This can be referred to in the following sections to help convert pressure to altitudes.

[8] The 4th reprocessing OSEs used ECMWF's IFS at CY48R1 (operationally implemented on 27 June 2023) using a TcO639 outer loop (~18 km grid).

Figure 57 is a time-series of the daily, global average O-B statistics (left axis) and data counts (right axis) for the L2B Mie-cloudy winds during the 4th reprocessing (28 June 2019 to 4 October 2022). The figure (and similar-style figures) includes the 3rd reprocessing (FM-A laser) from 3 September 2018 to 16 June 2019 for comparison. Also shown in the time-series plots for some context, are the mean values of L2B wind result horizontal group size (the horizontal extent over which the wind retrieval used L1B measurements) and the mean of the vertical range-bin thickness (both to be read off the left axis, using the units described in the legend).

The magenta line provides the estimated observation error 1σ as derived from the variance of O-B after subtracting the typical variance for HLOS wind background forecast error. The standard deviation of background error is assumed to be 2.0 ms^{-1}, however the error bars on the magenta line indicate the range in this estimate using background error varying from 1.5-2.5 ms^{-1} to indicate its uncertainty (the background error values were derived from Desroziers diagnostics with respect to radiosonde winds). The blue line is the mean of O-B as an estimate for the observation error bias when assuming that background error bias is small in the global daily average. The error bar on the blue line of ± 0.3 ms^{-1} indicates the uncertainty in the model background bias in the global daily average (via comparisons to conventional wind data e.g. aircraft, radiosondes, wind profilers which typically have negligible wind biases).

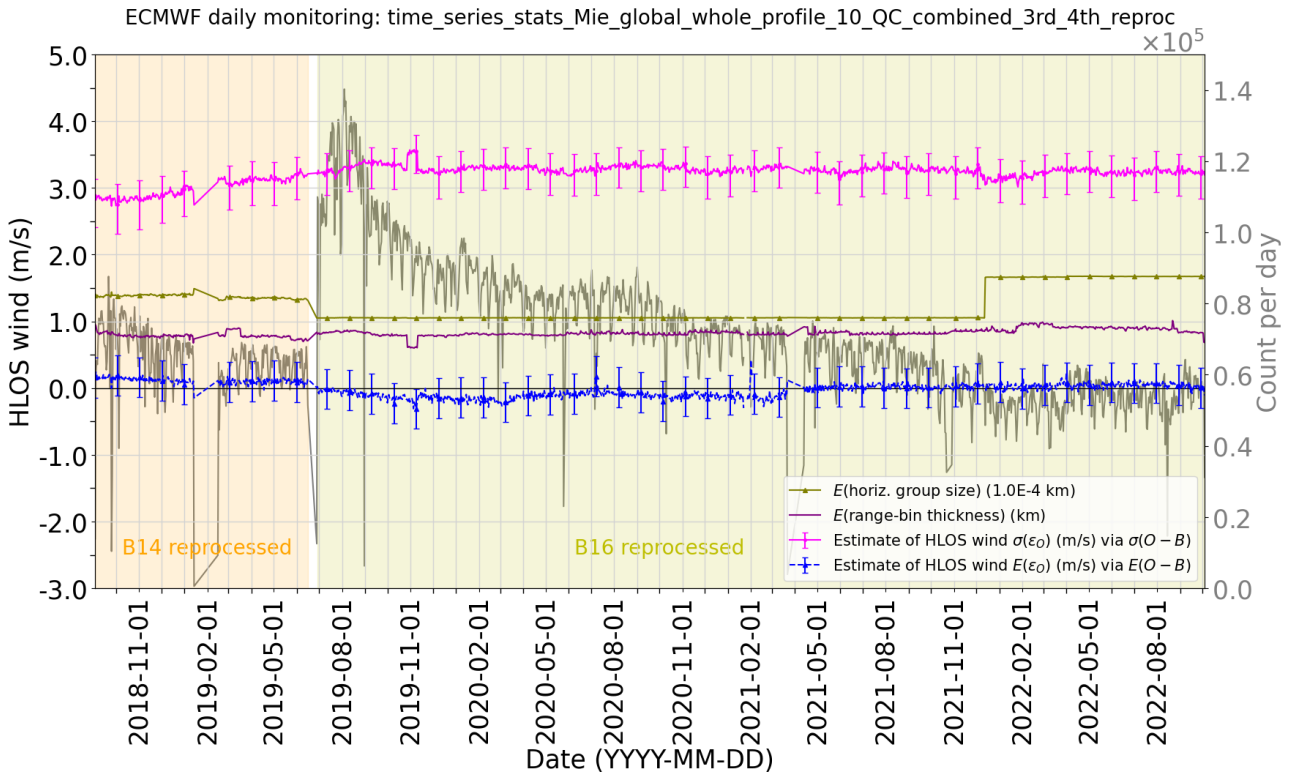

Figure 57. Time series of L2B Mie-cloudy daily, global and all pressure level O-B statistics from the controls of the combined third (FM-A, B14) and fourth reprocessing (FM-B, B16) (no-Aeolus control OSE runs). For the period 3 September 2018 until 4 October 2022.

The observation random error standard deviation for the Mie-cloudy (with the applied QC) is typically about 3.25 ms^{-1} for the 4th reprocessing. It was smaller for the FM-A laser data (3rd reprocessing). Smaller Mie errors for FM-A were also noted in NRT data in 2022-2023 and are thought to be due to a smaller Fizeau-fringe width with FM-A compared to FM-B. 3.25 ms^{-1} is much smaller than the 4.5 ms^{-1} found in Figure 49 earlier via the .HDR statistics, but note that the .HDR statistics showed the stdev(O-B), so still including the background error. Even removing the estimated background error, leaves ~4 ms^{-1}. It is thought that the abs(O-B) QC is much more effective at removing gross errors than the L2Bp estimated error 5 ms^{-1} check, hence the apparent improvement. As a non-robust statistic, the standard deviation is prone to inflation due to relatively few gross errors.

The global, all altitudes wind bias is close to zero, however there is a tendency towards a small negative bias (-0.2 ms^{-1}) in late 2019 to early 2020. The bias is improved to be closer to zero after the laser was switched on again in April 2021 – possibly due to a change in Mie calibration files. There is a marked decrease in the number of wind results with time, with the data count in late 2022 only ~46% of the peak which occurred in July-August 2019. The gradual decline in data counts is due to the decline in atmospheric path signal. The peak in July-August 2019 was due to enhanced aerosol backscatter in northern polar regions due to wildfire smoke present at that time (see Figures 47 and 48 of [RD-13]). This is also aided by much better instrument transmission in 2019.

The time-series are partitioned by orbit phase in Figure 58. The bias for ascending and descending orbits in the global, all altitude average is rather similar. There are more Mie winds for ascending compared to descending orbits, which has been noted before, and is thought to be due to more cloud being present at the 6 PM (ascending) compared to 6 AM (descending) local solar time. Also, the ascending orbit winds are slightly less noisy, again due to increased cloud backscatter.

Splitting the time-series into free troposphere (approximately 800 to 100 hPa) and the planetary boundary layer (pressures greater than 800 hPa) is done in Figure 59. Random error is smaller in the PBL than in the troposphere (by ~0.4 ms^{-1}, due to more strongly backscattering clouds), apart from during the thinner range-bin periods e.g. early FM-B and during the AMV RBS period. The bias is close to zero in the free troposphere but negative in the PBL (at worst ~-0.5 ms^{-1}), which is not explained yet.

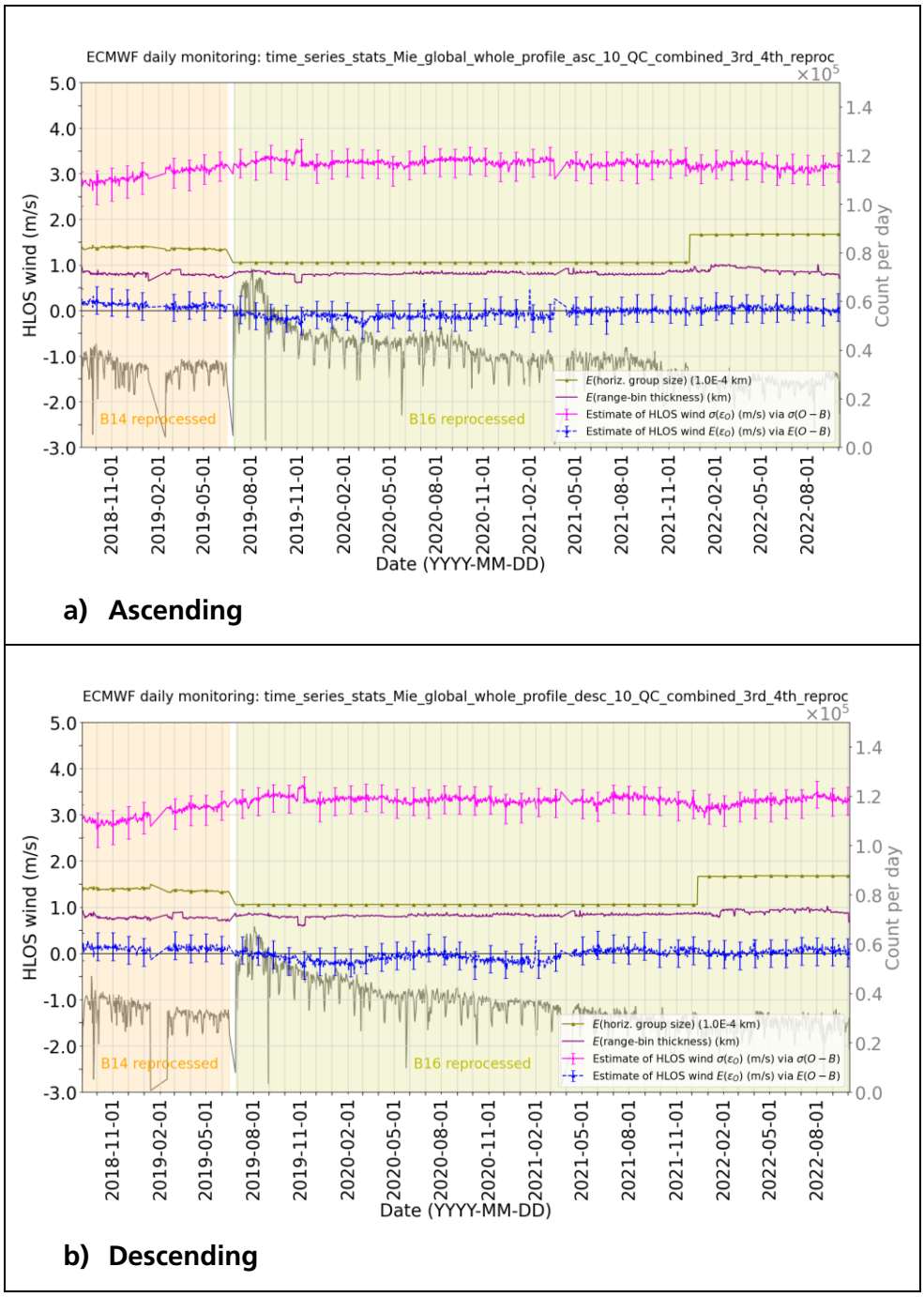

Figure 58. Time series of L2B Mie-cloudy daily, global and all pressure level O-B statistics from the controls of the combined third (FM-A, B14) and fourth reprocessing (FM-B, B16) (no-Aeolus control OSE runs). The results are split into a) ascending and b) descending orbits. For the period 3 September 2018 until 4 October 2022.

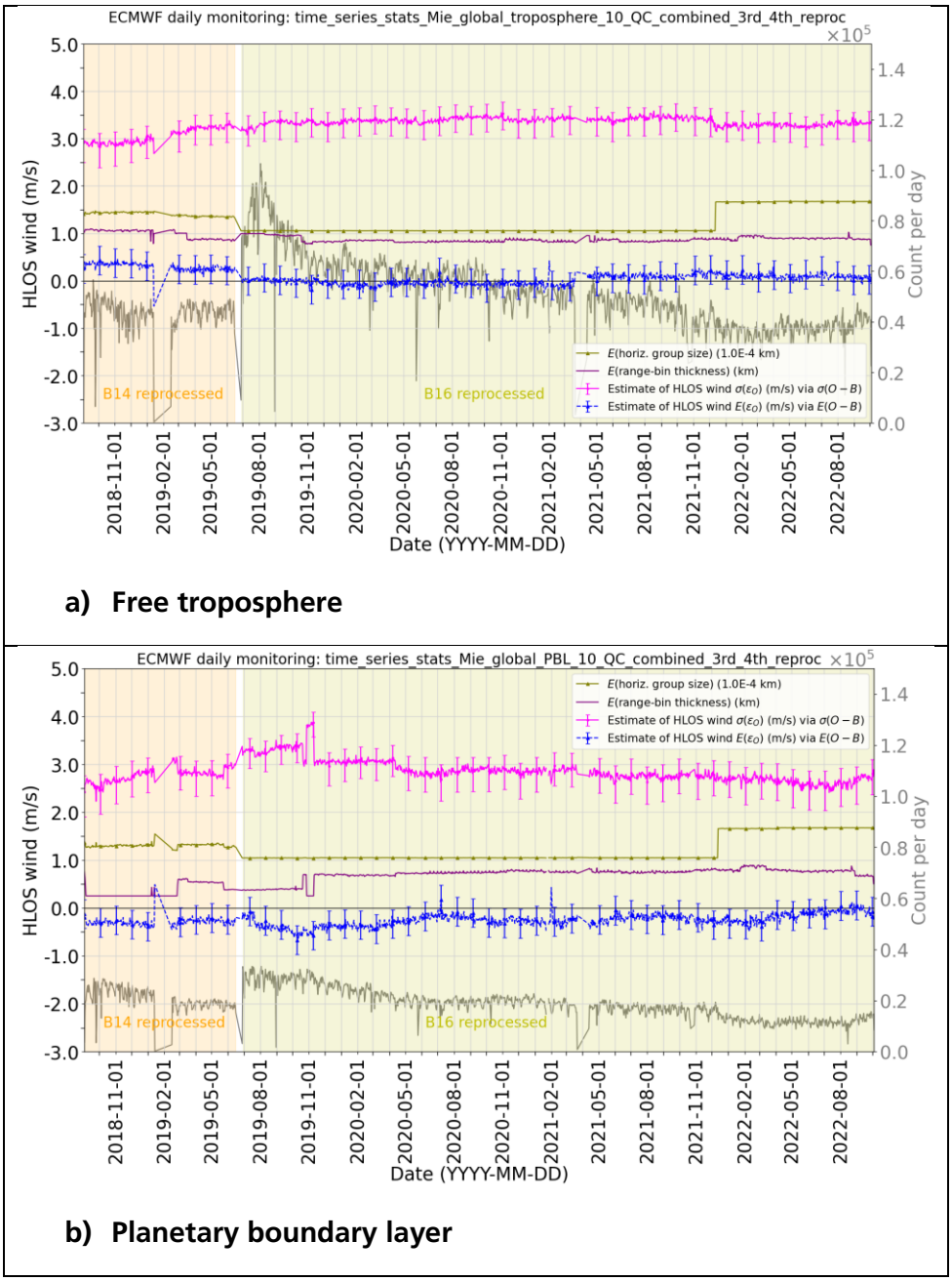

Figure 59. Time series of L2B Mie-cloudy daily, global level O-B statistics from the controls of the combined third (FM-A, B14) and fourth reprocessing (FM-B, B16) (no-Aeolus control OSE runs) for a) free troposphere and b) planetary boundary layer. For the period 3 September 2018 until 4 October 2022.

The time-series are partitioned into Northern Hemisphere extratropics (> 30 degrees latitude), tropics (within ±30 degrees latitude) and Southern Hemisphere extratropics (<-30 degrees latitude) in Figure 60. The estimated random errors appear to be rather similar in the different areas of the globe. There are hints of a seasonal cycle in the SH extratropics, with greater noise and data counts in the austral winter which is thought to be due to Polar Stratospheric Clouds. The negative bias in late 2019 into 2020 seems to be confined to the extratropics and more strongly the Northern Hemisphere.

Document Title

Verification report for phase 1 of the fourth reprocessing campaign for the FM-B laser from June 2019 till October 2022

NH extratropics	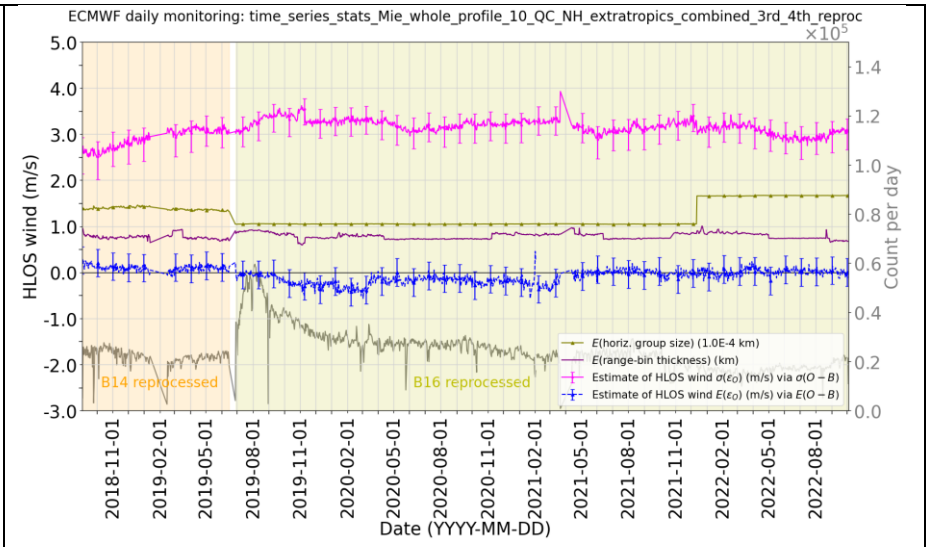
Tropics	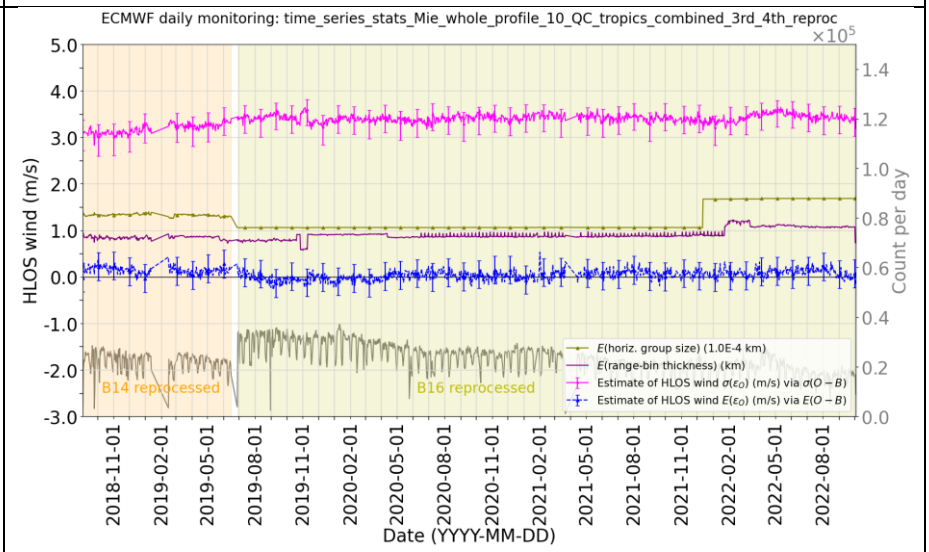

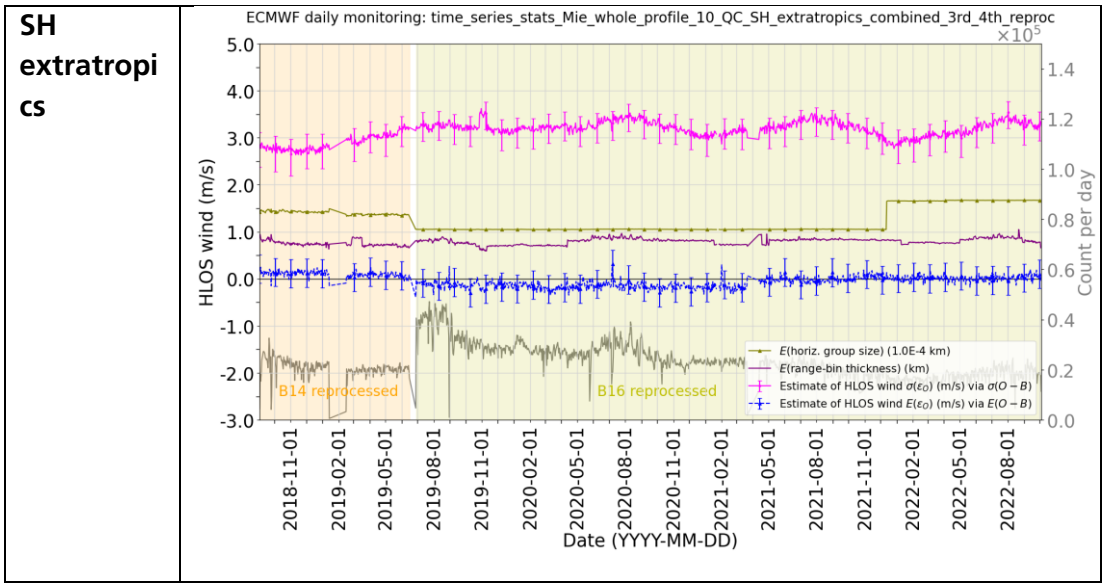

Figure 60. Time series of L2B Mie-cloudy daily, global level O-B statistics from the controls of the combined third (FM-A, B14) and fourth reprocessing (FM-B, B16) (no-Aeolus control OSE runs) for a) NH extratropics and b) Tropics and c) SH extratropics. For the period 3 September 2018 until 4 October 2022.

Vertical profiles of L2B Mie-cloudy departure statistics (versus pressure, with pressure bins chosen to roughly linear with altitude) are shown in Figure 61, for a selection of areas, for the early part of the 4th reprocessing period. Again, the statistics do not vary very much with area. The tendency for a small negative bias near the surface (as highlighted for the PBL previously) is seen. The noise is best in the lower troposphere.

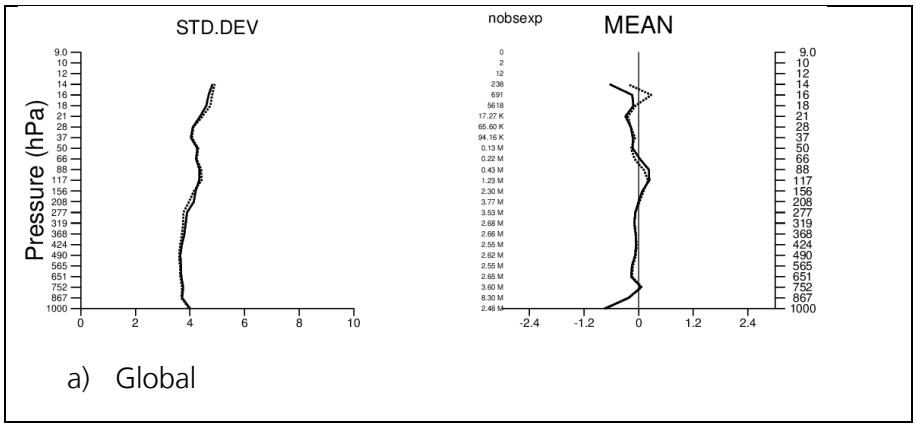

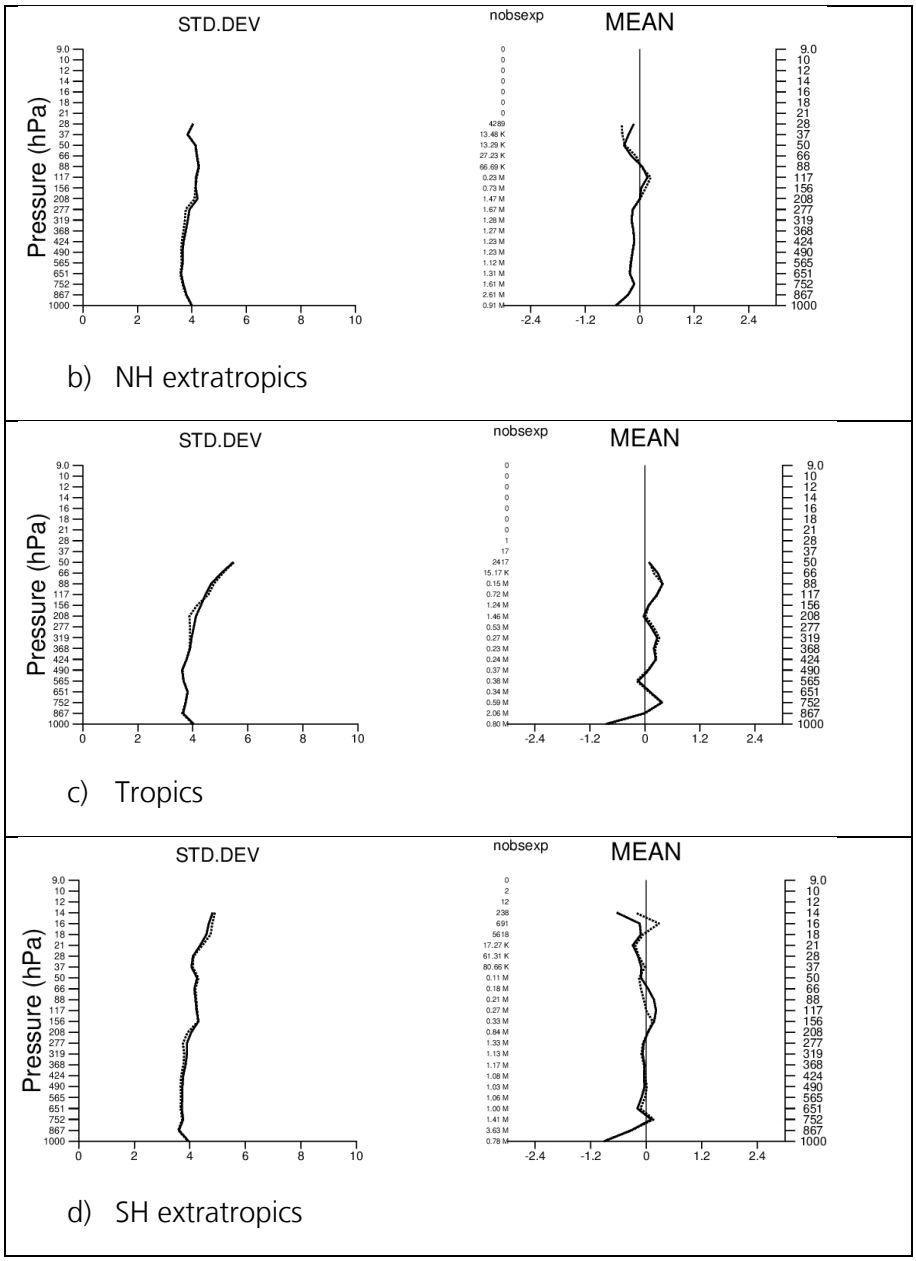

Figure 61. L2B Mie-cloudy HLOS wind O-B (solid line) and O-A (dashed line) departure statistics (m/s) as a function of pressure; standard deviation on the left and mean on the right. Data counts are printed (nobsexp) in the middle. The pressure bins are roughly linear with altitude going from surface to ~30 km. Data from the 4th (B16) reprocessing from 28 June 2019 to 9 October 2020.

A comparison of the global L2B Mie-cloudy departure statistics for assimilated data for the 1st, 2nd and 4th reprocessing for a period when all reprocessing campaigns have data (29 June to 31 December 2019) is shown in Figure 62. This shows improved standard deviation and bias for the 4th reprocessing compared to the previous version accompanied by a significant increase in data count. The improvements in departure statistics are due to fewer "valid" L2B winds in B16 having gross errors (one of the

expected improvements) and the increase in data count is due to lower backscatter (e.g. aerosol) winds entering the dataset.

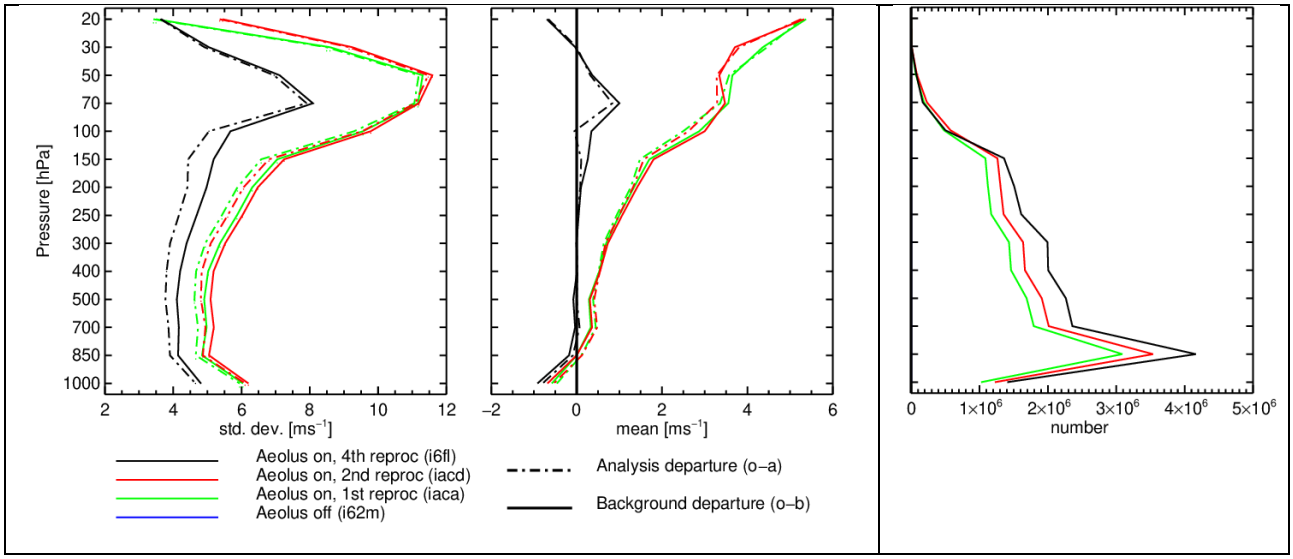

Figure 62. Global L2B Mie-cloudy O-B statistics from 29 June until 31 December 2019 from the 1st (B10), 2nd (B11) and 4th reprocessing (B16).

The relationship between the L2B Mie-cloudy and the background forecast HLOS wind is shown as 2D histograms in Figure 63, for the early part of the 4th reprocessing. This generally shows the good linear relationship between the observed and modelled HLOS wind. However, there is some evidence of the pdf being "trimmed" by the 10 ms^{-1} abs(O-B) QC, given the lack of blue shaded counts. The range of L2B HLOS winds is from -114.5 to 122.0 m/s globally, but in the tropics, it is more restricted, from -73.1 to 75.5 ms^{-1}. In these large dynamic range plots, there are no obvious issues with the wind-speed dependence of the data.

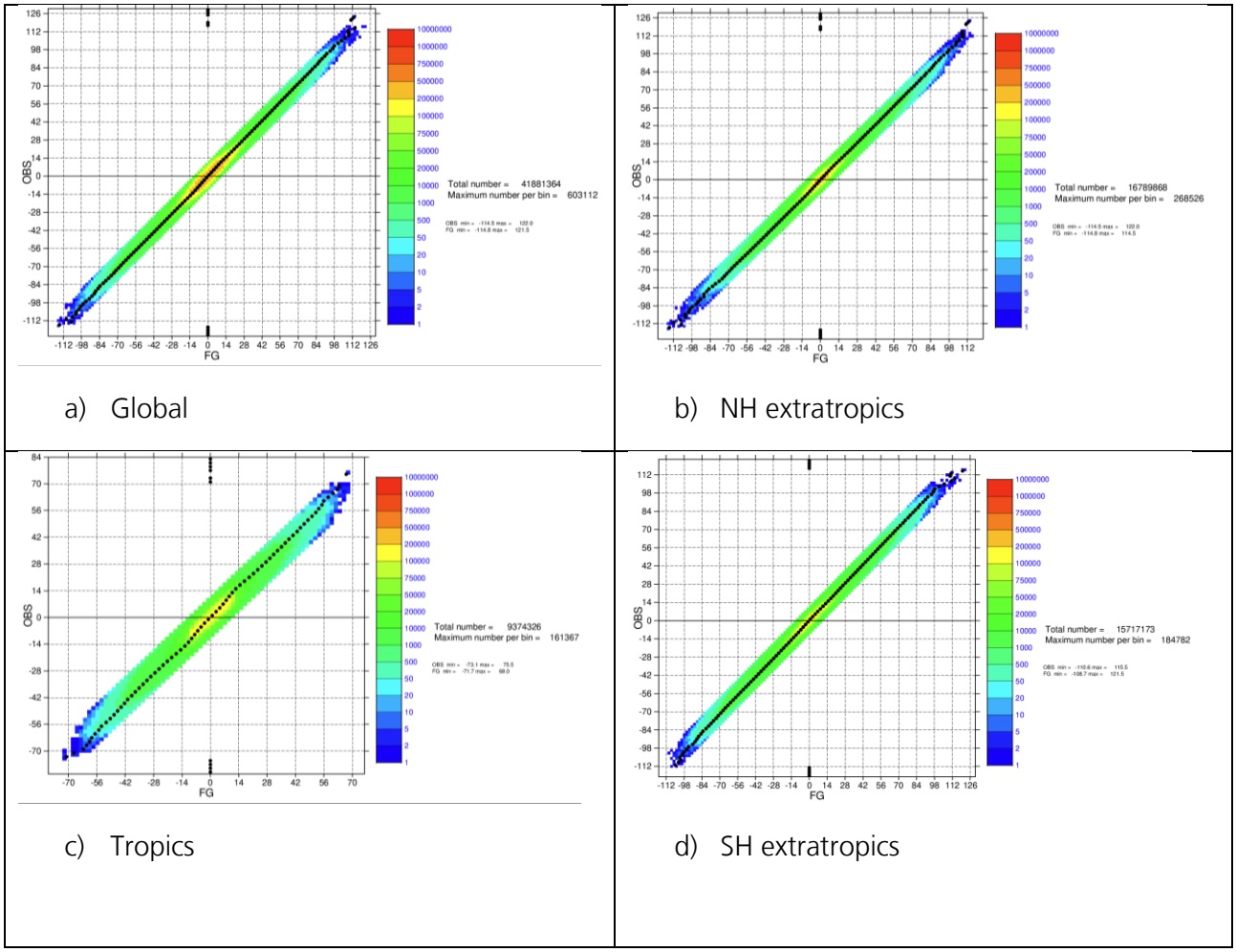

a) Global

b) NH extratropics

c) Tropics

d) SH extratropics

Figure 63. L2B Mie-cloudy HLOS wind (OBS) versus background (FG) 2D histogram for different areas. Units in m/s. Data from the 4th (B16) reprocessing from 28 June 2019 to 9 October 2020.

The plots of Figure 64 and Figure 65 show the dependence of the mean(O-B) on the B HLOS wind. One would expect a slightly negative slope due to regression dilution (errors in the independent variable, background HLOS wind). We expect a negative slope with linear fit of about -0.02 for a 2 ms^{-1} background HLOS wind 1-sigma error i.e. apparent bias of ∓ 2 ms^{-1} at ± 100 ms^{-1} HLOS wind. In Figure 64 the 4th reprocessing data is much more consistent with the expectation of the wind-speed dependent bias than the 1st and 2nd reprocessing data is. This is due to the improved Mie non-linearity calibration correction applied with B16.

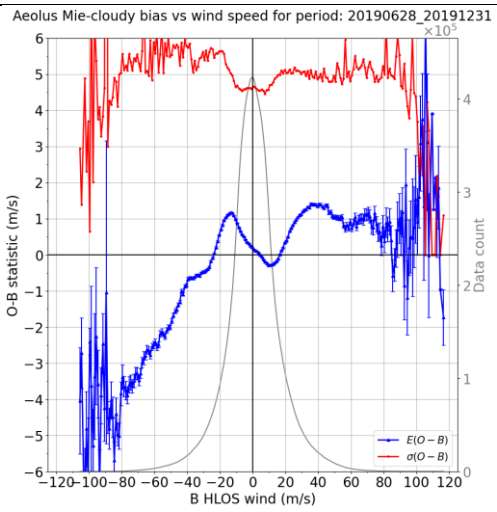

a) 1st reprocessing (B10)

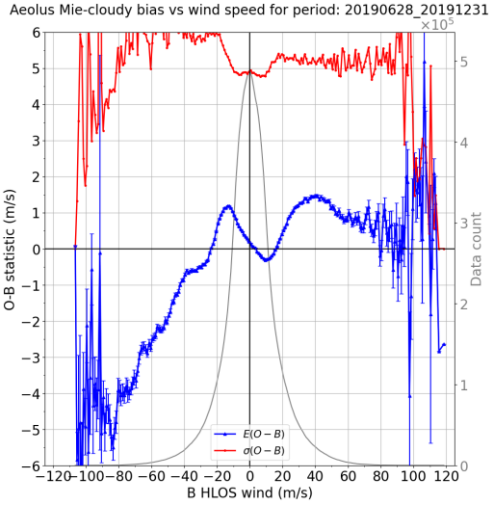

b) 2nd reprocessing (B11)

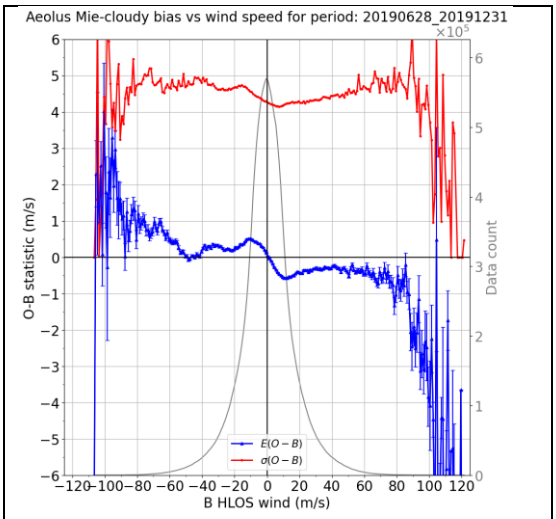

c) 4th reprocessing (B16)

Figure 64. Comparison of the wind speed dependence to the L2B Mie-cloudy bias for the period 29 June 2019 to 31 December 2019 for different reprocessing campaigns: a) 1st reprocessing (B10), b) 2nd reprocessing (B11) and c) 4th reprocessing (B12). This period is chosen for the availability of all three reprocessed datasets.

Figure 65 shows how the Mie-cloudy wind-speed dependent bias for a selection of periods of the 4th reprocessing changes. The shape of bias ("wiggles") varies somewhat with time but remains within ±1 ms^{-1} and is therefore OK; there are some "wiggles" particularly in 2022 indicating some imperfections in the applied Mie non-linearity.

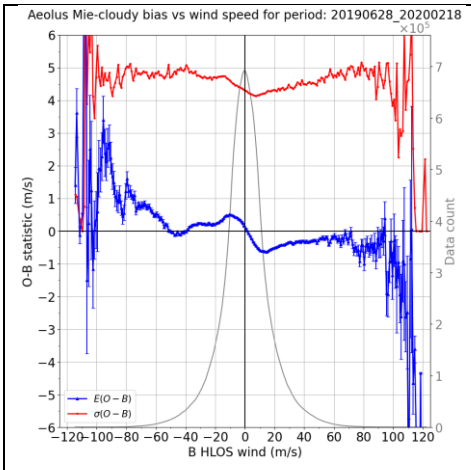

a) 28 June 2019 – 18 February 2020

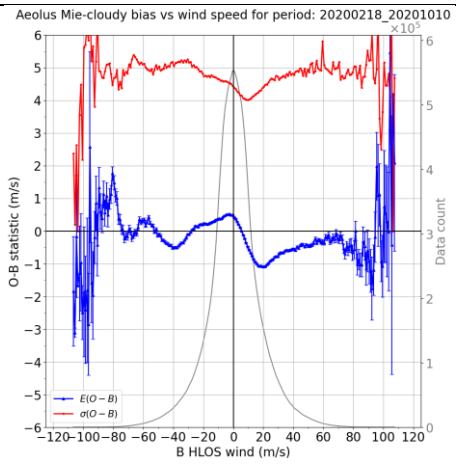

b) 18 February 2020 – 10 October 2020

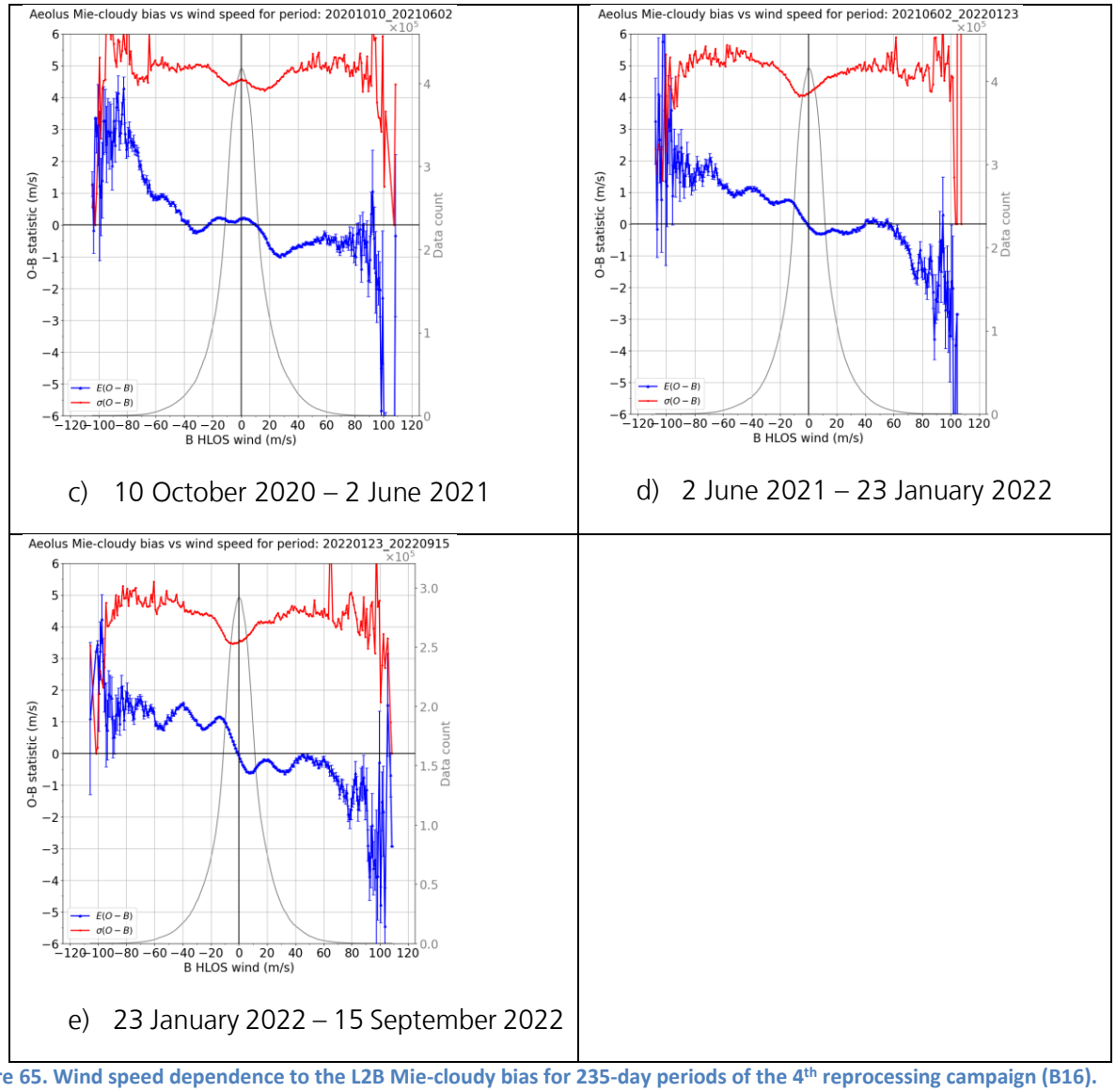

c) 10 October 2020 – 2 June 2021

d) 2 June 2021 – 23 January 2022

e) 23 January 2022 – 15 September 2022

Figure 65. Wind speed dependence to the L2B Mie-cloudy bias for 235-day periods of the 4th reprocessing campaign (B16).

The following figures show statistics as a function of pressure and time. The pressure bins are chosen to be roughly linear in altitude so the y-axis can be thought as roughly being from surface to 30 km (~10 hPa) altitude. Figure 66 shows data counts and mean observed HLOS wind as a function of pressure (~altitude) and time. The 3rd reprocessing is also included for comparison.

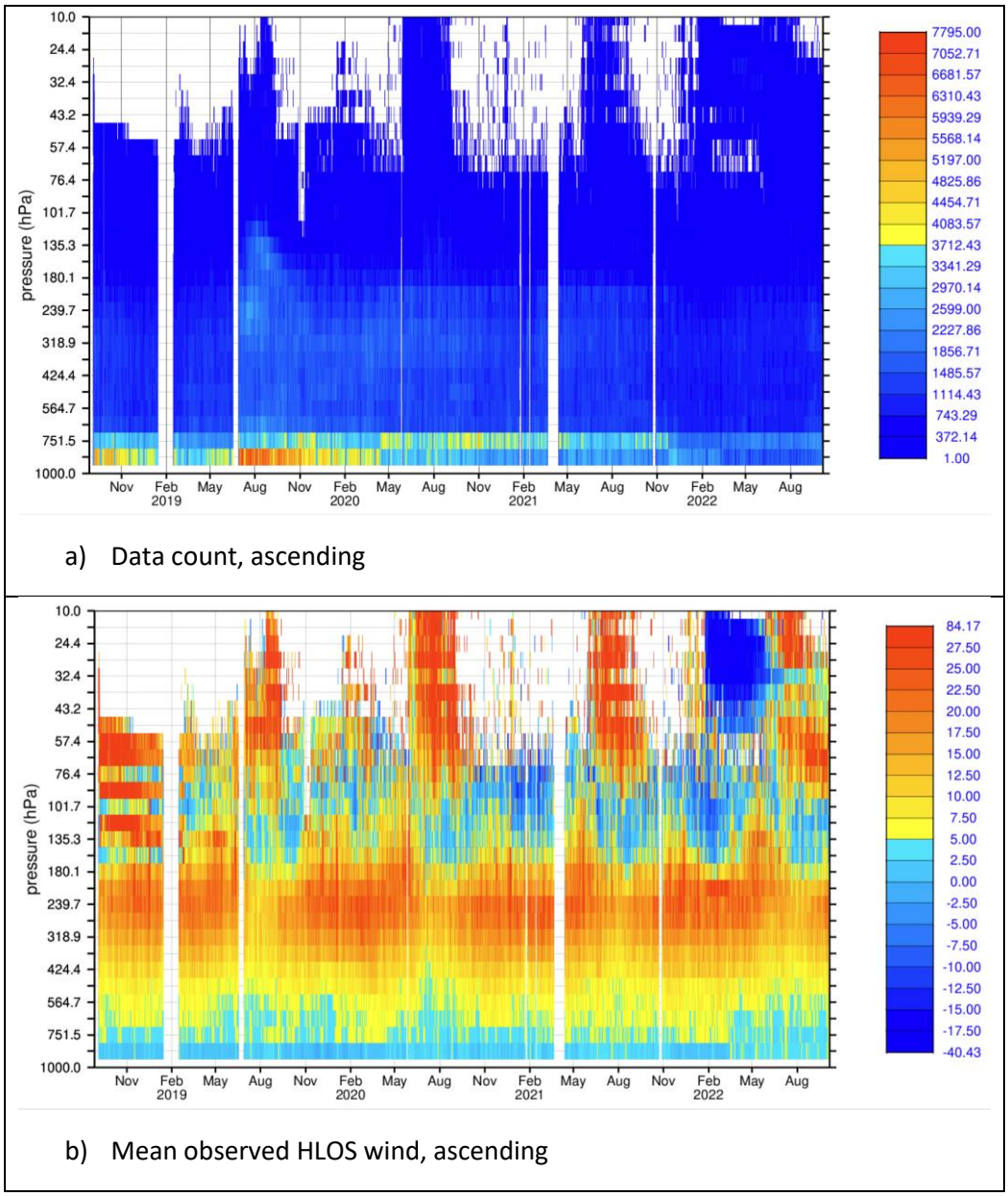

Figure 66. Pressure-time plots for L2B Mie-cloudy winds for ascending orbits of a) data counts and b) mean observed HLOS wind value (m/s), for the combined 3rd (B14) and 4th (B16) reprocessing for global data. Time-step is 12 hours.

In Figure 66, the increased data counts at ~230-130 hPa for the 4th reprocessing for June-December 2019 are due to the (already mentioned) wildfire smoke aerosol load over high northern latitudes

combined with good instrument performance. The data counts are dominated by winds in the PBL. Seasonal cycles in the observed HLOS winds are evident. A distinct patch of negative HLOS winds (ascending orbits, so easterlies) is evident from early 2022 at very high altitudes (~50-10 hPa). This is due to measuring Mie winds from the Hunga-Tonga volcanic eruption plume which occurred on 15 January 2022 (soon followed by the raising of the range-bins to 30 km (~10 hPa) to capture the plume). The negative HLOS winds are due to the easterly phase of the QBO (quasi-biennial oscillation) since the eruption plume was initially in the tropics (but spread to the extratropics with time). The patches of positive HLOS winds seen yearly in June-September above 100 hPa are due to Polar Stratospheric Clouds present in the Southern Polar Vortex – these strong westerlies are therefore positive HLOS winds. Weaker HLOS winds are evident near the surface with increasing westerlies above peaking at ~240 hPa (associated with jet streams, both polar and subtropical).

Mean(O-B) with time and pressure is shown in Figure 67. Slightly more negative bias is evident in the ascending orbits compared to the descending; it is unclear why this is the case. The near surface negative bias is quite persistent, particularly for descending orbits.

The standard deviation of O-B shows smaller departures near the surface, due to a combination of stronger backscatter from water clouds so reducing L2B wind error and reduced errors in background forecast winds. The ascending orbits again are less noisy than descending particularly in early 2020.

Zonal average plots are provided in Figure 69 to Figure 71 for the early part of the 4th reprocessing. Data counts indicate the climatological distribution of cloud cover with most Mie winds in the PBL and at around the upper troposphere. The mean HLOS winds highlight the climatological regions of strong westerlies associated with jet streams (peak winds at ~ 200 hPa) in mid-latitudes and easterlies in the tropics. The figures also show some differences in bias and noise between ascending and descending orbits. The smallest noise tends to be in the SH extratropics at ~750 hPa.

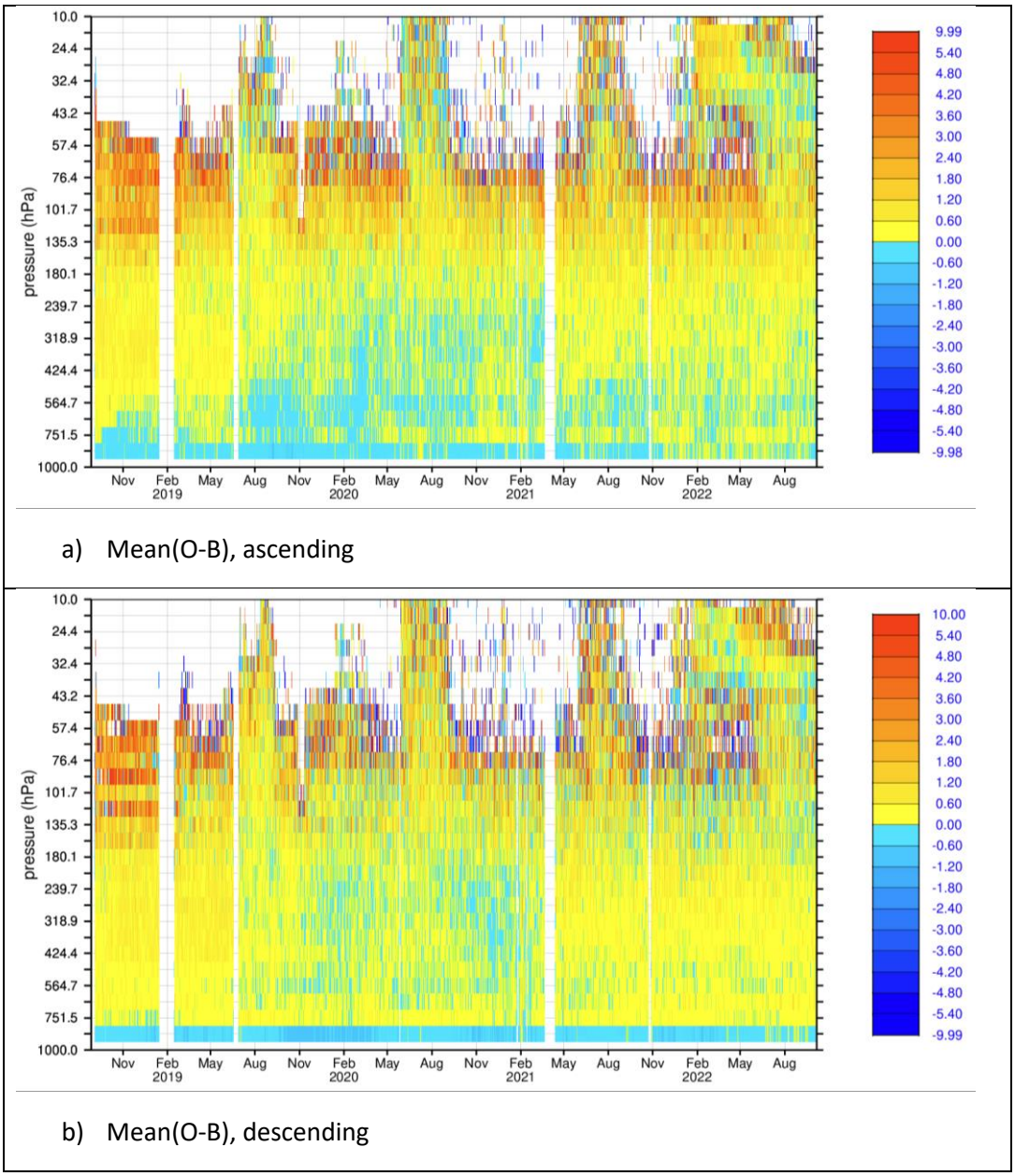

Figure 67. Pressure-time plots for L2B Mie-cloudy winds of mean(O-B) (m/s) for a) ascending and b) descending orbits for the combined 3rd (B14) and 4th (B16) reprocessing for global data. Time-step is 12 hours.

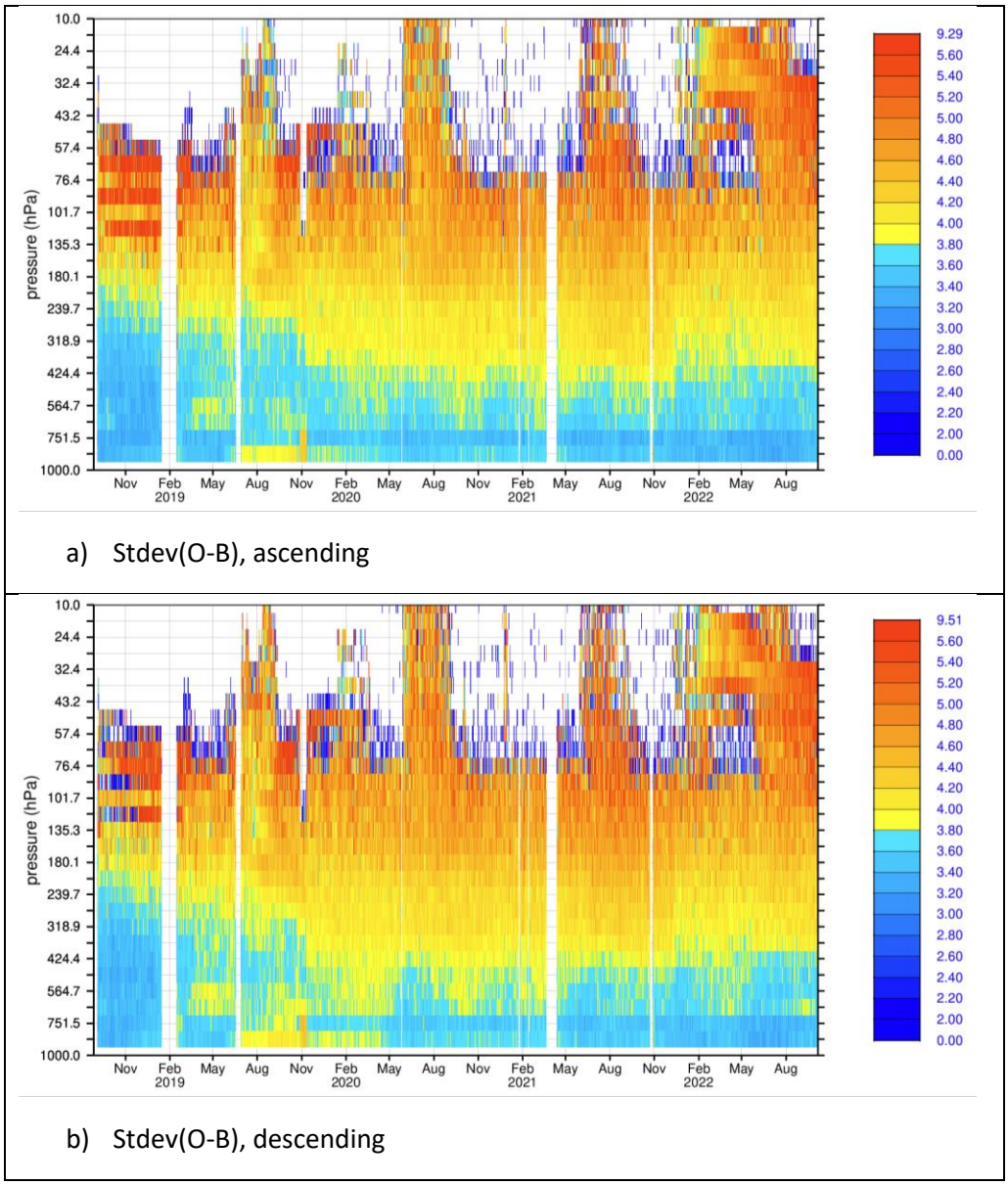

Figure 68. Pressure-time plots for L2B Mie-cloudy winds of standard deviation(O-B) (m/s) for a) ascending and b) descending orbits for the combined 3rd (B14) and 4th (B16) reprocessing for global data. Time-step is 12 hours.

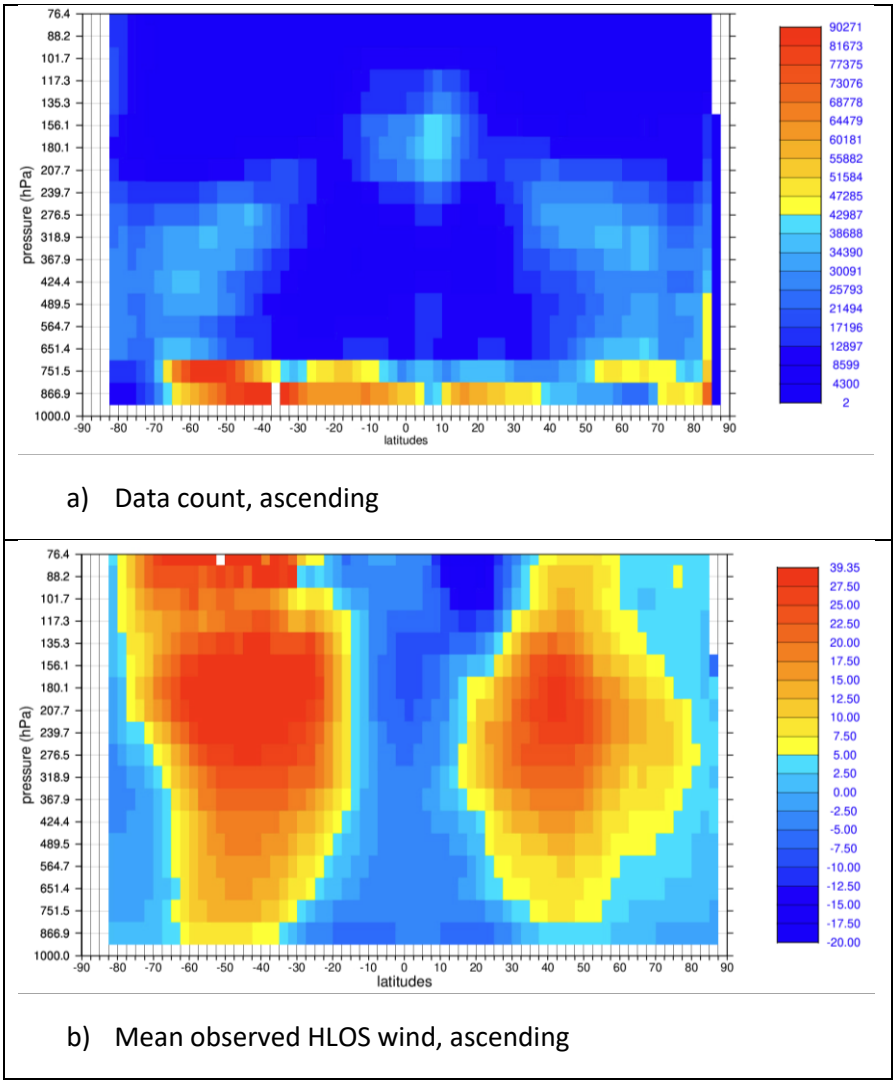

a) Data count, ascending

b) Mean observed HLOS wind, ascending

Figure 69. Zonal average plots for L2B Mie-cloudy winds for ascending orbits of a) data counts and b) mean observed HLOS wind value (m/s), for the 4th (B16) reprocessing from 28 June 2019 to 9 October 2020.

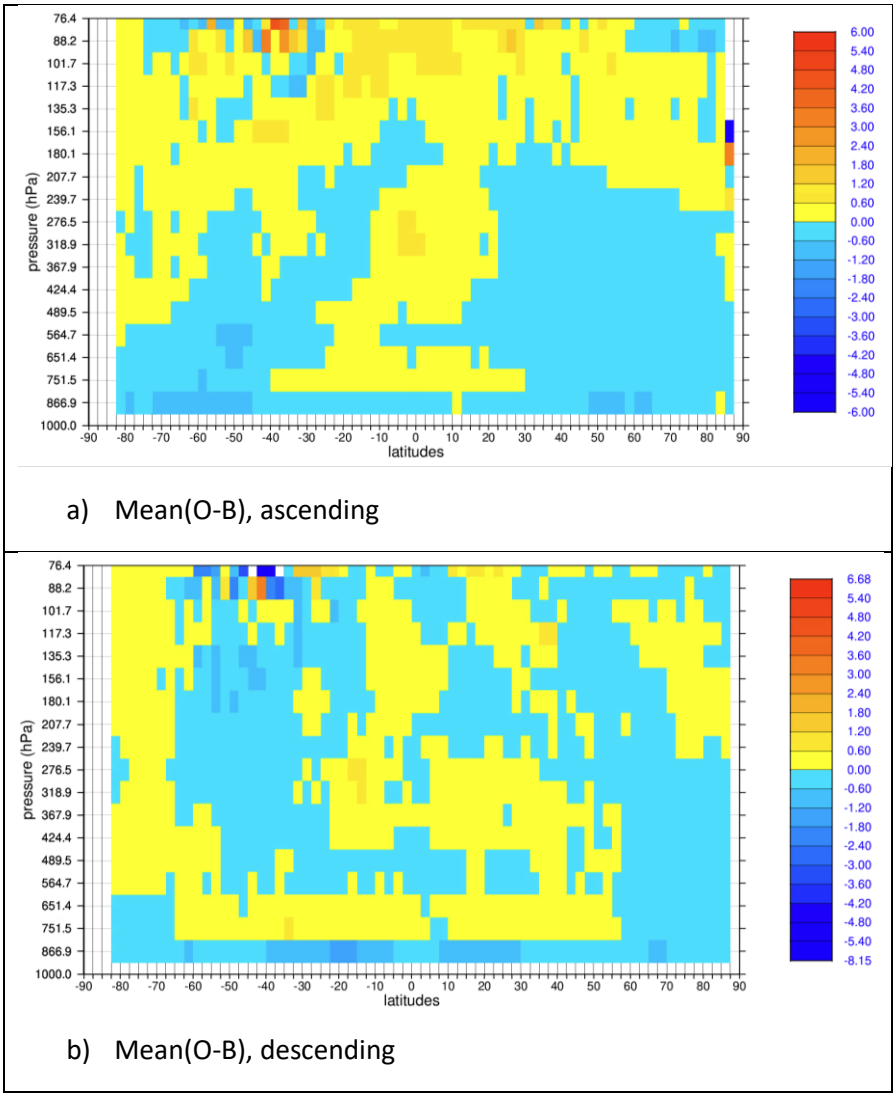

Figure 70. Zonal average plots for L2B Mie-cloudy winds of mean(O-B) (m/s) for a) ascending and b) descending orbits for the 4th (B16) reprocessing from 28 June 2019 to 9 October 2020.

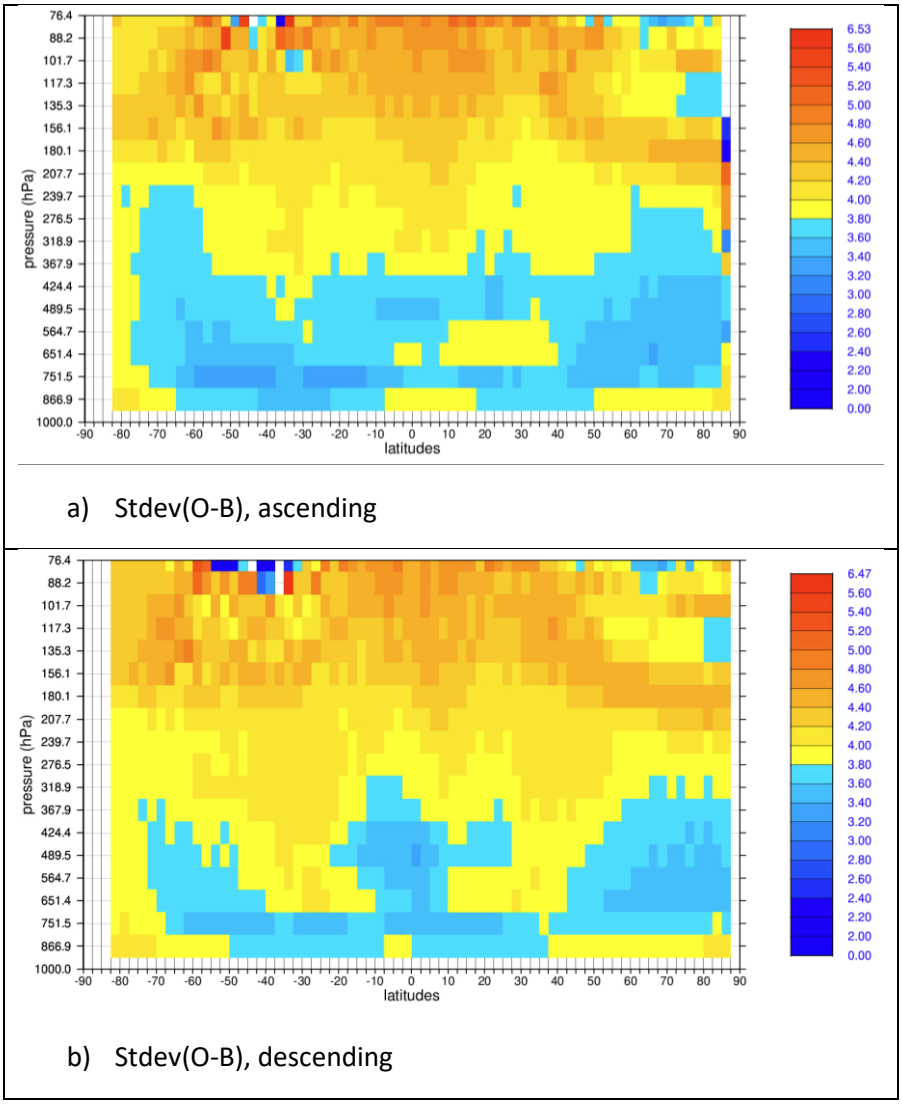

Figure 71. Zonal average plots for L2B Mie-cloudy winds of standard deviation(O-B) (m/s) for a) ascending and b) descending orbits for the 4th (B16) reprocessing from 28 June 2019 to 9 October 2020.

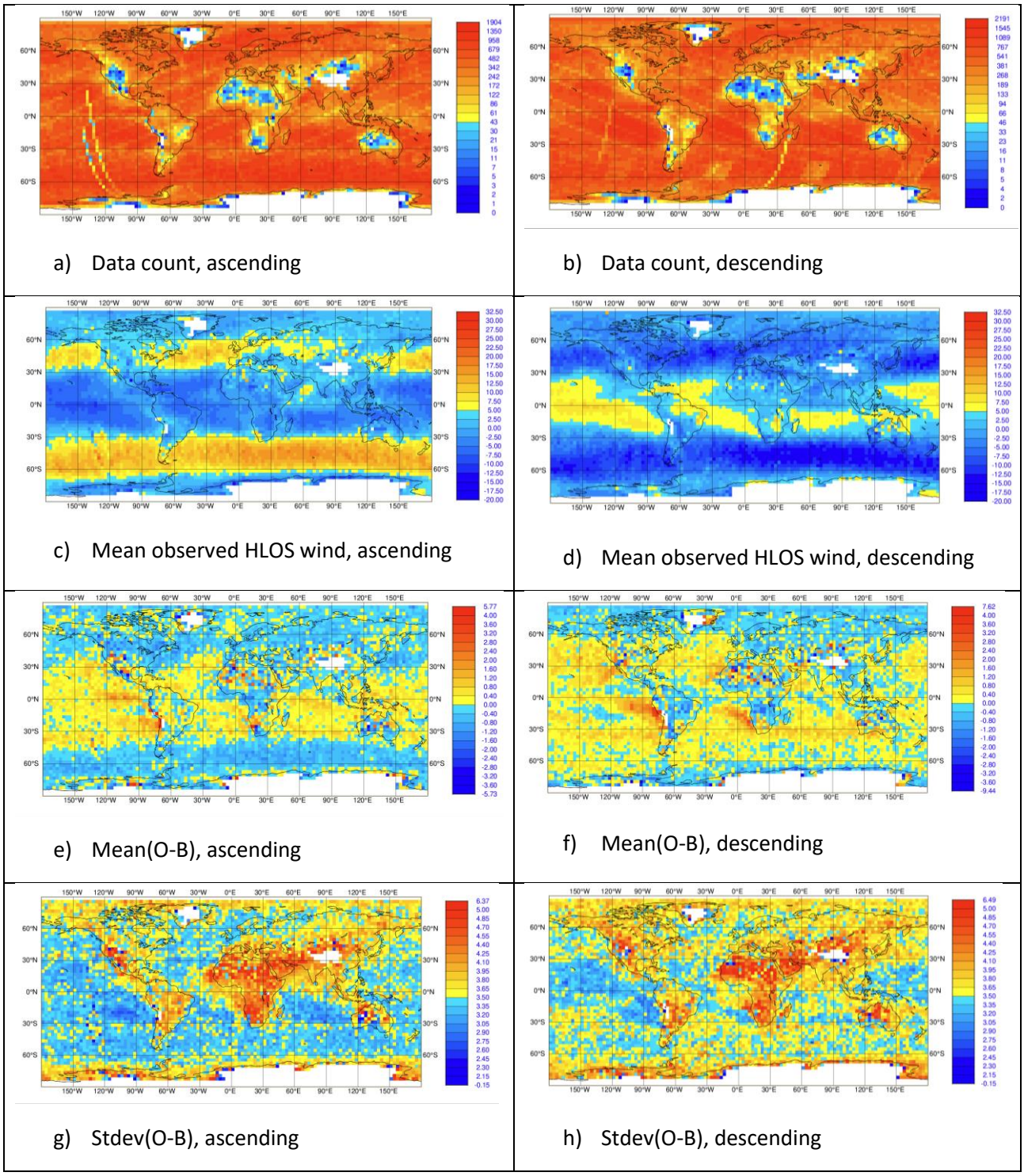

a) Data count, ascending

b) Data count, descending

c) Mean observed HLOS wind, ascending

d) Mean observed HLOS wind, descending

e) Mean(O-B), ascending

f) Mean(O-B), descending

g) Stdev(O-B), ascending

h) Stdev(O-B), descending

Figure 72. Map plots (3x3 degrees) for L2B Mie-cloudy winds at ~800 hPa (751-867 hPa) of: data counts for the top row; mean observed HLOS wind value (m/s) for the second row; mean(O-B) (m/s) for the third row; and stdev(O-B) (m/s) for the bottom row. Using the 4th (B16) reprocessing from 28 June 2019 to 9 October 2020.

Figure 72 and Figure 73 show maps of L2B Mie-cloudy statistics, focusing on pressure bins with the largest data counts i.e. ~800 hPa and around polar jet stream level ~250 hPa. There are some

interesting positive/negative bias structures evident at ~800 hPa off the tropical/subtropical western coasts of Africa and South America, which seem more likely to be ECMWF model biases due to their geographical distribution. The biases differ for ascending and descending orbits, as so may depend on local solar time. These regions typically have marine stratocumulus clouds, which provide strong lidar backscatter, hence the low wind noise also in these regions.

The mapped statistics look noisier at ~250 hPa, due to reduced data counts per 3-degree box. But there are hints of positive bias structures along the equator for ascending orbits at 250 hPa, which again may be ECMWF model bias.

The following figures show statistics as a function of latitude and time (split by ascending and descending) – often referred to as Hovmöller plots. In Figure 74, at 800 hPa the peak data counts occur in the Southern Hemisphere at around -50 to -60 degrees latitude (frontal clouds) and there are relatively large counts at -10 to -20 degrees latitude (due to marine stratocumulus). The predominantly westerly winds (ascending orbits positive HLOS winds) in the mid-latitudes (stronger in SH) and easterlies in the tropics are evident also. The faster westerlies at 250 hPa and narrower tropical band of easterlies are evident. Again, the peak in data counts at 250 hPa occurring at high northern latitudes in July 2019 was due to wildfire smoke.

In Figure 76, at 800 hPa the mean(O-B) shows some latitudinal variation with a tendency towards more negative biases in midlatitudes and positive towards the tropics – however these biases are small (less than 1 ms^{-1}). Some linear features associated with changes in range-bin settings with latitude are evident, particularly for the descending orbits (reason unknown). In Figure 77, at 250 hPa, the biases look "noisier" (partly due to reduced data counts) but with patterns of concern.

In Figure 78, the standard deviation in O-B is smaller in the Southern Hemisphere at 800 hPa, perhaps due to more cloud cover than in the Northern Hemisphere – again associated with marine stratocumulus regions and frontal clouds. The thinner range-bin settings for collocations with AMVs caused an increase in noise of the winds with respect to the ECMWF model in all areas in the lower troposphere. At 250 hPa the noise is more uniform over the globe, apart from the wildfire smoke area in 2019, for which the noise increased rather quickly with time, as the aerosol plumes dispersed.

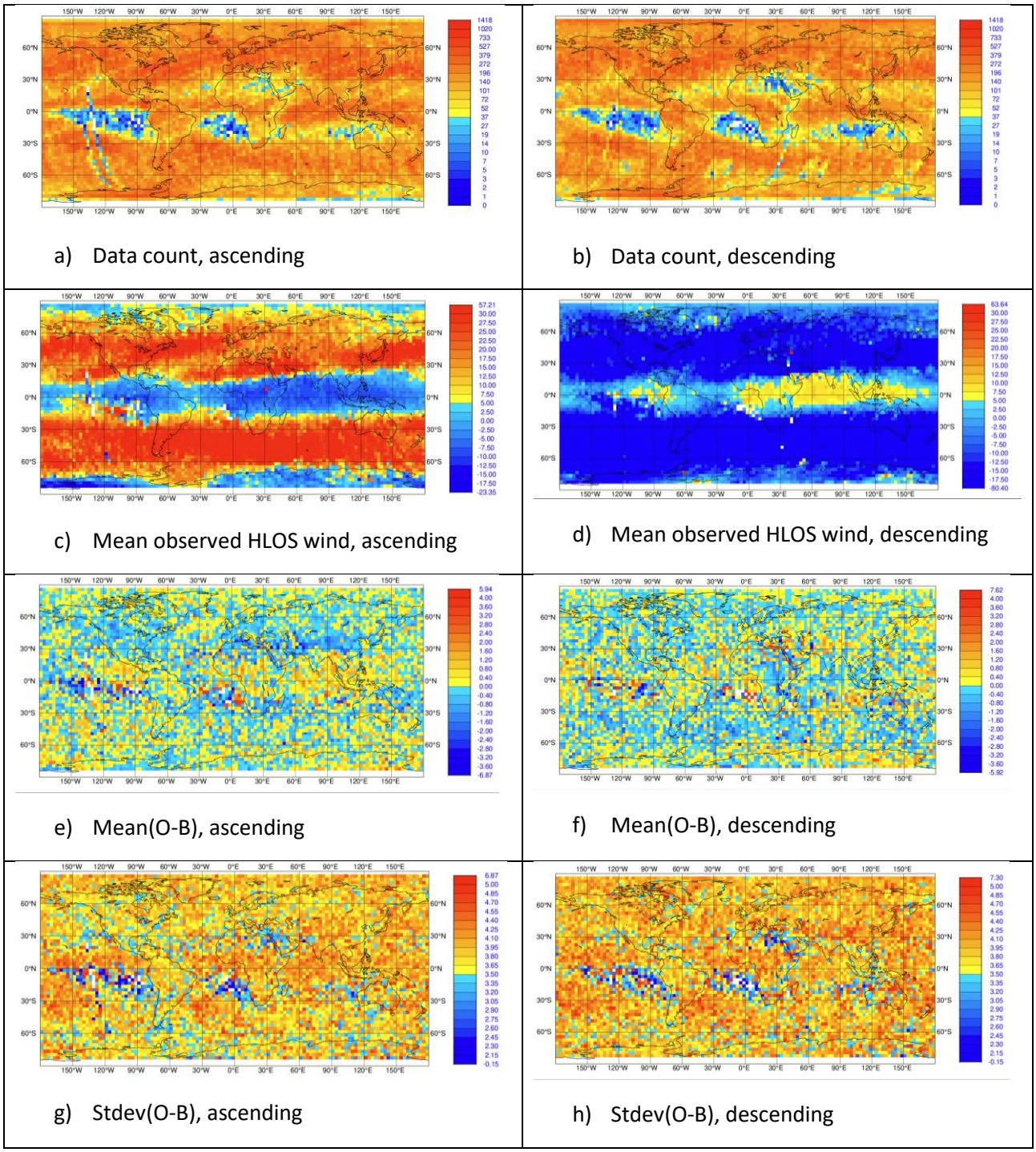

a) Data count, ascending

b) Data count, descending

c) Mean observed HLOS wind, ascending

d) Mean observed HLOS wind, descending

e) Mean(O-B), ascending

f) Mean(O-B), descending

g) Stdev(O-B), ascending

h) Stdev(O-B), descending

Figure 73. Map plots (3x3 degrees) for L2B Mie-cloudy winds at ~250 hPa (240-277 hPa) of: data counts for the top row; mean observed HLOS wind value (m/s) for the second row; mean(O-B) (m/s) for the third row; and stdev(O-B) (m/s) for the bottom row. Using the 4th (B16) reprocessing from 28 June 2019 to 9 October 2020.

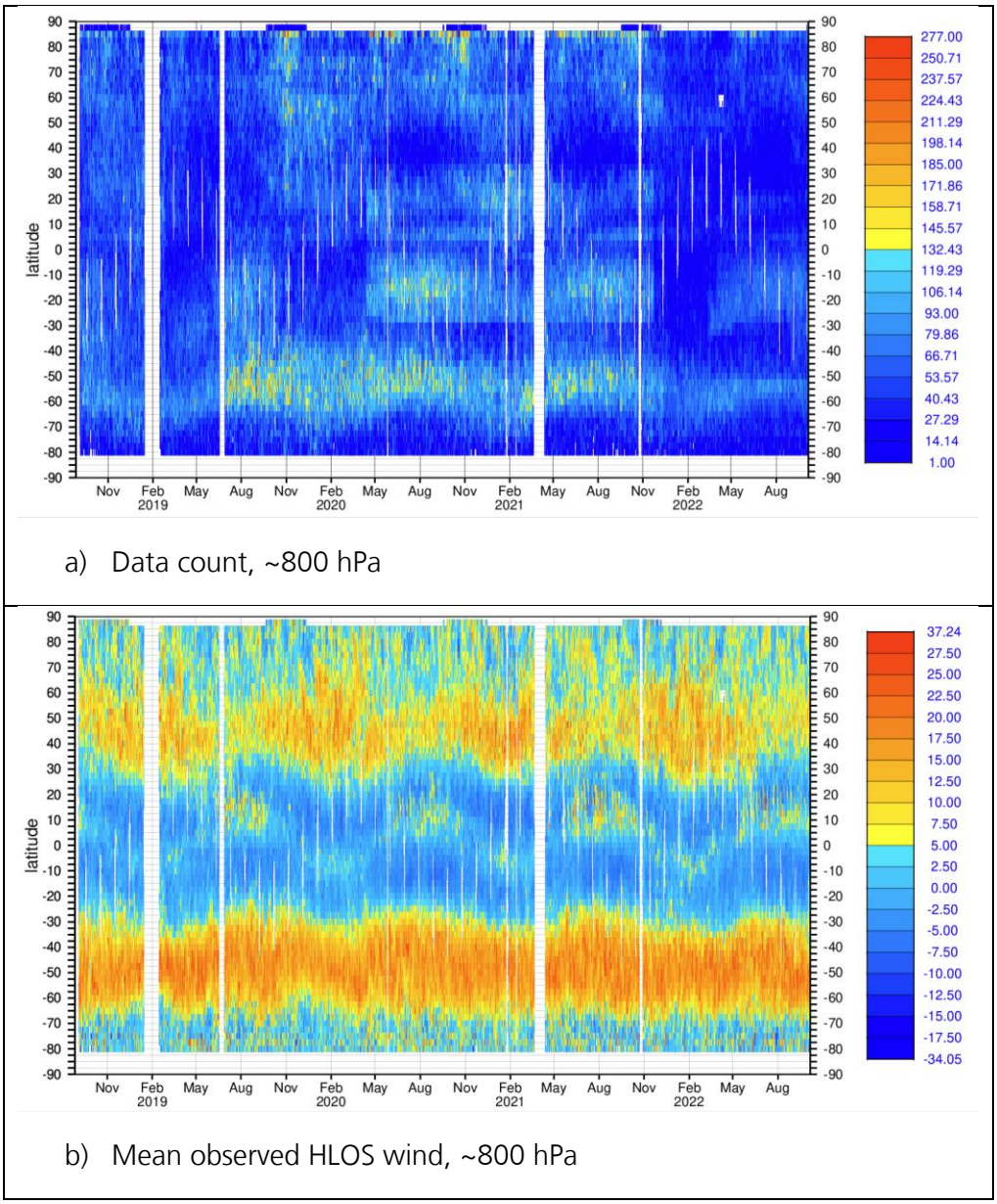

Figure 74. Latitude-time plots for L2B Mie-cloudy winds for ascending orbits of a) data counts and b) mean observed HLOS wind value (m/s), for the combined 3rd (B14) and 4th (B16) reprocessing for the pressure range with largest data counts i.e. 751-867 hPa. Time-step is 12 hours.

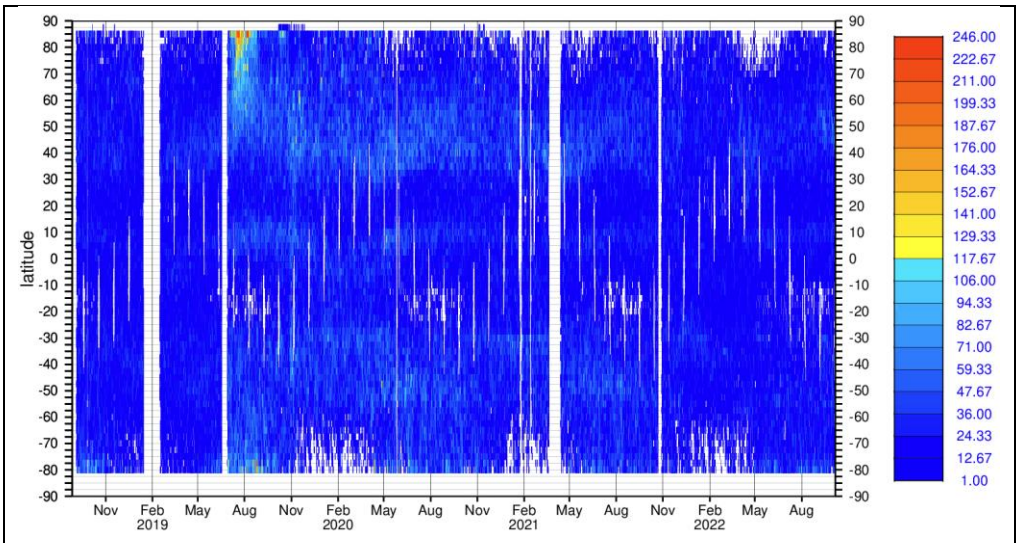

a) Data count, ~250 hPa

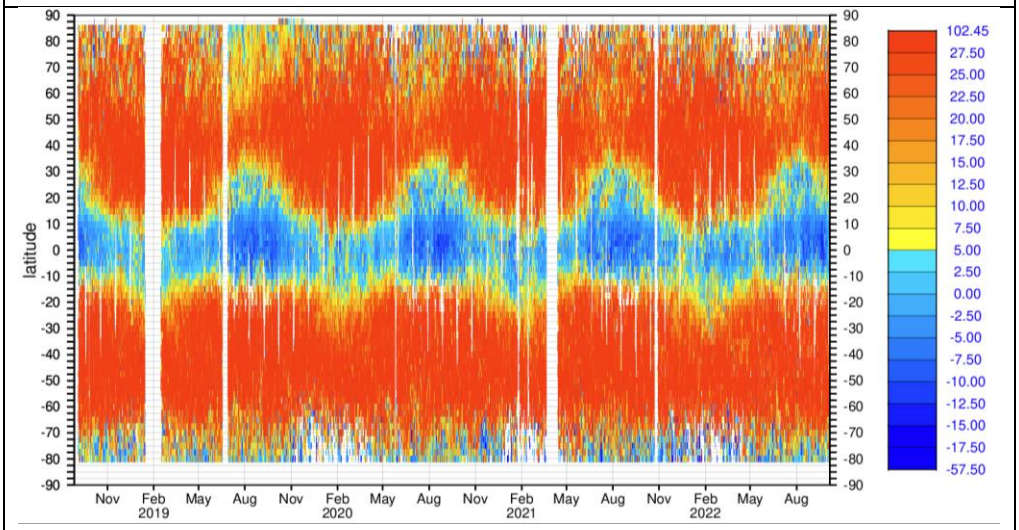

b) Mean observed HLOS wind, ~250 hPa

Figure 75. Latitude-time plots for L2B Mie-cloudy winds for ascending orbits of a) data counts and b) mean observed HLOS wind value (m/s), for the combined 3rd (B14) and 4th (B16) reprocessing for the pressure range with largest data counts i.e. 240-277 hPa. Time-step is 12 hours.

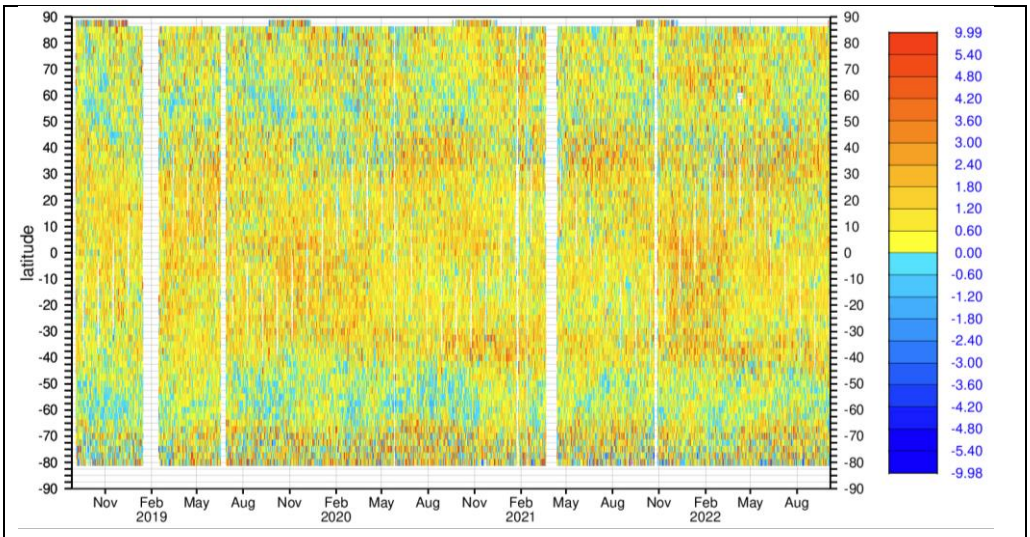

a) Mean(O-B), ascending, ~800 hPa

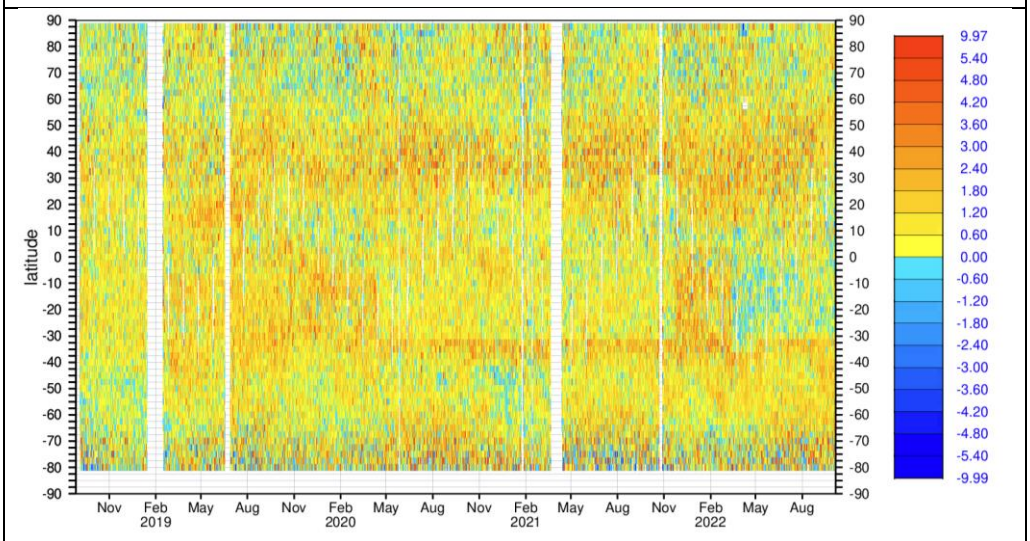

b) Mean(O-B), descending, ~800 hPa

Figure 76. Latitude-time plots for L2B Mie-cloudy winds of mean(O-B) (m/s) for a) ascending orbits and b) descending orbits, for the combined 3rd (B14) and 4th (B16) reprocessing for the pressure range with largest data counts i.e. 751-867 hPa. Time-step is 12 hours.

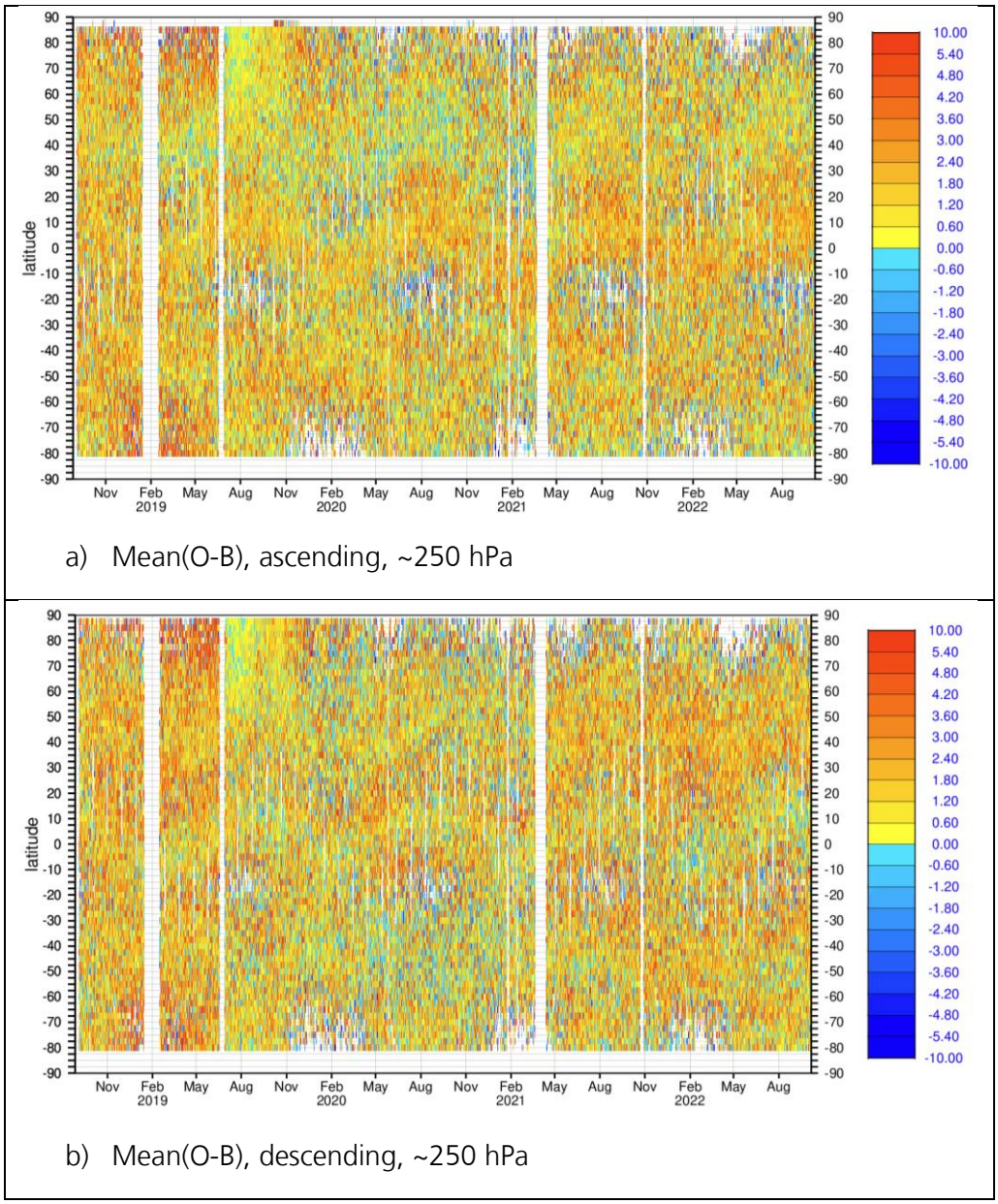

a) Mean(O-B), ascending, ~250 hPa

b) Mean(O-B), descending, ~250 hPa

Figure 77. Latitude-time plots for L2B Mie-cloudy winds of mean(O-B) (m/s) for a) ascending orbits and b) descending orbits, for the combined 3rd (B14) and 4th (B16) reprocessing for the pressure range with largest data counts i.e. 240-277 hPa. Time-step is 12 hours.

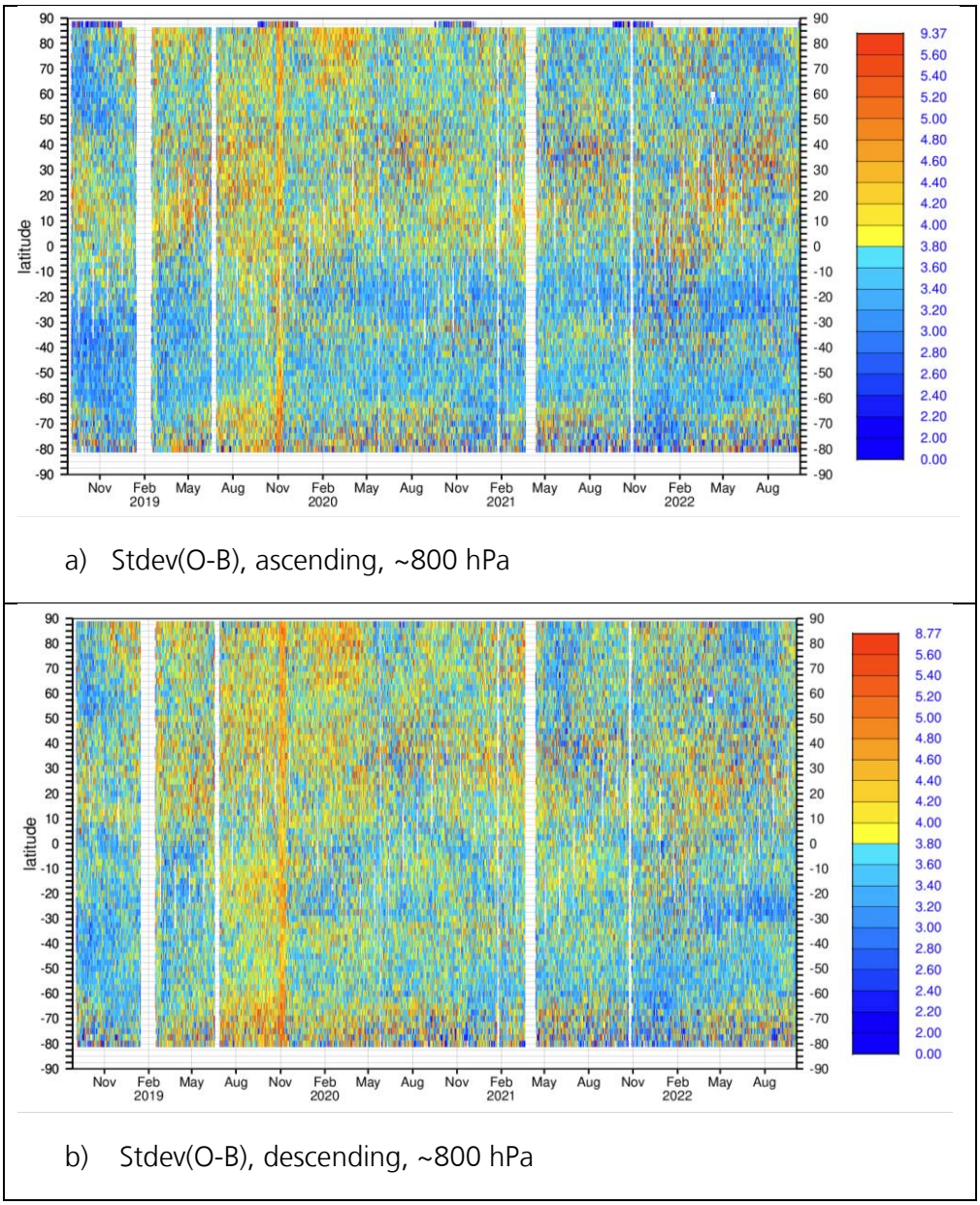

Figure 78. Latitude-time plots for L2B Mie-cloudy winds of standard deviation (O-B) (m/s) for a) ascending and b) descending orbits, for the combined 3rd (B14) and 4th (B16) reprocessing for the pressure range with largest data counts i.e. 751-867 hPa. Time-step is 12 hours.

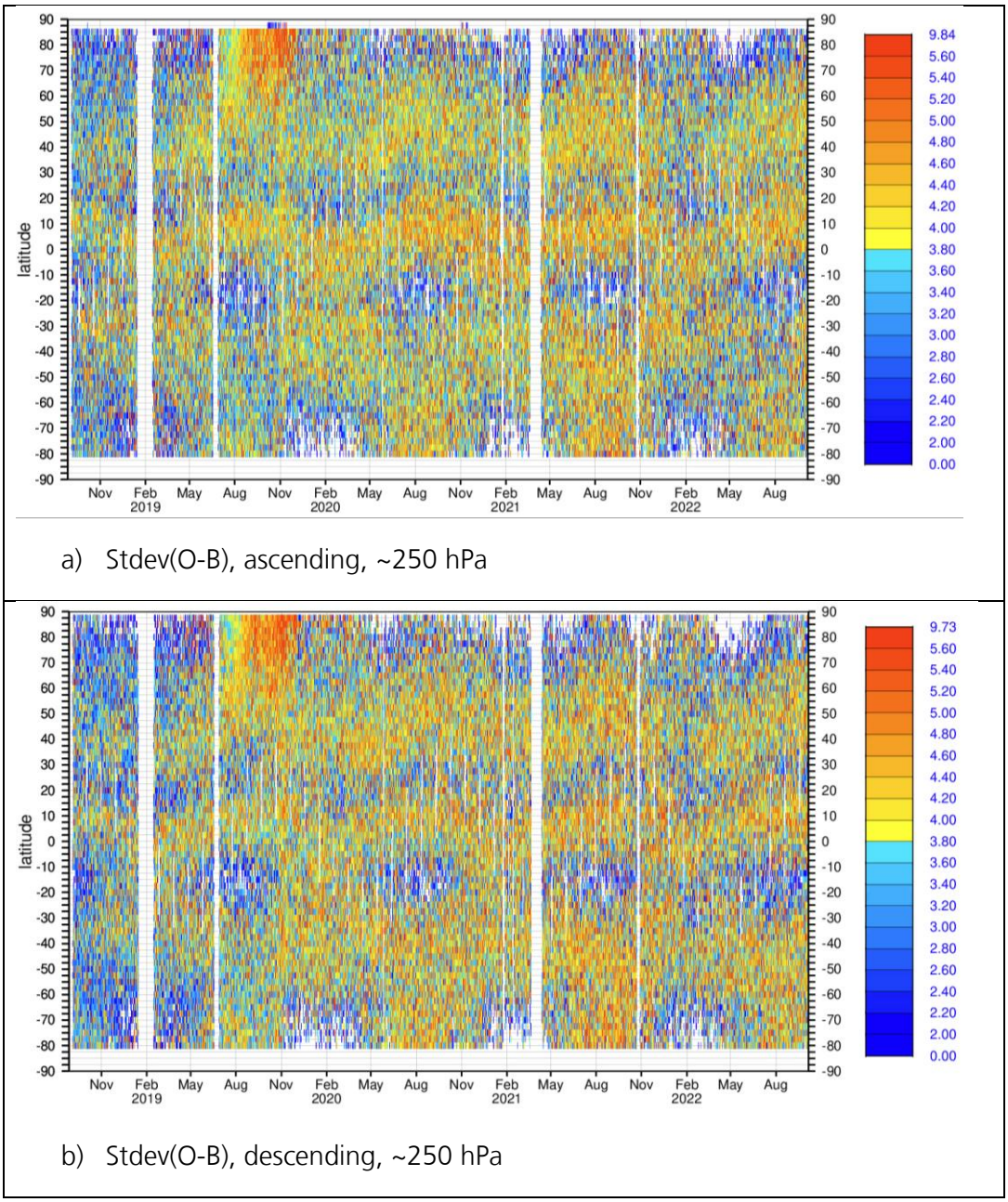

Figure 79. Latitude-time plots for L2B Mie-cloudy winds of standard deviation (O-B) (m/s) for a) ascending and b) descending orbits, for the combined 3rd (B14) and 4th (B16) reprocessing for the pressure range with largest data counts i.e. 240-277 hPa. Time-step is 12 hours.

7.5 L2B Rayleigh-clear winds, detailed verification

Figure 80 shows a time-series of the daily, global average O-B statistics (left axis) and data counts (right axis) for the L2B Rayleigh-clear winds during the 4th reprocessing (28 June 2019 to 4 October 2022). It also includes the 3rd reprocessing (FM-A laser) from 3 September 2018 to 16 June 2019 for comparison.

The QC applied for the time-series results for the Rayleigh-clear rejects winds with abs(O-B)> 25 m/s or if the L2B validity flag is false. There are relatively fewer gross errors in the Rayleigh-clear winds compared to the Mie-cloudy winds, therefore we can allow quite relaxed QC check, whilst not spoiling the non-robust metrics of mean and standard deviation. Also, the noise of the Rayleigh winds becomes very large in 2021-2022 meaning that a 25 ms^{-1} O-B check is roughly a 3σ check.

The random wind errors in the 4th reprocessing were smallest just after the FM-B laser switch-on in July-October 2019 (~5 ms^{-1} in profile average) thanks to the relatively large atmospheric path useful signal measured during that period. The random errors increased with time with some stabilisation in 2021 and 2022 at ~8 ms^{-1} (which is a 60% increase) due to various attempts to mitigate the transmission loss on the FM-B laser optical path e.g. N/P settings, laser energy boosts. The 4th reprocessing Rayleigh-clear random errors are smaller than the best period of the FM-A 3rd reprocessing (September 2018), until about May 2020.

The systematic wind errors are close to 0 ms^{-1} in the global daily average, apart from a slight tendency to negative bias in 2021. The data counts tended to decrease in 2021 and 2022 due to reduced signal and hence more winds failing the QC. The biweekly reductions in data counts are due to moon-blinding QC to avoid wind biases.

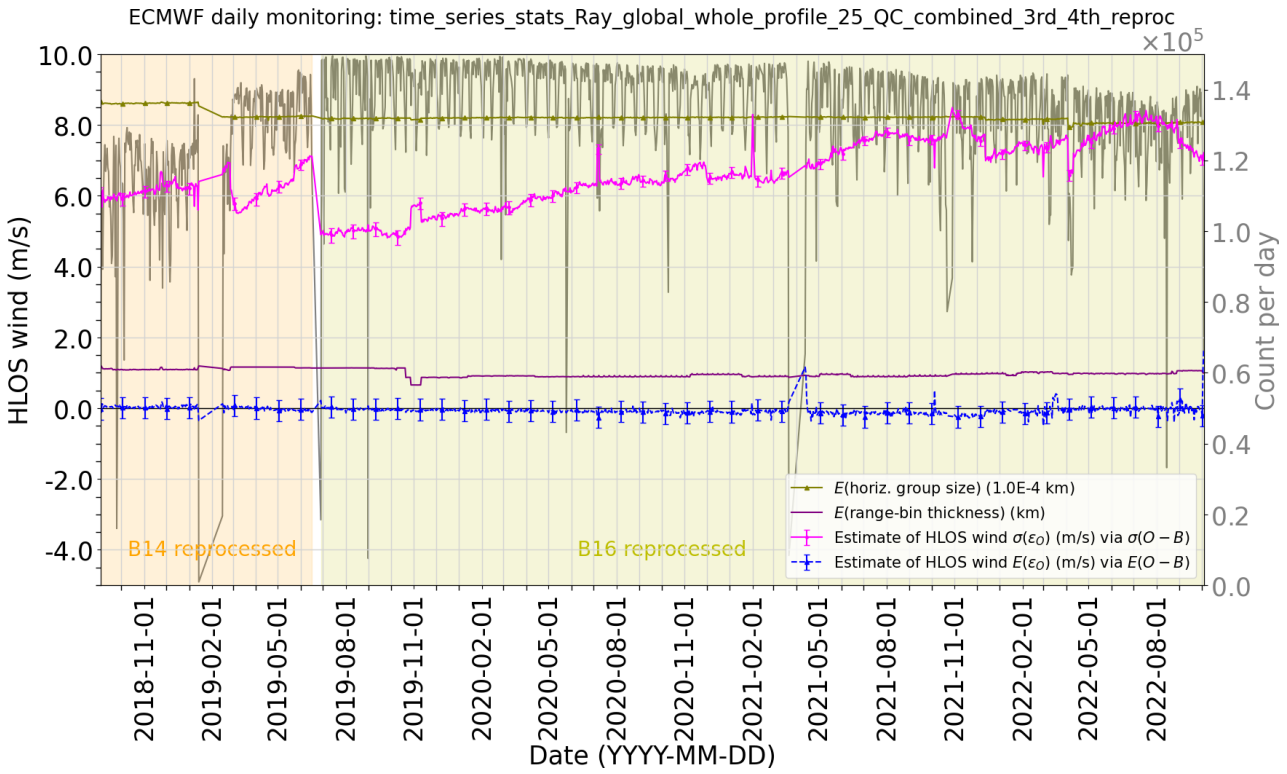

Figure 80. Time series of L2B Rayleigh-clear daily, global and all pressure level O-B statistics from the controls of the combined third (FM-A, B14) and fourth reprocessing (FM-B, B16) (no-Aeolus control OSE runs). For the period 3 September 2018 until 4 October 2022.

Splitting the statistics into ascending and descending orbits, as in Figure 81, shows biases remain close to zero, however the ascending orbits tend to have a more slightly negative bias than descending. The random errors are rather similar.

The time-series are partitioned into free troposphere (approximately 800 to 100 hPa) and the lower stratosphere (< 100 hPa) in Figure 82. The winds are significantly noisier in the lower stratosphere compared to the free troposphere, due to the expected reduction in clear air attenuated backscatter with altitude, with random errors approaching 10 ms^{-1} in 2021-2022. Random errors were ~4.2 ms^{-1} in the free troposphere in July to October 2019, which is slightly better than what was achieved in September-October 2018 for FM-A, despite the range-bins being a bit thicker (reducing counting noise) for FM-A.

In the lower stratosphere the random errors were at best ~5.5 ms^{-1}; 4 ms^{-1} was achieved for early FM-A due to 2 km thick range-bins compared to the 1.5 km thick range-bins for early FM-B. The bias in the free troposphere is close to zero, but was more unstable in the lower stratosphere, becoming negatively biased by -1.5 ms^{-1} after the FM-B laser was switched-on again in April 2021 (however the size of the bias is rather small relative to the noise). These biases perhaps have a relation to the very low useful signal levels e.g. stronger influence of imperfect dark current corrections or imperfect solar background corrections, or perhaps Rayleigh-response QC thresholds when very noisy. Improvements in laser energy and N/P settings (smaller N i.e. larger measurement-scale) may have mitigated this in 2022.

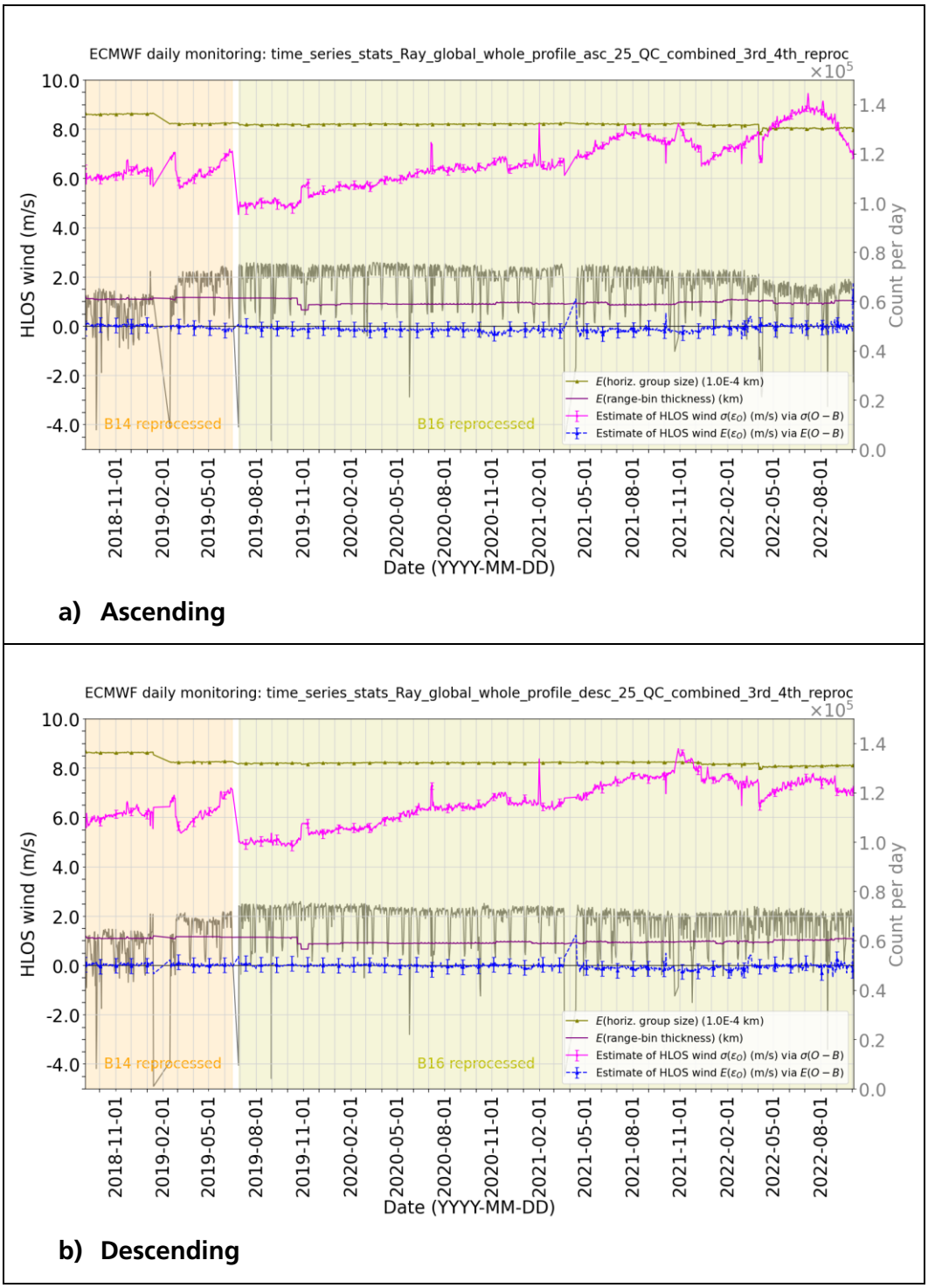

Figure 81. Time series of L2B Rayleigh-clear daily, global and all pressure level O-B statistics from the controls of the combined third (FM-A, B14) and fourth reprocessing (FM-B, B16) (no-Aeolus control OSE runs) for a) ascending and b) descending orbits. For the period 3 September 2018 until 4 October 2022.

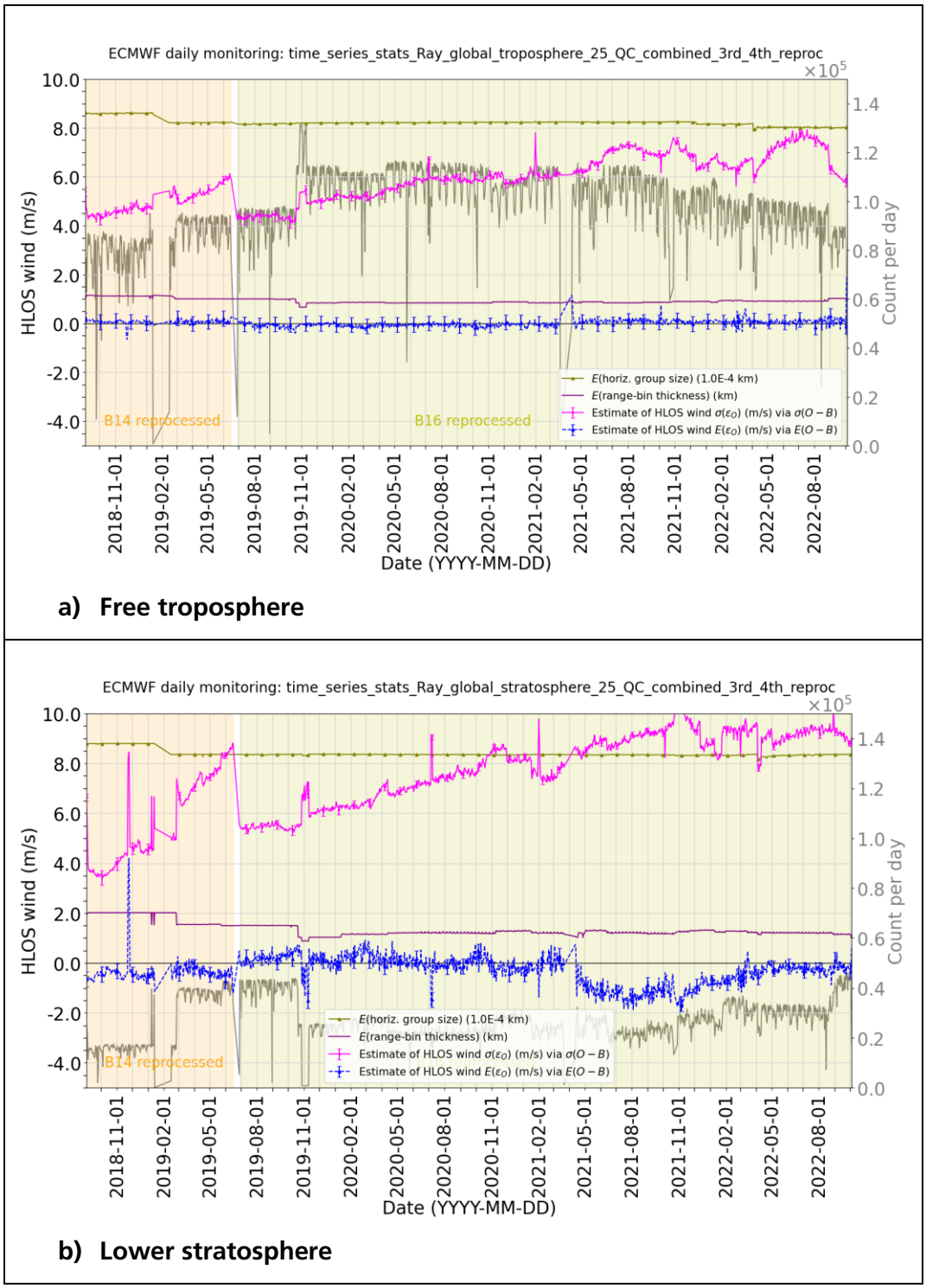

Figure 82. Time series of L2B Rayleigh-clear daily, global and all pressure level O-B statistics from the controls of the combined third (FM-A, B14) and fourth reprocessing (FM-B, B16) (no-Aeolus control OSE runs) for a) the free troposphere and b) the lower stratosphere. For the period 3 September 2018 until 4 October 2022.

The time-series are partitioned into Northern Hemisphere extratropics (> 30 degrees latitude), tropics (within ±30 degrees latitude) and Southern Hemisphere extratropics (<-30 degrees latitude) in Figure 83. The random errors increase in a more monotonic fashion in the tropics compared to the extratropics, due to much reduced seasonally varying solar background noise in the tropics compared to the extratropics. The improvements in noise due to changes in N/P settings (fewer measurements per BRC) in December 2021 and April 2022 are evident (by reducing the number of read-outs and the noise associated with that process). The Rayleigh-clear upper-level winds are very sensitive to solar background noise, particularly as the useful signal level decreased, which is why the NH extratropics has noticeably large noise increases in boreal summer. The asymmetry in satellite pointing means that solar background noise is greater over the northern polar regions compared to southern polar regions. There is a greater tendency to negative bias over the SH extratropics in 2020 and 2021, whereas elsewhere the biases are close to zero.

NH extratropics	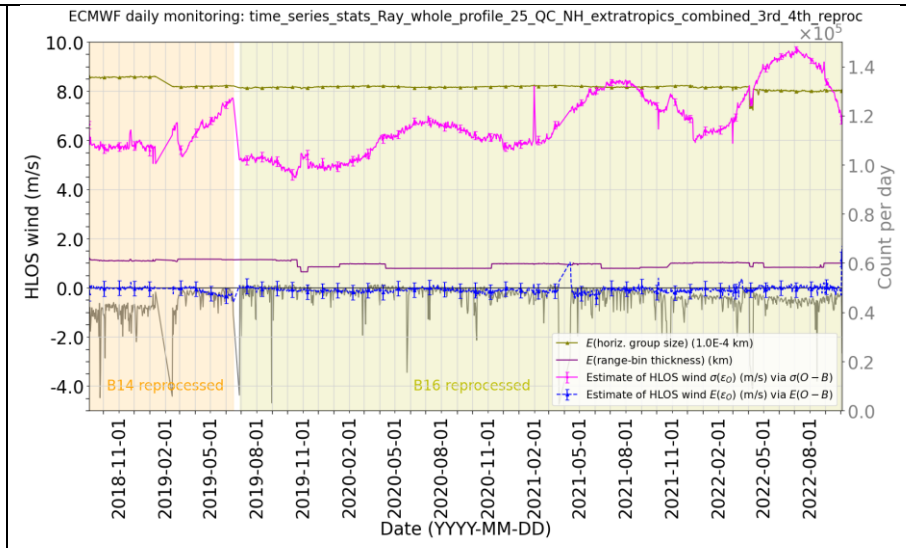
Tropics	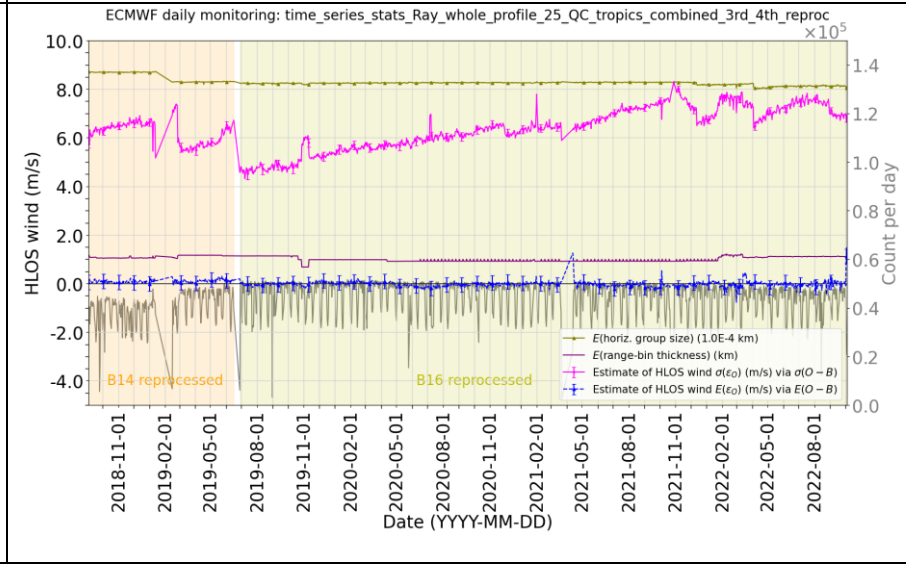

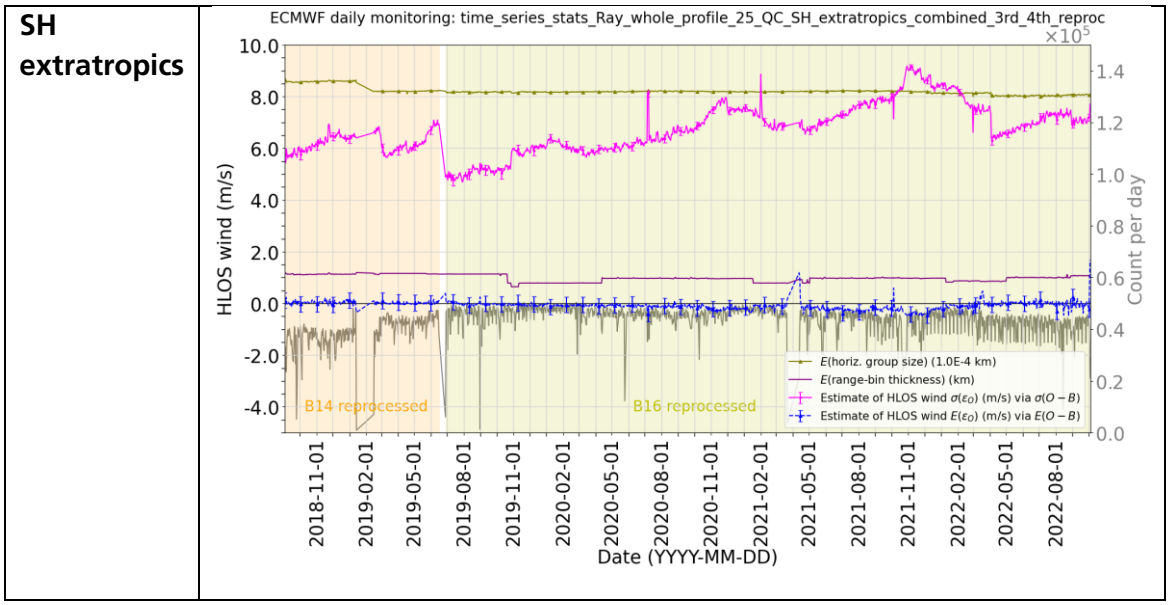

Figure 83. Time series of L2B Rayleigh-clear daily, global level O-B statistics from the controls of the combined third (FM-A, B14) and fourth reprocessing (FM-B, B16) (no-Aeolus control OSE runs) for a) NH extratropics and b) Tropics and c) SH extratropics. For the period 3 September 2018 until 4 October 2022.

Vertical profiles of L2B Rayleigh-clear departure statistics (versus pressure, with pressure bins chosen to roughly linear with altitude) are shown in Figure 84, for a selection of areas, for the early part of the 4th reprocessing period. The bias varying with height (or pressure), as already discussed with Figure 50, is evident. The bias is stronger in the tropics. Random errors are smallest in the tropical troposphere with stdev(O-B) at ~4.5 ms^{-1} (so estimated observation error ~4 ms^{-1}). As usual the random errors are largest near the surface (due to attenuation by the atmosphere) and at upper levels due to the smaller backscatter with lower density.

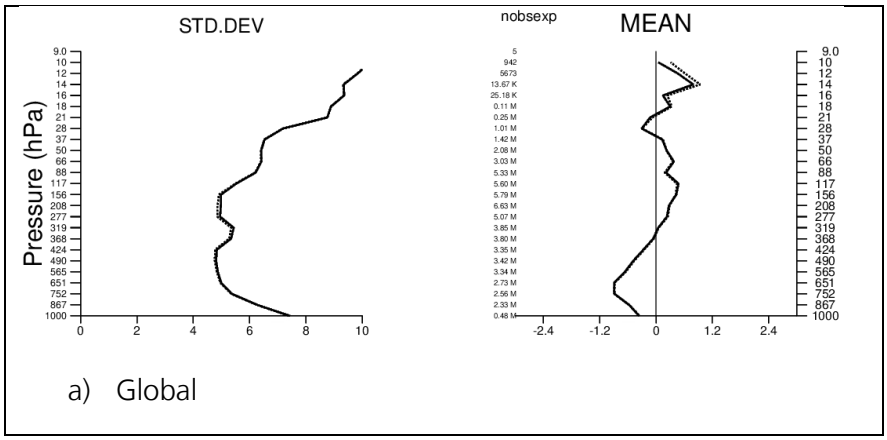

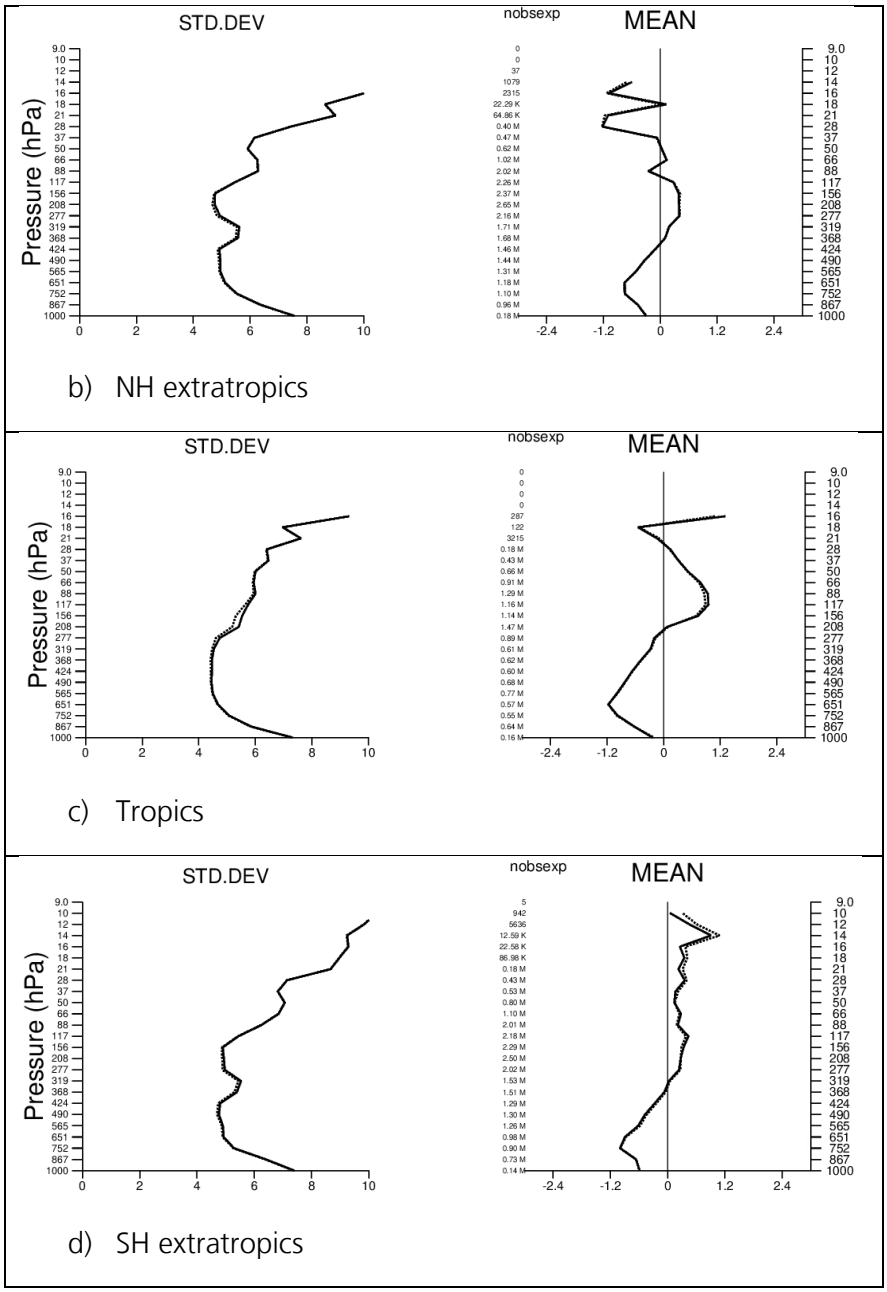

Figure 84. L2B Rayleigh-clear HLOS wind O-B (solid line) and O-A (dashed line) departure statistics (m/s) as a function of pressure; standard deviation on the left and mean on the right. Data counts are printed (nobsexp) in the middle. The pressure bins are roughly linear with altitude going from surface to ~30 km. Data from the 4th (B16) reprocessing from 28 June 2019 to 9 October 2020.

A comparison of the global L2B Rayleigh-clear departure statistics for assimilated data for the 1st, 2nd and 4th reprocessing for a period when all reprocessing campaigns have data (29 June to 31 December 2019) is shown in Figure 85. This shows some improvement in the standard deviation of O-B (and O-A) with the 4th reprocessing compared to the previous rounds. However, the bias variation with height (pressure) is a bit larger with the 4th reprocessing and the data counts is reduced in the mid-troposphere – perhaps due to better gross error removal.

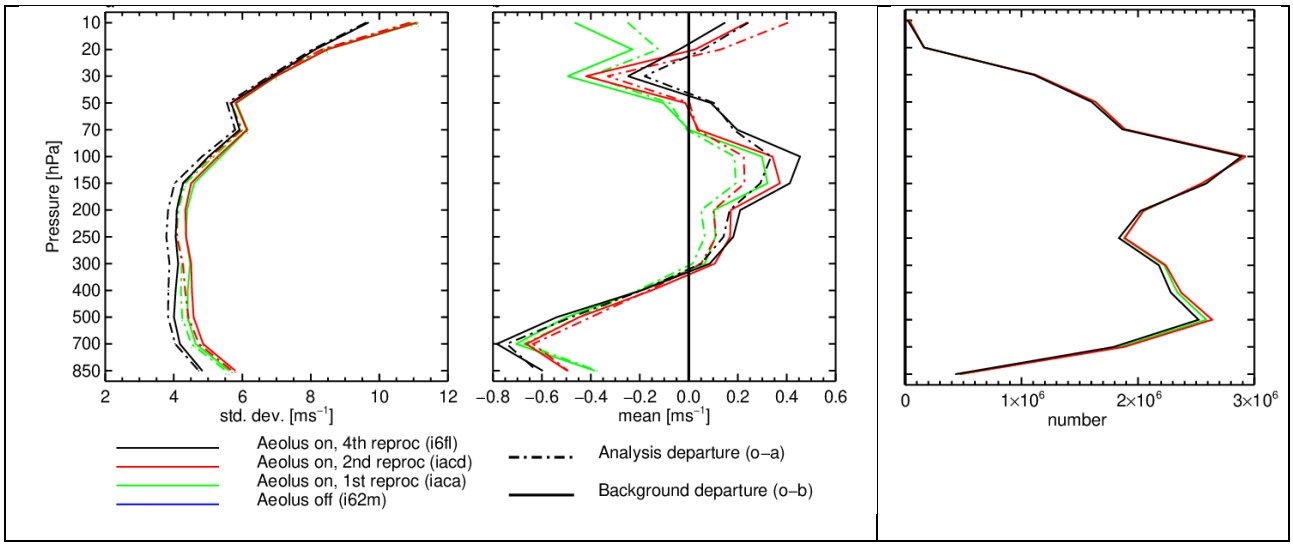

Figure 85. Global L2B Rayleigh-clear O-B statistics from 29 June until 31 December 2019 from the 1st, 2nd and 4th reprocessing.

The relationship between the L2B Rayleigh-clear and the background forecast HLOS wind is shown as 2D histograms in Figure 86, for the early part of the 4th reprocessing. This generally shows the reasonable linear relationship between the observed and modelled HLOS wind. However, there is some evidence of the pdf being "trimmed" by the applied QC of 25 ms^{-1} in abs(O-B), given the lack of low counts (blue) around the 0 ms^{-1} HLOS range. Globally, the range of L2B HLOS winds is from -120.0 to 116.1 ms^{-1}, but in the tropics, it is more restricted, from -76.2 to 74.2 ms^{-1}, as is typically seen.

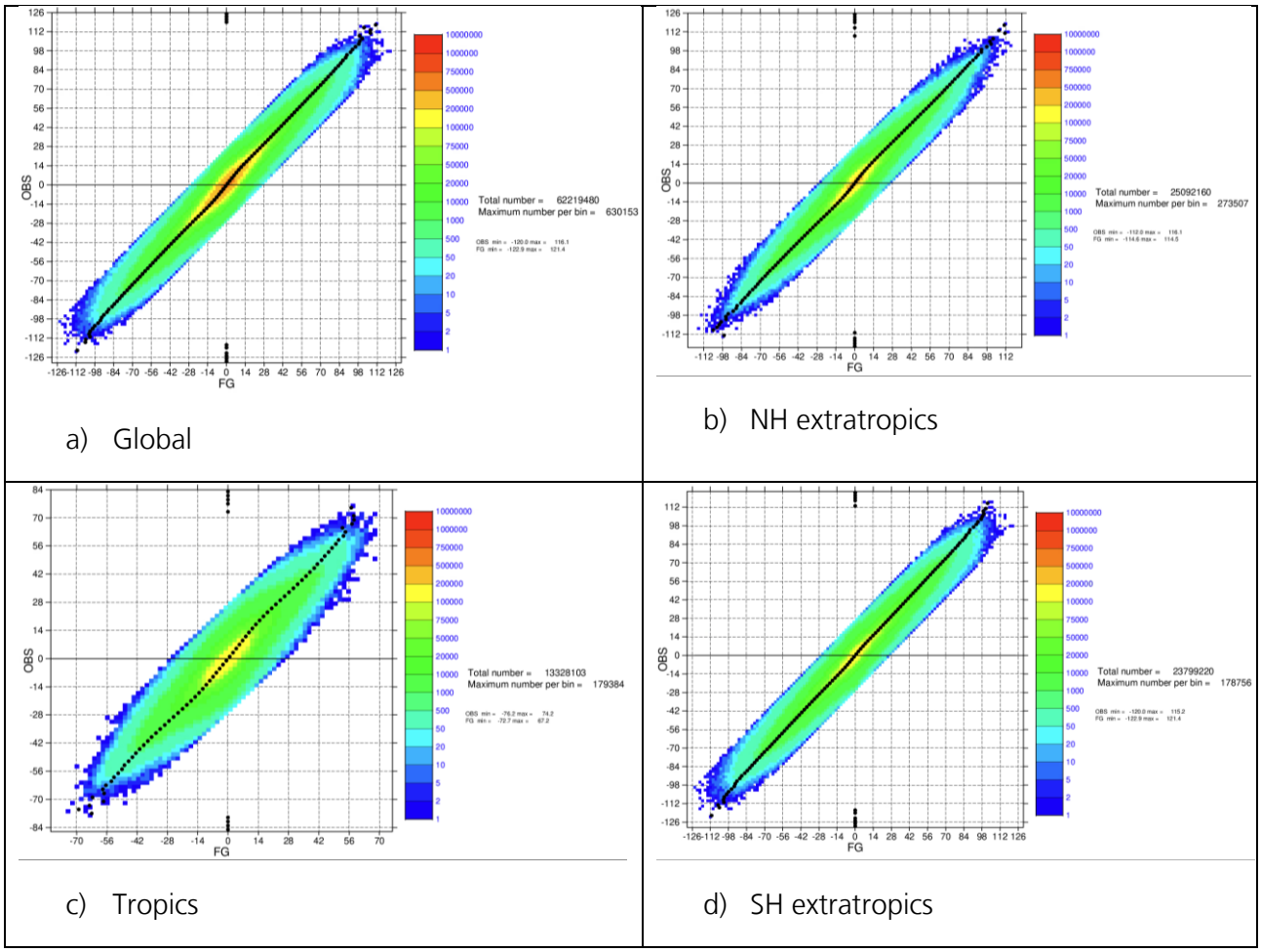

Figure 86. L2B Rayleigh-clear HLOS wind (OBS) versus background (FG) 2D histogram for different areas. Units in m/s. Data from the 4th (B16) reprocessing from 28 June 2019 to 9 October 2020.

The plots of Figure 87 and Figure 88 show the dependence of the mean(O-B) on the B HLOS wind. We expect a negative slope with linear fit of about -0.02 for a 2 ms^{-1} background HLOS wind 1-sigma error i.e. apparent bias of ∓ 2 ms^{-1} at ± 100 ms^{-1} HLOS wind. Therefore the 4th reprocessing does have the expected sign unlike the 1st and 2nd reprocessing, and so is an improvement. It also has a reasonable magnitude of slope given various uncertainties.

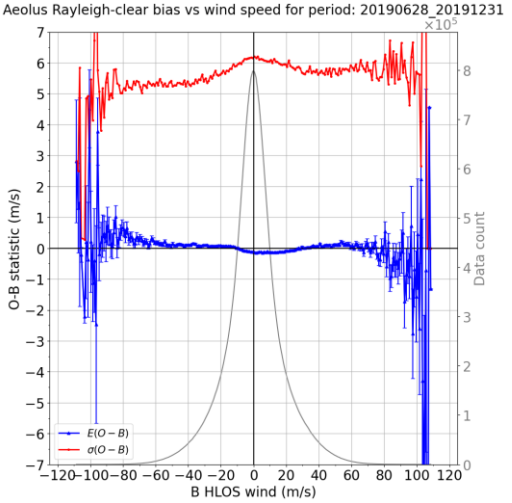

a) 1st reprocessing (B10)

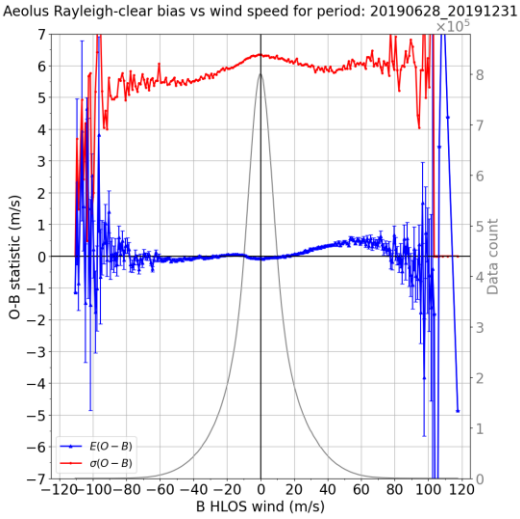

b) 2nd reprocessing (B11)

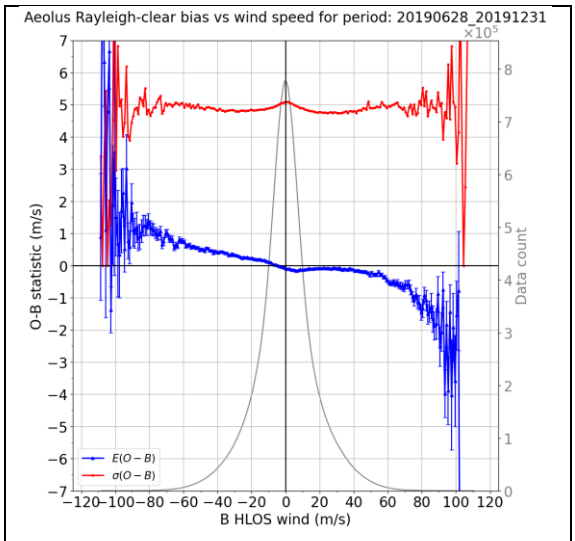

c) 4th reprocessing (B16)

Figure 87. Comparison of the wind speed dependence to the L2B Rayleigh-clear bias for the period 29 June 2019 to 31 December 2019 for different reprocessing campaigns: a) 1st reprocessing (B10), b) 2nd reprocessing (B11) and c) 4th reprocessing (B12). This period is chosen for the availability of all three reprocessed datasets.

Figure 88 shows the variations in the wind-speed dependent bias for Rayleigh-clear winds for a selection of periods of the 4th reprocessing. The shape of bias is reasonably stable until 2022, when it diverges from the expected slope to have almost zero slope (reason unknown).

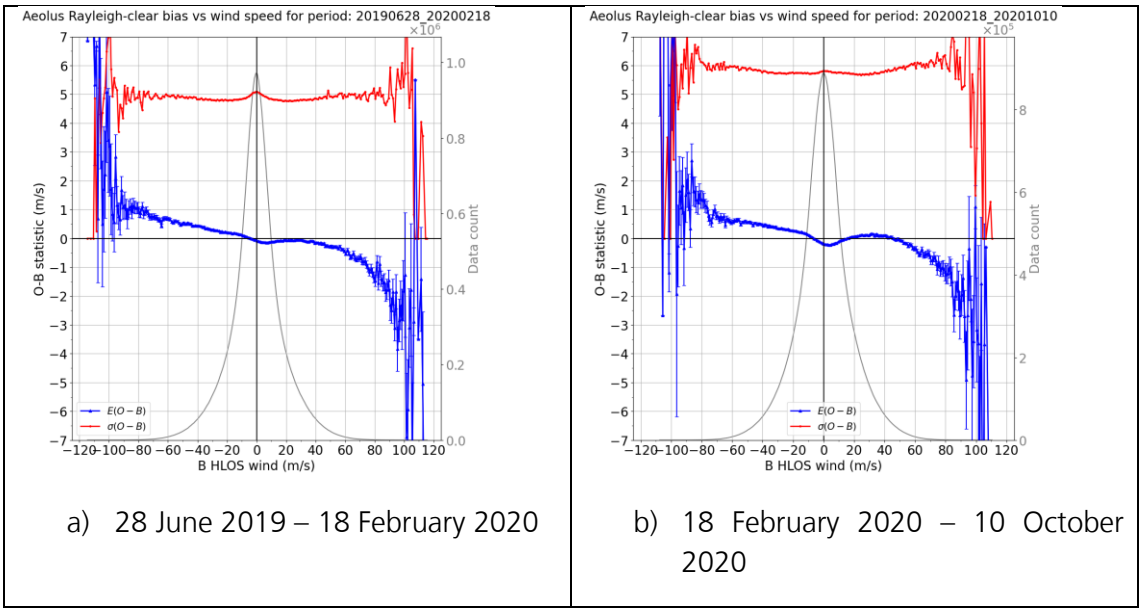

a) 28 June 2019 – 18 February 2020

b) 18 February 2020 – 10 October 2020

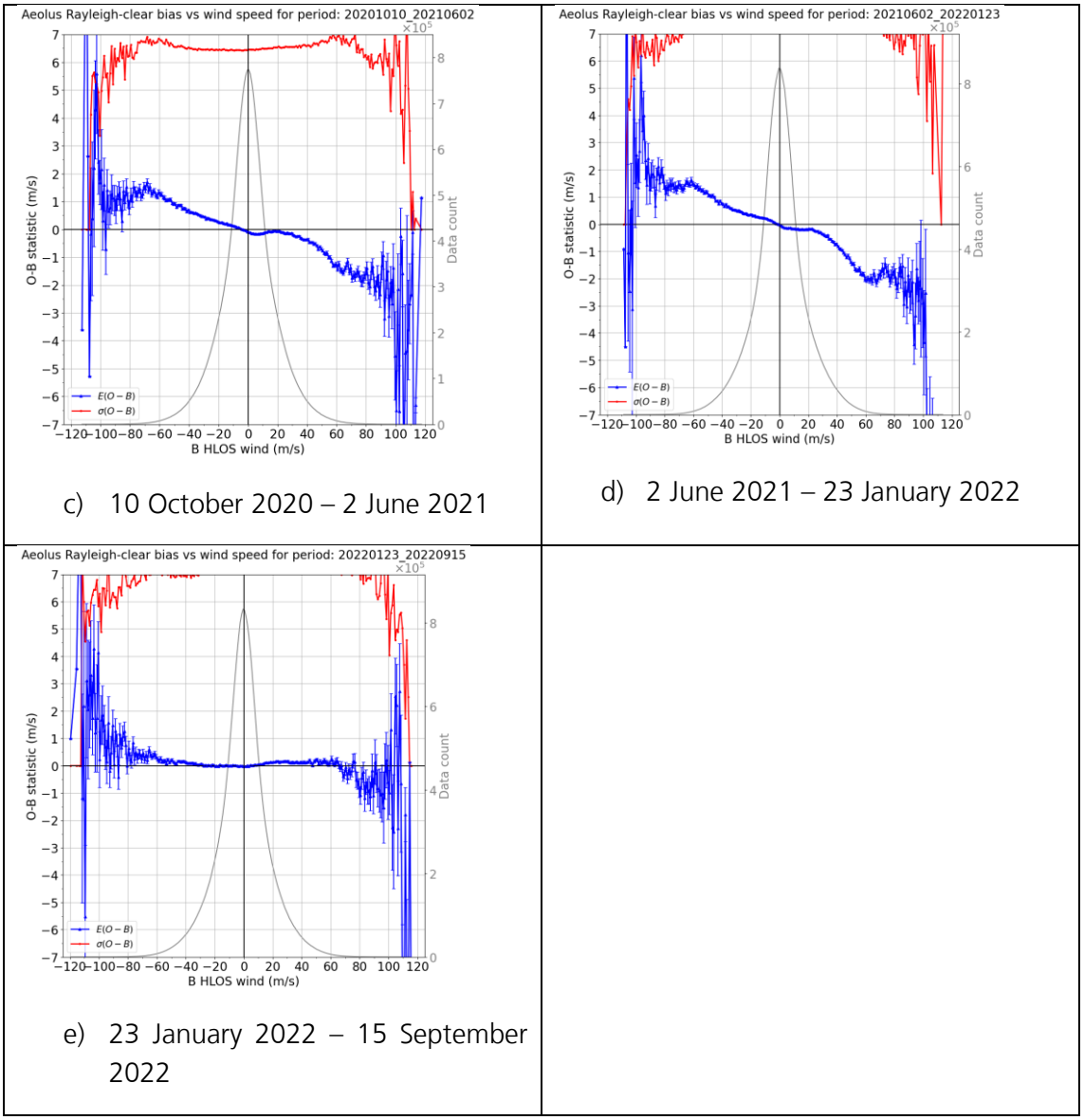

c) 10 October 2020 – 2 June 2021

d) 2 June 2021 – 23 January 2022

e) 23 January 2022 – 15 September 2022

Figure 88. Wind speed dependence to the L2B Rayleigh-clear bias for 235-day periods of the 4th reprocessing campaign (B16).

The following figures show statistics as a function of pressure and time. The pressure bins are chosen to be roughly linear in altitude so the y-axis can be thought as roughly being from surface to 30 km (~10 hPa) altitude.

Changes in range-bin settings for the Rayleigh winds are evident in the pressure-time data count plot of Figure 89 a); the most extreme example of which was from 28 October to 10 November 2019 due to the AMV range-bin settings. This was followed in November 2019 with an increase in vertical resolution for the mid to upper troposphere, hence the data counts increased there, focusing on regions where Aeolus gave largest NWP impact. Consequently, this reduced the number of Rayleigh winds in the lower stratosphere and lower troposphere due to the 24 range-bin limit.

There is a general tendency from negative HLOS winds (easterlies for ascending orbits) near the surface to positive HLOS winds (westerlies for ascending orbits) from ~400-70 hPa is seen in Figure 89 b). Higher still, there are striking periods of strong westerlies resulting from the deliberate sampling of the winter Polar Vortex and a negative period in early 2022 due to range-bins capturing the tropical lower stratosphere for the benefit of sampling the Hunga-Tonga eruption plume (negative phase of QBO).

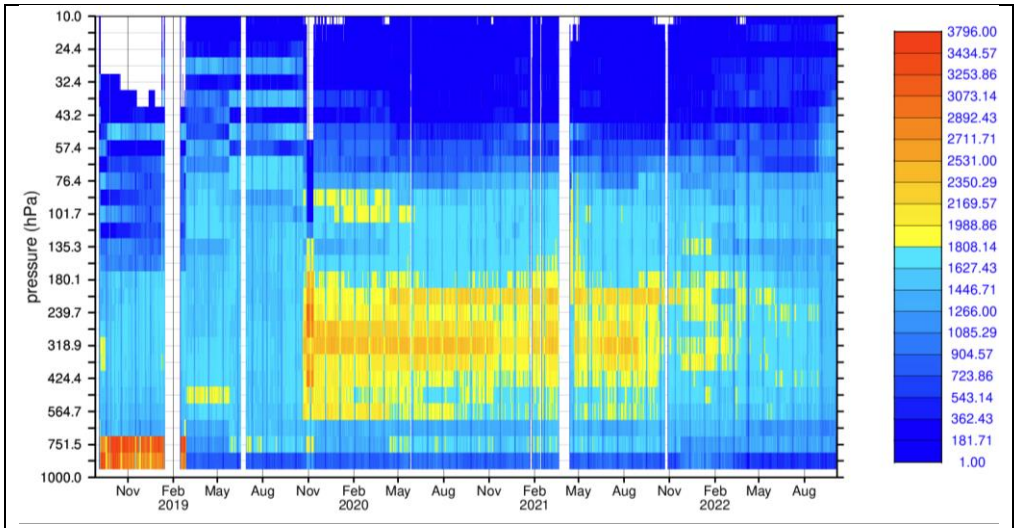

a) Data count, ascending

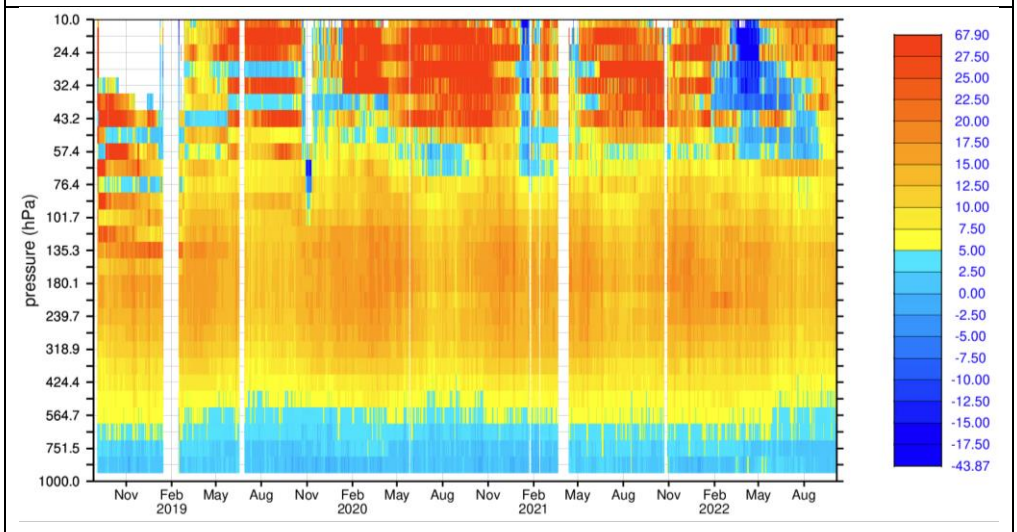

b) Mean observed HLOS wind, ascending

Figure 89. Pressure-time plots for L2B Rayleigh-clear winds for ascending orbits of a) data counts and b) mean observed HLOS wind value (m/s), for the combined 3rd (B14) and 4th (B16) reprocessing for global data. Time-step is 12 hours.

The bias versus pressure and time is shown in Figure 90 for ascending and descending orbits. The negative bias at lower altitudes (~> 400 hPa) and positive bias above is particularly strong from July 2019 to March 2021 (as also discussed in association with Figure 50) and then there is abrupt change

after the FM-B laser switch on in April 2021 onwards, due to the application of a new and presumably more accurate AUX_RBC_L2 file. Biases tend to be more negative at the very highest altitudes for ascending and positive for descending orbits. As already discussed, this is thought to be related to low signal levels and imperfections in corrections e.g. solar background, dark current or RR QC.

There is a negative bias at around 70-100 hPa in both ascending and descending orbits from around November 2019 onwards, which is probably due to a hot-pixel in one of the upper range-bins. The bias jumps in pressure due to changes in range-bin settings during the mission.

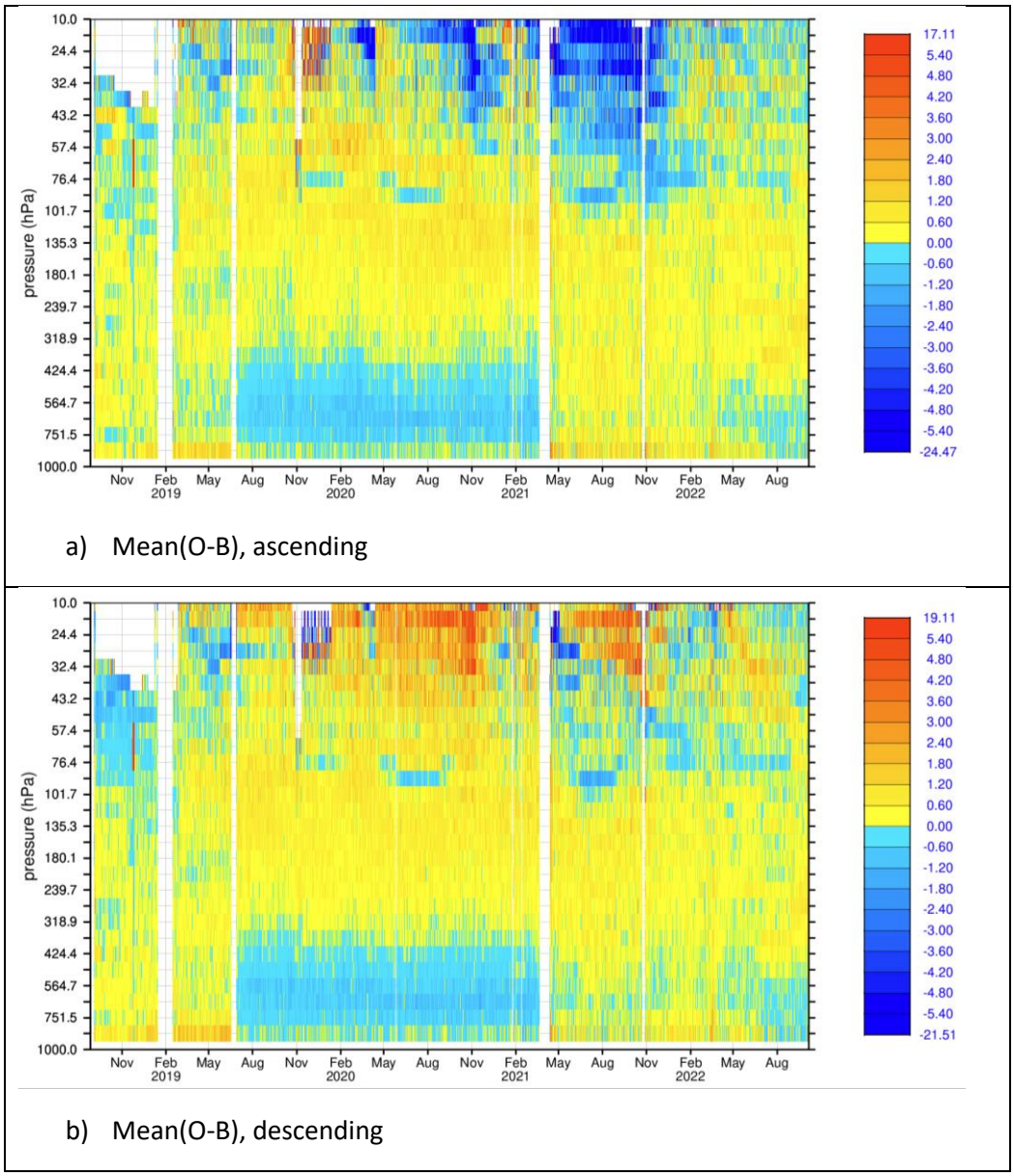

Figure 90. Pressure-time plots for L2B Rayleigh-clear winds of mean(O-B) (m/s) for a) ascending and b) descending orbits for the combined 3rd (B14) and 4th (B16) reprocessing for global data. Time-step is 12 hours.

The variation of the L2B Rayleigh-clear wind bias with atmospheric temperature is shown in Figure 91. Imperfections in the Rayleigh-Brillouin look-up table as a function of temperature may account for the bias varying with altitude. There is an apparent increased dependence of bias on temperature in the period of the first AUX_RBC_L2 file compared to the second period (after re-switch-on of FM-B laser when a new calibration file was used), which would agree with the hypothesis.

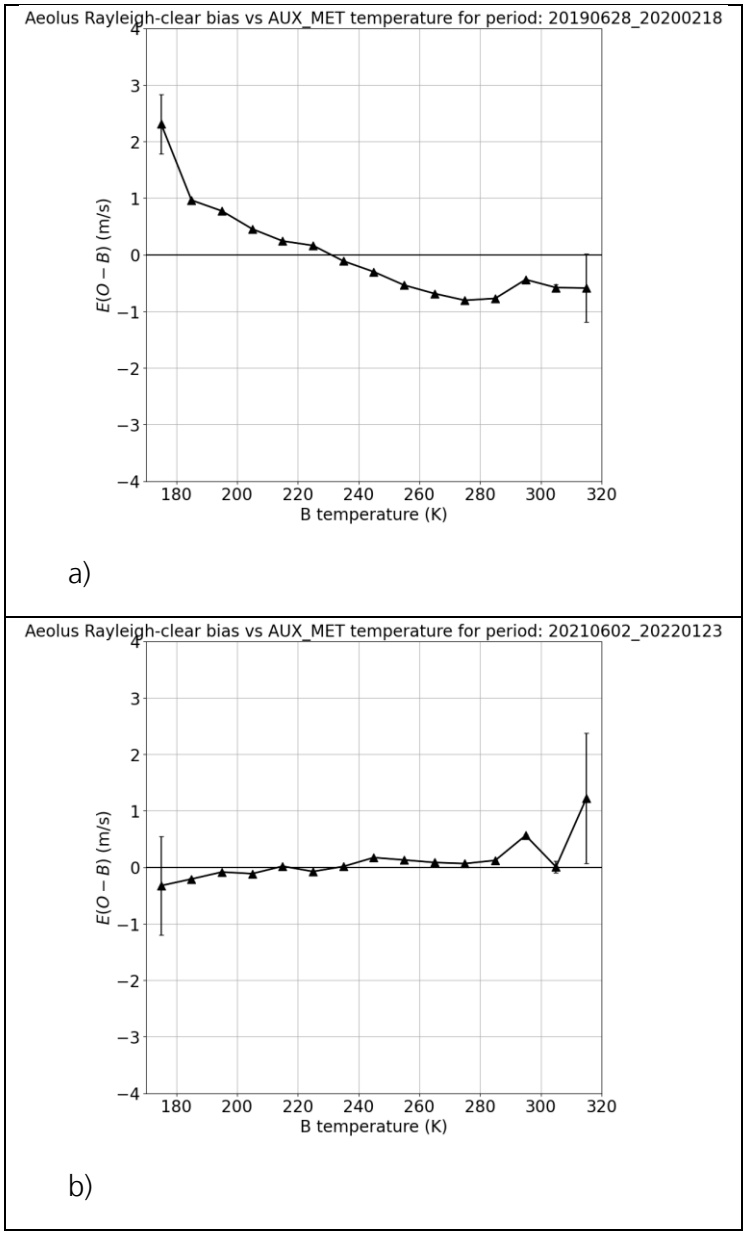

Figure 91. Dependence of L2B Rayleigh-clear mean(O-B) on atmospheric temperature (via AUX_MET) for a) 28 June 2019 to 18 February 2020 and b) 2 June 2021 to 23 January 2022. The two periods (before and after switch-off and recalibration) used different AUX_RBC_L2 (Rayleigh-Brillouin look-up table) files.

The large increase in HLOS wind noise with time, particularly for upper levels, is evident for the FM-B B16 reprocessing in Figure 92. The pattern is similar for ascending and descending orbits. The FM-

A B14 reprocessing from September 2018 to January 2019 (during the Commissioning Phase) had very thin (250 m) range-bins below ~2 km altitude, and relatively thick (1-2 km) range-bins for the troposphere and stratosphere, hence the pattern of large noise near surface and much improved noise above.

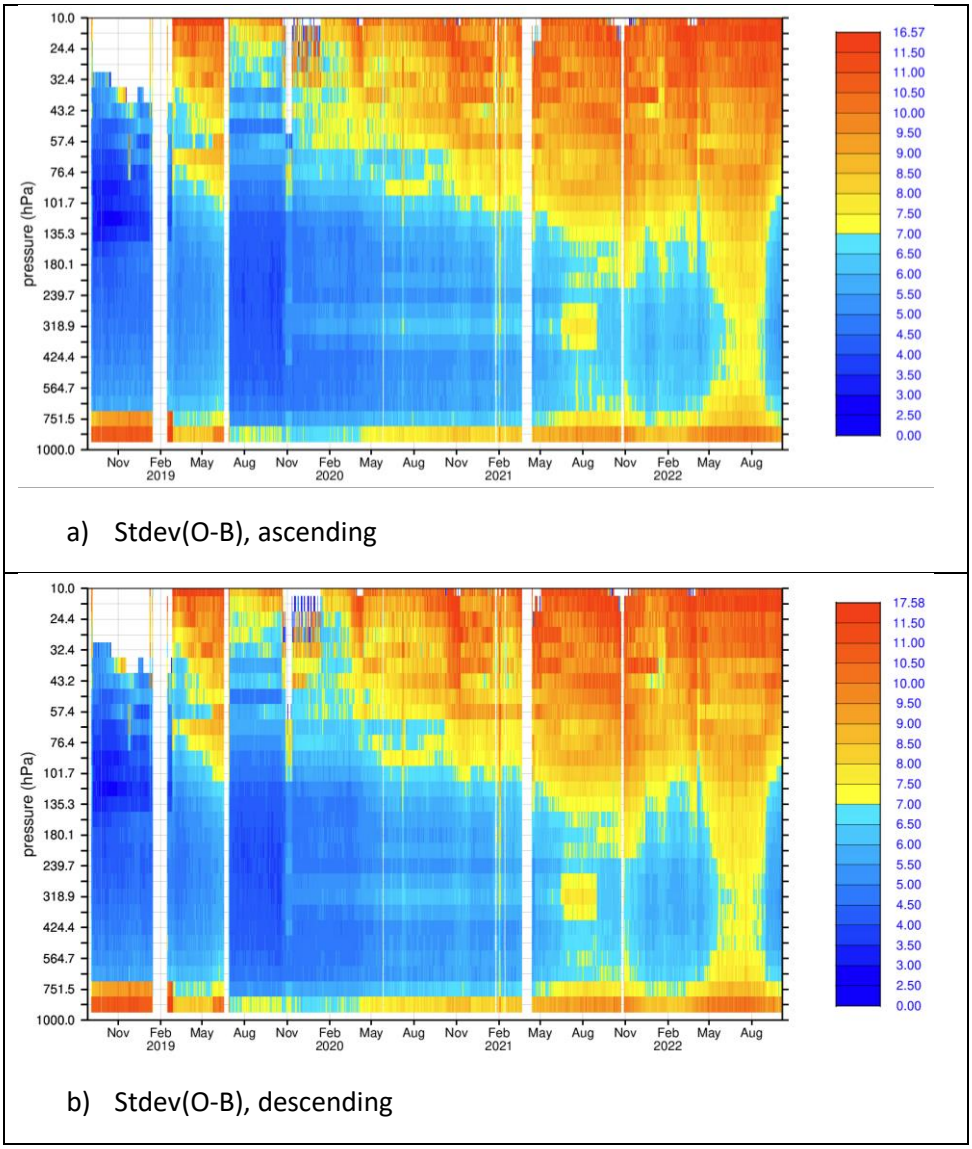

Figure 92. Pressure-time plots for L2B Rayleigh-clear winds of standard deviation(O-B) (m/s) for a) ascending and b) descending orbits for the combined 3rd (B14) and 4th (B16) reprocessing for global data. Time-step is 12 hours.

Zonal average plots are provided in Figure 93 to Figure 95 for the early part of the 4th reprocessing. The data counts increase towards the poles, as expected due to the polar orbit. Most of the Rayleigh-clear winds are provided outside the tropics at around 300 hPa (~9 km). The zonal average (ascending orbit) HLOS wind plot shows the strongest westerlies to occur in the SH extratropics jet streams (subtropical and polar) and the Polar Vortex. The dominance of easterlies in the tropics is evident.

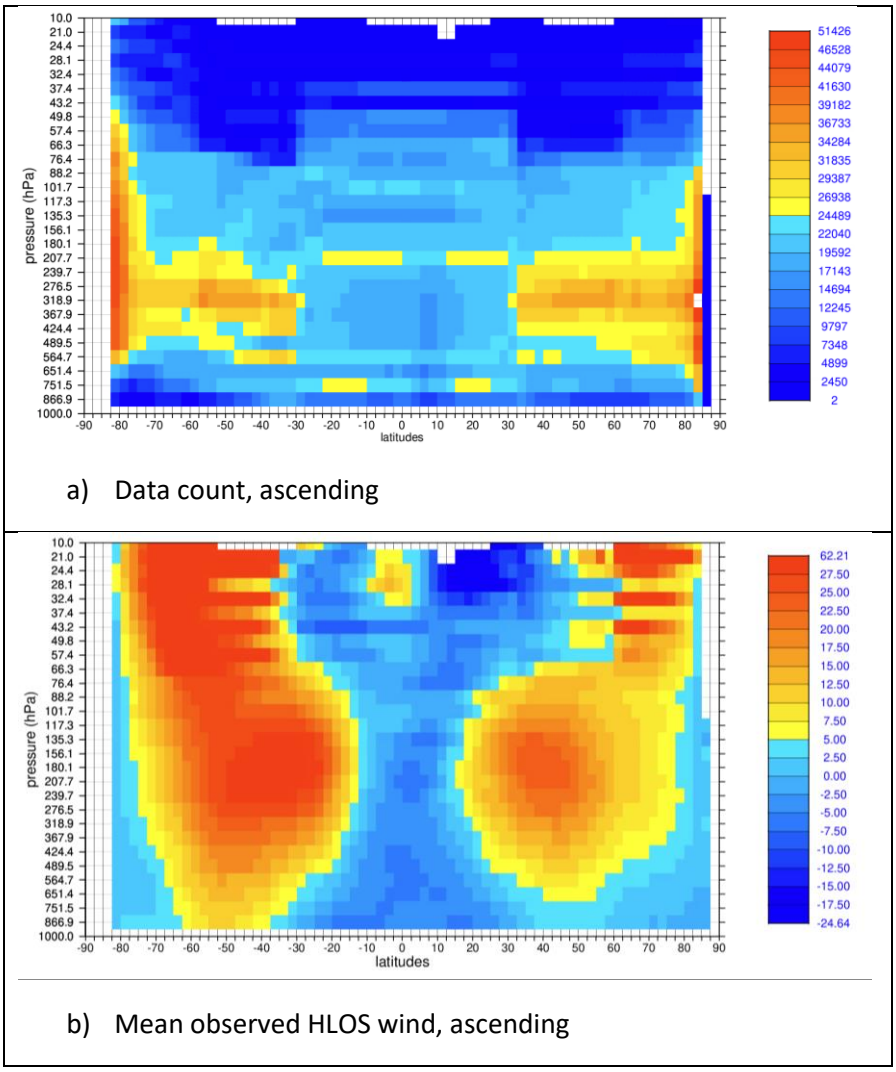

Figure 93. Zonal average plots for L2B Rayleigh-clear winds for ascending orbits of a) data counts and b) mean observed HLOS wind value (m/s), for the 4th (B16) reprocessing from 28 June 2019 to 9 October 2020.

In Figure 94, the troposphere shows negative bias from surface to about 300 hPa and positive bias above. This bias pattern is strongest at the equator – possibly due to the strongest temperature lapse rates there (and likely link of the bias to errors in temperature-dependence of the Rayleigh-Brillouin calibration tables). The bias pattern is reasonably similar for ascending and descending orbits. But with exceptions of dipole-like bias at the equator at ~30-60 hPa, which changes sign for ascending and descending and may well be a model bias due to lack of vertical wind shear; tendency to negative (positive) bias over South Polar regions for ascending (descending) orbits is seen – the cause of this is not yet understood.

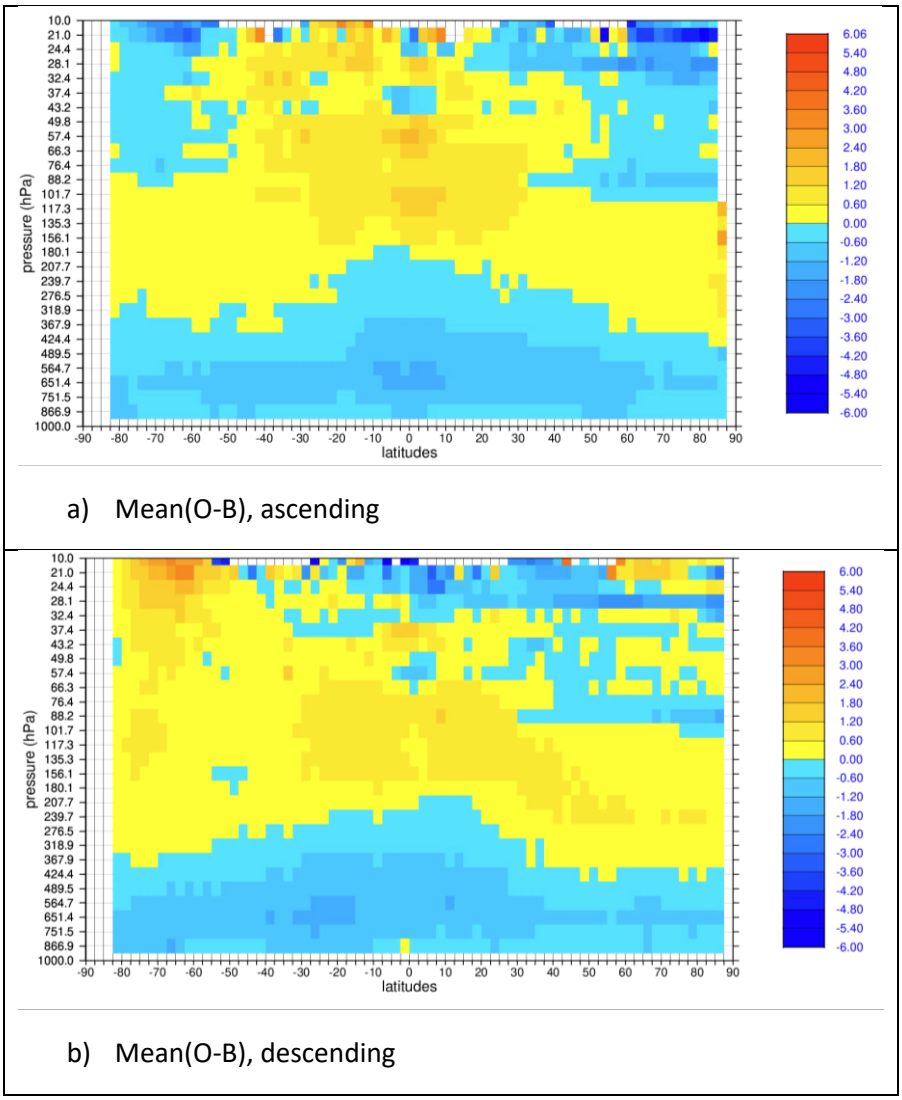

Figure 94. Zonal average plots for L2B Rayleigh-clear winds of mean(O-B) (m/s) for a) ascending and b) descending orbits for the 4th (B16) reprocessing from 28 June 2019 to 9 October 2020.

The random errors look rather similar for ascending and descending orbits as shown in Figure 95. The smallest random errors occur at ±10-30 degrees latitude at ~400 hPa (7 km). As shown in Figure 69, these are areas with mostly clear skies above the boundary layer, thus allowing maximum molecular attenuated backscatter.

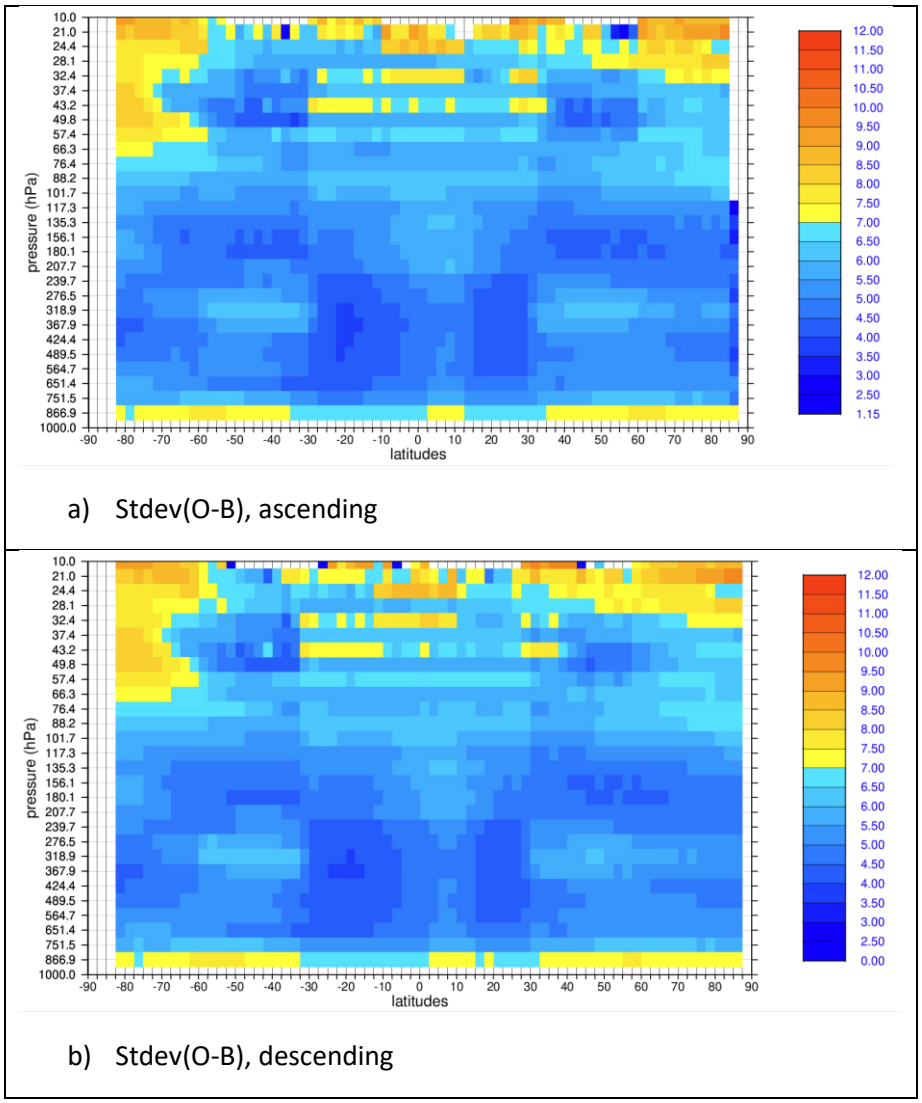

Figure 95. Zonal average plots for L2B Rayleigh-clear winds of standard deviation(O-B) (m/s) for a) ascending and b) descending orbits for the 4th (B16) reprocessing from 28 June 2019 to 9 October 2020.

The following pages focus on L2B Rayleigh-clear map and latitude-time plots for pressure-bins around ~100 hPa and ~500 hPa, due to the relatively large data counts are available at those levels[9].

The data count map plots of Figure 96 and Figure 97 show reduced data counts due for descending orbits in the SH (due to DUDEs) and perhaps a weekly calibration over the Pacific. At 500 hPa, the bias is generally slightly negative, particularly in the tropics (as discussed in the zonal average plots) and the random errors are smallest in the clear-air regions of the globe, e.g. subtropical high-pressure systems, as already discussed for the zonal average plots, and particularly large in tropical convective areas of e.g. central Africa. Bias is a bit more negative in the tropics. At 100 hPa the random errors look more

[9] Plots for all pressure ranges were produced, however it is far too many plots to include in this report.

uniform apart from slight increase towards the poles (solar background noise). Biases tend to be positive, more so in the tropics, with an area of larger positive bias in mid-Atlantic near Africa, for descending orbits, which could be ECMWF background bias.

In Figure 98, at ~500 hPa the periodic seasonal variations in ascending orbit HLOS wind (mostly zonal wind component) are evident with predominantly westerly winds in mid-latitudes and easterlies in the tropics. The westerlies are stronger and more consistent in the SH extratropics than the NH extratropics. Some of the many changes in range-bin settings (often with season) are evident in the data count plot.

In Figure 99, the data counts at ~100 hPa were particularly large in the tropics from November 2019 to April 2020 due to special range-bin settings aimed at collocations with stratospheric super pressure balloons of the Strateole-2 campaign. The data counts reduced at ~100 hPa after the Hunga-Tonga eruption (15 January 2022) due to the initial raising of the top range-bin to 30 km (~10 hPa) in the tropics, thus making the vertical sampling at ~100 hPa poorer. Seasonal variations in the mean observed HLOS wind are evident due to the Polar Vortex and QBO. The range-bins unfortunately did not go to a high enough altitude from September 2018 to February 2019 to capture the tropical 100 hPa winds.

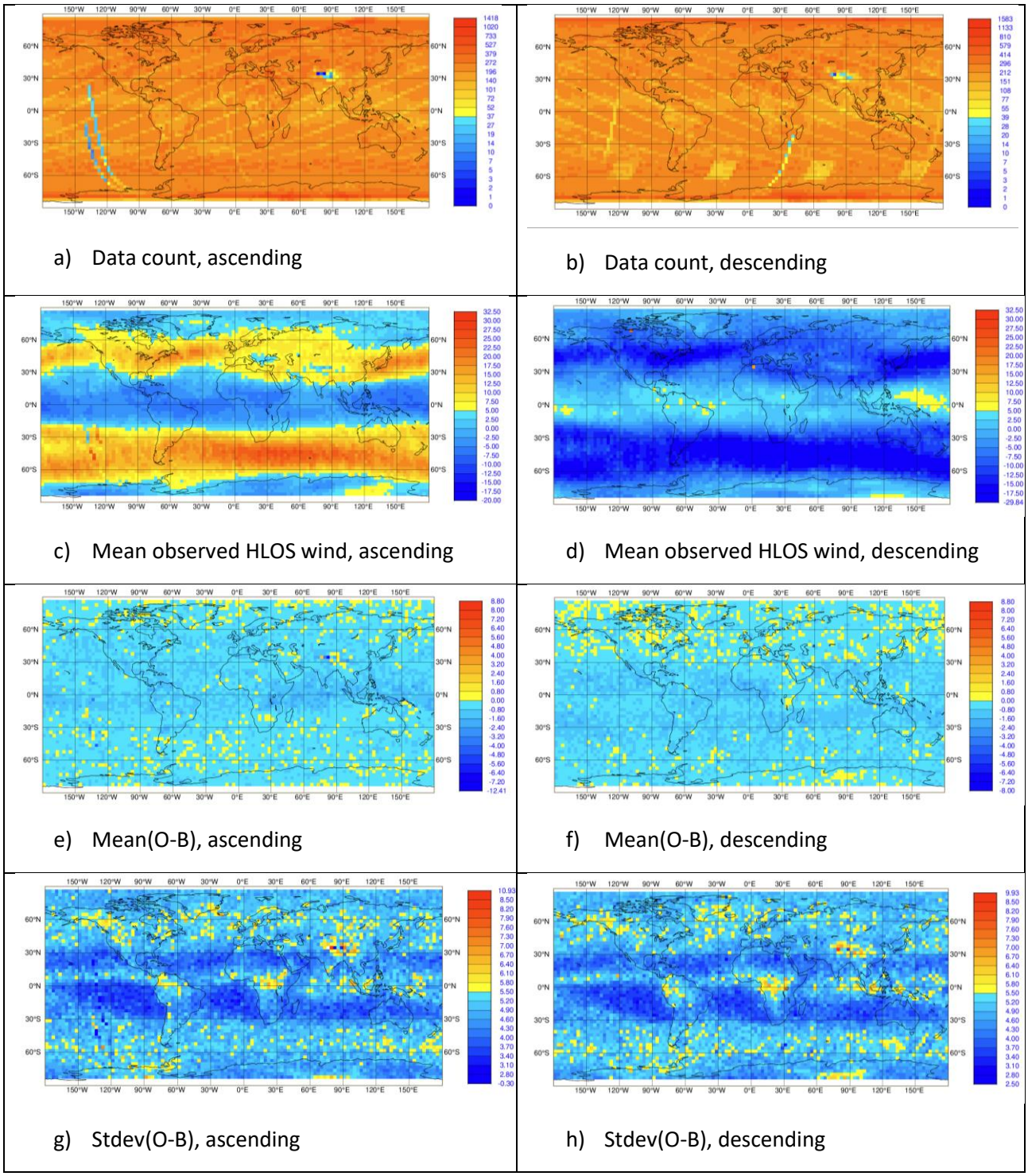

a) Data count, ascending

b) Data count, descending

c) Mean observed HLOS wind, ascending

d) Mean observed HLOS wind, descending

e) Mean(O-B), ascending

f) Mean(O-B), descending

g) Stdev(O-B), ascending

h) Stdev(O-B), descending

Figure 96. Map plots (3x3 degrees) for L2B Rayleigh-clear winds at ~500 hPa (489-565 hPa) of: data counts for the top row; mean observed HLOS wind value (m/s) for the second row; mean(O-B) (m/s) for the third row; and stdev(O-B) (m/s) for the bottom row. Using the 4th (B16) reprocessing from 28 June 2019 to 9 October 2020.

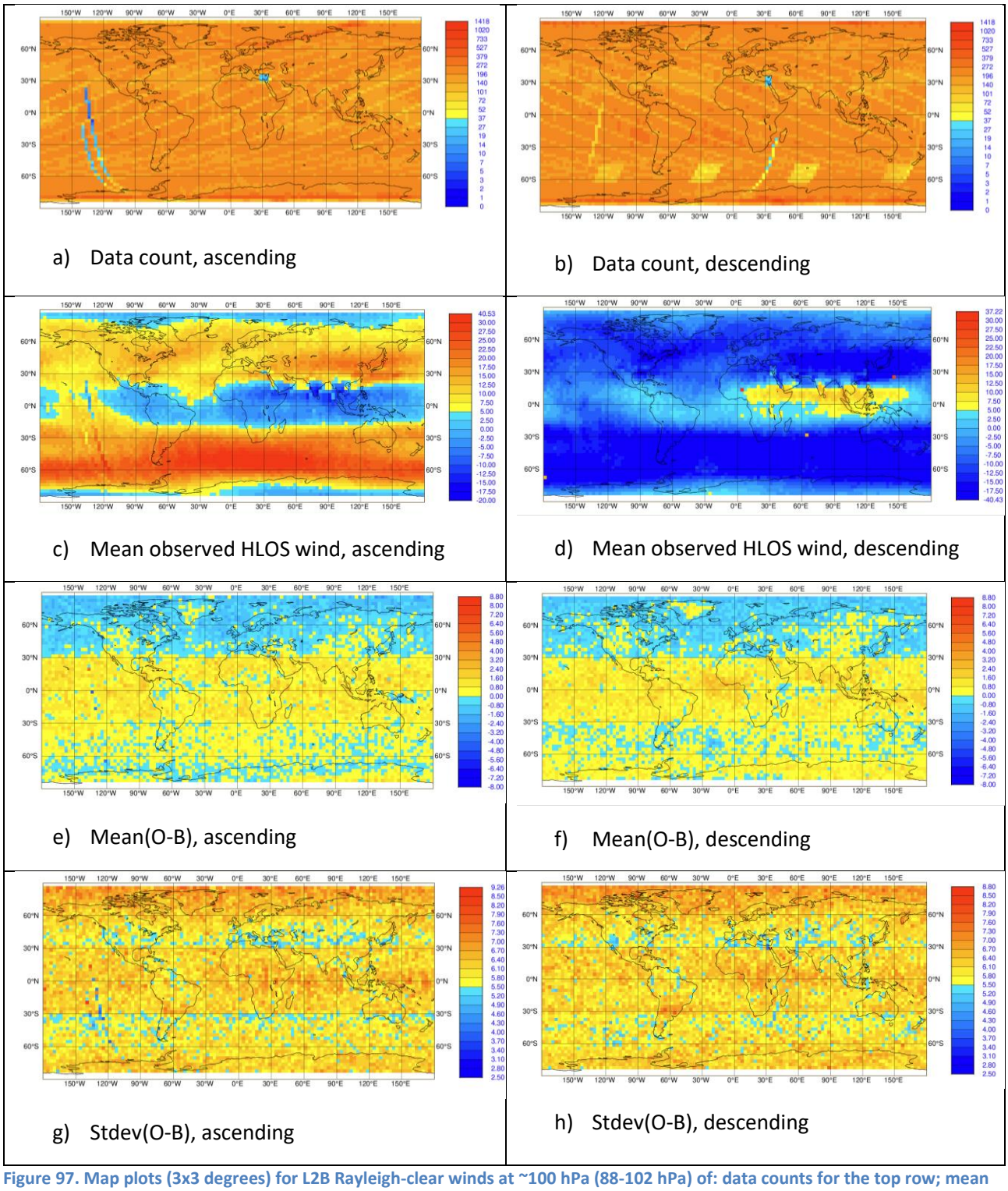

a) Data count, ascending

b) Data count, descending

c) Mean observed HLOS wind, ascending

d) Mean observed HLOS wind, descending

e) Mean(O-B), ascending

f) Mean(O-B), descending

g) Stdev(O-B), ascending

h) Stdev(O-B), descending

Figure 97. Map plots (3x3 degrees) for L2B Rayleigh-clear winds at ~100 hPa (88-102 hPa) of: data counts for the top row; mean observed HLOS wind value (m/s) for the second row; mean(O-B) (m/s) for the third row; and stdev(O-B) (m/s) for the bottom row. Using the 4th (B16) reprocessing from 28 June 2019 to 9 October 2020.

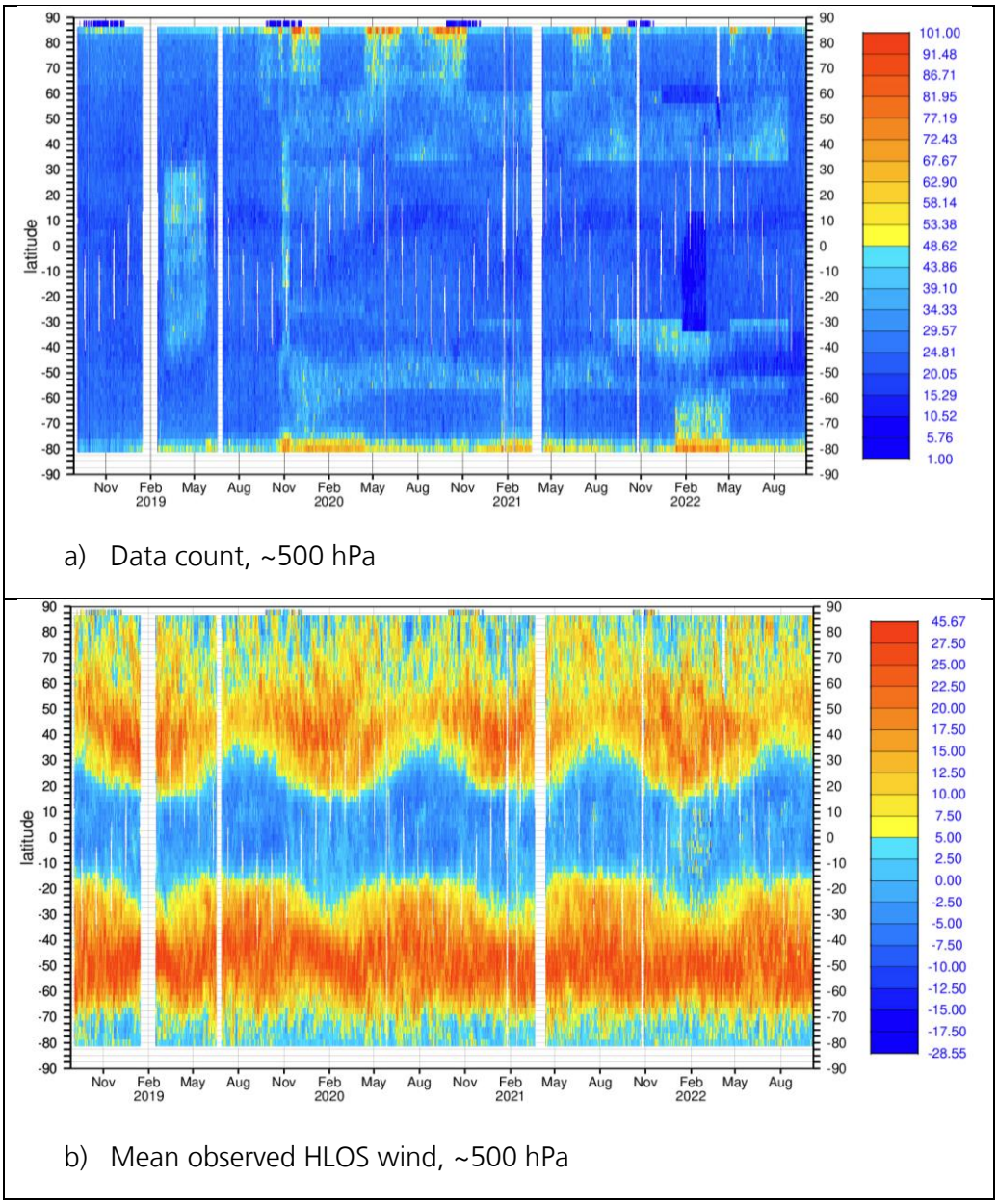

a) Data count, ~500 hPa

b) Mean observed HLOS wind, ~500 hPa

Figure 98. Latitude-time plots for L2B Rayleigh-clear winds for ascending orbits of a) data counts and b) mean observed HLOS wind value (m/s), for the combined 3rd (B14) and 4th (B16) reprocessing for the pressure range with largest data counts i.e. 489-565 hPa. Time-step is 12 hours.

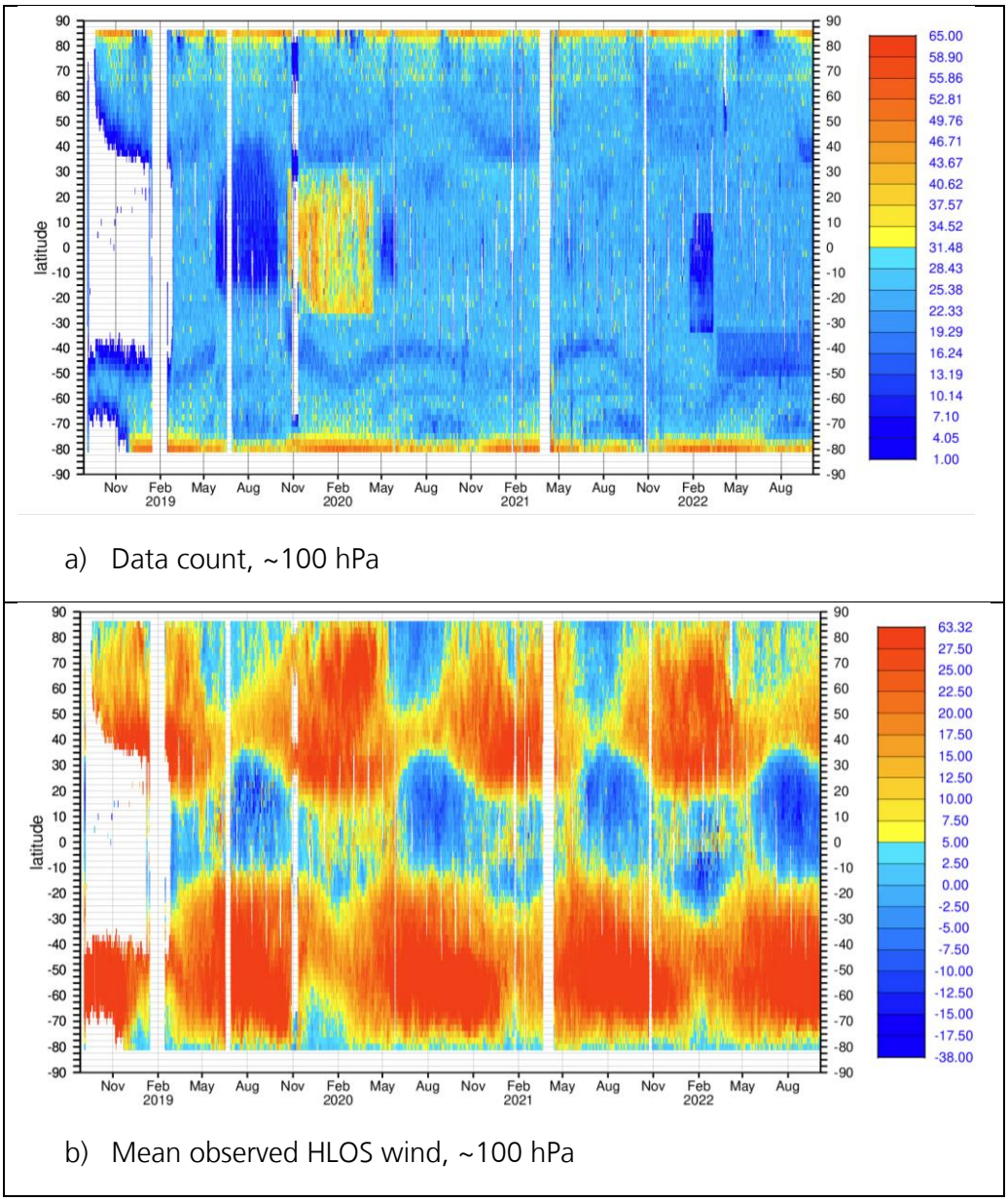

a) Data count, ~100 hPa

b) Mean observed HLOS wind, ~100 hPa

Figure 99. Latitude-time plots for L2B Rayleigh-clear winds for ascending orbits of a) data counts and b) mean observed HLOS wind value (m/s), for the combined 3rd (B14) and 4th (B16) reprocessing for the pressure range with largest data counts i.e. 88-102 hPa. Time-step is 12 hours.

In Figure 100, the bias at ~500 hPa is reasonably consistent and small for ascending and descending orbits. However, negative bias is more evident before April 2021 and the associated change in the Rayleigh-Brillouin calibration file. It appears that the M1 temperature bias correction (AUX_TEL_12) is working given the small bias variations with latitude. The Hunga-Tonga eruption led to distinct patches of degraded mean(O-B) and stdev(O-B) at ~500 hPa due to the strong attenuation of signal by the optically thick plume in the months after the eruption. This effect soon disappeared once the eruption plume dispersed as it circumnavigated the globe in the easterly lower stratospheric tropical winds.

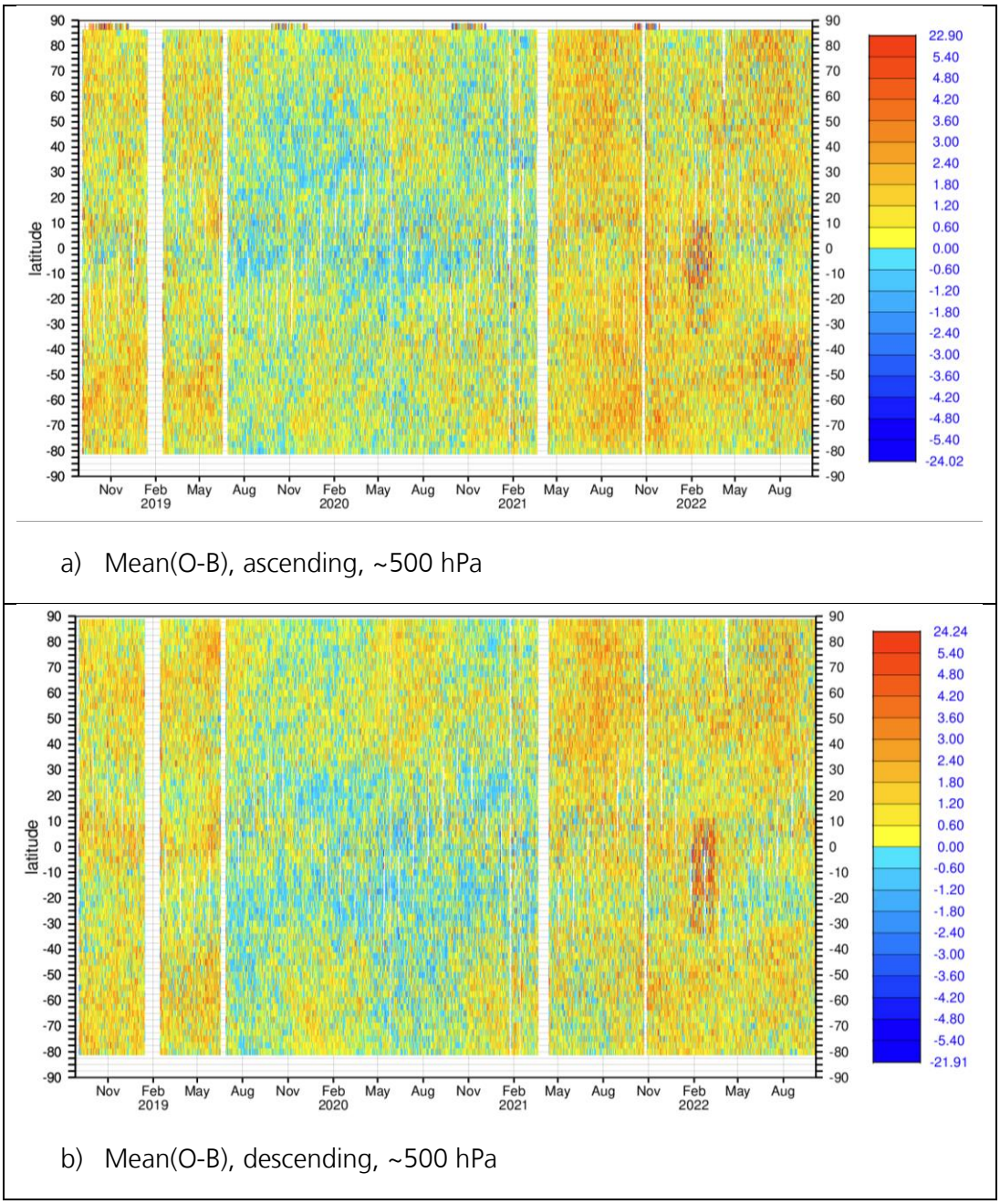

Figure 100. Latitude-time plots for L2B Rayleigh-clear winds of mean(O-B) (m/s) for a) ascending orbits and b) descending orbits, for the combined 3rd (B14) and 4th (B16) reprocessing for the pressure range with largest data counts i.e. 489-565 hPa. Time-step is 12 hours.

In Figure 101, at ~100 hPa large negative biases are evident at high latitudes, particularly for the polar summer in 2020 and 2021. *These biases are not yet fully understood* but are likely to be due to a range-bin specific bias (hot-pixel and imperfect dark current correction) which due to range-bin setting changes moves in and out of the 88-102 hPa pressure range, perhaps exacerbated by lower useful signals with time. Descending orbits tend to have more of a positive bias towards the south pole.

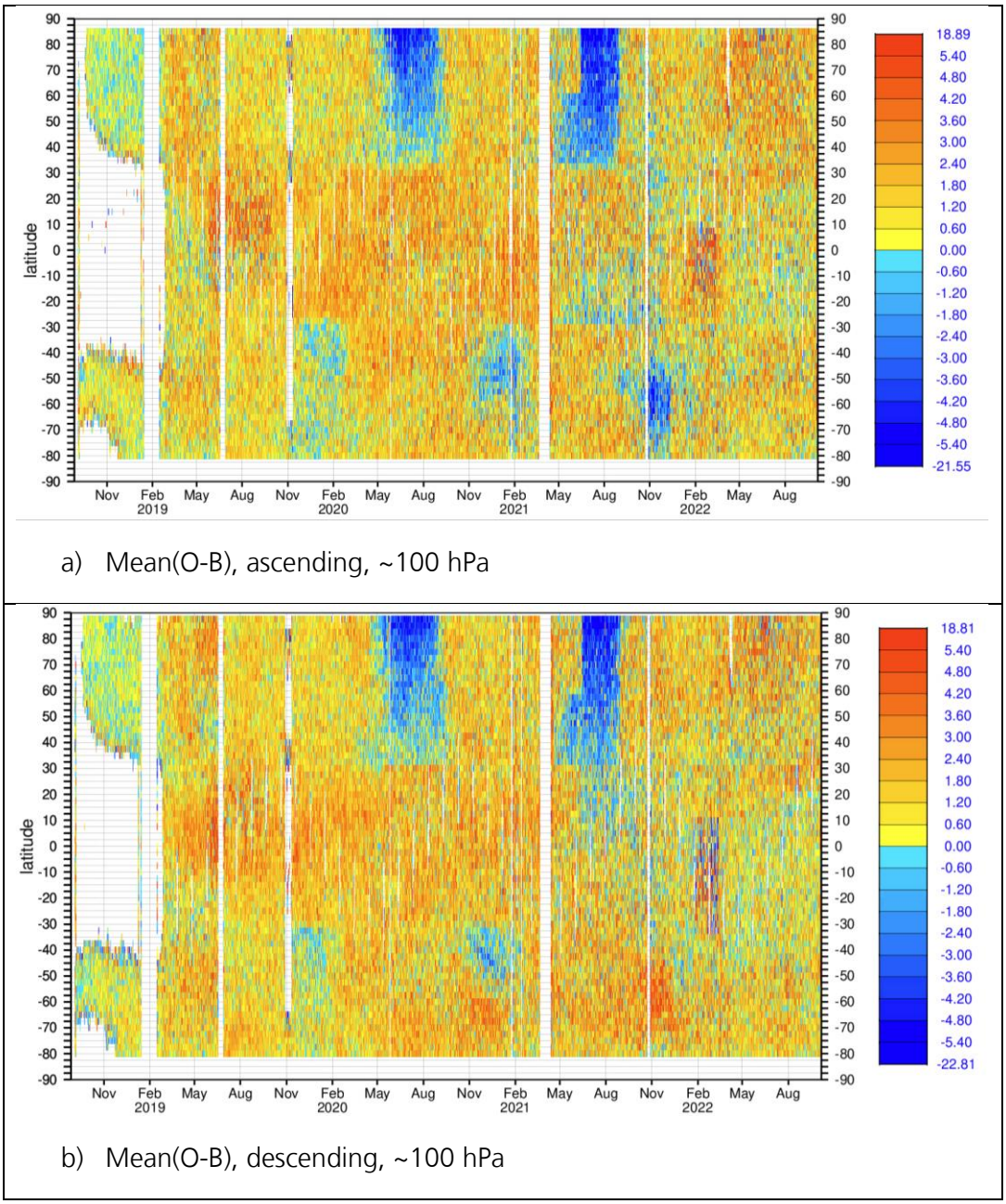

Figure 101. Latitude-time plots for L2B Rayleigh-clear winds of mean(O-B) (m/s) for a) ascending orbits and b) descending orbits, for the combined 3rd (B14) and 4th (B16) reprocessing for the pressure range with largest data counts i.e. 88-102 hPa. Time-step is 12 hours.

In Figure 102, random errors are relatively small at ~500 hPa until 2021-2022 when the increasing influence of solar background becomes evident in polar summer areas. There is also increased noise in the tropics which follows the ITCZ (Intertropical Convergence Zone) with concomitant increased signal attenuation below clouds, but also larger background forecast errors (in convective areas).

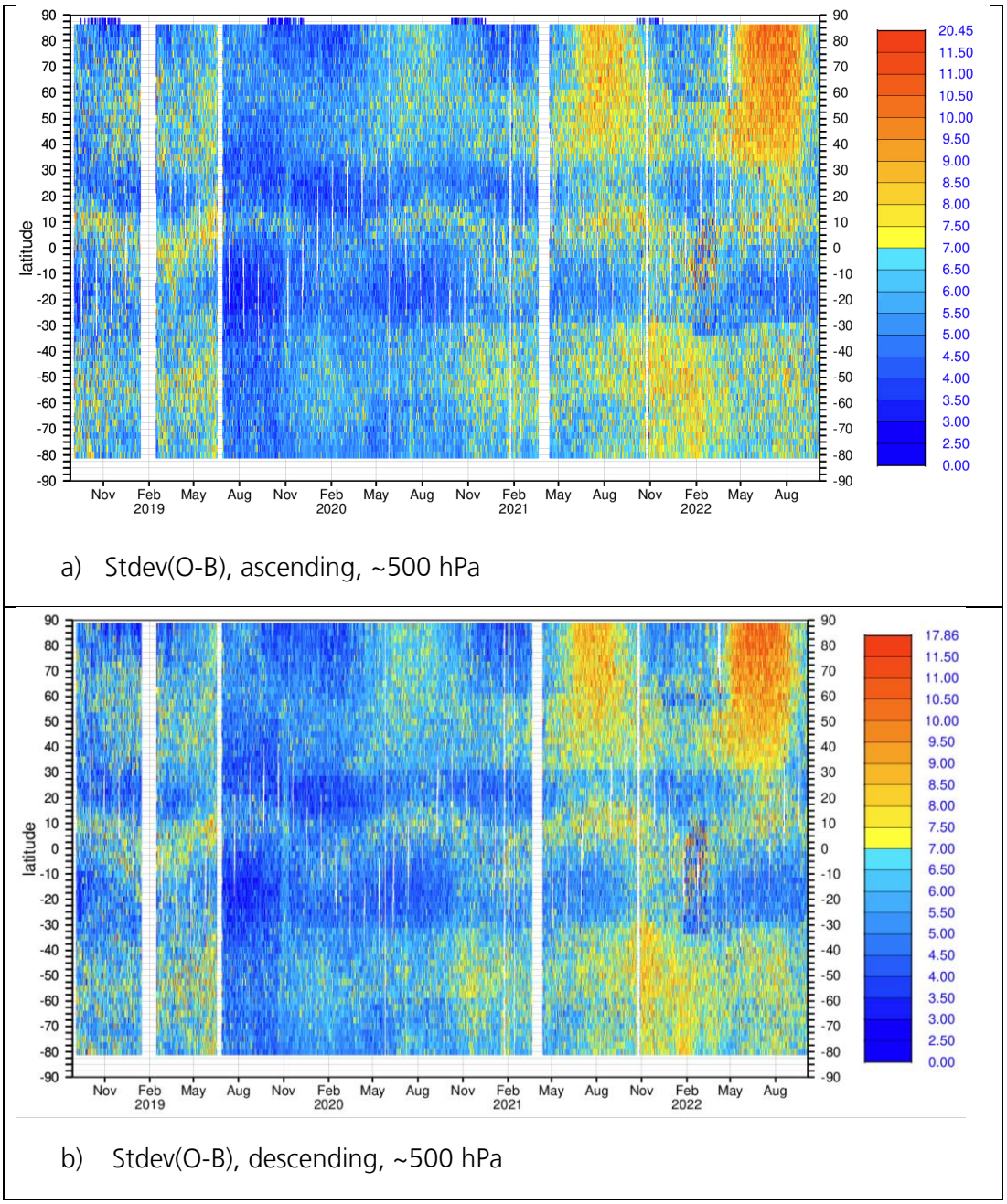

Figure 102. Latitude-time plots for L2B Rayleigh-clear winds of standard deviation (O-B) (m/s) for a) ascending and b) descending orbits, for the combined 3rd (B14) and 4th (B16) reprocessing for the pressure range with largest data counts i.e. 489-565 hPa. Time-step is 12 hours.

In Figure 103, at 100 hPa the noise is larger in the summer poles even during late 2019, with relatively good signal levels. The noise becomes very large (10 ms^{-1}) in 2022. Noise is reduced in the tropics following the Hunga Tonga eruption at 100 hPa due to much thicker than normal range-bin settings, to allow the upper range-bin to reach 30 km.

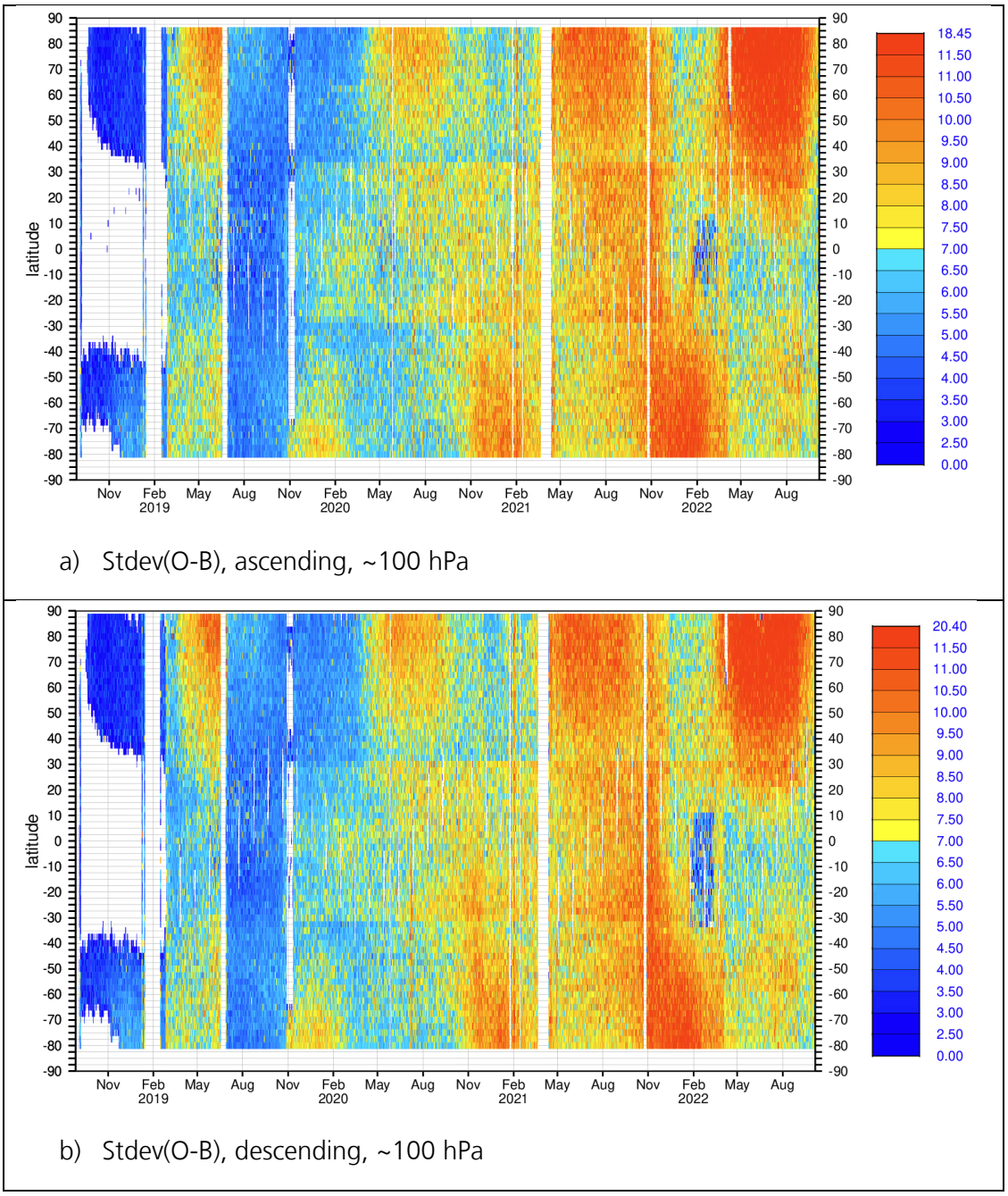

Figure 103. Latitude-time plots for L2B Rayleigh-clear winds of standard deviation (O-B) (m/s) for a) ascending and b) descending orbits, for the combined 3rd (B14) and 4th (B16) reprocessing for the pressure range with largest data counts i.e. 88-102 hPa. Time-step is 12 hours.

7.6 L2B Rayleigh-cloudy winds, detailed verification

Figure 104 shows a time-series of the daily, global average O-B statistics (left axis) and data counts (right axis) for the L2B Rayleigh-cloudy winds during the 4th reprocessing (28 June 2019 to 4 October 2022).

It also includes the 3rd reprocessing (FM-A laser) from 3 September 2018 to 16 June 2019 for comparison.

The QC applied for the time-series results for the Rayleigh-cloudy is to reject winds with abs(O-B)> 25 ms^{-1} or if the L2B validity flag is false i.e. the same as for Rayleigh-clear. There are thought to be relatively fewer gross errors in the Rayleigh-cloudy winds compared to the Mie-cloudy winds, therefore we can allow a quite relaxed QC check, whilst not spoiling the non-robust metrics of mean and standard deviation. Also, the noise of the Rayleigh winds becomes very large in 2021-2022 meaning that a 25 m/s O-B check is roughly a 3σ check.

The HLOS wind observation random error estimate varies between ~7.5 ms^{-1} at the start of FM-B and then increases with time to ~9.5 ms^{-1} in 2021. It then improved again with boosts of the laser energy and with reduced measurements per BRC (particularly N=5 in April 2022). The average horizontal accumulation length was ~40 km for most of the period but increased to ~50 km with N=5. The improvement in September 2022 was due to an increase in laser energy to 100 mJ. The systematic HLOS wind errors tended to be positive and ~+1 ms^{-1} from the start of FM-B until March 2021, then with the FM-B re-switch on in April 2021 and the application of new calibration the bias improved to be ~+0.5 ms^{-1}. The data counts tended to decrease with time due to reducing signal and more winds failing the QC checks. The performance of the Rayleigh-cloudy winds in FM-B B16 was not as good as expected and the reasons for this are being investigated with the aim of improving this for B17.

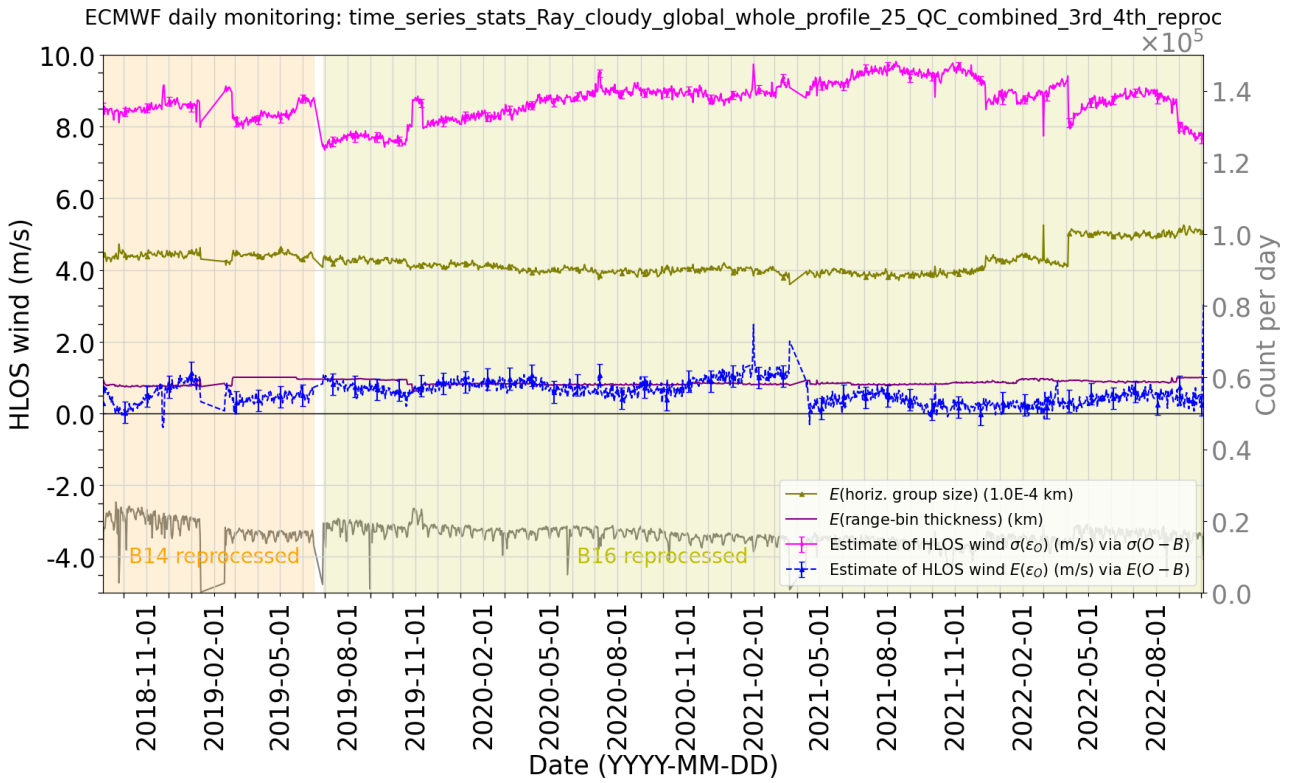

Figure 104. Time series of L2B Rayleigh-cloudy daily, global and all pressure level O-B statistics from the controls of the combined third (FM-A, B14) and fourth reprocessing (FM-B, B16) (no-Aeolus control OSE runs). For the period 3 September 2018 until 4 October 2022.

Splitting the statistics into ascending and descending orbits, as in Figure 105, shows different noise levels in 2022 for ascending and descending, which is not understood. The bias magnitude tends to differ somewhat between ascending and descending orbits also.

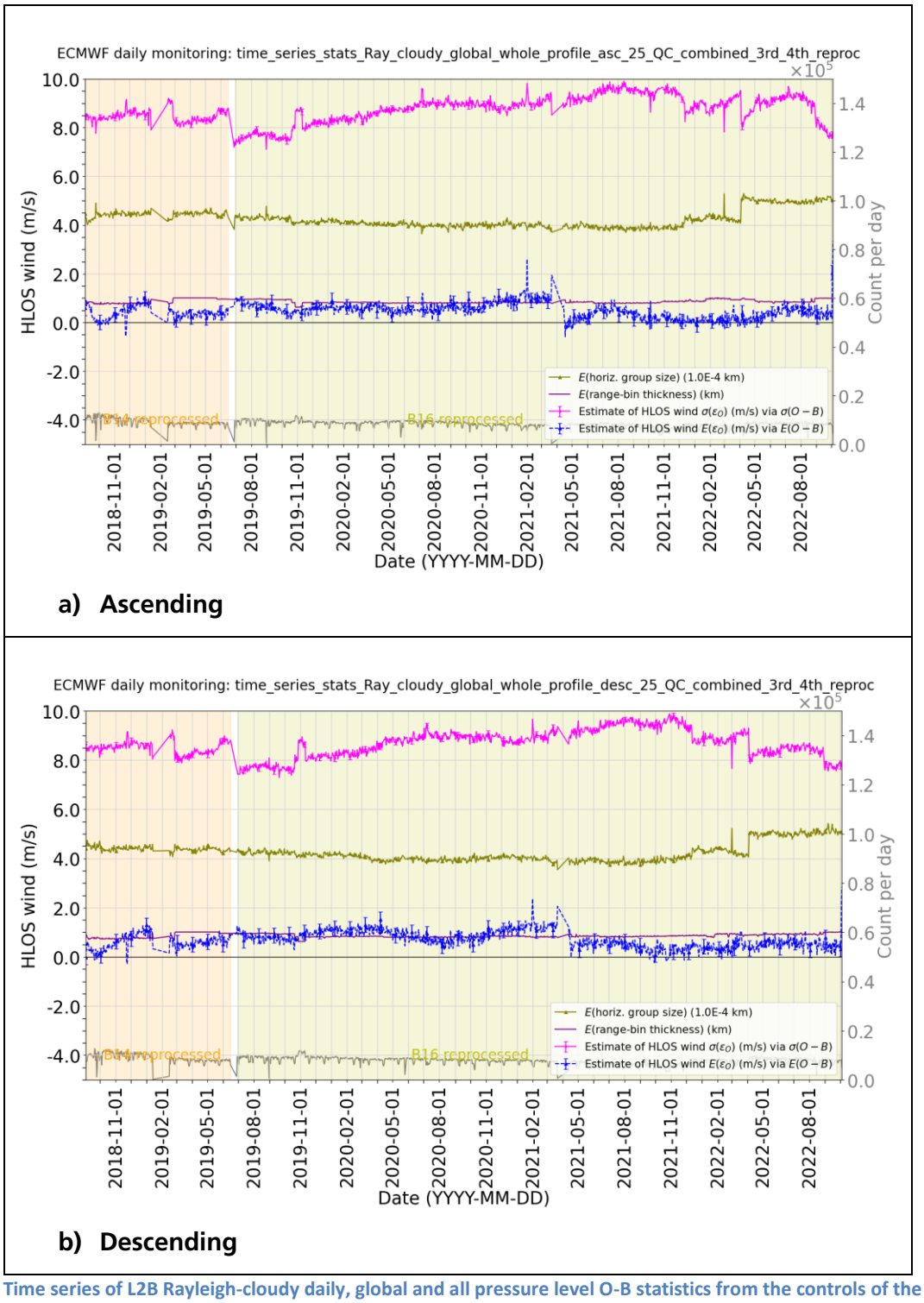

Figure 105. Time series of L2B Rayleigh-cloudy daily, global and all pressure level O-B statistics from the controls of the combined third (FM-A, B14) and fourth reprocessing (FM-B, B16) (no-Aeolus control OSE runs) for a) ascending and b) descending orbits. For the period 3 September 2018 until 4 October 2022.

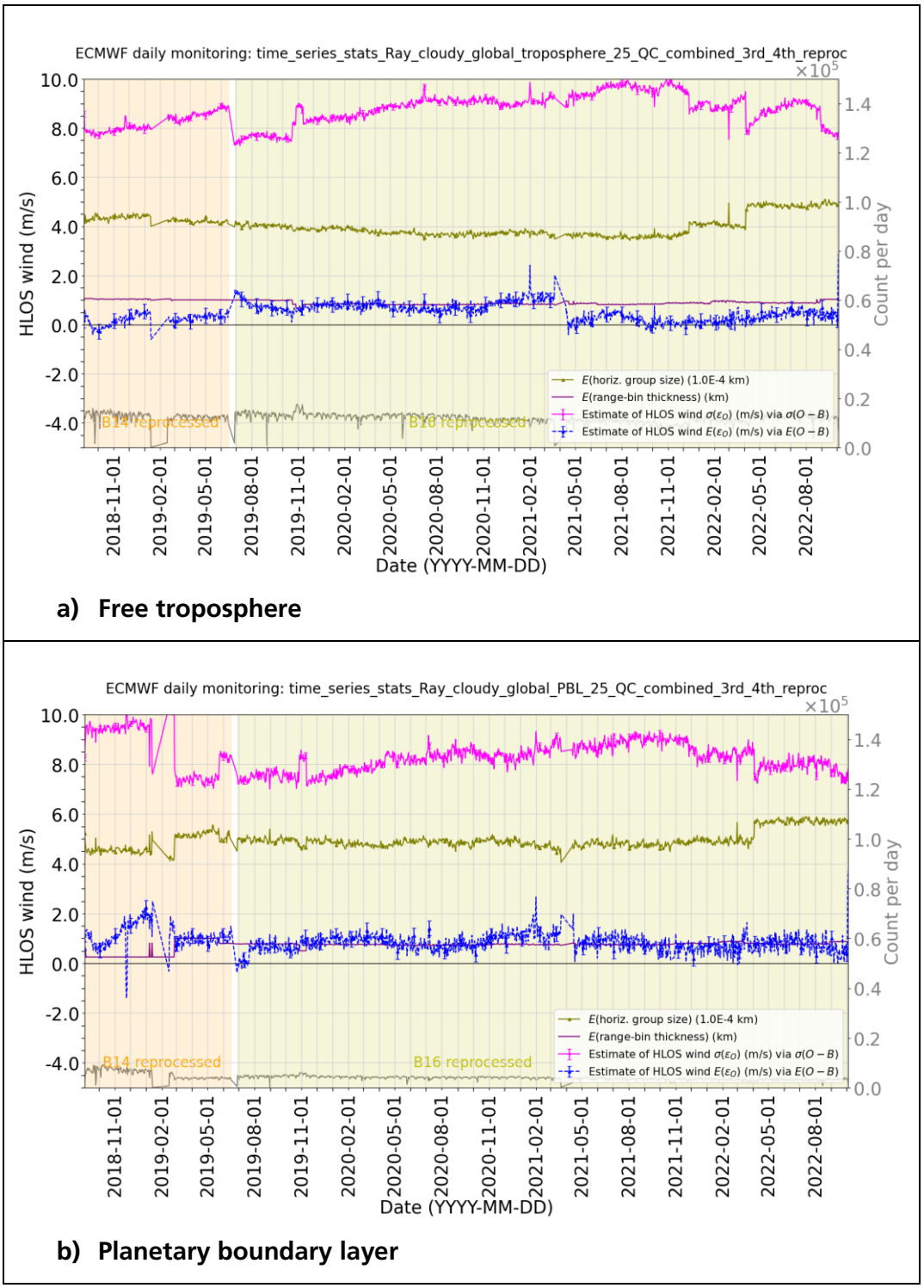

Figure 106. Time series of L2B Rayleigh-cloudy daily, global and all pressure level O-B statistics from the controls of the combined third (FM-A, B14) and fourth reprocessing (FM-B, B16) (no-Aeolus control OSE runs) for a) the free troposphere and b) the planetary boundary layer. For the period 3 September 2018 until 4 October 2022.

The time-series are partitioned into free troposphere (approximately 800 to 100 hPa) and the planetary boundary layer (< 800 hPa) in Figure 106. The random errors are smaller in the PBL than in the free troposphere, due to stronger cloud backscatter. After April 2021 the positive bias tends to be larger in the PBL than in the free troposphere.

The time-series are partitioned into Northern Hemisphere extratropics (> 30 degrees latitude), tropics (within ±30 degrees latitude) and Southern Hemisphere extratropics (<-30 degrees latitude) in Figure 107. The smallest random errors occur in the SH extratropics, possibly due to increased cloudiness there. However, the bias seems more variable with time (before April 2021) in the SH extratropics. The random errors jumped up in November 2019 in the SH extratropics due to a change to thinner range-bin settings.

NH extratropics	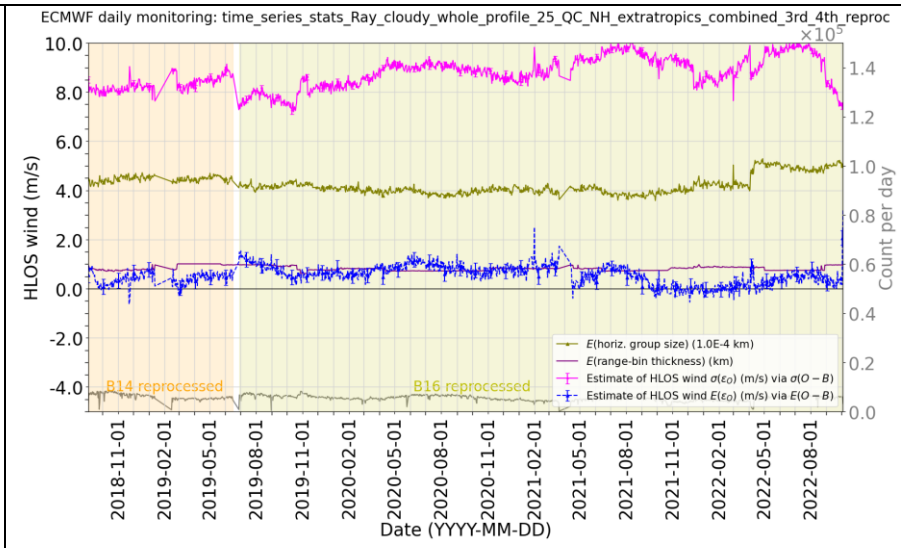

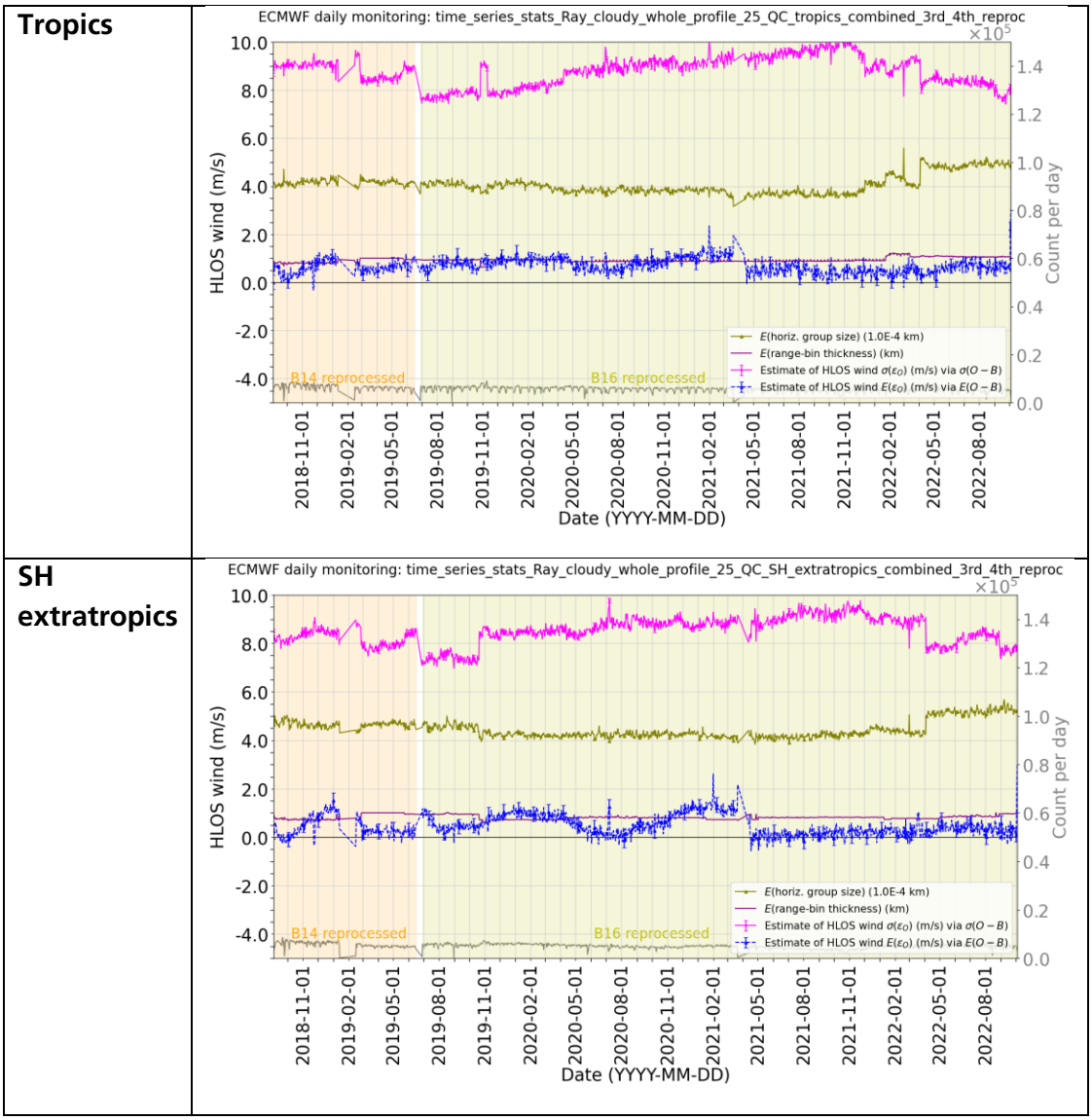

Figure 107. Time series of L2B Rayleigh-cloudy daily, global level O-B statistics from the controls of the combined third (FM-A, B14) and fourth reprocessing (FM-B, B16) (no-Aeolus control OSE runs) for a) NH extratropics and b) tropics and c) SH extratropics. For the period 3 September 2018 until 4 October 2022.

Vertical profiles of L2B Rayleigh-cloudy departure statistics (versus pressure, with pressure bins chosen to roughly linear with altitude) are shown in Figure 108, for a selection of areas, for the early part of the 4th reprocessing period. The bias remains reasonably constant with height for this period in different parts of the globe. The smallest random errors are evident in the SH extratropics PBL with ~6 ms^{-1}.

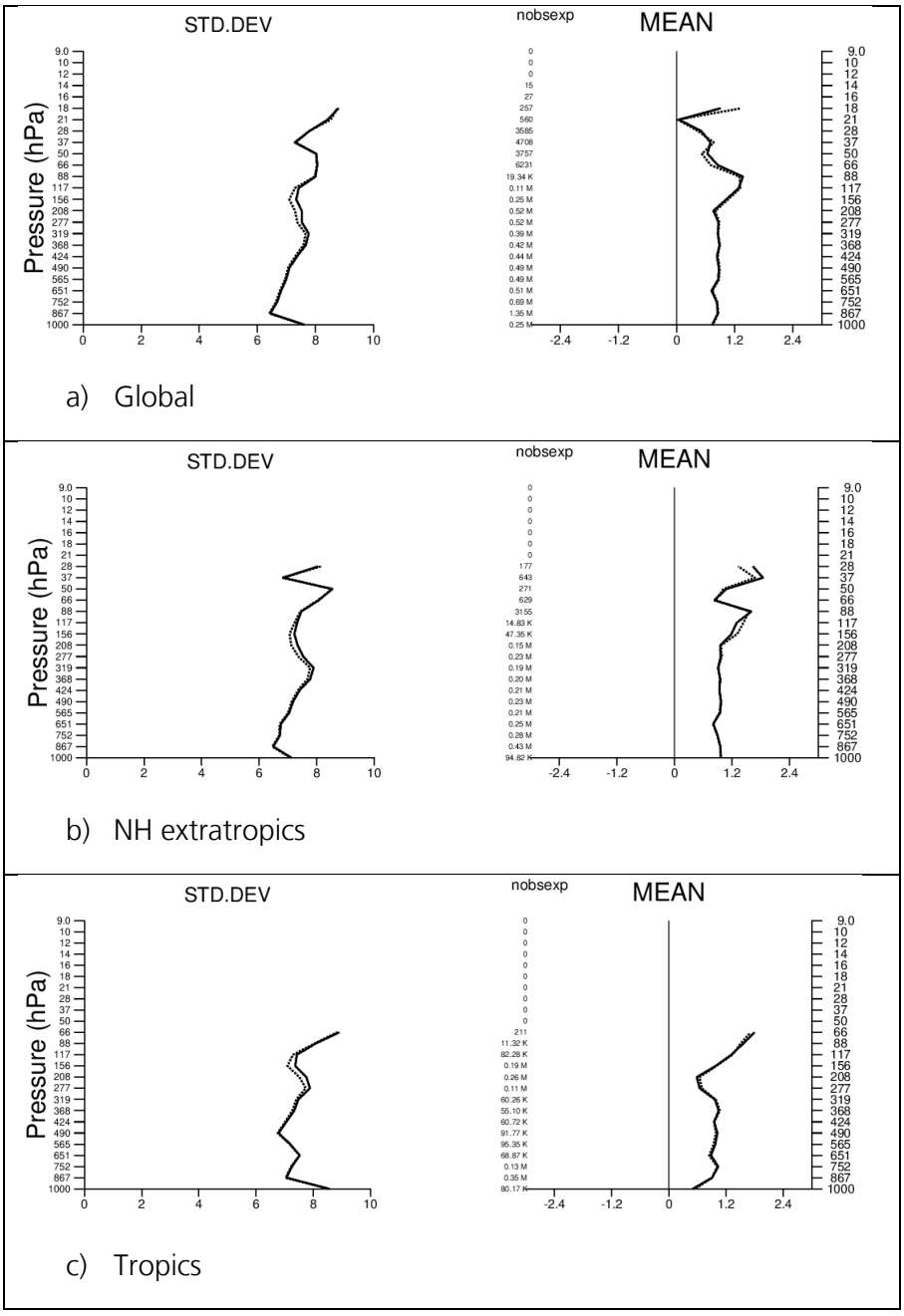
STD.DEV
nobsexp
MEAN
Pressure (hPa)
a) Global
b) NH extratropics
c) Tropics

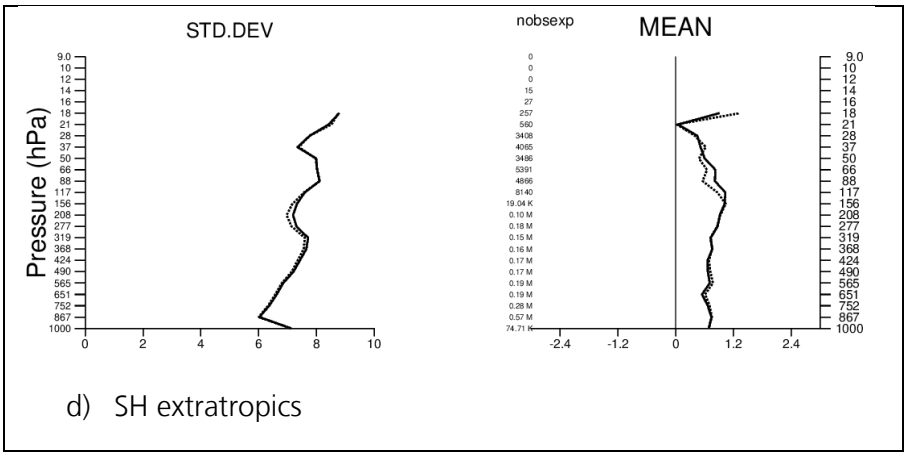

Figure 108. L2B Rayleigh-cloudy HLOS wind O-B (solid line) and O-A (dashed line) departure statistics (m/s) as a function of pressure; standard deviation on the left and mean on the right. Data counts are printed (nobsexp) in the middle. The pressure bins are roughly linear with altitude going from surface to ~30 km. Data from the 4th (B16) reprocessing from 28 June 2019 to 9 October 2020.

The relationship between the L2B Rayleigh-cloudy and the background forecast HLOS wind is shown as 2D histograms in Figure 109, for the earlier part of the 4th reprocessing. This generally shows the reasonable linear relationship between the observed and modelled HLOS wind. However, there is some evidence of the pdf being "trimmed" by the 25 ms^{-1} abs(O-B) QC, given the lack of blue shaded counts. The range of L2B HLOS winds is from -120.1 to 118.0 ms^{-1} globally, but in the tropics, it is more restricted, from -72.9 to 81.5 ms^{-1}, as expected.

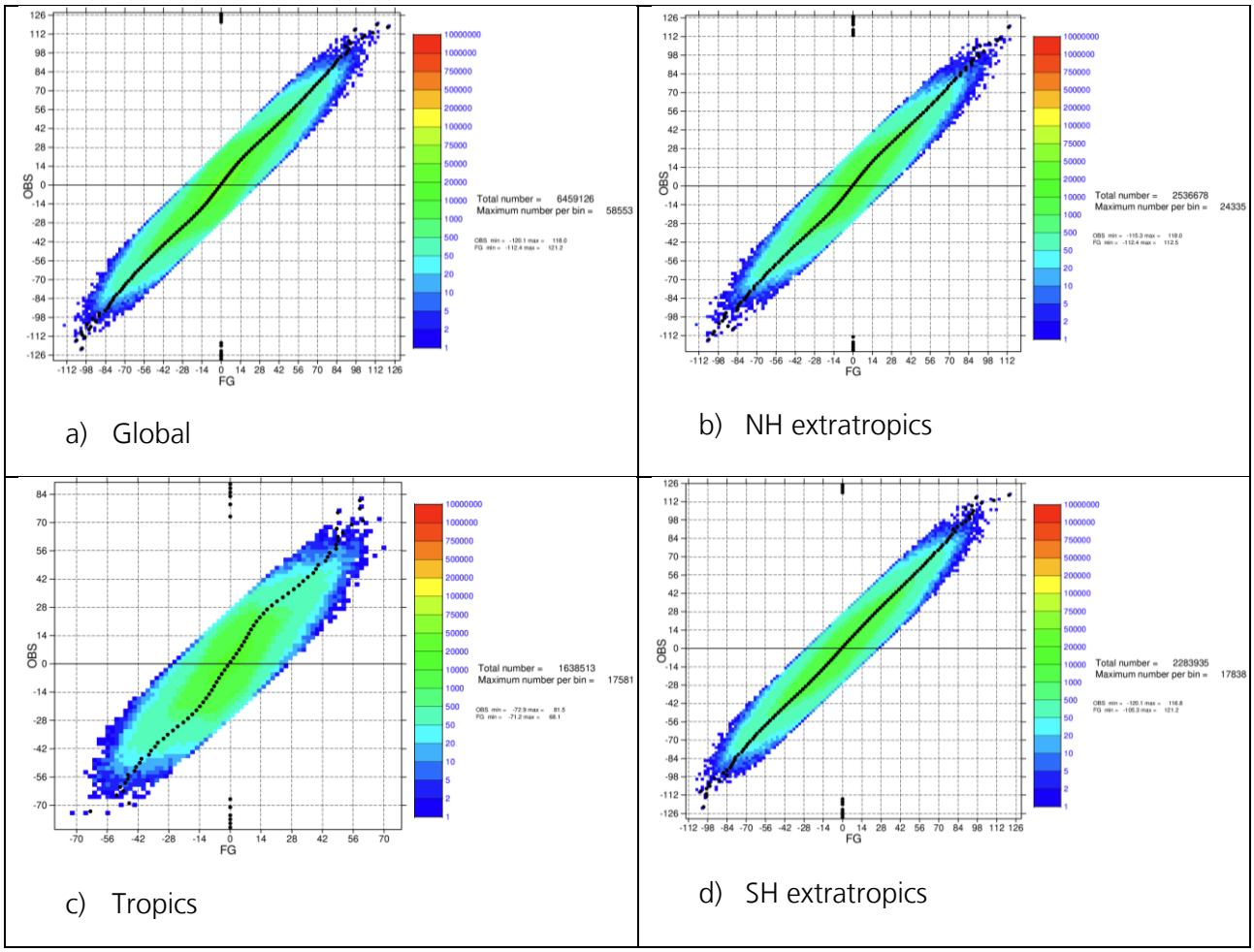

Figure 109. L2B Rayleigh-cloudy HLOS wind (OBS) versus background (FG) 2D histogram for different areas. Units in m/s. Data from the 4th (B16) reprocessing from 28 June 2019 to 9 October 2020.

The plots of Figure 110 and Figure 111 show the dependence of the mean(O-B) on the B HLOS wind. There were no "valid" L2B Rayleigh-cloudy winds available in the 1st reprocessing, hence it is absent from Figure 110. Note that the slope of the wind-speed varying bias changed dramatically from the 2nd to the 4th reprocessing. One would expect a slightly negative slope due to regression dilution (errors in the independent variable, background HLOS wind), so the 4th reprocessing has the expected sign, however the slope magnitude is too large. We expect a negative slope with linear fit of about -0.02 for a 2 ms^{-1} background HLOS wind 1-sigma error i.e. apparent bias of ∓ 2 ms^{-1} at ± 100 ms^{-1} HLOS wind. The slope looks to be twice as steep for the Rayleigh-cloudy winds of the 4th reprocessing i.e. the winds are too slow.

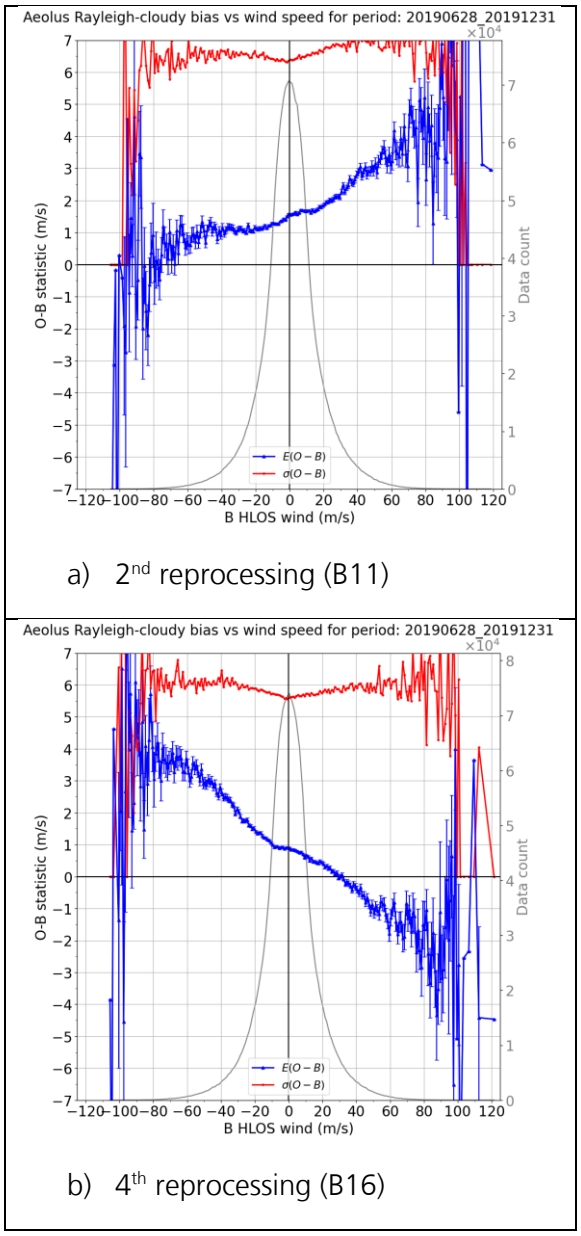

Figure 110. Comparison of the wind speed dependence to the L2B Rayleigh-cloudy bias for the period 29 June 2019 to 31 December 2019 for different reprocessing campaigns: a) 2nd reprocessing (B11) and b) 4th reprocessing (B12). This period is chosen for the availability of all three reprocessed datasets.

Figure 111 shows that the bias slope improves by 2022, but by comparing to a similar trend for the Rayleigh-clear winds, shown earlier, this may be an improvement for the wrong reasons.

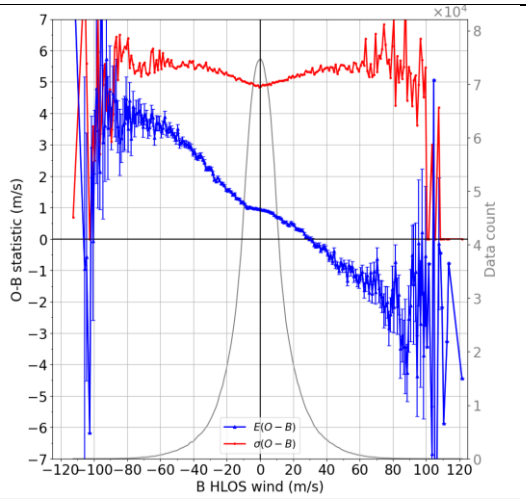

a) 28 June 2019 – 18 February 2020

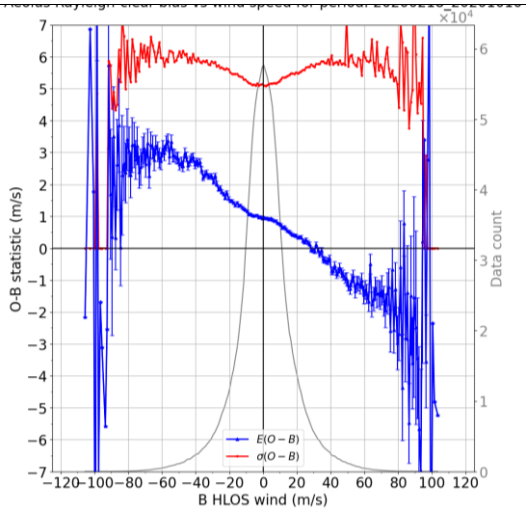

b) 18 February 2020 – 10 October 2020

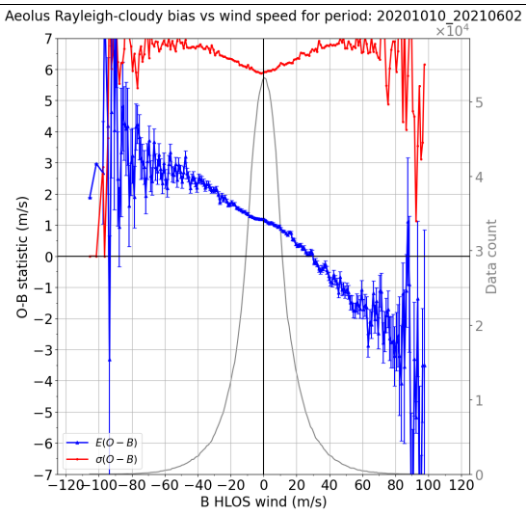

c) 10 October 2020 – 2 June 2021

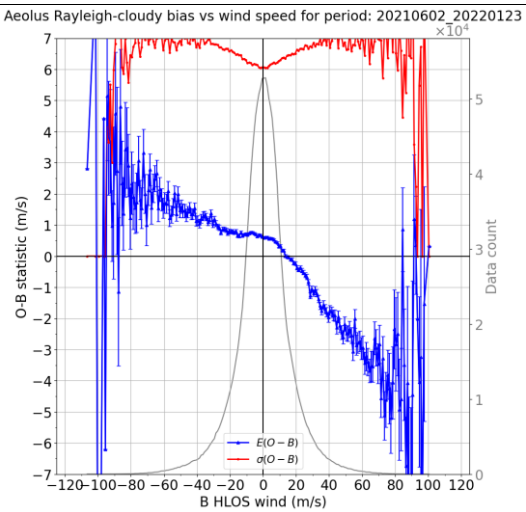

d) 2 June 2021 – 23 January 2022

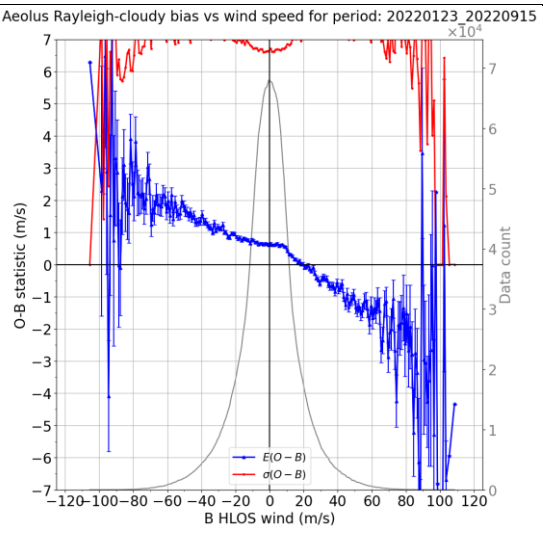

e) 23 January 2022 – 15 September 2022

Figure 111. Wind speed dependence to the L2B Rayleigh-cloudy bias for 235-day periods of the 4th reprocessing campaign (B16).

The following plots of pressure versus time in Figure 112 to Figure 114. The vertical pressure bins are chosen to be roughly linear in altitude so the y-axis can be thought as roughly being from surface to 30 km (~10 hPa) altitude. Figure 112 shows the largest data counts are at the top of the boundary layer due to the strong cloud backscatter there (as is the case also with Mie-cloudy). The Rayleigh-cloudy winds derived from the Hunga-Tonga plume (easterlies) in early 2022 is evident at 30-10 hPa.

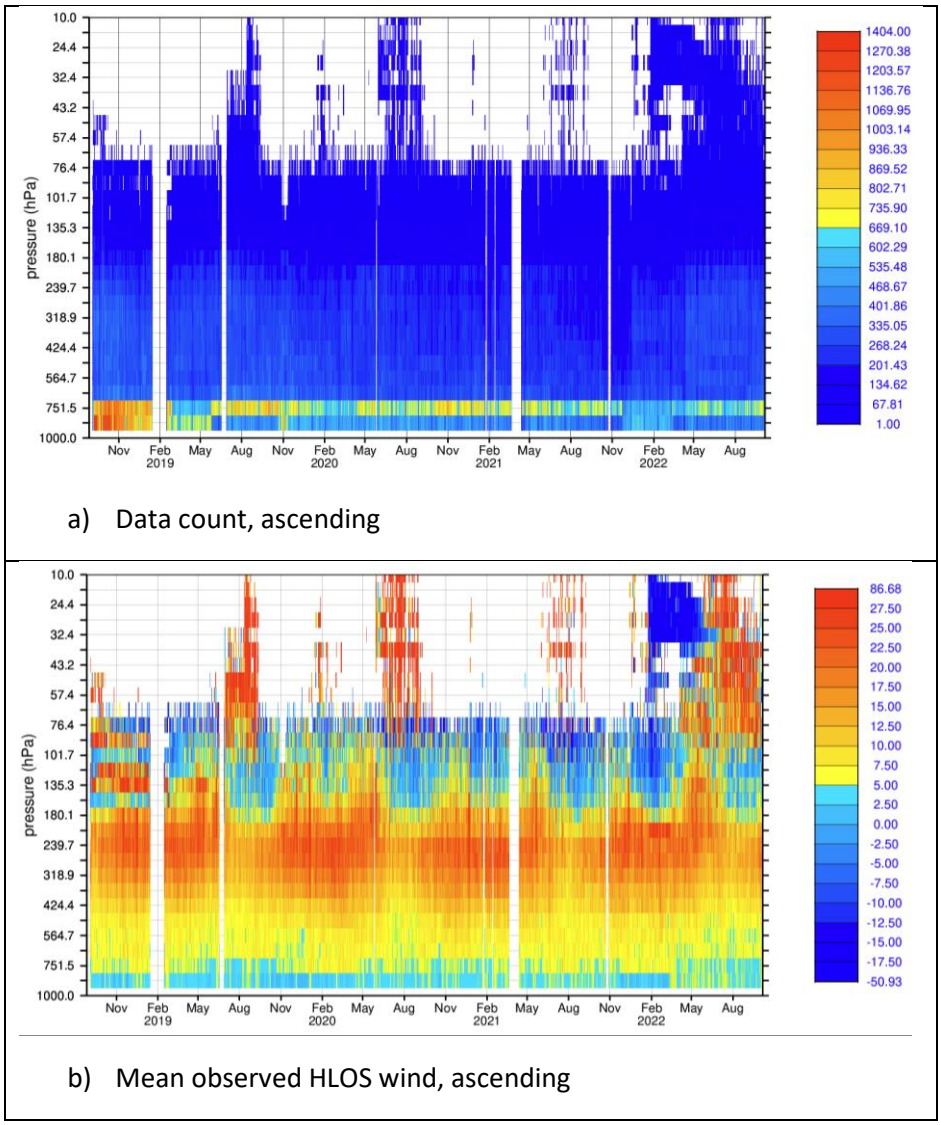

Figure 112. Pressure-time plots for L2B Rayleigh-cloudy winds for ascending orbits of a) data counts and b) mean observed HLOS wind value (m/s), for the combined 3rd (B14) and 4th (B16) reprocessing for global data. Time-step is 12 hours.

The behaviour of the biases in the vertical with time is evident in Figure 113. This shows a tendency for positive bias overall, but more negative bias at ~200 hPa (particularly from April 2021 to May 2022). It is unknown what causes this. The ascending orbits show the negative bias more strongly.

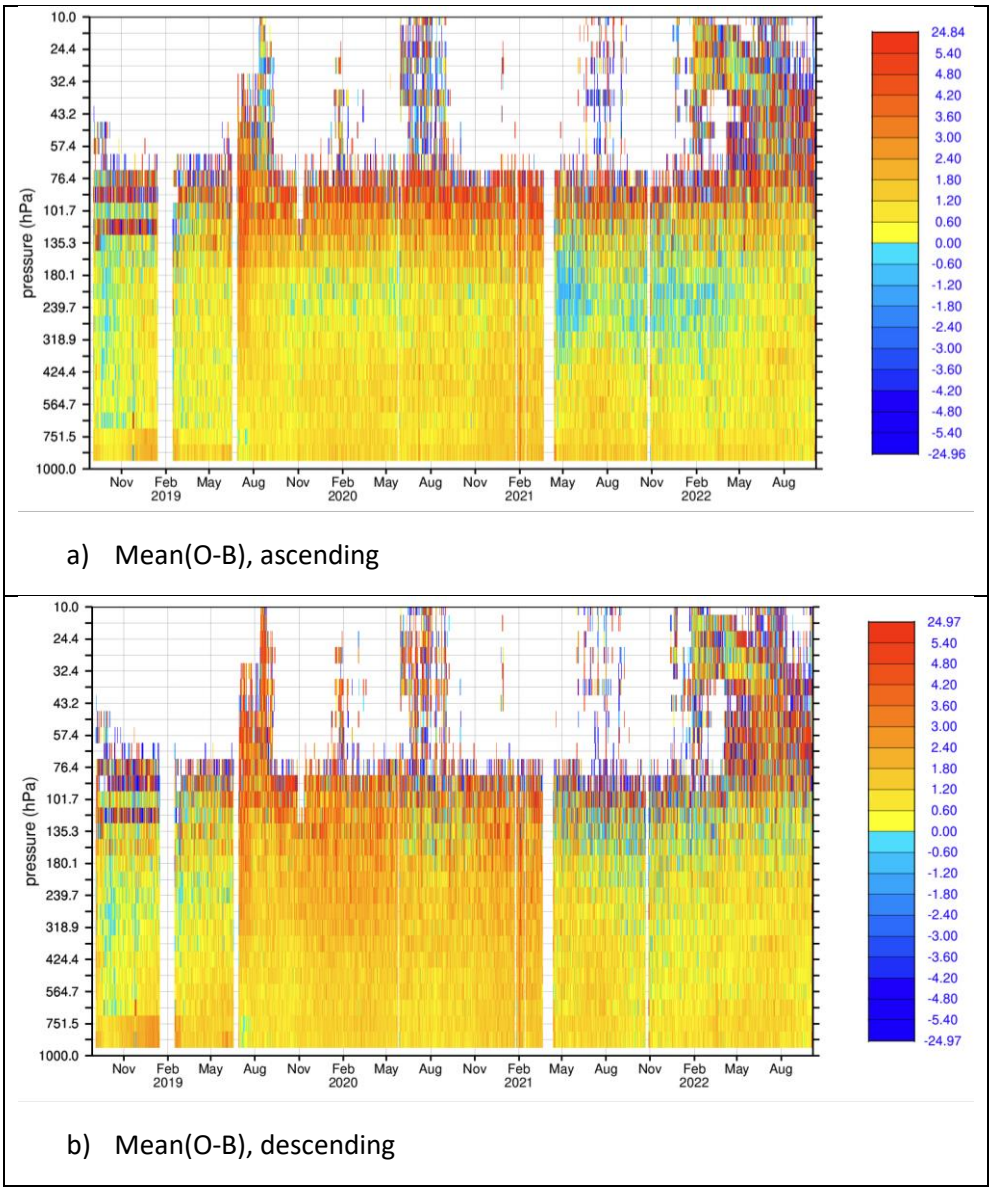

Figure 113. Pressure-time plots for L2B Rayleigh-cloudy winds of mean(O-B) (m/s) for a) ascending and b) descending orbits for the combined 3rd (B14) and 4th (B16) reprocessing for global data. Time-step is 12 hours.

In terms of random error (via stdev(O-B)) in Figure 114, the quality was much between from July 2019 to August 2020 particularly from the boundary layer cloud tops; the pattern is similar for ascending and descending orbits.

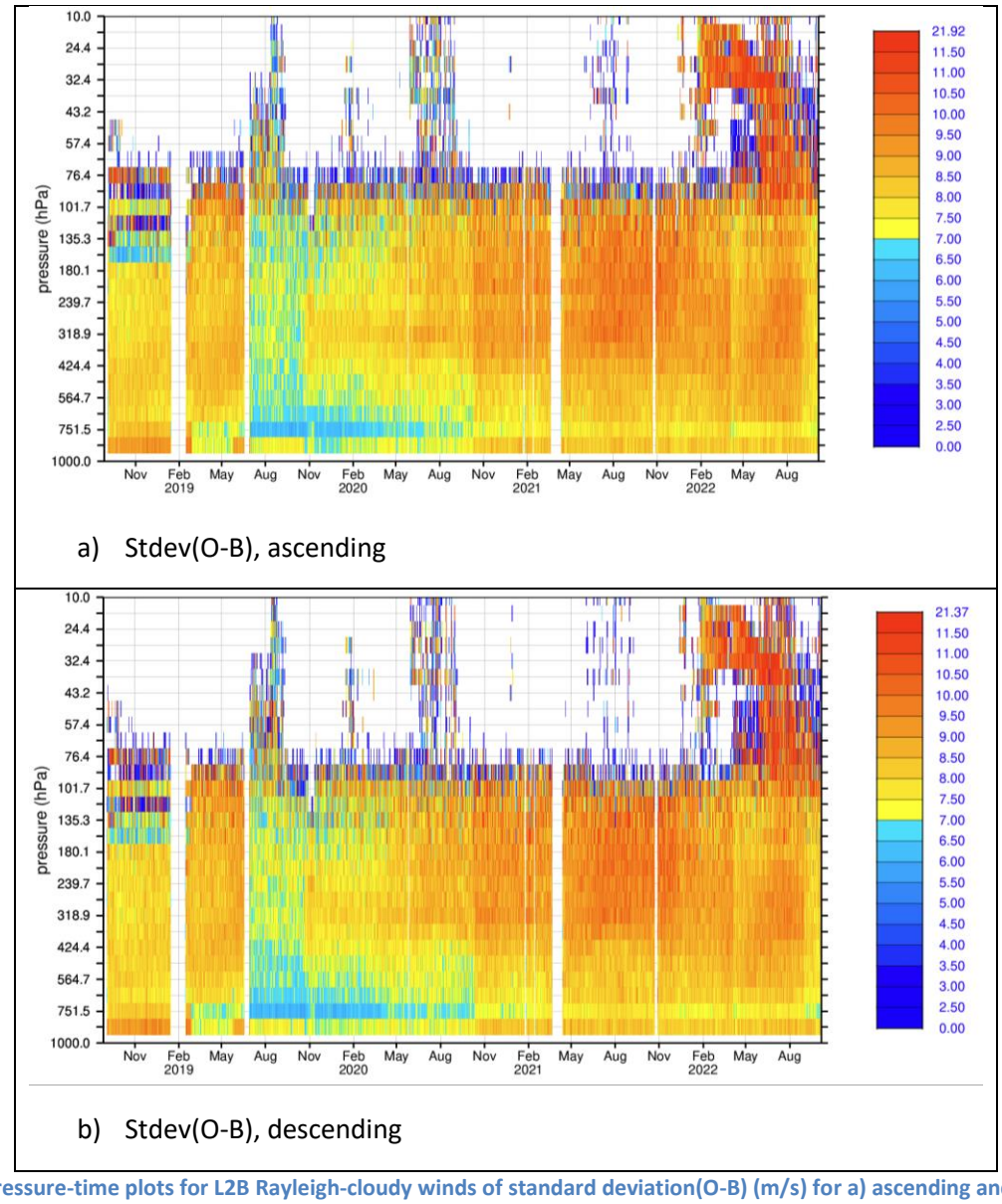

Figure 114. Pressure-time plots for L2B Rayleigh-cloudy winds of standard deviation(O-B) (m/s) for a) ascending and b) descending orbits for the combined 3rd (B14) and 4th (B16) reprocessing for global data. Time-step is 12 hours.

Zonal average plots are provided in Figure 115 to Figure 117 for the early part of the 4th reprocessing. The vertical sampling and average HLOS wind structure look very similar to that of the Mie-cloudy (Figure 69).

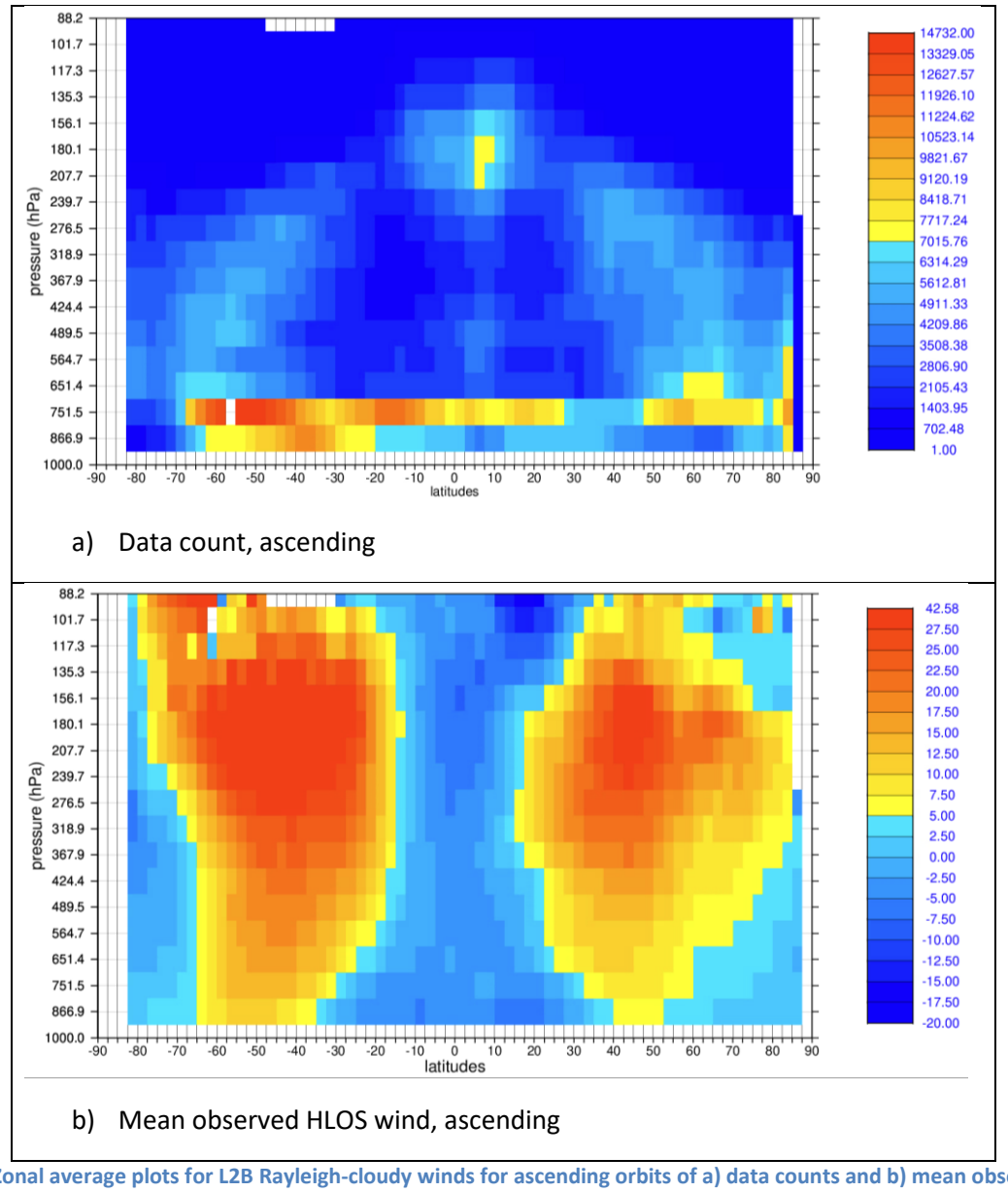

Figure 115. Zonal average plots for L2B Rayleigh-cloudy winds for ascending orbits of a) data counts and b) mean observed HLOS wind value (m/s), for the 4th (B16) reprocessing from 28 June 2019 to 9 October 2020.

The bias structure in Figure 116 looks quite different for ascending and descending orbits, with opposing bias sign tendency in around 200 hPa at mid-latitudes. The random errors in Figure 117 have a similar structure for ascending and descending orbits; with least noise at ~750 hPa in the SH extra-tropics.

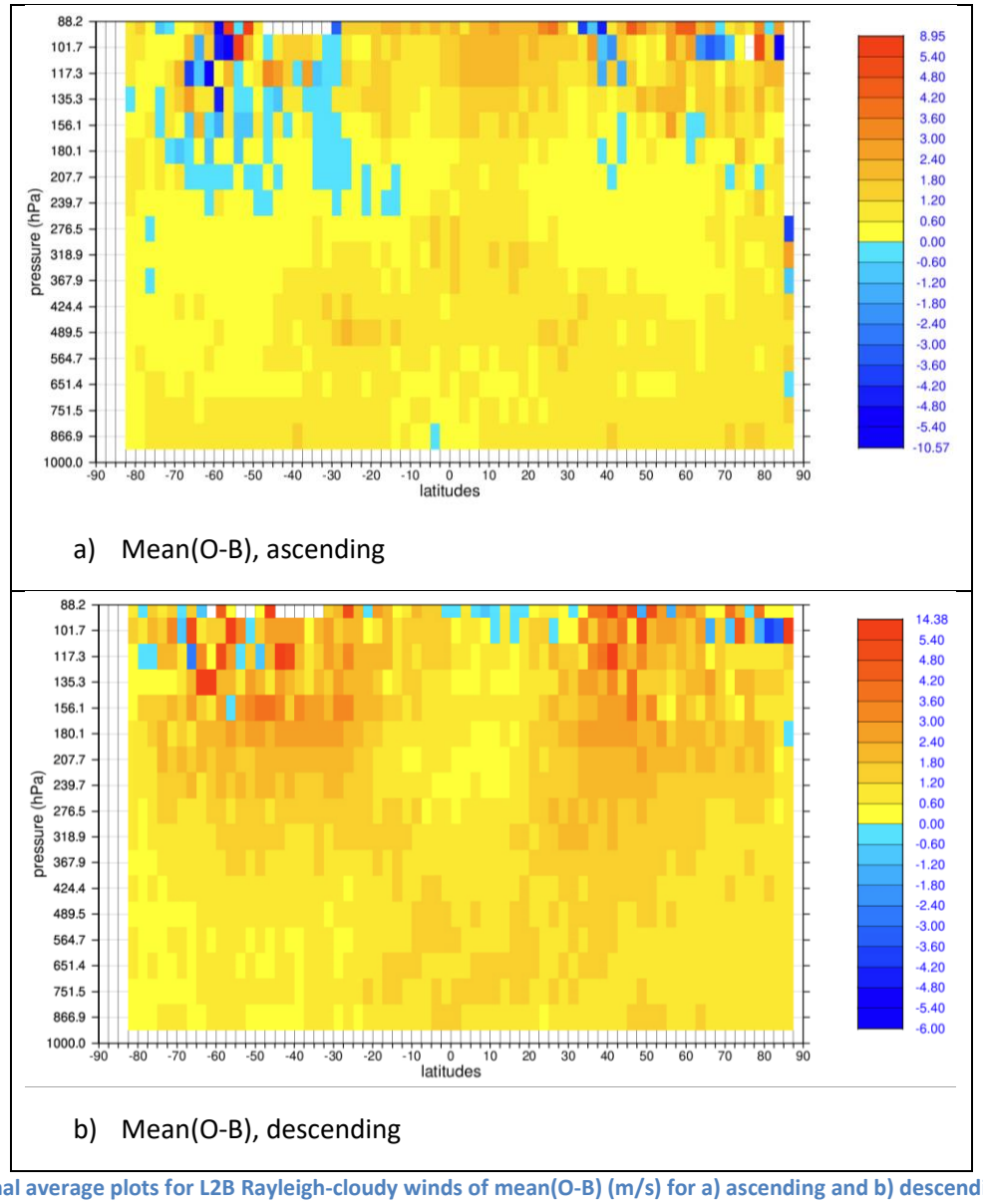

Figure 116. Zonal average plots for L2B Rayleigh-cloudy winds of mean(O-B) (m/s) for a) ascending and b) descending orbits for the 4th (B16) reprocessing from 28 June 2019 to 9 October 2020.

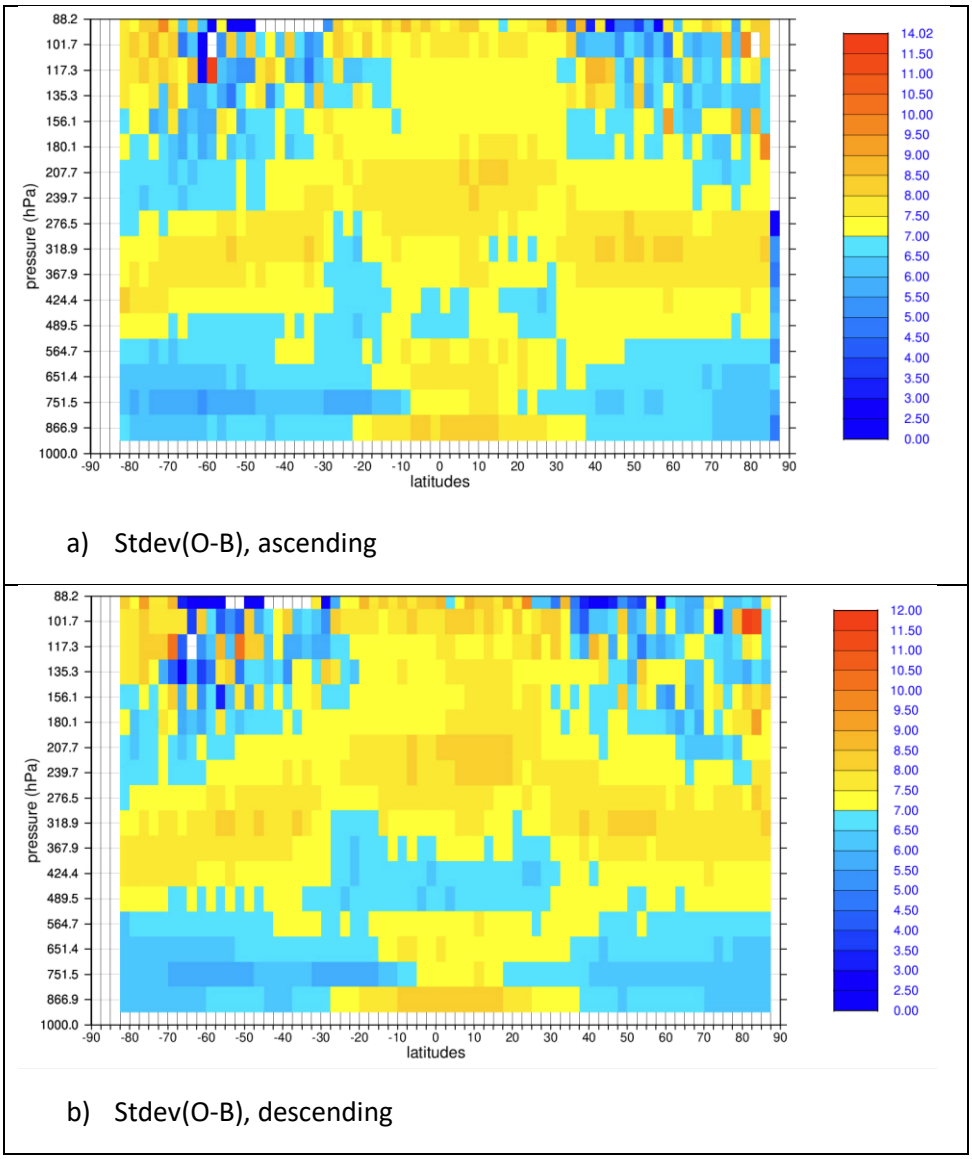

Figure 117. Zonal average plots for L2B Rayleigh-cloudy winds of standard deviation(O-B) (m/s) for a) ascending and b) descending orbits for the 4th (B16) reprocessing from 28 June 2019 to 9 October 2020.

The following pages focus on L2B Rayleigh-cloud map and latitude-time plots for pressure-bins around ~800 hPa and ~250 hPa, due to the relatively large data counts are available at those levels. In Figure 118 the positive bias structures for descending orbits to the west of Africa and South America have some similarities to that shown with the Mie-cloudy winds in Figure 72, which supports the source of the bias being the ECMWF background forecast e.g. it cannot be due to Mie fringe-skewness if also present for the Rayleigh-cloudy winds. The smallest random errors occur in marine stratocumulus regions to the west of continents. The largest random errors are in convective equatorial regions, due to strong attenuation of signal by clouds.

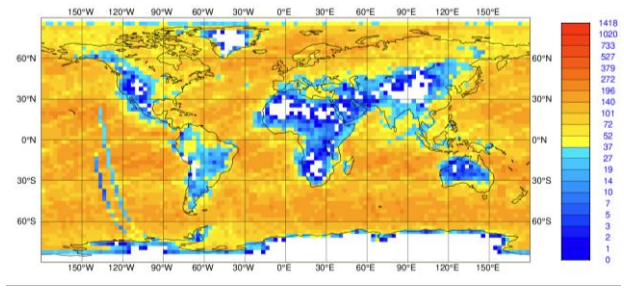

a) Data count, ascending

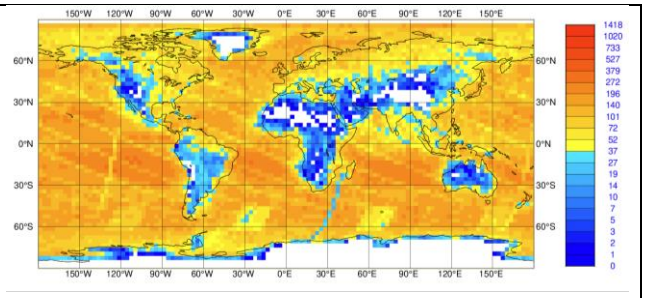

b) Data count, descending

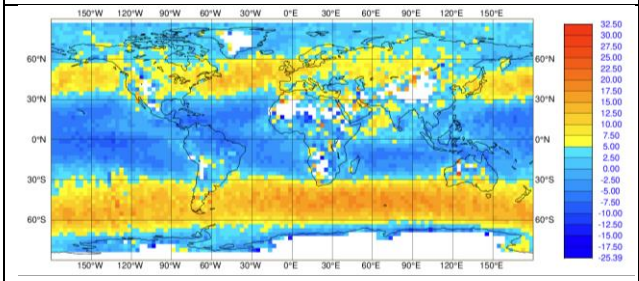

c) Mean observed HLOS wind, ascending

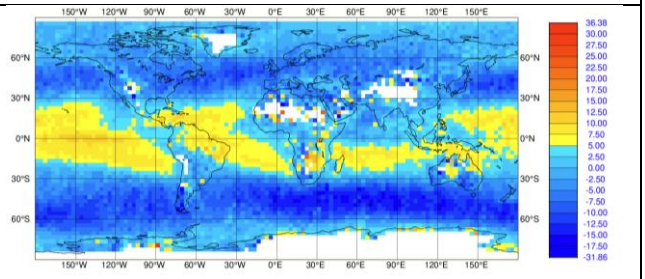

d) Mean observed HLOS wind, descending

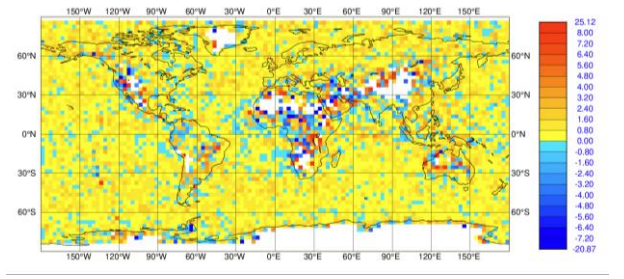

e) Mean(O-B), ascending

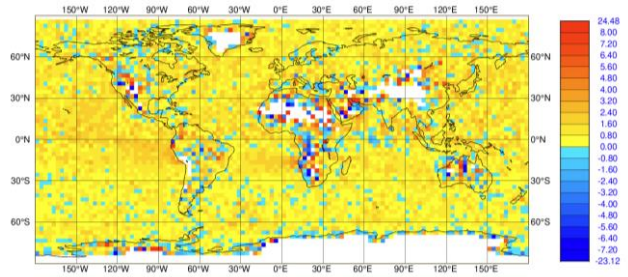

f) Mean(O-B), descending

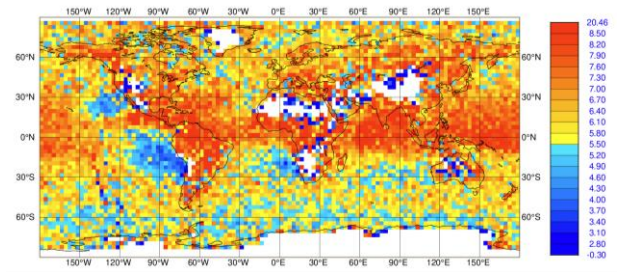

g) Stdev(O-B), ascending

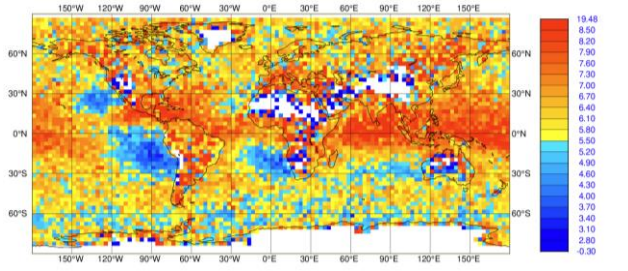

h) Stdev(O-B), descending

Figure 118. Map plots (3x3 degrees) for L2B Rayleigh-cloudy winds at ~800 hPa (751-867 hPa) of: data counts for the top row; mean observed HLOS wind value (m/s) for the second row; mean(O-B) (m/s) for the third row; and stdev(O-B) (m/s) for the bottom row. Using the 4th (B16) reprocessing from 28 June 2019 to 9 October 2020.

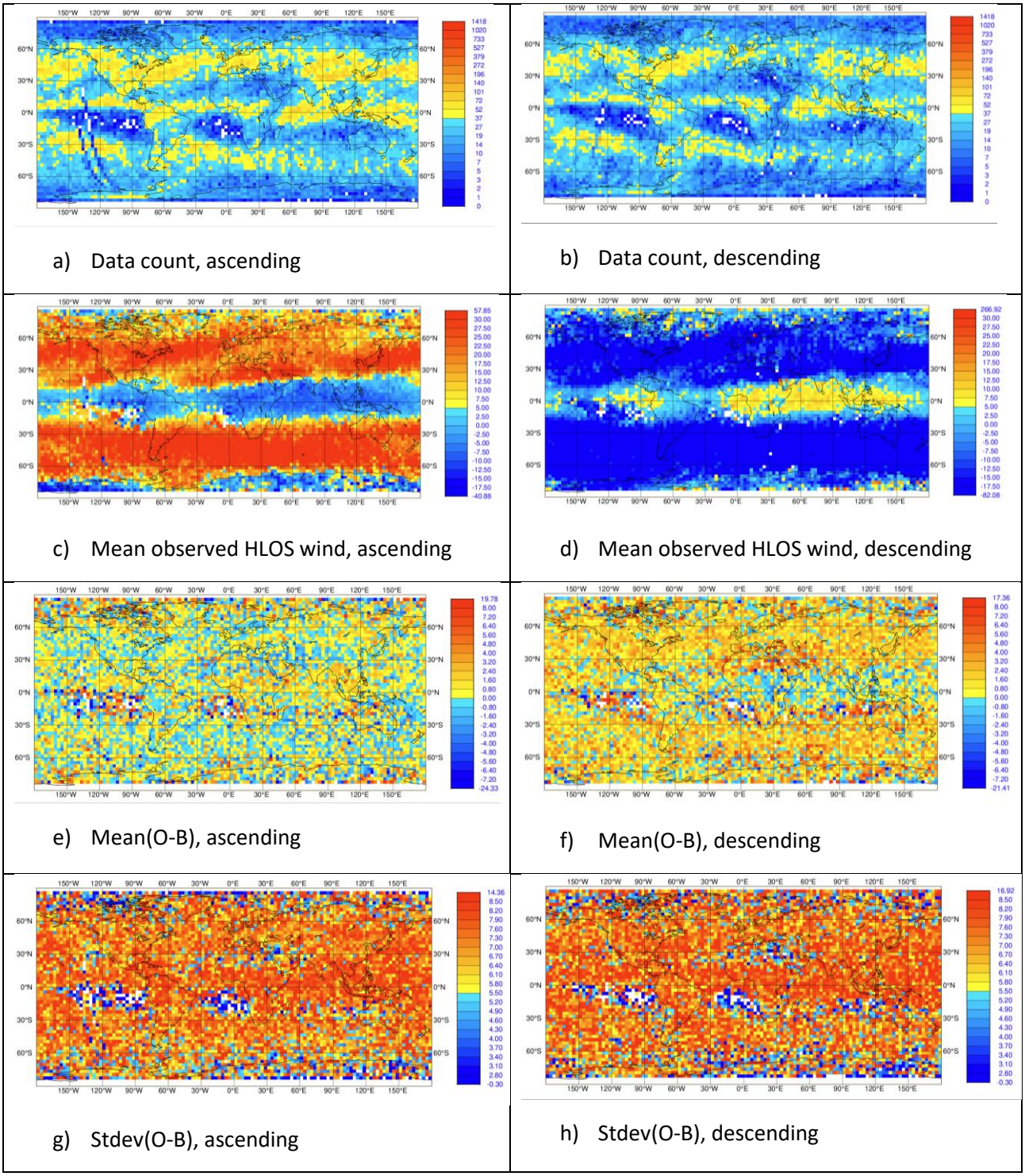

a) Data count, ascending

b) Data count, descending

c) Mean observed HLOS wind, ascending

d) Mean observed HLOS wind, descending

e) Mean(O-B), ascending

f) Mean(O-B), descending

g) Stdev(O-B), ascending

h) Stdev(O-B), descending

Figure 119. Map plots (3x3 degrees) for L2B Rayleigh-cloudy winds at ~250 hPa (240-277 hPa) of: data counts for the top row; mean observed HLOS wind value (m/s) for the second row; mean(O-B) (m/s) for the third row; and stdev(O-B) (m/s) for the bottom row. Using the 4th (B16) reprocessing from 28 June 2019 to 9 October 2020.

In Figure 119, at ~250 hPa, the differences in bias sign between ascending (negative) and descending (positive) is marked. The Rayleigh-cloudy winds at 250 hPa are mostly measured in the ITCZ and in extratropical storm-track regions. The noise is very large in all regions.

The following plots show statistics as a function of latitude and time (split by ascending and descending) – often referred to as Hovmöller plots.

In Figure 120, at 800 hPa the data counts peak in the Southern Hemisphere at ~-50 to -60 degrees latitude and there are relatively large counts at -10 to -20 degrees latitude (presumably due to marine stratocumulus). The predominantly westerly winds (ascending orbits positive HLOS winds) in the mid-latitudes and easterlies in the tropics are evident also. The much stronger westerlies at 250 hPa (Figure 121) and narrower tropical band of easterlies are evident.

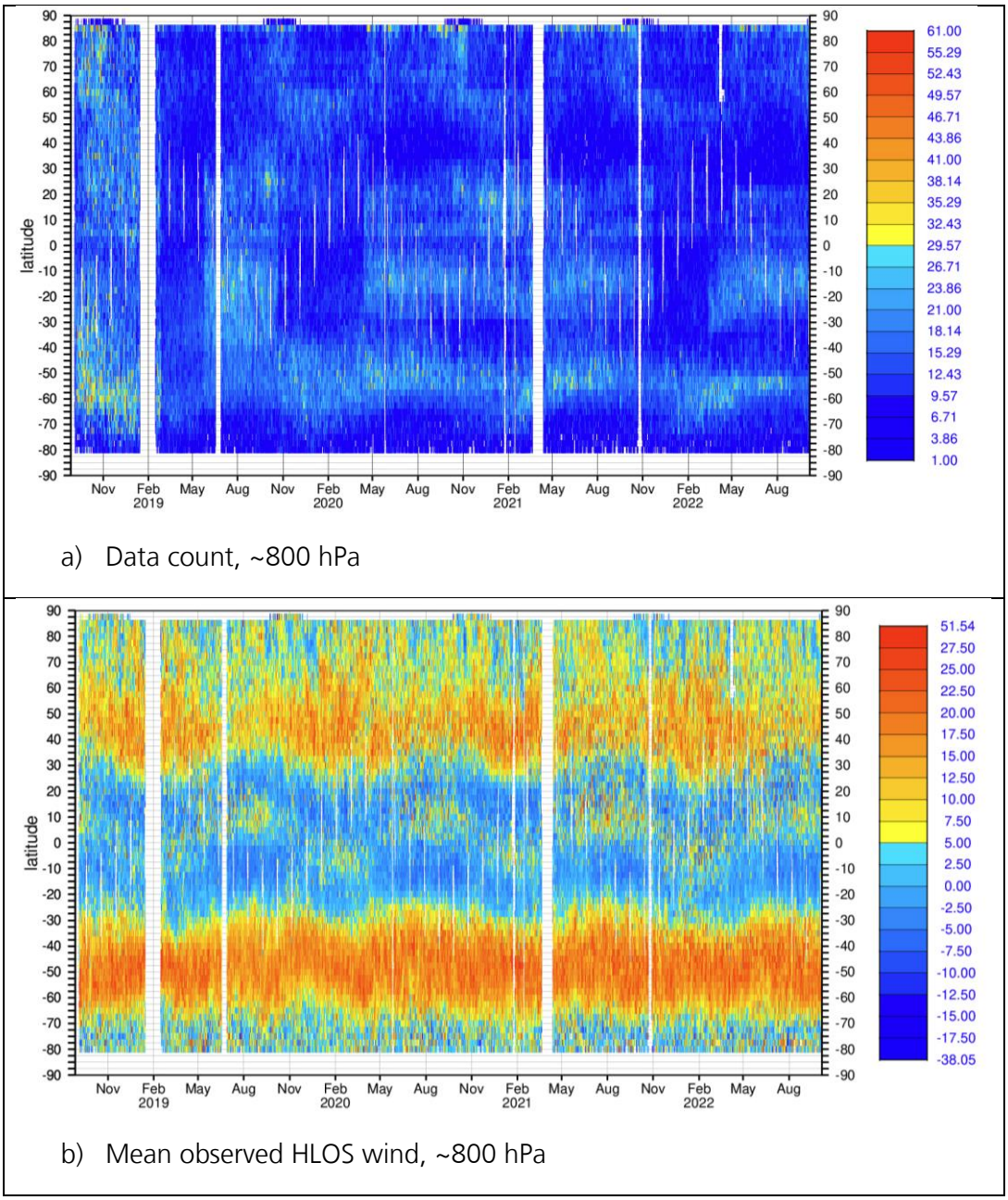

Figure 120. Latitude-time plots for L2B Rayleigh-cloudy winds for ascending orbits of a) data counts and b) mean observed HLOS wind value (m/s), for the combined 3rd (B14) and 4th (B16) reprocessing for the pressure range with largest data counts i.e. 751-867 hPa. Time-step is 12 hours.

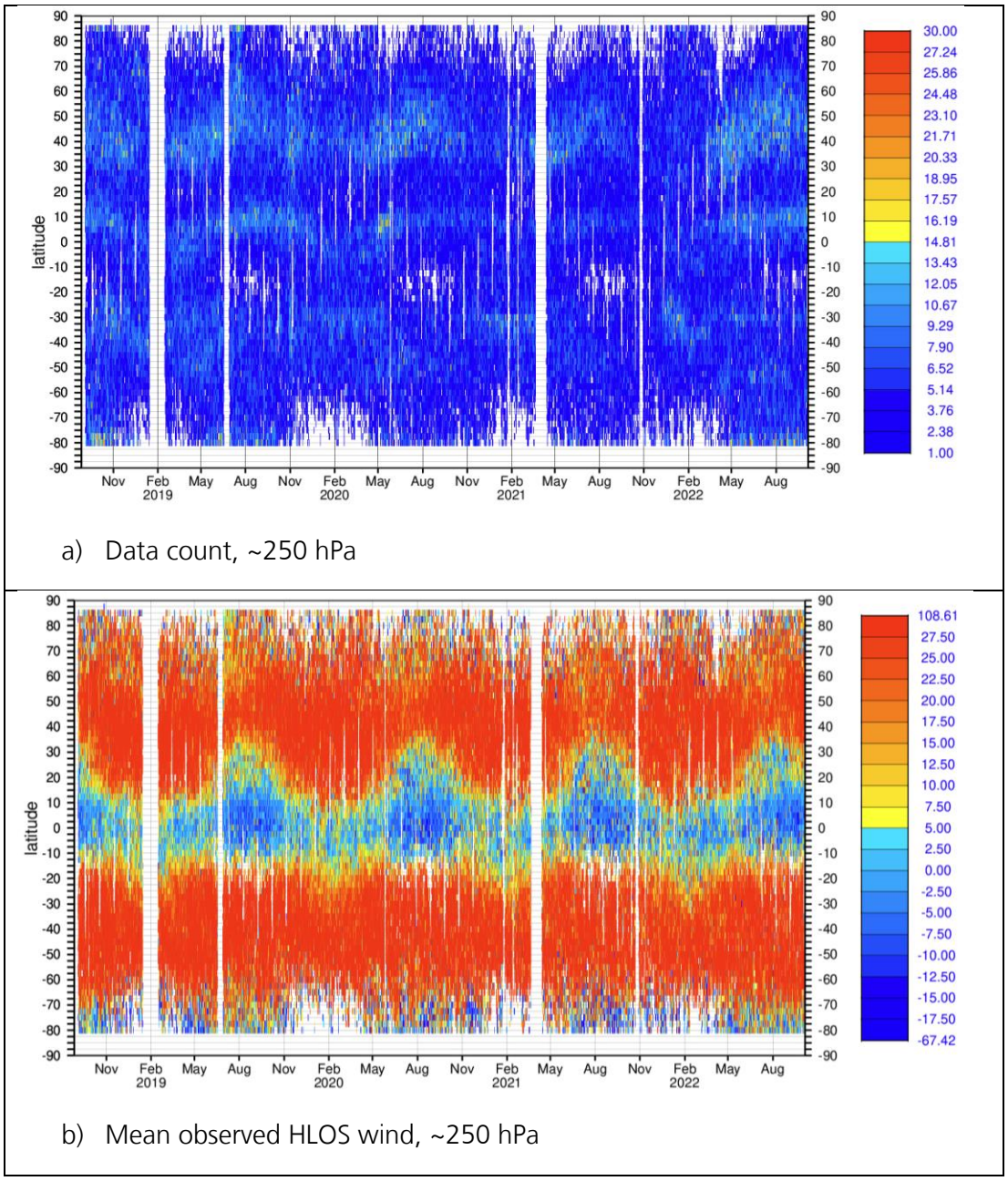

Figure 121. Latitude-time plots for L2B Rayleigh-cloudy winds for ascending orbits of a) data counts and b) mean observed HLOS wind value (m/s), for the combined 3rd (B14) and 4th (B16) reprocessing for the pressure range with largest data counts i.e. 240-277 hPa. Time-step is 12 hours.

In Figure 122, at ~800 hPa the biases look reasonably consistent between ascending and descending orbits. The least biased results tend to occur where most winds are measured.

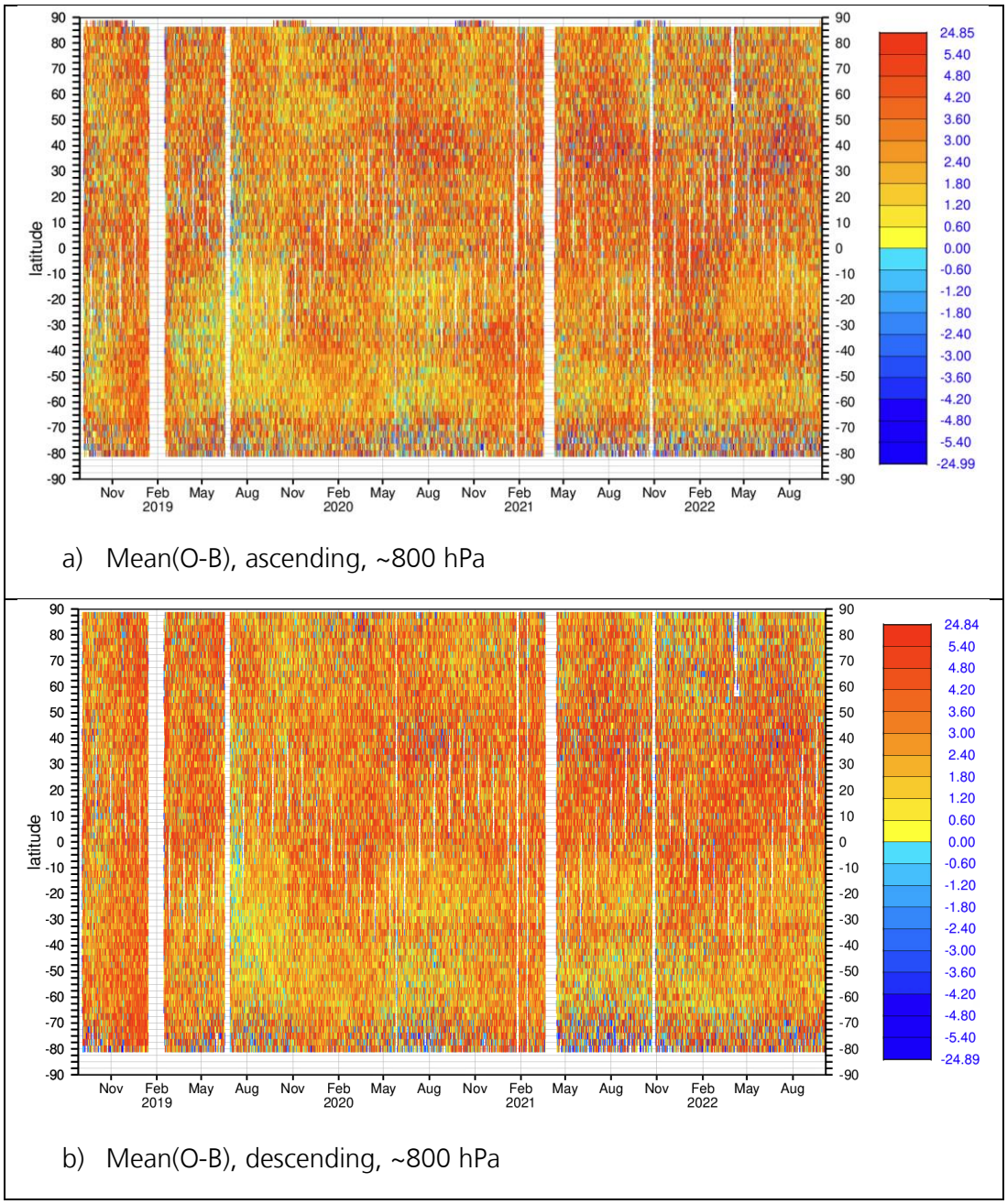

Figure 122. Latitude-time plots for L2B Rayleigh-cloudy winds of mean(O-B) (m/s) for a) ascending orbits and b) descending orbits, for the combined 3rd (B14) and 4th (B16) reprocessing for the pressure range with largest data counts i.e. 751-867 hPa. Time-step is 12 hours.

The tendency for larger positive bias in descending orbits is evident at 250 hPa in Figure 123.

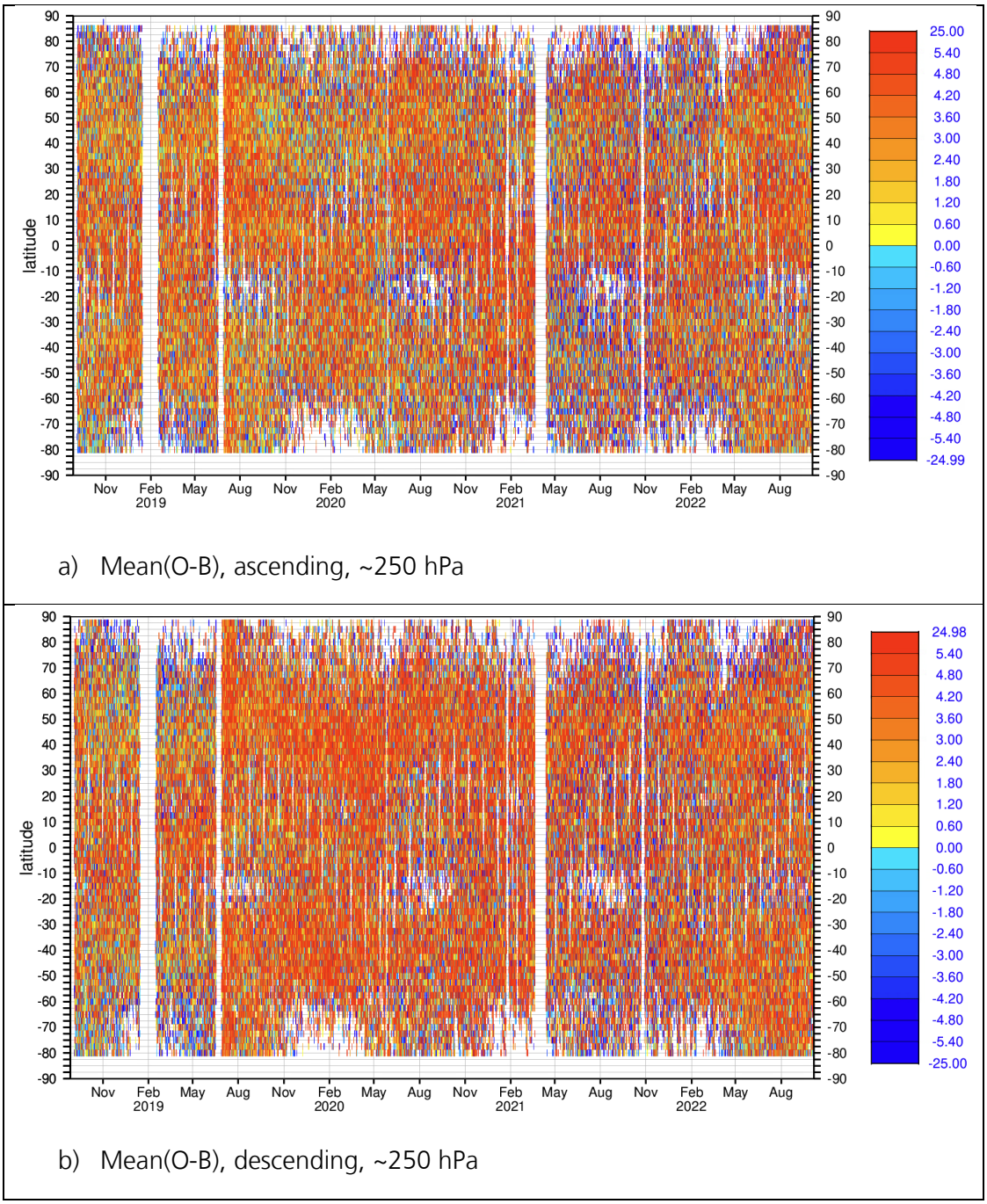

Figure 123. Latitude-time plots for L2B Rayleigh-cloudy winds of mean(O-B) (m/s) for a) ascending orbits and b) descending orbits, for the combined 3rd (B14) and 4th (B16) reprocessing for the pressure range with largest data counts i.e. 240-277 hPa. Time-step is 12 hours.

In Figure 124, random errors at ~800 hPa were smallest in the SH extratropics until November 2019 – this is when range-bin settings were altered to thinner range-bin thickness. The same is evident at 250 hPa in Figure 125.

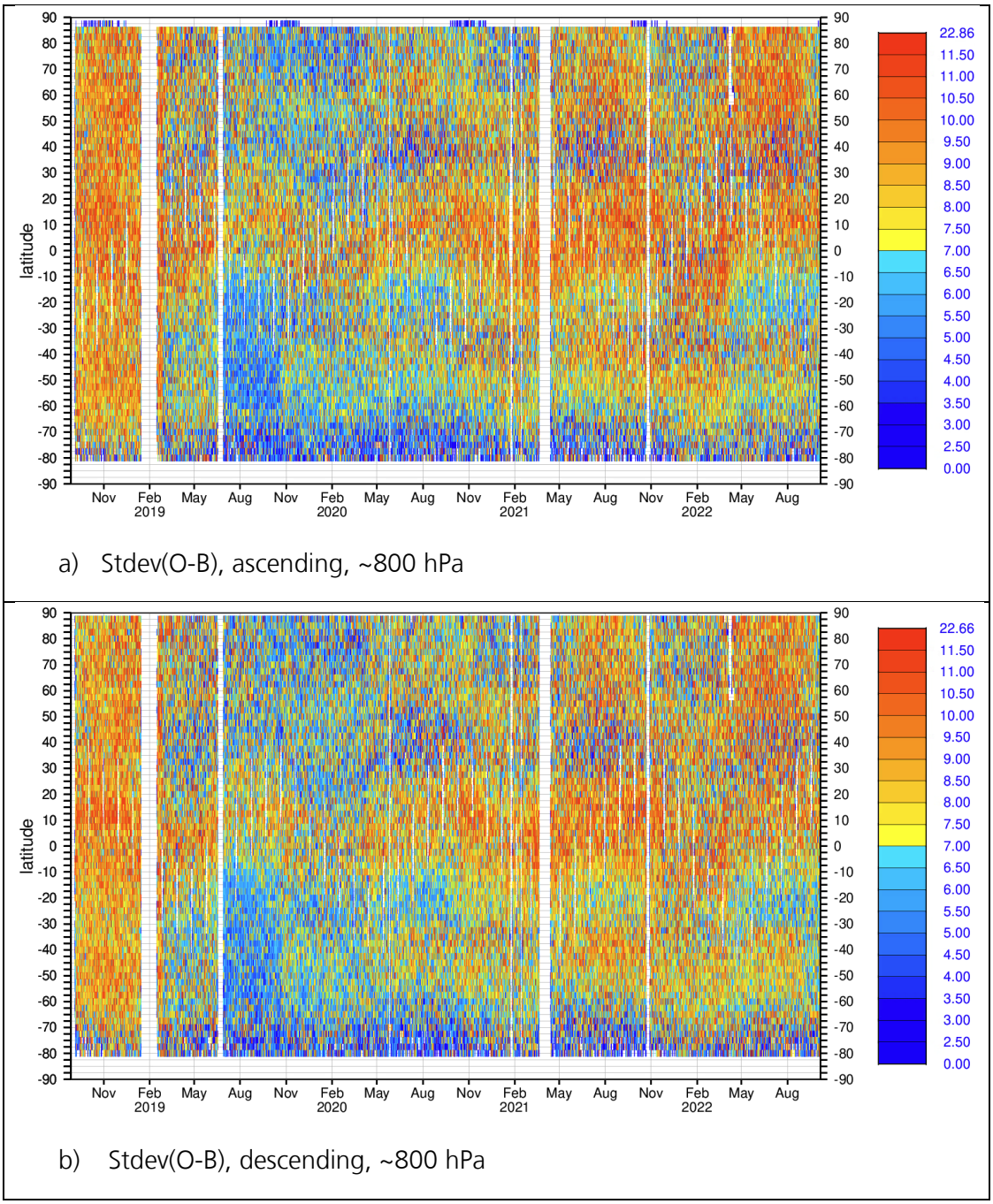

Figure 124. Latitude-time plots for L2B Rayleigh-cloudy winds of standard deviation (O-B) (m/s) for a) ascending and b) descending orbits, for the combined 3rd (B14) and 4th (B16) reprocessing for the pressure range with largest data counts i.e. 751-867 hPa. Time-step is 12 hours.

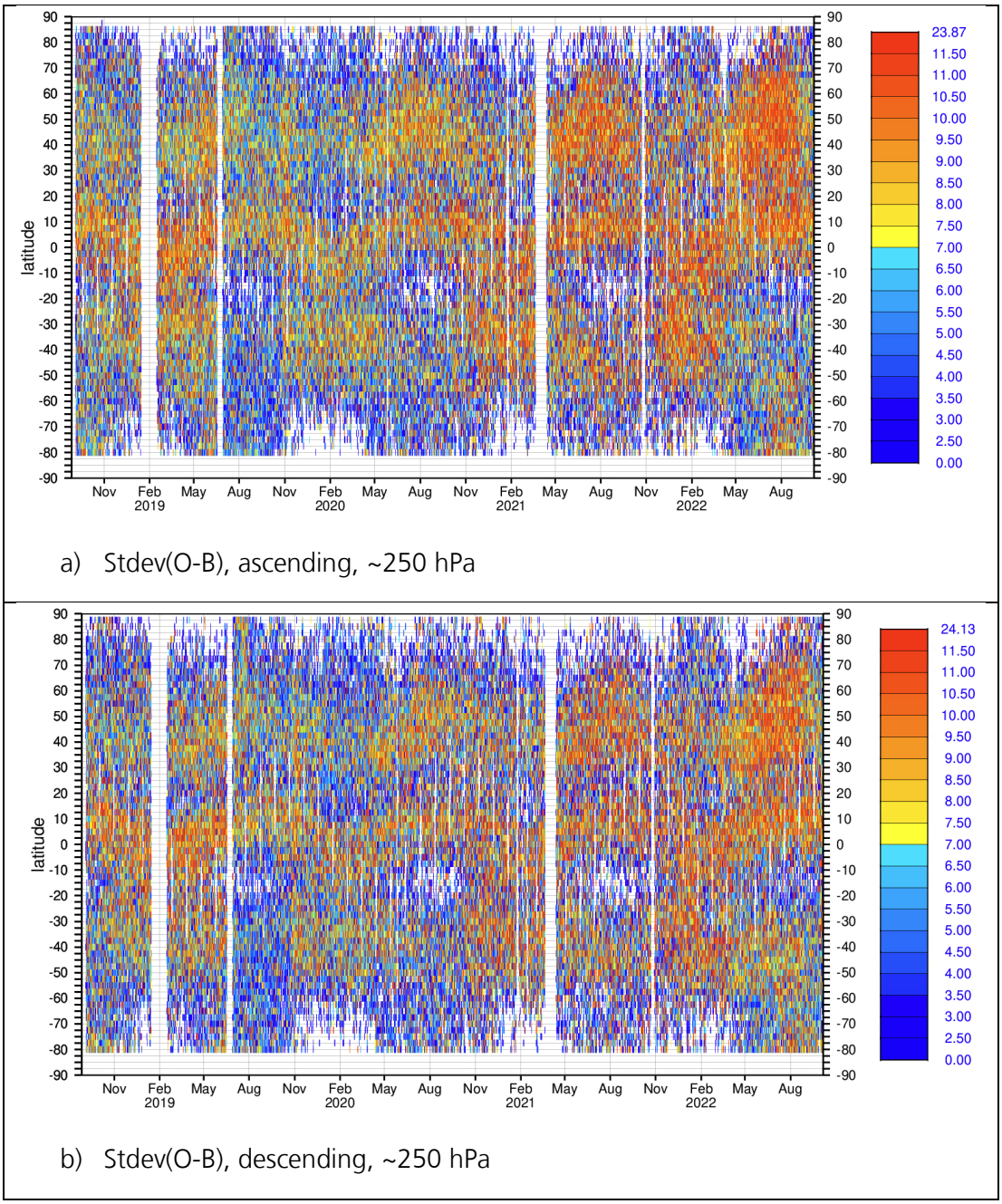

Figure 125. Latitude-time plots for L2B Rayleigh-cloudy winds of standard deviation (O-B) (m/s) for a) ascending and b) descending orbits, for the combined 3rd (B14) and 4th (B16) reprocessing for the pressure range with largest data counts i.e. 240-277 hPa. Time-step is 12 hours.

8 Conclusions

The 4th reprocessing campaign, using processor baseline B16, covers for the first time the period for continuous operation with the 2nd Flight-Model laser (FM-B) from 28 June 2019 to 4 October 2022. This is the longest consistently reprocessed dataset so far. The data was made available to the public on 22 May 2024 via ESA's website. Before and after this period the instrument was operated with the first laser (FM-A) and it is planned to release data products for these two FM-A periods with processor baseline B16 in early 2025 to provide a consistent dataset for the full mission with the B16 product quality; hence replacing the products from the 3rd reprocessing for the first FM-A period produced at B14. The current release of the 4th reprocessing data products for this FM-B period significantly improves the data quality for the L1B, L2A, and L2B product compared to the 2nd reprocessing campaign, which was performed for a shorter period for FM-B operation and with B11 processor versions. The baseline 16 processor versions were the last versions used for the near-real-time (NRT) production of the data products and was activated on 18 April 2023 for the last weeks of Aeolus operation in-orbit. The various improvements in the processing chain which benefitted the L2B winds were discussed in Section 7.2.

In the following a summary of the quality of the L2B wind and L2A aerosol products and their known limitations and known error characteristics is given, which might be improved in future reprocessing campaigns with the B17 processor versions, which are currently under development.

What is the quality of the L2B wind data product?

- A significant improvement in the Rayleigh-clear HLOS wind noise is evident. The standard deviation of O-B for the 4th reprocessing is improved relative to the 2nd reprocessing by ~15% in July 2019 and ~25% in October 2020. The profile average estimated HLOS wind error standard deviation is ~5 ms^{-1} in 2019 increasing to ~7-8 ms^{-1} in 2022 (N.B. absolute values are very sensitive to the choice of QC thresholds). At best it was ~ 4 ms^{-1} in the free troposphere in 2019.
- The Mie-cloudy noise is also improved with the 4th reprocessing compared to the 2nd reprocessing by ~9%, whilst the data count increased. The profile average estimated HLOS wind error standard deviation is ~3.3 ms^{-1} throughout the period.
- The L2B global wind bias is well constrained (close to 0 m/s) for the Rayleigh-clear and Mie-cloudy winds and the bias has smaller variability from orbit to orbit compared to the 2nd reprocessing.
- The Mie-cloudy and Rayleigh-clear wind-speed-dependent bias is improved in the 4th reprocessing compared to the 2nd reprocessing. Particularly for the Mie-cloudy, due to a new Mie non-linearity correction.
- The Rayleigh-cloudy winds also show a large improvement (~25%) in noise compared to the 2nd reprocessing, and improved bias thanks to the new parameterised correction based on scattering ratio. The profile average estimated HLOS wind error standard deviation is ~8 ms^{-1} in 2019

increasing to ~9 ms^{-1} in 2022 (N.B. applying stricter QC thresholds than here leads to more reasonable noise).

- The issue in the 2nd reprocessing of opposing sign biases for Rayleigh-clear for ascending and descending orbits in October 2019 and March 2020 has been resolved with the 4th reprocessing.
- The 4th reprocessing improves upon the NRT dataset (B13 to B15) in terms of bias and standard deviation of O-B for all L2B wind types.
- The 4th reprocessing has improved the Rayleigh-clear hot-pixel related wind biases compared to NRT dataset in 2021 and 2022 for range-bins 5, 9, 22 and 24.
- ***The following paragraph is based on the results of another activity not covered in this TN, but still of relevance:*** Based on an initial assessment of the L2B wind product and its error estimates using DLR's airborne wind-lidar campaign data from September 2019 around Iceland and September 2021 around Cape Verde we recommend to re-assess the use of Mie and Rayleigh error estimates for instrument comparison and Cal/Val. For Mie-cloudy winds, the error estimate slightly increased (< 1 ms^{-1}) in average and fewer gross errors are now more symmetrically distributed, such that the bias validation is less dependent on the error estimates-based QC-threshold. The number of valid Mie- cloudy winds has substantially increased (up to +50%), and Rayleigh-clear winds coverage has gained (~ +20%). For Rayleigh-clear the error estimate significantly increased (by up to ~ 2 ms^{-1} in average, depending on SNR), such that the number of values passing the QC is substantially reduced, when keeping the error estimate-threshold used in the validation of earlier baselines. The low number of gross errors and their homogeneous distribution leads to the recommendation to use the modified Z-score as QC-criterion for discarding gross outliers for the Mie and Rayleigh clear products.

What is the quality of the L2A aerosol data product?

- Radiometric coefficients K_{Ray} and K_{Mie} have been corrected using primary mirror M1 temperatures-based regression and provided per observation. They show continuous decrease from 2019 to 2022 partially compensated with N/P settings adjustment (i.e. switch from 30/19 to 15/38 on 2021-12-13, switch from 15/38 to 5/114 on 2022-04-04).
- Both MLE and MLEsub show valid scores despite higher error estimates. Compared to SCA and SCAMid the MLE and MLEsub show no negative outliers by concept, lower amount of non-processed bins and positive outliers except for very low altitude bins.
- The AEL-FM and AEL-PRO products are consistent with the corresponding products from the prototype processors. The feature mask shows clear features of aerosols and clouds. The AEL-PRO extinction coefficients are comparable to the extinction coefficients from the lidar on- board NASA´s lidar mission CALIPSO. This is checked with collocated orbits for some desert dust aerosols.

- We suggest using the lidar ratio when the extinction coefficient is greater than 10^{-5} m^{-1} for the AEL-PRO. All retrieved extinction coefficients and lidar ratios are provided.
- The most reliable extinction coefficients are between 10^{-6} m^{-1} and 10^{-2} m^{-1}. Valid lidar ratios are between 10 and 200 sr. The user should examine the estimated errors and the classification variable to appropriately screen the data for the purpose at hand.
- Classification between aerosols and clouds are not always reliable, especially in the areas when clouds are directly on top of aerosol layers.
- The particle effective area radius can be used for ice clouds, not for aerosols. This is not a main product. It must be used with caution.

What are the known limitations of the L2B wind data product?

- There were two long periods without L2B data due to the instrument not measuring winds: From 2021-03-22T02:56:59 until 2021-04-01T15:09:32, due to the FM-B laser switching off automatically (Survival Mode). From 2021-10-22T13:46:32 until 2021-10-29T07:56:41, due to the FM-B laser switching off automatically (Survival Mode).
- Twelve (shorter) periods occurred where the L2B winds were deliberately flagged invalid due to poor data quality which were related to instrumental tests or adjustments.
- Altitude varying Rayleigh-clear HLOS wind bias is present from June 2019 to March 2021, with a negative bias (-0.7 ms^{-1}) in the lower troposphere and a positive bias (+0.4 ms^{-1}) in the upper troposphere. This bias was also present in the 2nd reprocessing and is caused by the current choice of the calibration files. We aim at improving this for the next reprocessing.
- An increasing fraction of hot-pixel related wind biases is present for the Rayleigh-clear particularly in 2021 and 2022, as the number of hot pixels increased with time and the useful signal levels decreased. Range-bins 3, 5, 11, 13 and 22 are most strongly affected.
- The Mie-cloudy HLOS winds are slightly more negatively biased for ascending orbits compared to descending orbits in the troposphere and there is a tendency for more negative bias towards the surface more generally.
- Noise increases with time for the Rayleigh-clear winds due to a gradual decline in atmospheric path useful signal during this period. The profile, daily average Rayleigh-clear standard deviation (O-B) started at ~4.8 ms^{-1} in July 2019 and increased to 7-8 ms^{-1} by September 2022.
- The Mie-cloudy data counts decreased with time due to declining useful signal – fewer low backscatter (e.g. aerosol, cirrus) Mie winds.
- Rayleigh-cloudy HLOS winds are positively biased in the global average, up to 1.5 ms^{-1} in 2021, which we aim to improve for the next reprocessing.

What are the known limitations of the L2A aerosol data product?

- The L2A SCA and MLE products still show some limitations for isolated orbits with specific conditions linked to special operations (e.g. ALADIN instrument internal delay test, M1 telescope thermal test). The radiometric correction is degraded when top range bin is set below 16 km altitude (e.g. range-bin settings during October 2019). Both SCA and MLE products are also affected by signal attenuation above top range bin, e.g. early 2022 with Hunga volcanic aerosols spreading in southern hemisphere above up to 80 km altitudes. Moreover, the SCA appears degraded when top profile encompasses high altitude clouds or aerosols (i.e. the a-priori hypothesis of particles free condition being made for top first bin when calculating the extinction coefficient).
- The SCA product is affected by uncorrected hot pixel jumps but not the SCAmid, MLE and MLEsub.
- The assessment of the L2A SCA mid-bin data product quality was performed using the COMPO-IFS model (at ECMWF). The data seems to have similar characteristics to the 2nd reprocessing dataset and NRT data in 2022. As the ALADIN instrument only detects the co-polar component of the backscattered signal, it is underestimating the total backscatter coefficient in polarizing scenes used as model parameter in COMPO-IFS, e.g. during desert dust events. Thus, the co-polar backscatter coefficient shows lower values compared to the model in areas where desert dust is known to be present (via MODIS) and where the COMPO-IFS model contains dust plumes. For example, it is difficult to see any enhanced backscatter (above the noise) for the Godzilla event in June 2020 (in monthly average plots of the L2A observation backscatter compared to COMPO-IFS background equivalent, for which the enhanced backscatter is obvious). Areas of enhanced backscatter associated with central African wildfire smoke are however evident. It remains difficult to screen out areas of enhanced backscatter due to ice/water clouds, making it difficult to use the product for atmospheric composition applications.
- No imposed cut-off in extinction coefficients for extreme large and small values for the AEL- PRO product. This will be improved for the next reprocessing.
- Some hot pixel jumps are still present in the reprocessed data. It shows up as high values in the parameters attenuated_mie_backscatter_msp close to surrounding values and low values in attenuated_rayleigh_backscatter_msp.
- The retrieved lidar calibration constant is set to zero and will be added in next version.